Title
MICROFABRICATION AND CHARACTERIZATION OF MICROFLUIDIC ELECTROSPRAY THRUSTERS AND C-MEMS COMPOSITES

Author
Cisquella Serra, Albert

Publication Date
2022

UNIVERSITY OF CALIFORNIA,
IRVINE

MICROFABRICATION AND CHARACTERIZATION OF MICROFLUIDIC ELECTROSPRAY THRUSTERS AND C-MEMS COMPOSITES

DISSERTATION

submitted in partial satisfaction of the requirements
for the degree of

DOCTOR OF PHILOSOPHY

in Engineering with a concentration in Materials and Manufacturing Technology

by

Albert Cisquella Serra

Dissertation Committee:
Professor Manuel Gamero Castaño, Chair
Professor Marc Madou, Co-Chair
Professor Lorenzo Valdevit

2022

DEDICATION

Al meu pare Ramon,
a la meva mare Margarita
i a la meva germana Marina
a tota la meva familia Cisquella i Serra
i als que ja no hi son

Pel seu amor incondicional i la seva confiança en mi.

To Eva,
for her love,
for always think positive and keep me going,
for cheering me up even during the most challenging days of this journey.

TABLE OF CONTENTS

Page

LIST OF FIGURES **vi**

LIST OF TABLES **xiii**

ACKNOWLEDGMENTS **xiv**

VITA **xv**

ABSTRACT OF THE DISSERTATION **xviii**

1 Introduction **1**
- 1.1 History of electrospray 1
- 1.2 Electrospray propulsion 6
- 1.3 Electrospray of polymer jets: Electrospinning. 10
- 1.4 Microelectromechanical systems (MEMS) and Carbon Microelectromechanical systems (C-MEMS) 12
- 1.5 Objectives and Thesis Outline 18

2 Electrospray of high conductive liquids **20**
- 2.1 Introduction 20
- 2.2 Experimental Setup 22
- 2.3 Experimental characterization of electrospray beams 26
  - 2.3.1 Ion and droplet populations 26
  - 2.3.2 Tandem retarding potential and time-of-flight analysis 30
- 2.4 Analysis and discussion 35
  - 2.4.1 Determination of the velocity and potential of the jet in the breakup region 35
  - 2.4.2 Self-heating effects and universal jet radii 38
  - 2.4.3 Equipotential jet breakup, droplet radii and the effects of Coulomb explosions and ion evaporation 40
- 2.5 Conclusions 52

3 Microfabrication of microfluidic electrospray thrusters 55
3.1 Introduction 55
3.2 Design and Microfabrication 57
    3.2.1 Microfabrication of the emitter array electrode 58
    3.2.2 Microfabrication of the extractor electrode 70
    3.2.3 Micromachined Borofloat glass, anodic bonding and integration of all the components 72
3.3 Testing, results and discussion 79
    3.3.1 Life Time performance test 88
    3.3.2 Thrust measurements of the microfabricated electrospray sources . . 101
3.4 Conclusion 107

4 Jet initiation in polymer solutions 108
4.1 Electrospray to Electrospinning 108
4.2 Materials preparation and experimental methods 113
4.3 Jet initiation model 116
4.4 Results and discussion 123
    4.4.1 Metal tip initiation 130

5 Controlled Joule-Heating of Suspended Glassy Carbon Wires for Localized Chemical Vapor Deposition 132
5.1 Introduction 132
    5.1.1 Carbon-TMOs composites 136
5.2 Experimental Methods 138
    5.2.1 Annealing and measurement of the temperature coefficient of resistance 140
    5.2.2 Localized Chemical Vapor Deposition 141
5.3 Results and discussion 142
    5.3.1 Process parameters required for LCVD of WO3-x 142
    5.3.2 coating formation and temperature profiles 144
    5.3.3 Sample Characterization 152

6 CVD farfield electrospinning 160
6.1 Introduction 160
6.2 Experimental Methods 161
    6.2.1 Sample preparation 161
    6.2.2 IR Thermography 161
    6.2.3 Localized Chemical Vapor Deposition of WO_{3-x} 163
    6.2.4 Sample Characterization 163
6.3 Results and discussion 164
    6.3.1 Thermal characterization of the pyrolyzed mats 164
    6.3.2 Joule heating-assisted CVD 168

7 Conclusions and future work 175
7.1 Experimental study of the the electrospray beam of the ionic liquid EMI-Im 175
7.2 Microfabrication of electrospray thrusters 176

7.3 Study of the fiber initiation in Near-Field electrospinning 177
7.4 C-MEMS-$WO_{3\text{-}x}$ composites through Joule heating and CVD 179

Bibliography **182**

Appendix A Chapter 3 **194**

Appendix B Chapter 4 **196**

LIST OF FIGURES

Page

1.1 Electrospray photogram of Ethyl alcohol reported by Zeleny. (Reprinted from[146] with the permission of APS Publishing) 2
1.2 Schematic of an electrospray emitter operating in cone-jet mode. 5
1.3 Electrospinning set up configurations. a) Traditional electrospinning set up displaying the Near-field and Far-field regions.b) Typical NFES set up c) current Far-field set up 11
1.4 Spin coating process 13
1.5 Positive and negative photoresist photolithography outcome. 14
1.6 Schematic of a a) DRIE and b)Lift-off process 15
1.7 a) Schematics of C-MEMS process and models for the structure of Glassy Carbon obtained at b) low-temperature and c) high-temperature [60] 17
1.8 Schematics of C-MEMS process. Scale bar is 100 μm. 18

2.1 Ionic liquid pair [EMIM$^+$][NTf$_2^-$]. a) Atomic composition of the cation and anion and b) 3D molecular structure, (Reprinted from[131] with the permission of ACS Publishing) 21
2.2 Experimental setup: electrospray source, vacuum chamber and detectors. . . 23
2.3 Retarding potential (electrostatic mirror) and time-of-flight analyzers operated in tandem. 26
2.4 Time-of-flight curves of the whole beam, for several beam currents and two emitter temperatures. 28
2.5 Retarding potential curve illustrating multiple ionic peaks. Red and black traces are same spectra with different vertical scales. 30
2.6 Retarding potential distributions for several beam currents at 21 °C. 32
2.7 Time-of-flight spectra at different retarding potentials (see black dots in Fig 2.6) for $I_B = 230$ nA, 21 °C. 34
2.8 Average mass-to-charge ratio vs. retarding potential of droplet populations and ion peak P$_1$ from spectra in Fig. 2.13. Main droplets and P$_1$ ions are emitted from the jet breakup. 37
2.9 Average mass-to-charge ratio vs. retarding potential of main droplets and ion peak P$_1$, for several beam currents at 21 °C. 38
2.10 Critical droplet radius R_D^* normalized with the radius of the jet, as a function of the Taylor Ψ and Ohnesorge numbers, $Oh = J^{-1/2}$; and Rayleigh limit of the droplet with the mass-to-charge ratio of the jet. 45

2.11 Droplet radius normalized with the critical droplet radius $R_D^*(J, \Psi)$, for a beam current of 230 nA at 21 °C and three different mechanisms: equipotential breakup R_ϕ; Rayleigh limit R_{Ray}; and ion evaporation limit R_{IFE}, with $E_{IFE} = 1.2eV$. 48
2.12 Retarding potential curves for several beam currents at 50 °C. 50
2.13 a-c).TOF spectra for a 255 nA beam at 50 °C. d) average mass-to-charge ratios with standard deviations of the droplet populations. 51

3.1 a) Exploded view of the components of the electrospray source; micromachined glass wafer, emitter array electrode, and extractor electrode b) Section view of the assembled electrospray head thruster showing the side gap and top gap between the emitter array electrode and the extractor electrode granting voltage isolation between them. 58
3.2 Schematic of the microfabrication process of the emitter array electrode. . . 59
3.3 a) 4 inch Si wafer with 64 microfluidic pattern b) 4 inch Si wafer with 256 microfluidic pattern 59
3.4 a-c) profilometry inspection of the etched microchannels 60
3.5 Emitter array lithography backside aligned with the microlfuidic channels ends with 100, 80 and 70 μm external diameters and 40 μm inner diameter 62
3.6 a-b)Gradual etching of the SiO_2. c)Profile view from profilometer of the SiO_2 etched mask. 63
3.7 Photolithography mask covering the SiO_2 mask with an opening matching the inner hole of the emitters with different external diameters. 63
3.8 a) Photoresist after the inner hole etch b) SiO_2 mask exposed after the etching of the inner hole and the stripping of the photoresist. 64
3.9 a) Optical image from the top of the well and emitter after the final Si etch step. b) Side view of the array from the profilometer. c-d) over etched well displaying the match of the microfluidic channels of the backside with the emitters on the front side of the Si wafer. 65
3.10 SEM image of an emitter, part of the array, after the final Silicon etch step with the SiO_2 mask, and details of the etch-passivation etch marks typical of the bosh process. 66
3.11 SEM pictures of the etch through of the inner holes of the emitter array matching the end of the microchannels in the back side of the wafer with the SiO_2 dry oxidation stopping layer. 66
3.12 Etching rate of the SiO_2 thermal oxide layer on the microchannels side of the emitter array electrode, using BOE. 67
3.13 Etching rate of the SiO_2 thermal oxide layer and PECVD layer on the emitters side of the emitter array electrode, using BOE. 68
3.14 Etching rate of the SiO_2 thermal oxide layer and PECVD layer on the emitters side of the emitter array electrode, using BOE. 69

3.15 64 and 256 fabricated emitter array electrodes. (a) photograph of the top view of the 64-array emitter electrode with the emitters and the surrounding well. (b) photograph of the backside view of the 64-array emitter electrode with the microfluidic channels. (c) Amplified view of the 64 emitter microchannel arrays. (d) photograph of the top side view of the 256-emitter array electrode with the microfluidic channels (e) photograph of the back side view of the 256-array emitter electrode with the microfluidic channels. 70
3.16 a. Schematic of the fabrication of the extractor electrode. b and e) top and back side view of the extractor for a 64 emitter electrospray source. c-d) top and back side view of the extractor for a 256 emitter electrospray source. . . 71
3.17 a)Schematics of the custom set up used for bond anodically the emitter array electrode to the glass wafer aligned using Zirconia mica rods.b) Depletaion layer that generates the permanent bonding. c) Final result after the bonding. 73
3.18 a-b) Photographs of the microchannels side of a 64 for emitter array electrode and a 256 emitter array electrode anodically bonded to the glass wafer.c) Optical Picture of the orifice to insert the fused silica line matching the main microfluidic channel. d) Top side of the emitter array electrode shown in a), showing the emitter array. e) Test of the sealing of the channels with a discontinued microchannel. 74
3.19 a) Schematic of the anodic bonding of the extractor electrode to the glass wafer aligned with the emitter array electrode.b) Schematic of the compact electrospray thruster head bonded. 75
3.20 Layout of the emitter array section aligned and bonded with the extractor electrode, displaying different wafer thicknesses used to fabricate the emitter array electrode and with a fixed depth of the extractor to 750 μm. All distances are in μ, and the distance between emitters is always 1mm. a) Gap between emitter array electrode fabricated with a 500 μm wafer with extractor electrode. b) Gap between emitter array electrode fabricated with a 450 μm wafer with extractor electrode. b) Gap between emitter array electrode fabricated with a 400 μm wafer with extractor electrode. 76
3.21 Completed 64 and 256 emitter electrospray thruster head. a-b) Microfluic channels side view. c-d) emitter array and extractor view. 77
3.22 a) SEM image showing of the extractor electrode and the emitter array. b-c) Optical images focusing the emitter array and the extractor electrode aligned and bonded. 78
3.23 Assembly process of a single emitter source. a) Single emitter electrode b) Extractor electrode c) Emitter electrode and extractor electrode aligned and bonded to the glass wafer. d) Profile view of the etched emitter. e) Etch through of the single emitter in one single microchannel 79
3.24 a) Schematic exploded view of the assembly b) 256 emitter array assembled with the vacuum flange. 80
3.25 a) Schematic of the testing b) vacuum chamber and assembly used. c) 256 emitter head trhuster inside the vacuum chamber facing the collector. 81

3.26 P-I curves for the electrospray thrusters heads tested. a) P-I curve for the 256 emitter array electrode operated at 1800V. b) extractor current amplified from a) c) P-I curve for the 64 emitter array operated at 2000V d) P-I curve for the single emitter electrode operated at 1715 V. 85
3.27 a) Emitter current as a function of the normalized ΔP driving the propellant for the tested thrusters b) Total flow rate and beam current per emitter. Flow rate is obtained using pressure ramps shown at Figure 3.26 86
3.28 a) Voltage-Beam current ramp for two 64 emitter sources operating at 314 Torr and 130 Torr propellant pressure fixed with a 225 μm gap and 280 μm gap between emitters and extractor electrode. b) Voltage-Beam current ramp for a 256 emitter source operating at 430 Torr propellant pressure fixed and with a 225 μm gap and 280 μm gap between emitters and extractor electrode. 87
3.29 64 emitter source 42 hours test, beam current and pressure of the propellant reservoir is highlighted. 89
3.30 Beam current and extractor current from Figure 3.29 90
3.31 a-f)Evolution of the electrochemical film deposition that clogs the emitters . 91
3.32 Schematics of the electrochemical system during electrospray of an ionic liquid. 92
3.33 schematic of the emitter array electrode microfabrication process to add a nobel metal 94
3.34 a)64 emitter array electrode coated with gold before the anodic bonding. b) 64 emitter array electrode with gold coating clearly damaged after the anodic bonding c) SEM image of one of the emitters after the coating and anodic bonding showin anoxidized material d-e) SEM-EDX results displaying a diffusion and oxidation of the silicon on the gold layer 95
3.35 si diffusion observed in a 40 nm platinum layer after anodic bonding 96
3.36 a) 256 emitter source with a 100 nm platinum coating. b) back of the coating without source without any deposition or impurities. c) source after the first bonding. d) SEM detail of the 100 nm coating e) EDX scan of the emitter. f) 64 emitter source bonded wih 100 m Pt coating 97
3.37 86 hours performance test of a 256 emitters electrospray source. a) Pressure-Beam current over time b) Extractor current and beam current of one day test highlighted in a) 98
3.38 Flow rate computed using P from Figure 3.37 and the temperature measurement. Green crosses are measurements of weigh in the propellant reservoir. . 99
3.39 Computed propellant mass consumption over time. The highlighted points are used to compare it with real propellant consumption measurements. . . 100
3.40 Schematics of the beam opening angle 104
3.41 Set up used in NASA Jet Propulsion Laboratory to test the electrospray thruster fabricated in this thesis with a 64 emitter source assembled for testing. 104
3.42 Set up used in NASA Jet Propulsion Laboratory to test the electrospray thruster fabricated in this thesis with a 64 emitter source assembled for testing 105
3.43 Thrust measurements of the 256 emitter array electrospray at different beam currents and emitter voltages 106

4.1 Electrospray deposition of SU-8 nanoparticles. Scale bar is 5 μm. 109

4.2 Electrospry thin film deposition of SU-8 and obtained patterns after lithography 110
4.3 Pattern obtained after a 3 second deposition and a 10 second deposition. Scale bar is 5 μm. 110
4.4 a)Electrospray jet breaks into a beam of droplets b) The jet disintegration is inhibited, and a polymer fiber is ejected 111
4.5 (a) Schematic of the experimental setup used for the analysis of jet initiation; (b) jet initiation in the emitter/plate configuration; (c) jet initiation in the emitter/rod/plate configuration. 114
4.6 Evolution of the liquid meniscus at increasing potential in the emitter/rod/plate configuration : (a) photographs at increasing voltage, up to the ejection of the jet; (b) high speed imaging of the fast evolution from spherical to conical meniscus preceding jet ejection. 116
4.7 Computational domain and boundary conditions. 117
4.8 Algorithm for solving the model. Starting with an ad-hoc spherical meniscus, an iterative scheme is used to progressively modify the free surface until convergence 121
4.9 Correlation between the height of the liquid column and the radius of curvature of the meniscus in the absence of electric field, used to obtain the surface tension of the fluid 122
4.10 High speed photographs of the liquid meniscus transitioning to a conical shape and the jet formation. (a) and (b) are for the emitter/plate configuration, and emitter potentials of 500 V and 1000 V respectively. (c) and (d) are for the emitter/rod/plate configuration and emitter potentials of 1100V and 1500 V respectively 124
4.11 Percentage of successful jet initiations for the emitter/plate and emitter/rod/plate configurations, as a function of the emitter potential. The statistical value is obtained from 15 experiments at each condition 125
4.12 Electric potential field surrounding the meniscus for the emitter/plate and emitter/rod/plate configurations at jet initiation, for a tip angle of 89.95^o. The gaps between emitter and grounded plate are identical (2.73 mm). Contour lines are 50 V apart; (b) electric field on the meniscus surface for both configurations. 126
4.13 Instant just before the jet is formed in the emitter/rod/plate configuration. In each case the collector is moved towards the emitter at fixed voltage. From 500V to1100V the meniscus touches the rod before releasing a jet *(contact jet mode)*. From 1200V to 2000V the jet is released from a free-standing conical meniscus *(non-contact jet mode)* 128
4.14 Comparison of the experimental and model onset voltage laws for the emitter/plate (a) and (c), and emitter/rod/plate configurations (b) and (d); (a) and (b) show typical potential fields and the definitions of the initiation distances; (c) and (d) show the onset voltage laws (emitter potential vs gap between meniscus and collector at jet initiation). The envelopes of the shaded areas correspond to a surface tension ±10% of the nominal value γ=0.046 N /m 129
4.15 131

5.1 a) Schematic of the fiber deposition on a lithography pattern b) Fiber suspended in a lithography scaffold before pyrolysis. 133
5.2 a) Overview of a suspended carbon fiber in a carbon scafold with different gaps b) Two suspended glassy carbon wires with different diameters. 134
5.3 a) Overview of a suspended carbon fiber in a carbon scafold with different gaps width b) Fiber suspended in a lithography scaffold before pyrolysis. . . 135
5.4 Figure 1. Schematics of the microfabrication steps for performing LCVD on a suspended GCW: (a) deposition of a polymer fiber on a SU-8 patterned scaffold using near-field electrospinning; (b) pyrolyzed carbon monolithic structure with suspended GCWs; (c) e-beam deposition of silver pads for electrical contacts; (d) integration of the carbon monolith in a ceramic package including an RTD sensor; (e) annealing and measurement of the temperature coefficient of resistance of the GCW; (f) LCVD of WO_3-x on GCW. 139
5.5 Schematics of the 4-probe voltage driven set-up used to perform LCVD. The current and voltage at the terminals of the GCW are measured to obtain its resistance. 141
5.6 GCWs after LCVD process at pressures above 160 mbar. The GCW appears burnt or thinned 143
5.7 a) SEM pictures of suspended GCWs before and after the LCVD process; b) overview of multiple fibers suspended from scaffolds, illustrating how they can be locally coated (bright fibers) or left uncoated (darker fibers) without contaminating the carbon scaffold. 143
5.8 a) SEM pictures of suspended GCWs before and after the LCVD process; b) overview of multiple fibers suspended from scaffolds, illustrating how they can be locally coated (bright fibers) or left uncoated (darker fibers) without contaminating the carbon scaffold. 146
5.9 Temperatures profiles along the GCW, equation (7), for and , and different lengths of the coating : Curve 1 is for an uncoated GCW; Curve 2 is for a GCW with a coated section having a resistivity one third of the original GCW and extending 20% of the GCW length; Curve 3 is for a coated section with negligible resistivity and extending 20%. 149
5.10 Profiles of the A and B GCWs (black), together with their profiles after deposition of $WO_{3\text{-x}}$ (red). 151
5.11 Local coating melting at high values of I/I_{on} during LCVD. In a) the coating has melted at some points along the fiver, while in b) the GCW appears stripped of coating which, after melting, has deposited in surrounding areas . 152
5.12 Procedure for making cross-sectional cuts of coated GCWs. a-b) A protective Pt layer is deposited with the electron/ion beam. c) The fiber is attached to an omniprobe and cut on either end to free it from the scaffold. d) The fiber is transferred to a TEM grid and the cross section is polished by ion beam to smooth the surface observation. 153
5.13 a & b) SEM images of the surface microstructure of typical coatings; c) SEM image of the cross section of a coated GCW; d-f) EDX elemental mappings of carbon, oxygen and tungsten of the cross section in c); g) Raman spectrum of an uncoated GCW; h) Raman spectrum of a GCW coated with $WO_{3\text{-x}}$. . . 155

5.14 a) bright-field TEM image showing the polycrystalline tungsten oxide coating surrounding the amorphous carbon wire; b) magnified image of the area outlined in a); c) dark-field TEM image of the coating, interface and GCW showing isolated voids in the coating; d-f) HR-TEM images of the bulk of the coating, interface and amorphous GCW core. 157
5.15 Indexed selected-area electron diffraction (SAED) pattern of the tungsten oxide coating (SAED pattern in Figure 5.14.d The dominant phase is monoclinic WO_3 (JCPDS Card No. 830951), based on the best match for the atomic plane d-spacings in combination with the corresponding plane Miller indixes shown in Table B.2 in Apendix XX 158
5.16 HR-TEM images with measurements of lattice spacings. a) Bulk of the $WO_{3\text{-x}}$ phase; b) interface between coating and GCW; c) detail of the crystalline phase in the interface, away from the GCW; d) detail of the crystalline phase in the interface, near the GCW 159

6.1 a) carbon nanofiber mat with rectangular shape connected to copper connections; b) SEM image of the carbon nanofiber mat; c) SEM image of the cross-section of the mat. 162
6.2 a) IR-Thermogram of the carbon nanofiber mat during the voltage ramp at an applied voltage of 6.6 V; b) $I(V)$ curve during Joule heating; c) average temperature of the mat computed from the IR-thermogram as a function of dissipated electric power; d) resistance of carbon mat as a function of average temperature. 165
6.3 Comparison between measured (left) and computed (right) temperature fields for different values of the dissipated electric power, for two different carbon nanofiber mats a) and b) 167
6.4 Average temperature vs dissipated power density for two mats with different areas. Comparison between measured and computed average temperatures. . 169
6.5 (a) Schematics of the process steps to obtain uniformly WO3-x coated carbon nanofibers by joule heating. (b) SEM pictures of carbon nanofiber matrix before and (c) after the WO3-x deposition by joule-heating. 170
6.6 a) $I(V)$ curve of a carbon nanofiber mat during Joule heating, signaling the start of CVD; b) SEM pictures of the carbon nanofibers right before the onset of CVD; c) image of the nanofibers right after the onset of CVD. 171
6.7 a) $I(V)$ curves of several samples during Joule heating-assisted CVD; b) Photograph of a mat exhibiting a the typical coloration of WO_{3-x} coatings; c)-f) SEM images of the coated nanofibers in different samples. 172
6.8 a) Raman spectrocscopy of a non-coated carbon nanofiber mat; b) Raman spectroscopy of a coated carbon nanofiber mat. 173
6.9 X-ray photoelectron spectroscopy of a coating showing main photoelectron lines of tungsten 4f (a) and oxygen 1s (b). 174

7.1 Initiation of Near-field electrospinning on the bases of first principles 178
7.2 A) Joule Heating CVD of a single suspended fiber. B) Joule Heating CVD of a CNF mat. 181

LIST OF TABLES

Page

1.1 Subcategories of smallsats based on its total mass 8

2.1 Ionic peaks in Fig. 2.5. The comparison between the ratio of retarding potentials and masses indicate the composition of each ion. 31
2.2 Relevant parameters of EMI-Im electrosprays at 21C: flow rate Q; beam current I_B; dimensionless flow rate $\tilde{Q}$ and beam current $\tilde{I}$; nominal mass-to-charge ratio ζ_J and velocity v_J of the jet in the brekup; nominal jet radius R_J, and value normalized with Gañán-Calvo's characteristic length $\tilde{R}_J$; Rayleigh limit radius $R_{Ray}(\zeta_J)$ of droplet with mass-to-charge ratio ζ_J; potential drop along the cone-jet $\phi_E - \phi_J$; normal electric field on the jet's surface $E^o_{n,J}$; jet's viscosity J and electrification Ψ parameters 39

3.1 Design parameters of the assembled microfabricated electrospray head thrusters 83

5.1 Values of the diameter, length, resistance at room temperature R_0 and TCR of different GCWs before WO_{3-x} deposition, together with the coating thickness and resistance at room temperature after deposition. 146
5.2 Information of the parameters used in the qualitative analysis performed by EDX and the Weight %, statistical error (σ) and Atomic%. 155

ACKNOWLEDGMENTS

I want to start by thanking my research supervisor, Professor Manuel Gamero Castaño. I recognize how lucky I have been to work under his supervision. Professor Gamero has spent countless hours in the Electric Propulsion Laboratory patiently guiding me through very complex electronics and physics involving electrospray experiments. His knowledge in electrospray atomization, electric propulsion, fluid dynamics and thermodynamics have been invaluable. I want to thank him also on the personal side, for his support, dedicated involvement, and to always keep me motivated and productive while enjoying the day-by-day research of my PhD journey.

I also want to thank my co-supervisor Professor Marc Madou. Professor Madou opened the door of University of California, Irvine to me. Joining the Biomems Lab under his direction for my master's thesis and early beginning of my PhD. The microfabrication knowledge I acquired under his supervision and the opportunity to collaborate with colleagues in India and Mexico has been exceptional.

I also extend my appreciation to Professor Lorenzo Valdevit, committee member of this thesis, for being also part of my Qualification Exam committee providing excellent comments and ideas to improve my research and myself as a researcher. My deepest gratitude to Dr. Colleen Marrese for her help and delightful discussions during the collaborative project with NASA JPL.

I would also thank all the members of the Electric Propulsion Lab and Biomems Lab that I had the pleasure to encounter in these years. A particular thanks to Marco Magnani, Laia Ferrer-Argemi and Marc Galobardes, who I have worked closely with, and I am fortunate to have them as friends. Part of the work described in this thesis has been a collaborative effort with them.

The support of my family and friends from Ibiza and Barcelona has been extraordinary and has made to be thousands of miles away a light feeling. Gracies Papa, Mama, Manucha, Guelus, avia, cosins i tiets. Thanks to all my Ibiza gang and to my IQS family for always being there, for the visits and for making me feel I never left when I am there with you.

My life as a graduate student has been defined by my environment and it could not have been better. I will always be grateful to my new American and international friends for expanding my world and make my stay in the US a unique experience so far.

Finally, I would like to acknowledge the different sources and organizations that funded my PhD; UC Irvine MMT Program Admission Fellowship, the Balsells Fellowship, the National Science Fundations (NSF) and the National Aeronautics and Space Administration (NASA)

CURRICULUM VITAE

Albert Cisquella Serra

EDUCATION

Doctor of Philosophy in Engineering with a concentration in Materials and Manufacturing Technology **March 2022**
University of California, Irvine *Irvine, California*

Masters of Science in Materials Science & Engineering **June 2017**
IQS School of Engineering *Barcelona, Spain*

Bachelor of Science in Chemical Engineering **June 2015**
IQS School of Engineering *Barcelona, Spain*

RESEARCH EXPERIENCE

Graduate Student Researcher **2017-2022**
University of California, Irvine *Irvine, California*

- Developed and optimized a scalable microfabrication process of silicon micro-emitters for a compact microfluidic electrospray propulsion system. The process to microfabricate the electrospray thruster involves: Photolithography, Deep Reactive Ion etching (DRIE), wet etching, Plasma Enhanced Chemical Vapor Deposition (PECVD), anodic bonding, Atomic Layer Deposition (ALD) and sputtering. More than 1000 hours of experience working in a 1000-100 class cleanroom facility.
- Testing of the electrospray thrusters in custom vacuum chambers coupled with electronics measuring currents of the order of pA. Experience in testing electrosprays of ionic liquids with time of flight (TOF) and retarding potential techniques.
- Fabricated monolithic glassy carbon structures with suspended glassy carbon nanowires (GCW) using photolithography, Near-field electrospinning, and pyrolysis.
- Fabricated Carbon Nanofibers mats through far-field electrospinning and pyrolysis.
- Measured the thermal and electrical conductivities of GCW and carbon nanofibers (CNF) mats and its joule-heating behavior.
- Optimized a new technique for conformal chemical vapor deposition on micro-nano carbon structures using controlled Joule heating to trigger the decomposition of chemical precursors of transition metal oxides

Research specialist **2016-2017**
University of California, Irvine *Irvine, California*

Synthesis of carbon fibers with far-Field electrospinning technique and pyrolysis. Analysis of the degree of graphitization through Raman spectroscopy.

TEACHING EXPERIENCE

Teaching Assistant **Spring 2019**
University of California, Irvine *Irvine, California*

MAE 60 Electrical Cirtcuits

REFEREED PUBLICATIONS

A. Cisquella-Serra, M. Galobardes-Esteban and M. Gamero-Castaño, "Improved Life Time performance of microfabricated silicon based electrospray thrusters without voltage alternation operation," *Under preparation.*

A. Cisquella-Serra, M. Galobardes-Esteban and M. Gamero-Castaño, "Scalable microfabrication of Silicon Micro-Emitters for a compact Microfluidic electrospray propulsion system," *Under Review.*

A. Cisquella-Serra, M. Magnani, M. Madou and M. Gamero-Castaño,, "Electrospun PAN-derived carbon nanofibers coated with $WO_{3\text{-x}}$ with high resolution Chemical Vapor Deposition," *Under Review.*

M. Gamero-Castaño and **A. Cisquella-Serra**, "Electrosprays of highly conducting liquids: A study of droplet and ion emission based on retarding potential and time-of-flight spectrometry," *Phys. Rev. Fluids*, vol. 6, no. 1, Jan. 2021.

F. Cecconi, S. Reifsnyder, R. Sobhani, **A. Cisquella-Serra**, M. Madou, and D. Rosso, "Functional behaviour and microscopic analysis of ammonium sensors subject to fouling in activated sludge processes," *Environ. Sci. Water Res. Technol.*, vol. 6, no. 10, pp. 2723–2733, 2020.

A. Cisquella-Serra, M. Gamero-Castaño, L. Ferrer-Argemi, J. Wardini, and M. Madou, "Controlled joule-heating of suspended glassy carbon wires for localized chemical vapor deposition," *Carbon N. Y.*, vol. 156, pp. 329–338, 2020.

A. Cisquella-Serra, M. Magnani, Á. Gual-Mosegui, S. Holmberg, M. Madou, and M. Gamero-Castaño, "Study of the electrostatic jet initiation in near-field electrospinning," *J. Colloid Interface Sci.*, vol. 543, pp. 106–113, 2019.

L. Ferrer-Argemi, **A. Cisquella-Serra**, M. Madou, and J. Lee, "Temperature-Dependent Electrical and Thermal Conductivity of Glassy Carbon Wires," in *Proceedings of the 17th InterSociety Conference on Thermal and Thermomechanical Phenomena in Electronic Systems, ITherm 2018*, 2018, pp. 1280–1288

L. Ferrer-Argemi, E. S. Aliabadi, **A. Cisquella-Serra,** A. Salazar, M. Madou, and J. Lee, “Size-dependent electrical and thermal conductivities of electro-mechanically-spun glassy carbon wires,” *Carbon N. Y.*, vol. 130, pp. 87–93, 2018.

REFEREED CONFERENCE PRESENTATIONS

Cisquella-Serra.A Gamero-Castaño,M. “Microfabrication Strategies and Performance Evaluation of Silicon-Based Electrospray Micro Thrusters With Different Emitter Densities”. 2021 AIAA Propulsion & energy Forum

Cisquella-Serra.A, Madou,M Gamero-Castaño,M (2020, May). “High-Resolution Nanopatterning Method of Carbon Nanofibers with Transition Metal Oxides for Electrocatalysis and Gas Sensing Applications Using Joule Heating and Chemical Vapor Deposition”. 239th ECS Meeting with International Meeting on Chemical Sensors.

Cisquella-Serra.A, Gamero-Castaño,M Madou, M. (2018, December) “Suspended Glassy Carbon Wires as a platform for Localized Chemical Vapor Deposition triggered by Joule heating”. 4th International Carbon-MEMS Meeting, Hydebarad, India.

AWARDS

Balsells Fellowship (2019)

MMT Henry Samueli Fellowship, outstanding research award (2020)

PROFESSIONAL EXPERIENCE

Project Engineer Intern **May-September 2016**
TechnipFMC *Barcelona, Spain*

Product Manager Assistant **January-September 2015**
Elion *Barcelona, Spain*

ABSTRACT OF THE DISSERTATION

MICROFABRICATION AND CHARACTERIZATION OF MICROFLUIDIC ELECTROSPRAY THRUSTERS AND C-MEMS COMPOSITES

By

Albert Cisquella Serra

Doctor of Philosophy in Engineering with a concentration in Materials and Manufacturing Technology

University of California, Irvine, 2022

Professor Manuel Gamero Castaño, Chair

Progress on miniaturization techniques in the last two decades has made it possible to scale down spacecraft subsystems to smaller sizes and power levels, which resulted on a new category of satellites with mass below 600 Kg, called smallsats. The scale-down of satellites into smallsats, the decreasing service price of commercial rocket launchers, and standardization in the manufacturing of smallsats have boosted space technology activity. However, many smallsats in orbit lack a propulsion system due to the complexity of scaling it down to the volume, mass, and low power requirements. Electrospray propulsion is a natural fit for the micropropulsion required by smallsats because it is a soft ionization technique that does not involve the formation of a plasma. A single electrospray emitter, electrospraying a high conductive liquid such as an ionic liquid, efficiently converts electric power into beam kinetic power while operating at the available power levels. Successful integration of electrospray emitter arrays requires, however, both microfabrication expertise and detailed knowledge of the fundamentals of electrosprays.

The first part of this work integrates an in depth study of a highly conductive liquid for its interest for electrospray propulsion with a scalable microfabrication method of silicon micro-emitters for a compact microfluidic electrospray propulsion systems. Its components, that include an emitter array electrode with fractal-like microchannels etched on the back side and perpendicular to the out-of-plane emitters, an extractor electrode, and a supporting micromachined glass substrate, are permanently bonded and precisely aligned using anodic bonding. The number of emitters, the hydraulic resistance of the microfluidic system, and the gap between the extractor electrode and the emitter electrode can be tailored during the initial design and fabrication steps to achieve the desired pressure and voltage operation range. The system presented demonstrates good performance, uniformity, synchrony of emission in each emitter part of the array, and a rapid response to the applied pressure in the propellant reservoir. The deposition of counter ions during operation is identified as key performance issue and addressed by adding an interface of platinum on the emitter array. The performance tests (86 hours and ongoing) demonstrate the largest operational lifetime of a microfabricated electrospray source with capillary-like emitters actively fed. The thrust measurements show thrust up to 174 μN with room for higher values. The design, fabrication, and performance of the micro-emitters shown in this work can lead to real primary propulsion solutions for smallsats.

The second part of this work utilizes the electrospray expertise to study the fiber initiation on electrosprays of high molecular weight polymer solutions, also known as electrospinning. First, I focused on the electrostatic jet initiation of a SU-8 polymeric solution studied with two different geometries in the so-called Near-Field regime to quantify the initiation parameters and illustrate the optimization of the electric field. Then, I functionalized suspended glassy carbon fibers derived from the same polymer solution using chemical vapor deposition. The temperature required for the deposition of $WO_{3\text{-}x}$ is generated by imposing a constant electrical current through the wire that causes joule heating. The deposition starts in the midpoint of the wire, extends to its ends as the current increases, and can be monitored in real-time by measuring the voltage drop across the wire. The resulting thickness and length of the coating are functions of the imposed current. This work showcases uniform and polycrystalline $WO_{3\text{-}x}$ coatings with thickness from 71 nm to 1.4 μm in glassy carbon

wires with diameters between 780 nm and 2.95 μm. The same process is scaled-up by using carbon nanofiber mats, fabricated with far-field electrospinning, where the uniform temperature increase is homogenous to a good approximation by the dominance of radiative heat transport leading to very uniform $WO_{3\text{-}x}$ coatings. The functionalization of carbon micro-nano materials described in this work can lead to novel, inexpensive, and bioavailable sensing solutions.

Chapter 1

Introduction

1.1 History of electrospray

Electrospray technique can atomize liquids into sprays of charged small droplets, ions, or a combination of both [41]. In electrospray, a liquid is typically flown to an emitter tip where it is stressed into a conical shape, known as Taylor cone, under an imposed electrical field, forming a steady jet. We can trace the beginning of electrospray to 1882, when Rayleigh estimated the maximum amount of charge a liquid droplet could carry (known as Rayleigh limit) [109]. Rayleigh predicted that a droplet reaching the Rayleigh limit could emit out jets of liquid. But the first description of an electrospray had to wait until 1914, when John Zeleny reported for the first time the electrospray phenomenon of a liquid[145], and in 1917 published the first photograms of it.

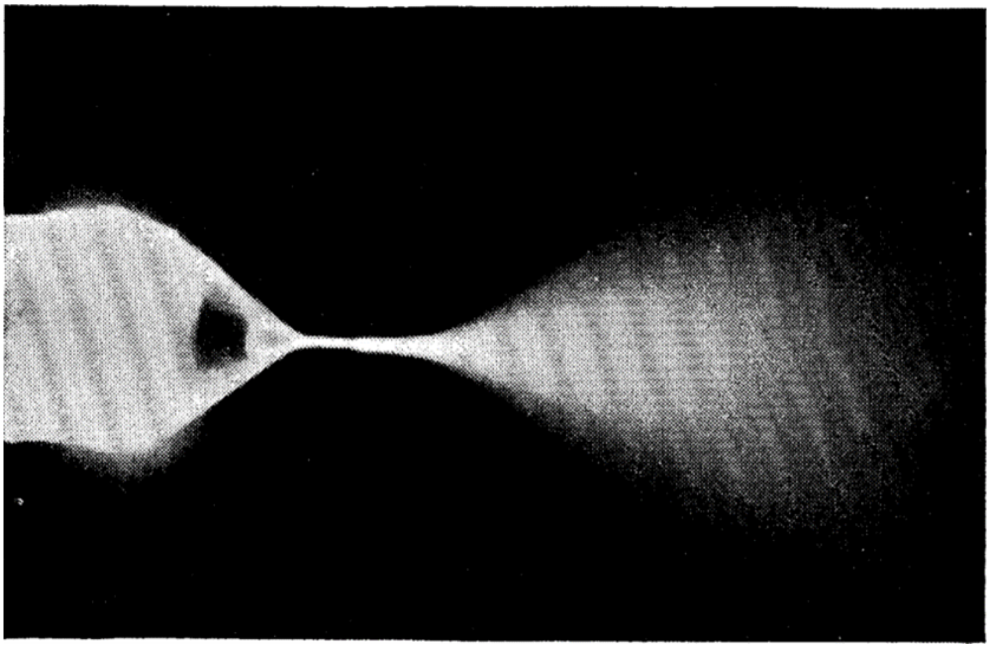

Figure 1.1: Electrospray photogram of Ethyl alcohol reported by Zeleny. (Reprinted from[146] with the permission of APS Publishing)

Following Zeleny's work, G. I. Taylor, in 1964, studied the behavior of electrically conductive liquid under an electric field. Taylor supposed that the transition from a round shape to a conical shape, resulting from applying an electric field, is a result of the perfect balance between the surface tension of the liquid and the electrostatic forces of the applied field[122] [123]:

$$\frac{1}{2}\varepsilon_0 E_\theta^2 = \gamma \nabla \cdot \overrightarrow{n} \tag{1.1}$$

Where ε_0 is the electrical permittivity of free space, E_θ is the electric field normal to the liquid surface, γ is the surface tension of the liquid, and $\overrightarrow{n}$ is the surface normal vector. He found that when the electric field overcomes the surface tension of the liquid, independent of the liquid nature and field intensity, an equilibrium solution existed: an equipotential cone with a half angle $\alpha = 49.3^{\text{o}}$, now referred as a Taylor cone. Taylor's solution predicts that the electric field normal to the liquid surface is inversely proportional to the distance from the tip[122]:

$$E_\theta = \sqrt{\frac{2\gamma \cot \alpha}{\epsilon_0 r}} \tag{1.2}$$

Where r is the distance from the apex along the liquid surface. It is important to point out, that Taylor's analytical solution accounts only for an ideal static fluid, acting as a perfect conductor, where charged particles in the fluid respond instantly to the electric field. Electrosprays in cone-jet mode operate at a given flow rate of fluid, where fluid motion cannot be ignored, with liquids of defined conductivity. The Taylor solution cannot be exact since the electric field at the apex leads to singularities such as an infinite electric field. Further research was needed to explain the physics near the apex, where the fluid velocity is high due to the conservation of mass flow rate and the electric pressure dominates over the surface charge, forming a liquid jet that breaks up into charged droplets.

The interest in narrowing down the physics of electrospray resurfaced in the late 1980's and early 90's after J.B Fenn at Yale University introduced electrospray ionization (ESI) as a tool for mass spectrometry to analyze biological macromolecules [27] [28] (which granted him the nobel prize of chemistry in 2002). Pantano et al[103] modeled an interesting zeroth order solution for electrospray in cone jet mode and, almost at the same time, Fernandez de la Mora and Loscertales found the characteristic length for the jets where Taylor's model breaks down[20]:

$$L_{FM} = \left(\frac{\epsilon \epsilon_0 Q}{k}\right)^{1/3} \tag{1.3}$$

Where Q is the flow rate, κ is the electrical conductivity and ϵ is the electrical permittivity. Together with the first scaling laws of electrospray where the current I emitted scales with the flow rate, conductivity and electrical permittivity of the liquid as[20]:

$$I \propto \sqrt{\frac{\gamma k Q}{\epsilon}} \tag{1.4}$$

Later Gañan-Calvo improved the scaling laws of the characteristic length, and proved to be in better accordance with the jet base diameter and droplet size with [52][50]:

$$L_{GC} = \left(\frac{\rho \epsilon_0 Q^3}{\gamma K}\right)^{1/6} \tag{1.5}$$

Where ρ is the fluid density. Further research helped to keep improving prediction models of the behavior of cone-jet electrosprays [30]. As long as the imposed electrification is sufficiently high to maintain the sharpness of the meniscus tip, the physics in this small region are largely decoupled from far fields and fully determine the properties of the transition region and its jet [52, 67]. Thus, in this electrospraying mode, local properties of the transition region (e.g. surface profile, surface charge density, flow field) as well as the current, only depend on the physical properties of the liquid and its flow rate, and are largely independent of the potential and geometry of the emitter[66]. The minimum flow rate to operate electrosprays in cone jet mode were also recently described [45]with the first modeling approach of the angle and current density of an electrospray beam[43]. Current research focuses on the explanation of electrosprays of high conductive liquids [41], where pure ionic emission or a mix of droplets and ions can be generated from an electrospray, increasing complexity on the physics by introducing ion emission equations. Figure 1.2 shows a schematic of an electrospray emitter operating with a high conductive liquid.

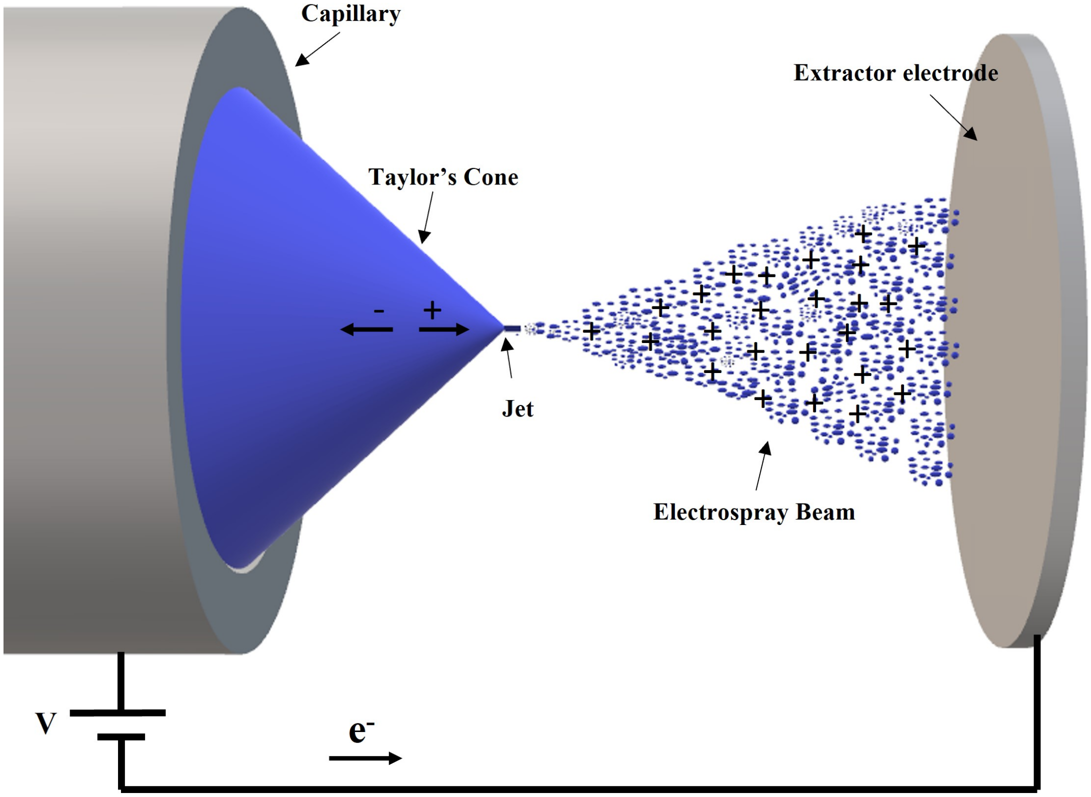

Figure 1.2: Schematic of an electrospray emitter operating in cone-jet mode.

The progress on physics understanding of electrospray has been alongside its use in different applications. Besides the famous electrospray ionization for mass spectrometry, electrospray is finding relevant applications as a micro-nano manufacturing technique to create nanoparticles and nanofibers and applications in the space industry as a promising electric propulsion technology. Those applications are further explained in the following sections of this introductory chapter.

1.2 Electrospray propulsion

Before introducing electrospray propulsion, it is essential to review some basic propulsion equations, which are key to compare and understand a propulsion system. One starting equation would be the specific impulse (I_{sp}). I_{sp}(s), measures how efficiently a propulsion system transform the propellant into thrust as shown in:

$$I_{sp} = \frac{F}{\dot{m} g_0} = \frac{ve}{go} \tag{1.6}$$

Where F is the thrust magnitude (N), $\dot{m}$ the propellant mass flow rate (Kg s-1), g_0 the Earth's gravitational acceleration constant and ve the exhaust velocity (m s^{-1}). To obtain the total impulse of a thruster I_{total}, the integral of the thrust over the total firing time must be done. Where F here is defined with the propellant mass m :

$$F = m_p I_{sp} g_0 \tag{1.7}$$

$$I_{total} = \int_0^t F dt \tag{1.8}$$

and t is the total time (s) firing the thruster. Then the Tsiolkovsky rocket equation helps to relate the I_{sp} to the propellant need for a maneuver which requires a specific ΔV in m/s (difference in velocity required by the maneuver):

$$\Delta V = ve \ln \frac{m_0}{m_{0-} m_p} \tag{1.9}$$

where m_p is the total consumption of propellant during the maneuver and m_0 is the initial total mass of the spacecraft, including propellant. By using the definition of I_{sp} given in the previous equation, it is possible to substitute and relate both terms to the need of propellant for a given maneuver:

$$m_p = m_0 \left(1 - e^{\frac{-\Delta V}{I_{sp} g_0}}\right) \tag{1.10}$$

These basic equations make it easy to explain why electrospray did not succeed when it was first recognized as a potential technology for propulsion. The first conceptual design of an electrospray thruster, also called colloid thruster, was developed by Krohn in the 60's using glycerin as propellant [83][84]. Before Taylor's physics description of the Taylor cone. The maximum charge to mass ratio of the droplet beam generated was low due to low conductivity and high vapor pressure of the propellant, which relates to low I_{sp} and the need of high electric potentials in the order of tens of Kv. That, together with a thrust level of a single electrospray emitter below 1 μN made it impossible to use it as a propulsion technology on spacecrafts of that time, which mass were on the order of thousands of kilograms. Thousands of electrospray emitters would be needed to achieve the thrust requirements, and micromachining techniques were unavailable.

Progress on miniaturization techniques on the last two decades have made it possible to scale down spacecraft subsystems to smaller sizes and power levels. Miniaturization of spacecrafts picked up in the last ten years defining a new category of satellites with mass below 600 Kg, called smallsat. smallsats are also subdivided into the subcategories described in table1.1 based on its total mass:

Table 1.1: Subcategories of smallsats based on its total mass

Mass Class Name	**Kilograms (kg)**
Femto	0.01-0.09
Pico	0.1-1
Nano	1.1 - 10
Micro	11-200
Mini	201-600

The scale-down of satellites and the decreasing service price of commercial rocket launchers have boosted space technology activity in the last years. Standardizations on the manufacturing of micro and nanosatellites such as CubeSats [92], satellites built on modular 10 cm cubes, have also provided a standard development of satellites with small budgets. During 2020, 1202 smallsats have been launched, representing 94% of the total spacecrafts launched, soaring from 389 smallsats launched in 2019 or 39 in 2011[1]. The smallsat industry is becoming the path to space capabilities for small companies, countries, and worldwide research groups that were out of reach due to cost limitations. However, one downside of the capabilities on smallsats is the lack of efficient propulsion systems. Many Cubesats in orbit lack a propulsion system [107] due to the complexity of scaling down propulsion systems to the volume, mass, and low power requirements. Chemical propulsion requires a considerable amount of propellant to achieve typical delta-V maneuver, due to their relatively low exhaust velocities (low-moderate specific impulse) and are difficult to downsize to the level of smallsats. Electric propulsion systems are better suited for small spacecrafts and typically operate with specific impulses one order of magnitude higher than chemical propulsion. Reducing significantly the amount of propellant needed for a maneuver with a given delta V. Two

---

[1] Data obtained from BryceTech" smallsat by the Numbers 2021" report.

electric propulsion technologies with extensive flight heritage are Hall thrusters and Gridded ion thrusters. Hall thrusters and gridded ion thrusters use electromagnetic radiation or high energy electrons to ionize noble gases such as xenon or krypton, forming a plasma that is accelerated at high velocities using an electric field, producing thrust with high I_{sp}. But when it comes to miniaturization, these technologies fall into several constraints due to its higher amount of components [92]. Scaling down ion gridded and Hall thrusters come with a lower ionization efficiency due to the smaller size of the ionization chamber which can only be compensated with a higher plasma density. High density plasmas are more difficult to confine with magnetic fields, even more when miniaturized[142], leading to important particle collisions with its associated material erosion, reducing its operational lifetime significantly [142].

Electrospray propulsion resurfaced as a potential alternative to conventional electric propulsion technologies when novel substances, called ionic liquids (ILs), with very high conductivities (usually $\geq$ 0.8 S m^{-1}) and very low vapor pressure, were identified as outstanding propellants. ILs are molten salts at room temperature that consist entirely of positive and negative molecular ions. It was observed that electrosprays of ionic liquids were able to generate tiny droplets with a very high charge to mass ratio distribution together with ions and, in some operational conditions, pure ion emission can also be achieved providing outstanding I_{sp}. The capacity of ILs electrosprays to generate high-velocity droplets and ions, without the need of an ionization chamber, together with the possible capability to miniaturize and multiplex electrospray emitters with MEMS technology, to increase the total thrust, makes electrospray propulsion the perfect candidate as the primary propulsion system for the smallsat arena.

1.3 Electrospray of polymer jets: Electrospinning.

The ability of electrospray to generate steady jets of droplets or fibers with diameters down to a few nanometers has also found important technological applications as microscale and nanoscale manufacturing tool. Energetic beams generated through electrospray have been reported to be used to sputter Si, Sic, inas, Ge, GaAs, Gasb, and gan [47] [114] [6] Electrospray has also been widely used as a nanoparticle deposition technology [150] [70]. But one exciting application that will be studied in detail in this dissertation is its application to generating nanometric polymer jets. Also known as electrospinning technique. There is evidence of reports about the electrospinning process during the mid-XX century. However, Darell H Reneker at the University of Akron was the pioneer describing it in scientific peer-reviewed publications [26][34] . The physical property that seems to separate an electrospray jet to break into small nanodroplets of polymer solution, leading to polymer nanoparticles, from the generation of a polymer fiber appears to fall into the molecular weight of the polymer used and its concentration in solution [116] [80]. The entanglement between polymer chains of high molecular weight in solution results in the viscoelastic nature of the liquid, essential to inhibit the natural instability of the jet, and its tendency to disintegrate into droplets. The speed and flexibility of electrospinning have led to applications in numerous fields as diverse as tissue engineering [117] [105], drug delivery [93], filtration [56] [108], gas sensors [25][23], optical photoelectric sensors [24] and catalysis [35]. Figure 1.3.a shows a typical schematic of an electrospinning set up.

Over the last decade, a significant effort has been made to adapt electrospinning into a controlled nano writing process with the capability of rapidly pattern submicron features. This work has led to a variant of electrospinning known as near-field electrospinning (NFES) [120] [63]. NFES reduces the distance between the emitter and collector to a few millimeters, avoiding bending instabilities and the associated random motion of the jet typical in traditional electrospinning as the one shown in Figure 1.3.a [141]. Thus, whereas traditional electrospinning results in mats of micro or nanofibers usually collected in a rotating drum, as shown in Figure 1.3.c, NFES is characterized by single fiber deposition with high spatial resolution. NFES has shown great potential for producing controlled sub-micron fibers of polymers, carbon, and ceramic materials.

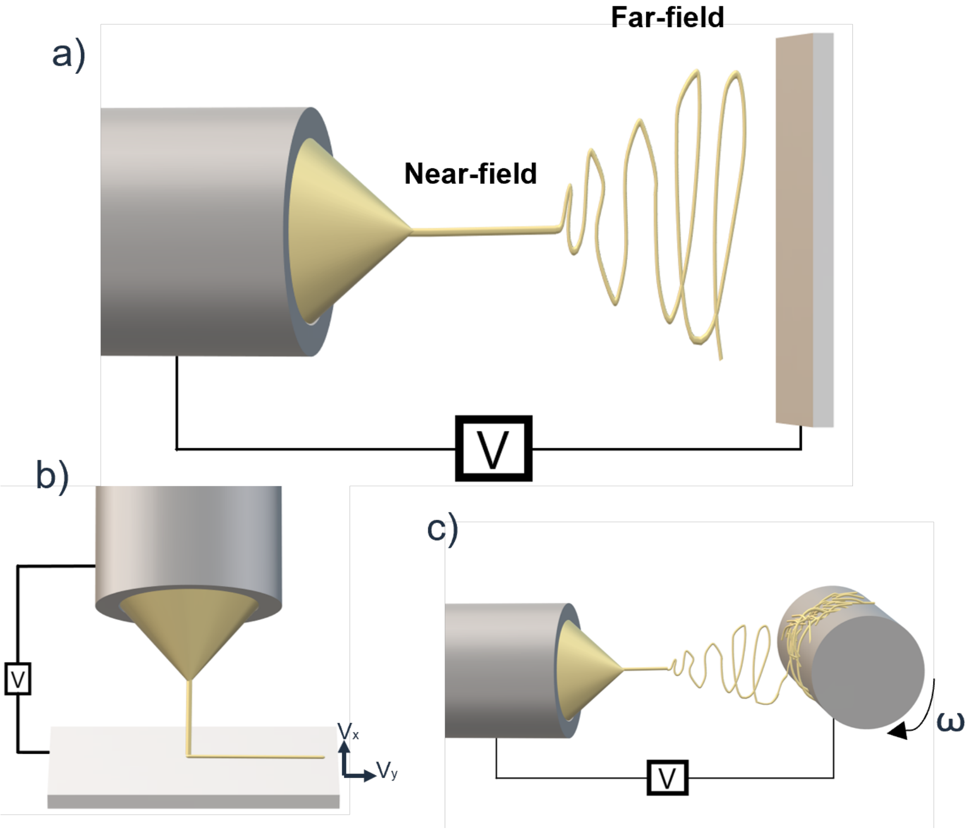

Figure 1.3: Electrospinning set up configurations. a) Traditional electrospinning set up displaying the Near-field and Far-field regions.b) Typical NFES set up c) current Far-field set up

Most of the research on electrospinning has focused on its applications and properties of the generated fibers[5] [32], while its physics has received less attention. Successful electrospinning operation is largely based on the user's familiarity with the technique and trial and error practices, probably due to the lack of a fundamental understanding of the processes involved. For example, a key step in electrospinning is the initiation of the jet. It is expected that once the jet is initiated the physics behind the process detach at some degree from the ones in electrospray, where an intersection between hydrodynamics and polymer science must be involved to explain the trajectory and nature of the fiber. But the jet initiation itself should fall in the same physics of the electrospray phenomenon, being able to describe the jet initiation in electrospinning by imputing the properties of the solution. However, the literature reports different electric fields to initiate a polymer jet using the same polymer solution [9], justifying the dimensions of the emitter and collector. This is paradoxical because the local electric field at the apex of the meniscus required to initiate the jet should be only function of the fluid's properties, not the dimensions of the emitter and collector. That triggered the interest to study the jet initiation on electrospinning, on the basis of electrospray first principles, in this dissertation. Specially polymer solutions that after electrospinning could become carbon fibers by undergoing a process of pyrolysis. The carbonization and integration of these jets into carbon microstructures fall into a recent process called Carbon microelectromechanical systems (C-MEMS), explained in the next section.

1.4 Microelectromechanical systems (MEMS) and Carbon Microelectromechanical systems (C-MEMS)

In general, MEMS refer to devices and systems that have at least one of their dimensions or components in the micrometer range. The advance of technologies to microfabricate MEMS over the last 50 years has been driven by the Integrated Circuit and Semiconductor industry. Typical processes associated with the fabrication of MEMS are photolithography, physical vapor deposition (PVD), chemical vapor deposition (CVD), Atomic Layer deposition (ALD), Deep reactive ion etching (DRIE), wet etching, surface micromachining, etc. Silicon is the material that dominates in the MEMS industry due to the maturity of its processing technologies in the micro and nanoscale. But other materials such as SiN, SiC, GaAs and carbon are finding its slot. Many of these processes to build functional devices at the microscopic level have been adapted in a wide range of industries such as biomedical, aerospace and telecommunications. In chapter 3 of this dissertation, many of these processes are used and described to miniaturize and microfabricate silicon-based electrospray emitter arrays for propulsion applications. So, it's essential to slightly describe them to understand the microfabrication strategies adopted during this work.

One of the most popular processes involved in fabricating MEMS is called photolithography. Photolithography is a patterning method that uses UV light to selectively expose, typically using a mask with the exact copy of the desired pattern, a photoresist thin film. Photoresists are polymer resins that change their chemical structure under light exposure at different wavelengths, usually being at the UV range. The process at which a thin layer of uniform photoresist is deposited on top of a substrate of interest is called spin coating. A typical spin coating process is shown in Figure 1.4.

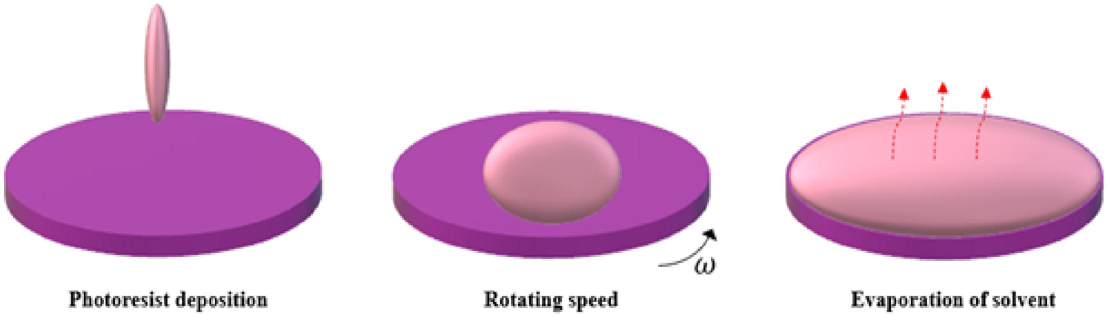

Figure 1.4: Spin coating process

The viscosity of the photoresist, the rotational speed at which the substrate is spun, and the total spinning time will dictate the thickness of the photoresist layer, usually on the order of a few micrometers. Depending on the change in the chemical structure of the photoresist after the light exposure, we can distinguish two different photoresists: negatives and positives. Some photoresists generate new chemical bonds because of the light exposure in a process called cross-linking, and others experience dissociation of chemical bonds upon exposure. The photoresist that undergoes cross-linking upon exposure is called negative photoresists, while the ones that experience dissociation of chemical bonds are called positive photoresist. The dissolving agent of the photoresist is called developer, which dissolves the non-exposed photoresist on the negative resists and the exposed photoresist for the positive ones, as shown in Figure 1.5.

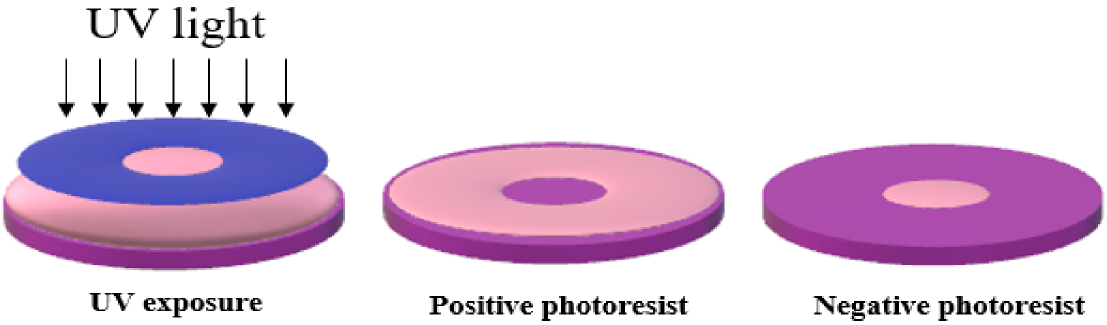

Figure 1.5: Positive and negative photoresist photolithography outcome.

This photolithography process is usually the departure (after some cleaning and adhesion promotion treatments of the substrate's surface to coat) of so many more processes in the MEMS industry, which usually involve etching or deposition processes. The technological advances in the resolution at which we can expose selectively photoresist areas have dictated the capabilities of manufacturing MEMS and NEMS (nanoelectromechanical systems) at lower scales. Current processes such as Electron-beam lithography (EBL or e-beam lithography) can directly expose areas of photoresist as low as 10 nm by focusing a beam of electrons directly on the resist without the need of a photomask. Extreme ultraviolet lithography (EUV) is another advanced tool to achieve resolutions below the 10 nm threshold. EUV uses extreme ultraviolet wavelengths reflected through Bragg diffraction alternating 40 silicon and molybdenum layers or more. It is essential to understand that these lithography technologies have as primary purpose creating a resists mask for next processes to follow, for example, Deep Reactive Ion etching, ALD or Sputtering deposition. Deep Reactive ion etching is a highly anisotropic etch process where a generated plasma of ions, of specific chemical gases, are directed with momentum to the target substrate to create openings, step-sided holes, and trenches with high aspect ratios in silicon wafers and other substrates. Figure 1.6a. shows a schematic of a deep reactive ion etching process.

Figure 1.6: Schematic of a a) DRIE and b)Lift-off process

A common process in deep reactive ion etching of Silicon is the Bosch process. The Bosch process is a pulsed or time-multiplexed etching that repeatedly alternates between two modes to achieve vertical structures on silicon with a high aspect ratio. In the first step, the plasma generated is an etching agent directed vertically; generally, SF_6 for silicon etching followed by a plasma of C_4F_8 that deposits a passivation layer similar to Teflon. These etch/deposition steps are repeated many times, resulting in a large number of short isotropic etch steps taking place only at the bottom of the etched pits. Another interesting process described in Figure 1.6.b is called Lift-off. In the Lift-off process, a target material, which is usually a thin metal layer, is deposited on the whole surface of the substrate. The thin metal layer covers the resist and the opening previously done with lithography. After stripping the photoresist, a thin layer of the metal of interest remains with the defined pattern in the previous lithography.

Several hundreds of pages would be needed just to describe the physics, instruments involved, and different outcomes of these microfabrication processes, and many more not mentioned. But the main point of this brief introduction is to set the ground to understand some of the techniques used in chapter 3 and describe a different type of MEMS called C-MEMS that will be fabricated and used in chapter 5.

As mentioned above, the photolithography process is usually an intermediate step to generate the desired micropattern by masking the substrate for further etching or deposition processes, which usually involves very expensive equipment. The photoresist pattern by itself does not usually have any capability or practical use. However, it was found that some photoresists, especially negative ones called SU-8, have a carbon-rich structure that remains after a process called carbonization. This property was used as a unique way of patterning carbon at the micro and nanoscale into a process called C-MEMS.

In C-MEMS processes, complex carbon microstructures can be generated by the carbonization of patterned photoresists or carbon-rich polymer nanofibers. During carbonization, also called pyrolysis, the carbon precursors are heated up at very high temperatures, usually $\geq 800^{o}$C in an inert atmosphere where all the non-carbon atoms are removed from the material, shrinking its volume and leading to a carbon microstructure referred to as Glassy Carbon. Glassy carbon has the advantage of being electrochemical stable and having good thermal and electrical conductivities. Figure 1.8 shows a schematic of the process.

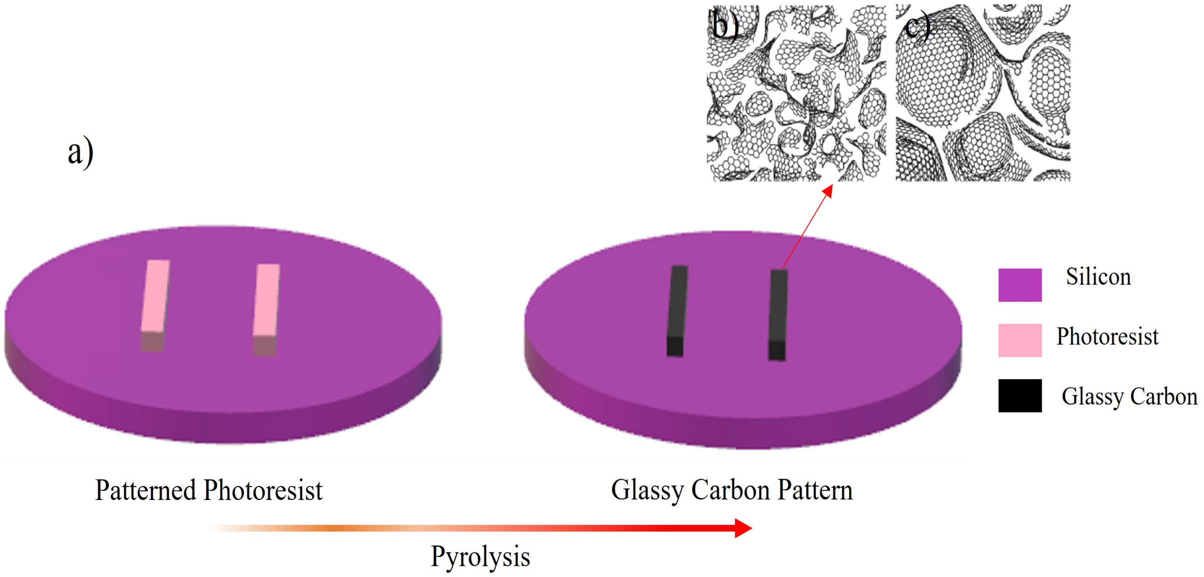

Figure 1.7: a) Schematics of C-MEMS process and models for the structure of Glassy Carbon obtained at b) low-temperature and c) high-temperature [60]

C-MEMS can integrate other techniques, like electrospinning, to shape polymers into carbon structures and increase the complexity of the fabricated carbon patterns. Using Near-Field electrospinning, it is possible to suspend a SU-8 based fiber on top of a photolithography pattern that, upon pyrolysis, becomes a monolithic carbon structure with a suspended glassy carbon wire with a wide variety of applications. Figure 1.8 shows a SU-8 lithography pattern with a suspended fiber on top before and after pyrolysis. Since the resist used in the lithography is the same as the solution used during Near-Field electrospinning, the integration during pyrolysis leads to a compact structure.

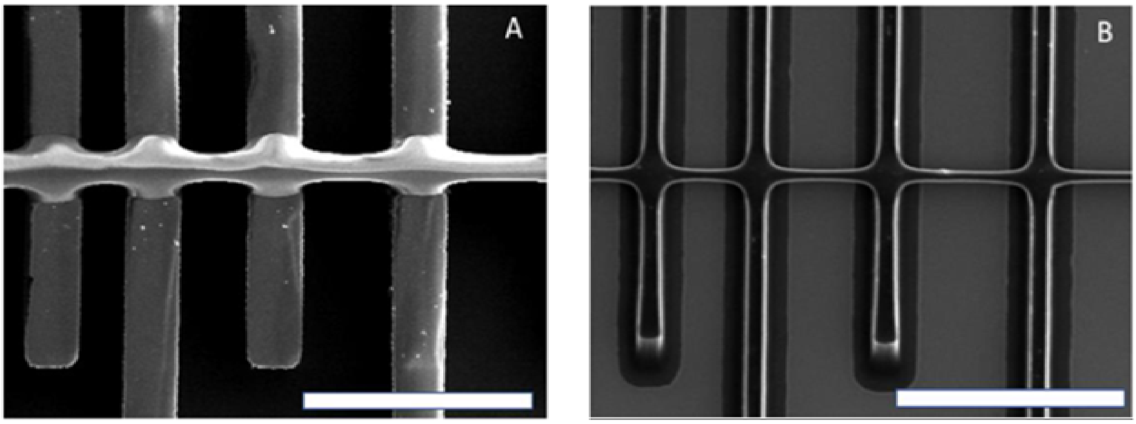

Figure 1.8: Schematics of C-MEMS process. Scale bar is 100 μm.

The last chapters of this thesis will explain how these suspended carbon fibers, obtained as a combination of nearfield electrospinning, lithography, and pyrolysis, can be later precisely functionalized with other materials by locally heating them using joule heating and chemical vapor deposition.

1.5 Objectives and Thesis Outline

This introductory chapter intends to lay the groundwork for the different goals this thesis has pursued and achieved. From expanding fundamental knowledge of electrospray of highly conductive liquids, using a novel experimental technique, to the complete microfabrication and optimization of an electrospray head thruster for electric propulsion using MEMS technology. Applications of electrospray to generate polymer jets are also analyzed in detail and their integration into C-MEMS. Expanding C-MEMS capabilities, different properties and applications of C-MEMS are studied, focusing on its thermal and electrical properties and developing a process to functionalize them at the micro and nanoscale level. The work is divided into seven chapters structured as follow:

The following chapter, Chapter 2, provides a detailed experimental characterization of electrospray of high conductive liquids, focusing on the ionic liquid EMI-Im, through retarding potential and time of flight techniques. In Chapter 3, a scalable microfabrication process to manufacture a compact microfluidic electrospray propulsion system is demonstrated and tested with the ionic liquid EMI-Im studied in Chapter 2. The fabrication, testing and results are discussed in detail.

Detaching from electric propulsion applications, Chapter 4 studies nanoparticle and fiber generation through electrosprays of polymer-based solutions. Near-Field Electrospinning is introduced, and a detailed study of the fiber initiation of a SU-8 based solution is described.

Chapter 5 describes how the Su-8 based fibers created through electrospray-electrospinning studied in Chapter 4 can be carbonized into carbon suspended microfiber through pyrolysis. C-MEMS is introduced, and a process to functionalize a single suspended carbon microfiber through joule heating and CVD is shown.

In Chapter 6, the process described in Chapter 5 to functionalize a single suspended fiber through joule heating and CVD is scaled up and demonstrated into carbon nanofiber mats fabricated using far-field electrospinning.

Chapter 7 describes general conclusions of this dissertation work together with a discussion of future research directions.

Chapter 2

Electrospray of high conductive liquids

2.1 Introduction

[1] As mentioned in the introductory chapter, electrosprays of highly conducting liquids operated in the cone-jet mode produce charged nanodroplets of controllable size, as well as molecular ions. The study of this electrospraying regime is challenging due to the lack of experimental techniques for probing these nanometric systems, and the higher complexity of the physics associated with the onset of ion field emission and self-heating. Jet parameters in the breakup region such as its radius, velocity, potential and electrification level are key to understanding the formation of droplets and emission of ions, and useful to validate numerical models of the cone-jet. In the case of micron-nano size jets, these jets can be determined with the values of retarding potentials and mass-to-charge ratios of the droplets produced by

---

[1] Portion of this chapter are reprinted or adapted from M. Gamero-Castaño and A. Cisquella-Serra, "Electrosprays of highly conducting liquids: A study of droplet and ion emission based on retarding potential and time-of-flight spectrometry," Phys. Rev. Fluids, vol. 6, no. 1, Jan. 2021.https://doi.org/10.1103/PhysRevFluids.6.013701. With permission of APS publishing.

the breakup. This chapter will introduce the use of this technique to investigate the parameters of nanometric jets. Retarding potential and mass-to-charge distributions of the beam are measured with retarding potential and time-of-flight analyzers operated in tandem. This combination makes it possible to differentiate between droplets of similar mass-to-charge ratios which, unlike in the case of micrometric jets, is needed to apply the technique. Besides the jet parameters, the experimental characterization also reveals with great detail the composition of the beam, which includes primary ions emitted from the jet breakup; ions resulting from the desolvation of primary ions; stable main droplets produced at the breakup; smaller droplets resulting from the Coulomb explosion of unstable main droplets; and small main droplets that evaporate a significant fraction of their charge in flight. An analysis of the breakup, based on the jet parameters measured, explains this complexity. The experimental characterization only studies the electrosprays of the ionic liquid 1-ethyl-3-methylimidazolium bis(trifluoromethylsulfonyl) imide (EMI-Im or $[\text{EMIM}^+][\text{NTf}_2^-]$) for its interest for electrospray propulsion and the later use of this propellant in chapter 3 to test microfabricated electrospray thrusters. Figure 2.1 shows atomic composition of EMI-Im and its 3D structure.

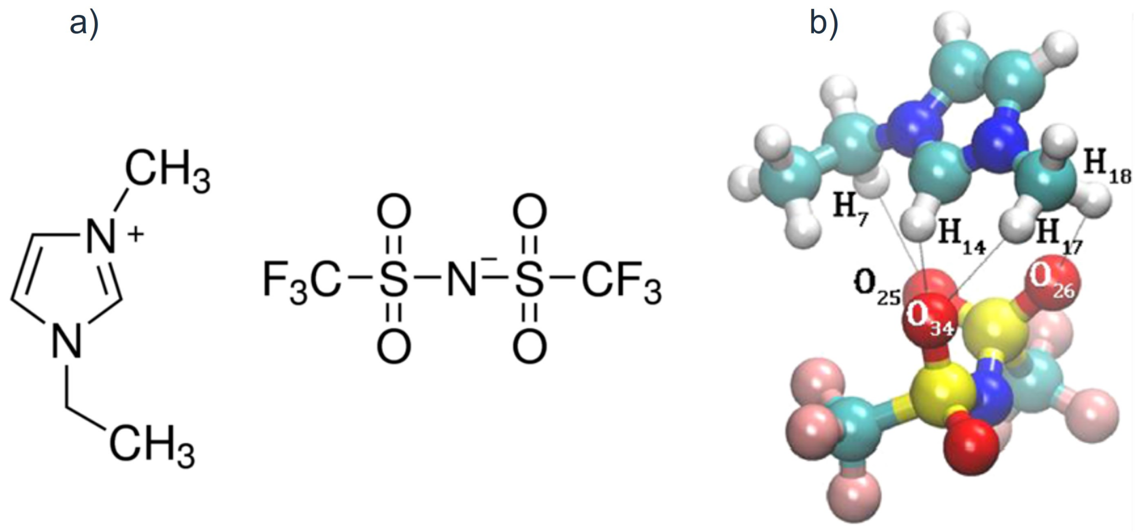

Figure 2.1: Ionic liquid pair $[\text{EMIM}^+][\text{NTf}_2^-]$. a) Atomic composition of the cation and anion and b) 3D molecular structure, (Reprinted from[131] with the permission of ACS Publishing)

.

However, the analysis is general and can be used to understand the beams of other highly conducting liquids.

2.2 Experimental Setup

Figure 2.2 is a sketch of the experimental setup. The electrospray source is operated inside a vacuum chamber, needed to characterize its beams with time-of-flight and retarding potential analyzers[36]. The emitter is the chamfered and metallized end of a fused silica tube with an outer diameter of 360 μm, and inner diameter of 40 μm and a length of 0.688 m. The opposite end exits the chamber through a vacuum fitting, and is submerged in a vial with EMI-Im placed at the bottom of a hermetic glass bottle. Surrounding the vial there is a bed of Drierite desiccant for eliminating water vapor molecules that could be absorbed by the hydrophilic EMI-Im. A cylinder with pressurized argon, a mechanical pump, a pressure gauge, and a manifold with a system of valves are used to control the pressure in the bottle and feed the desired amount of EMI-Im to the emitter. The hydraulic resistance of the fused silica line was calibrated with a bubble flow meter, which confirmed the validity of using the Poiseuille law with the nominal length and inner radius of the line to determine the liquid flow rate Q from the applied pressure. During operation a roughing mechanical pump and a turbomolecular pump bring the pressure in the vacuum chamber down to 2×10^{-6} torr.

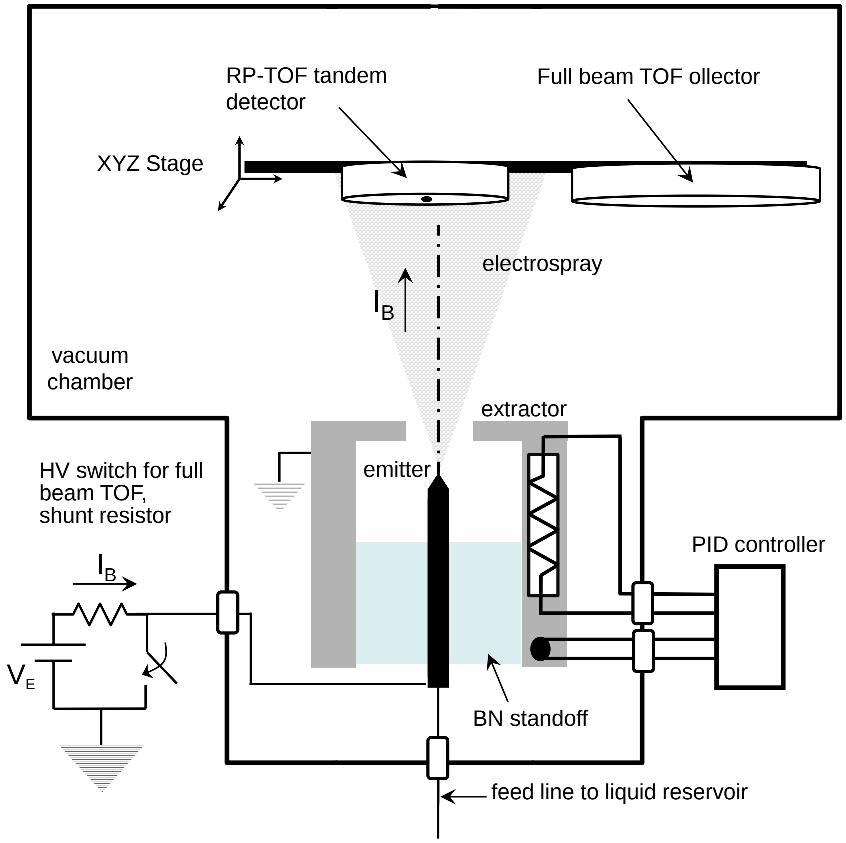

Figure 2.2: Experimental setup: electrospray source, vacuum chamber and detectors.

The liquid is electroprayed into charged droplets and ions by setting a voltage difference V_E between the emitter and an extractor electrode. All data reported in this chapter were taken at $V_E = 1690$ V. The extractor is connected to the laboratory ground. The charged particles are accelerated towards the extractor by the electric field, exit this inner region through an orifice perforated in the extractor and aligned with the emitter, and enter the outer, field-free region where they are analyzed. The temperature of the electrospray source is controlled below and above room temperature with the help of an electric heater, a thermoelectric cooler (peltier) and a thermocouple, all mounted on the extractor and connected to a PID controller. Heat is readily transferred between the emitter and extractor through a cylindrical standoff of boron nitride, a material with good thermal conduction and electrical isolation properties, and which can be mechanized to enforce axial alignment between the emitter tube and the extractor. The current emitted by the electrospray is measured in the high voltage line powering the emitter, using a shunt resistor and an isolation amplifier for transfering this small voltage signal to laboratory ground. The full beam is characterized with a time-of-flight, TOF, setup that measures the beam current striking a large collector with an electrometer, and uses a high voltage switch for rapidly shorting to ground the electrospray source [44]. The mapping between mass-to-charge ratio ζ and time-of-flight τ_{tof}

$$\zeta = 2\phi_{RP} \left(\frac{\tau_{tof}}{L_{tof}} \right)^2 \tag{2.1}$$

provided by this detector is approximate due to two experimental uncertainties: the collector is a plane perpendicular to the beam axis and the length L_{tof} travelled by a particle varies along the surface of the collector; and the particles have a distribution of retarding potentials ϕ_{RP}. The retarding potential of a charged particle, defined as the sum of its kinetic and potential energy divided by the charge

$$\phi_{RP} = \frac{1}{2}\zeta v^2(\mathbf{x}) + \phi(\mathbf{x}), \tag{2.2}$$

is a constant of motion in an electrostatic field. When an approximate $\zeta(\tau_{tof})$ mapping is needed from the signal of this instrument, for example to estimate the mass-to-charge ratio distribution of the whole beam, its thrust or mass flow rate [44], we use (2.1) with the average value of the retarding potential and the axial distance between the extractor and collector.

The retarding potential and time of flight analyzers in Fig. 2.3, operated in tandem, eliminate these two uncertainties. The mirror, with a voltage difference V_{RP} between plates, filters the incoming particles by retarding potential and only those with $\phi_{RP} = V_{RP}$ are transferred through [38]. The distance between the entry and exit orifices, the gap between the plates, the plate thickness, and the diameter of the orifices are 5.08 cm, 2.54 cm, 0.95 cm and 1.58 mm respectively. The current of the particles exiting the mirror and striking a small collector is measured with a fast electrometer. The collector is 15.6 cm downstream from an electrostatic gate placed at the exit of the mirror. When the electrostatic gate is off and V_{RP} is swept the electrometer yields the retarding potential density distribution $dI/d(\phi_{RP})$. On the other hand, when the gate is rapidly turned on to deflect the beamlet at fixed V_{RP}, the electrometer yields the time-of-flight distribution across the drift tube. With both ϕ_{RP} and L_{tof} precisely known, this instrument provides an accurate mass-to-charge distribution.

The relevant physical properties of EMI-Im are its electrical conductivity K, viscosity μ, density ρ, surface tension γ, and dielectric constant ε. We investigate the electrosprays at two emitter temperatures, 21 °C and 50 °C. In this range only the conductivity and viscosity vary significantly. For reference, we use the following values for the physcial properties [98, 16]: $\rho = 1520$ kg/m^3, $\gamma = 0.0349$ N/m, $\varepsilon = 12.2$; $K(21\ ^{\circ}\mathrm{C}) = 0.74$ S/m, $K(50\ ^{\circ}\mathrm{C}) = 1.56$ S/m; and $\mu(21\ ^{\circ}\mathrm{C}) = 0.032$ Pa/s, $\mu(50\ ^{\circ}\mathrm{C}) = 0.012$ Pa/s.

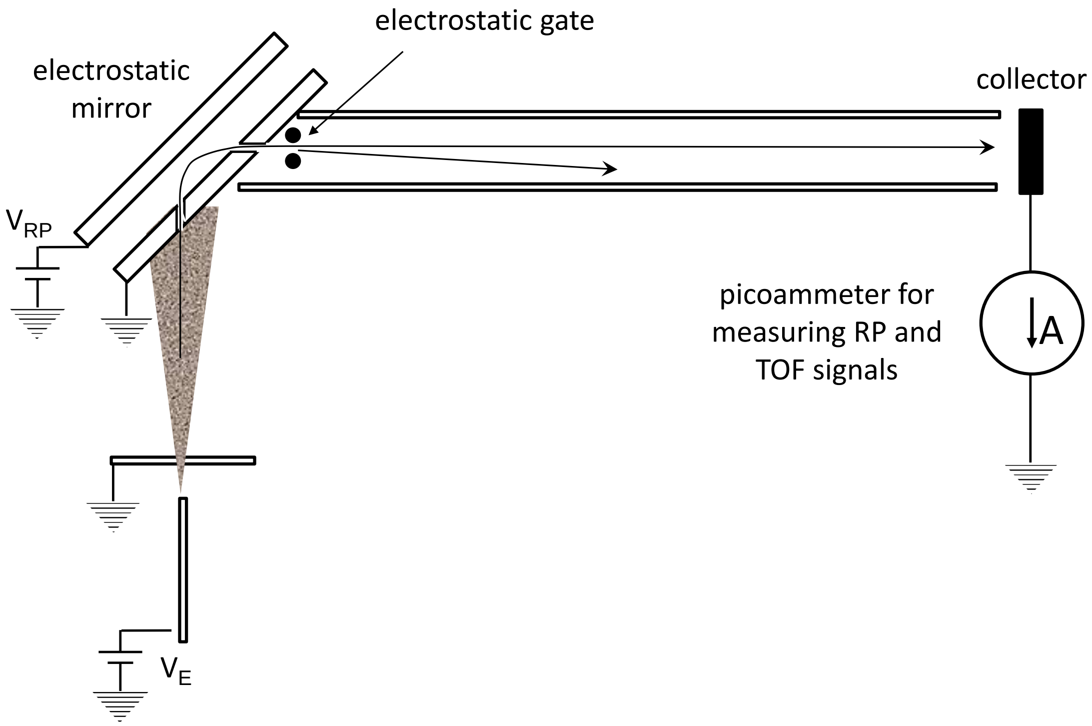

Figure 2.3: Retarding potential (electrostatic mirror) and time-of-flight analyzers operated in tandem.

2.3 Experimental characterization of electrospray beams

2.3.1 Ion and droplet populations

Cone-jets of fluids with low and moderate conductivities ($K \lesssim 0.1$ S/m) produce sprays of charged droplets. At higher conductivities the electric field on the surface of the jet and droplets reach values that induce ion emission, and the sprays contain both charged droplets and molecular ions [42]. EMI-Im operate in this dual droplet/ion emission regime. Figure

2.4 shows time-of-flight curves of full beams for several electrospray currents, at both 21 °C and 50 °C emitter temperature. In each measurement the electrospray is initially operated steadily and turned off at $\tau_{tof} = 0$, so that the current reaching the collector goes down to zero during a period reflecting the variation of times of flight of the particles in the beam. The derivative of this curve thus yield the distribution density function $dI/d\tau_{tof}$ of the full beam. All beams in Fig. 2.4 are formed by two families of particles, fast molecular ions and slower charged droplets. The fraction of the current emitted as ions is significant. The flux of ions j_{IFE} emitted from the surface is expected to follow Iribarne-Thomson's kinetic law [75]

$$\begin{aligned} j_{IFE} = \quad & \frac{k_B T}{h} n \, exp\left(-\frac{\Delta G_S^0 - G_E}{k_B T}\right) \\ & \text{with } G_E = \left(e^3 E/4\pi\varepsilon_0\right)^{1/2}, \end{aligned} \tag{2.3}$$

k_B, h, e and ε_0 are the Boltzmann and Planck constants, the elementary charge and the permittivity of the vacuum. T stands for the temperature, and E for the normal component of the electric field on the surface, on the vacuum side. ΔG_S^0 is the ion solvation energy and n the ion surface density. At fixed emitter temperature the ion fraction is a weak function of the flow rate, in agreement with the scaling of the electric field on the surface of the cone-jet, $E_n^o \propto (\rho^{1/6}\gamma^{1/3}K^{1/3}/\varepsilon_o^{5/6})$, which does not depend on Q [49, 46]. The ion current increases with the temperature of the emitter, as expected for this kinetic law. The average mass-to-charge ratio of the droplets emitted by cone-jets scales as $\zeta \propto \rho I_B/\sqrt{\gamma K}$ [31], a trend that the TOF spectra reproduce: the time-of-flight of droplets increases with beam current at constant emitter temperature, and decreases with increasing temperature at constant beam current (K increases with temperature). The time-of-flight distributions of the droplet population, and therefore their mass-to-charge ratio distributions, are broad, extending to the values of molecular ions. The ζ-distributions of electrosprayed droplets for liquids with lower conductivities are much narrower [48], typically narrower than the diameter distributions [37].

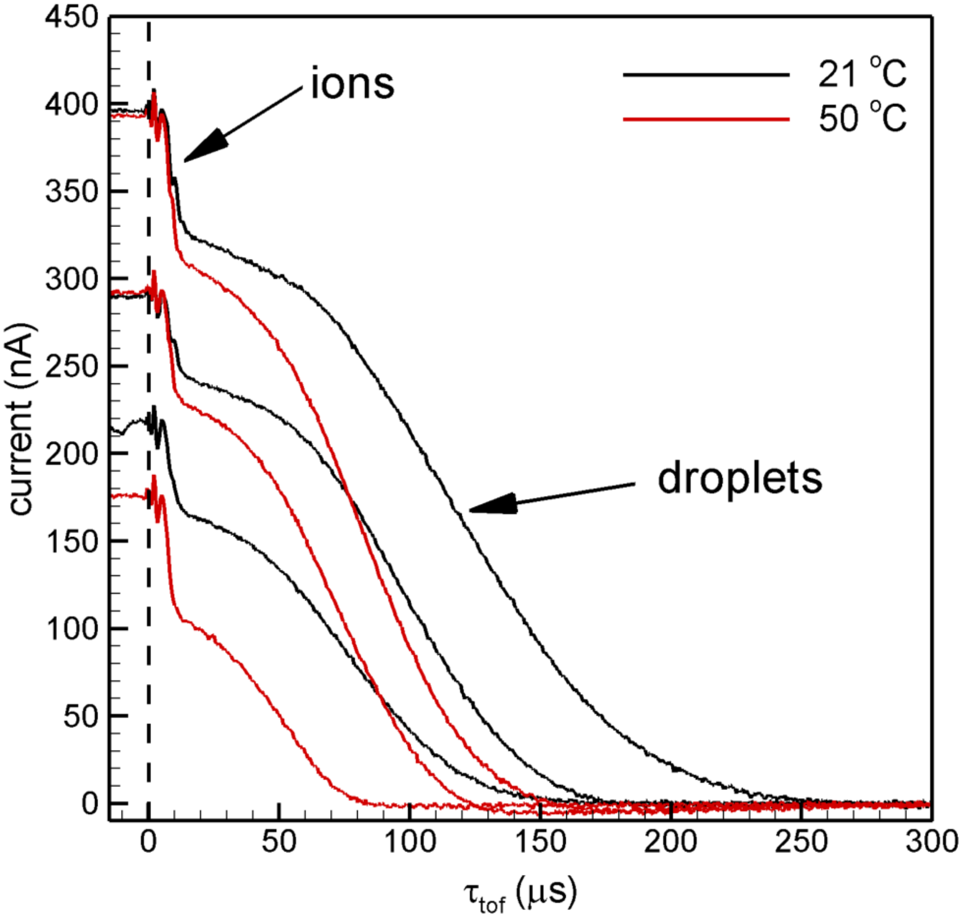

Figure 2.4: Time-of-flight curves of the whole beam, for several beam currents and two emitter temperatures.

The two TOF detectors are designed to study the slower droplet population and, although they can differentiate between the velocities of droplets and ions, they cannot resolve the masses of different molecular ions present in these beams. This diversity is observable in the retarding potential curves, and a simple analysis can be used to find the molecular masses and origins of these ions (some ions are emitted from the surface of the cone-jet while others are produced by desolvation of EMI-Im molecules from ions in flight). The retarding potential distribution in Figure 2.5 is for a beam current of 255 nA and an emitter temperature of 50 °C. The black trace shows the overall spectrum, while the smaller vertical scale of the red trace highlights ionic peaks. The overall spectrum displays a continuum of particles starting at retarding potentials $\phi_{RP} \approx 1200$ V. Within this continuum, TOF analysis identifies the particles at $\phi_{RP} \gtrsim 1650$ V as droplets, while the peak P$_1$ at $\phi_{RP} \lesssim 1650$ and with a low energy tail extending to 1200 V, is formed by ions. In addition to P$_1$, a series of isolated peaks P$_2$ $-$ P$_7$ can be distinguished from the background at smaller retarding potentials. The composition $A^+(AB)_{n-m}$ of these isolated peaks can be deduced under the assumption that they result from desolvation events

$$A^+(AB)_n \rightarrow A^+(AB)_{n-m} + m(AB) \tag{2.4}$$

happening to molecular ions $A^+(AB)_n$ from the P$_1$ peak, occurring at ground potential upstream of the electrostatic mirror. A^+ stands for the EMI cation, and AB for the EMI-Im molecule. Since the desolvation of a molecule from an ion with a kinetic energy over 1000 eV insignificantly changes its velocity, it follows from (2.2) that the mass of the original ion divided by the mass of the desolvated ion must be equal to the ratio of their retarding potentials. Table 2.1 shows the retarding potentials of each ionic peak, their inferred composition and desolvation reactions, the experimental ratios between the retarding potentials of P$_1$ and peaks P$_2$ $-$ P$_7$, and the ratios of the masses. The ratio of the masses of the parent and desolvated ion, which always compares well with the ratio of the retarding potentials, confirm the composition assignments. We have observed that the intensities of desolvated ions increase with the background pressure, indicating that collisions with gas molecules is a significant energy source enabling ion decomposition. However these peaks still appear, although with lower intensities, at the regular working pressure of 2×10^{-6} torr. Since the likelihood of such collisions along the ion path is extremely small at this pressure, it is possible that a fraction of the molecular ions emitted from the cone-jet is unstable and spontaneously decomposes [99].

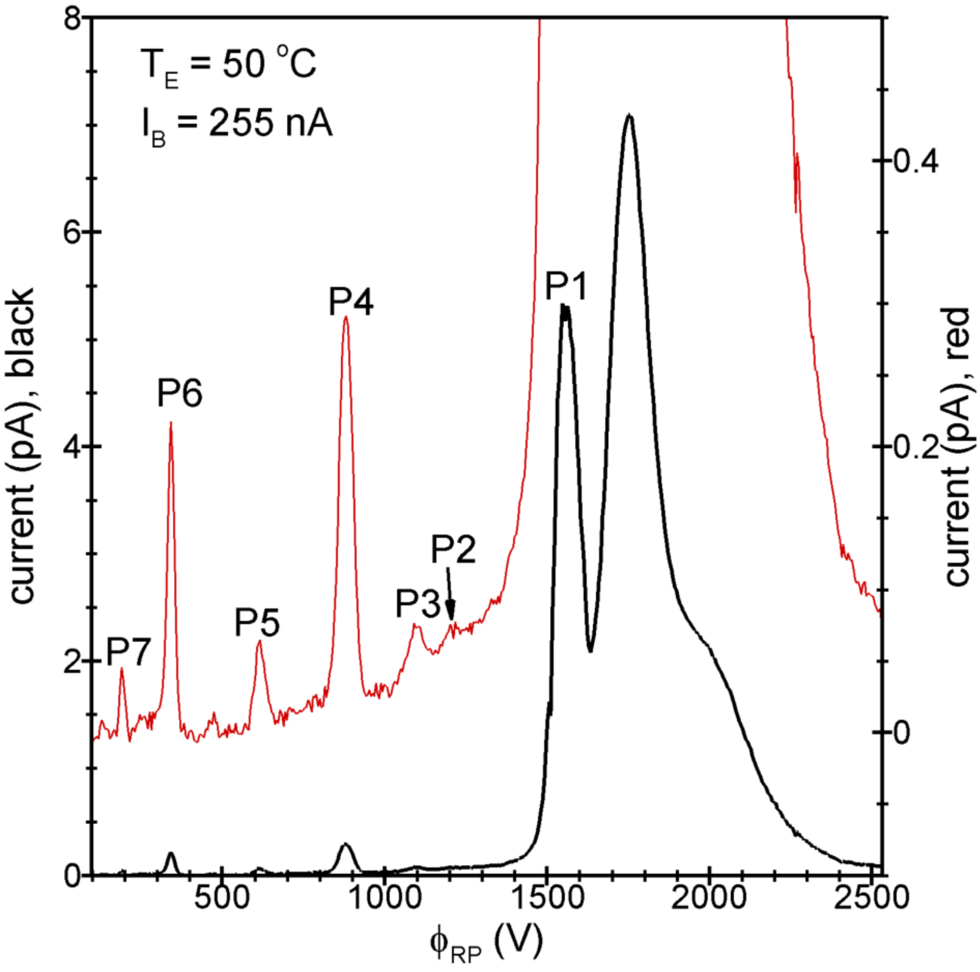

Figure 2.5: Retarding potential curve illustrating multiple ionic peaks. Red and black traces are same spectra with different vertical scales.

2.3.2 Tandem retarding potential and time-of-flight analysis

Figure 2.6 shows retarding potential curves for several beam currents. In all cases the emitter potential and temperature are $V_E = 1690$ V and 21 °C. All curves display a broad range of

Table 2.1: Ionic peaks in Fig. 2.5. The comparison between the ratio of retarding potentials and masses indicate the composition of each ion.

Ion Peak	ϕ_{RP} (V)	Composition	Transition	P_1/P_i ϕ_{RP} ratio	P_1/P_i mass ratio
P_1	1560	A^+, $A^+(AB)$, $A^+(AB)_2$, $A^+(AB)_3$	-	-	-
P_2	1212	$A^+(AB)_3$	$A^+(AB)_4 \to A^+(AB)_3 + AB$	1.29	1.30
P_3	1097	$A^+(AB)_2$	$A^+(AB)_3 \to A^+(AB)_2 + AB$	1.42	1.44
P_4	882	$A^+(AB)$	$A^+(AB)_2 \to A^+(AB) + AB$	1.77	1.78
P_5	616	$A^+(AB)$	$A^+(AB)_3 \to A^+(AB) + 2(AB)$	2.53	2.56
P_6	342	A^+	$A^+(AB) \to A^+ + AB$	4.56	4.52
P_7	190	A^+	$A^+(AB)_2 \to A^+ + 2(AB)$	8.22	8.05

droplets, with most of its area and maximum at retarding potentials smaller than V_E and a tail extending above V_E. The droplet region transitions into the sharper ionic peak P_1 in all cases. The desolvated ionic peaks are also present but barely visible in this vertical scale, except for the most intense P_6. In a related series of experiments in which V_E is kept at 1690 V while biasing the extractor with a positive potential V_B with respect to ground, the droplet and the P_1 regions (including the low energy tail of P_1 but not the desolvated isolated peaks) translate with V_B while the retarding potential of the desolvated ionic peak P_i translates by the smaller amount $(\zeta_i/\zeta_1)V_B$. This agrees with the observation that the desolvated ions in $P_2 - P_7$ originate at ground potential, and confirms that the particles in the droplet and P_1 regions are emitted from the cone-jet. The emission velocity of an ion evaporated from the cone-jet is of the order of the fluid velocity, and therefore its kinetic energy at emission is negligible compared to that associated with its retarding potential, $e\phi_{RP}$. Therefore the retarding potential of an ion in the P_1 region is a direct measure of the potential from which it evaporates. As the beam current increases the voltage difference $V_E - \phi_{RP}(P_1)$ increases as well, indicating that the ion emission region moves downstream at increasing beam current. The fraction of droplets with retarding potentials larger than V_E is at odds with the ohmic and viscous dissipation of energy occurring in the cone-jet [39]. These dissipation losses translate into a voltage deficit that lowers below V_E the retarding potential of the liquid in the jet.

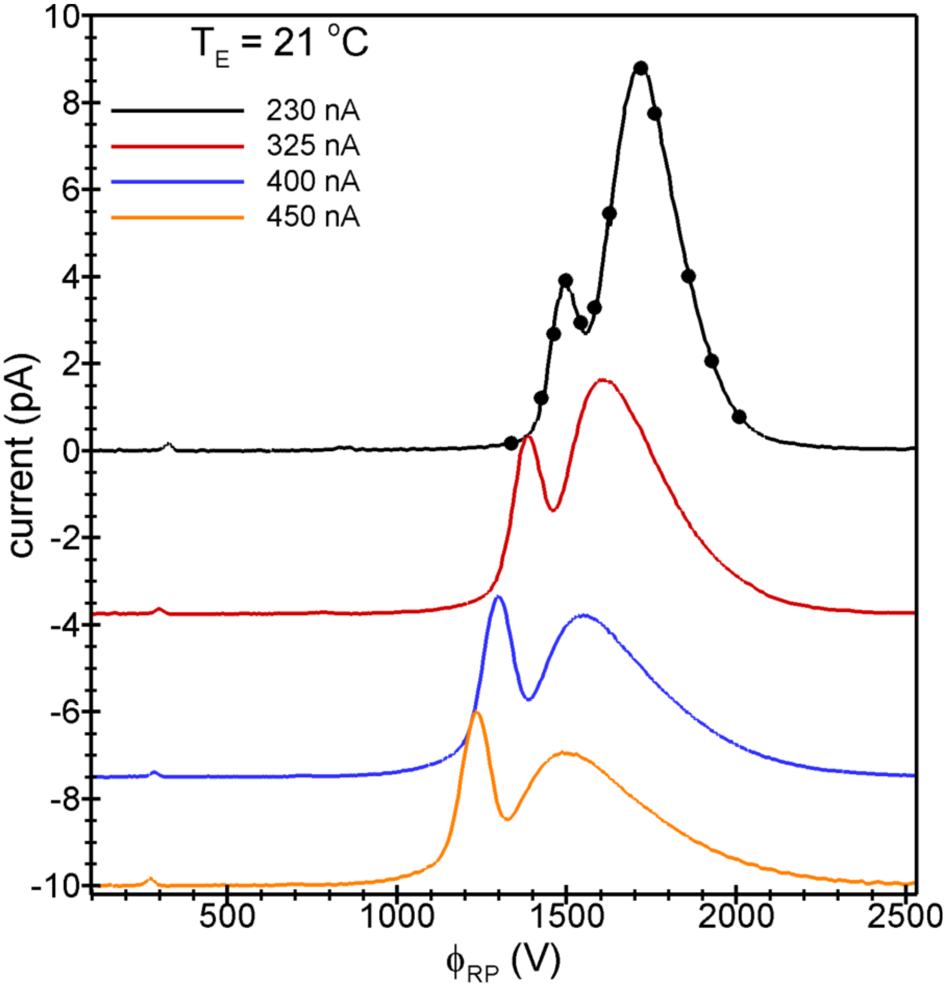

Figure 2.6: Retarding potential distributions for several beam currents at 21 °C.

Figure 2.7 shows time-of-flight spectra at several retarding potentials the 230 nA beam. The retarding potentials are shown as black dots in Fig. 2.6. Each red trace is the average of 25,600 TOF measurements. The experimental curve is fitted to an error function (black trace) modeling a particle population, or to the sum of two error functions when there is evidence of two populations. The time of flight spectra of the beamlets with retarding potentials of 1338 V, 1427 V and 1465 V, within P_1 but at ϕ_{RP} lower than its maximum, have a single particle family with very high velocities, readily identifiable as molecular ions (the average mass-to-charge ratio of these particles is 0.0134 g/C, i.e. 1295 u for a singly charged ion). The curve at the maximum of P_1, ϕ_{RP} = 1498 V, contains mostly molecular ions and a second population of particles with $< \zeta >= 0.587$ g/C. This second group of particles are charged droplets, with an estimated average radius of 11.8 nm. We use the maximum radius of a stable droplet, or Rayleigh limit

$$R_{Ray}(\zeta) = \left(\frac{6\, \varepsilon_0^{1/2} \gamma^{1/2}}{\rho} \right)^{2/3} \zeta^{2/3}, \tag{2.5}$$

for this estimate [29]. At a retarding potential larger than 1498 V but still within P_1, $\phi_{RP} = 1542$ V, the TOF curve has the same two populations of ions and charged droplets, but the current of the droplets is now the larger fraction. The next spectrum at $\phi_{RP} = 1576$ V, immediately after the local minimum in the retarding potential curve, shows a single population of droplets with a relatively narrow distribution, similarly to the spectrum at $\phi_{RP} = 1623$ V. The next spectrum, taken at the maximum of the retarding potential distribution $\phi_{RP} = 1714$ V, is mostly formed by the same family of droplets, with the addition of a small fraction of droplets with lower mass-to-charge ratios. The spectra for the next three retarding potentials contain the same two droplet families, becoming more separated and having an increasing presence of the low-ζ population at increasing ϕ_{RP}. The last spectra at $\phi_{RP} = 2008$ V is dominated by the low-ζ droplet population.

The phenomenology is similar for all beam currents at 21 °C: the retarding potential distribution has a region of droplets that extends several hundred volts on either side of the emitter potential, a joined region of ions P_1 at lower retarding potentials, and several isolated ion peaks at still lower retarding potential resulting from the desolvation of P_1 ions; there is a narrow overlap between the droplet region and P_1 where both ions and droplets coexist; there are two distinct groups of droplets, one with higher mass-to-charge ratios distributed along a continuous range on either side of V_E, and a second group with lower mass-to-charge ratios present in both the ion-droplet overlap and, mixed with the high-ζ droplet population, at retarding potentials near and above the maximum of the droplet distribution. In the latter case the current fraction of the low-ζ population increases with the retarding potential.

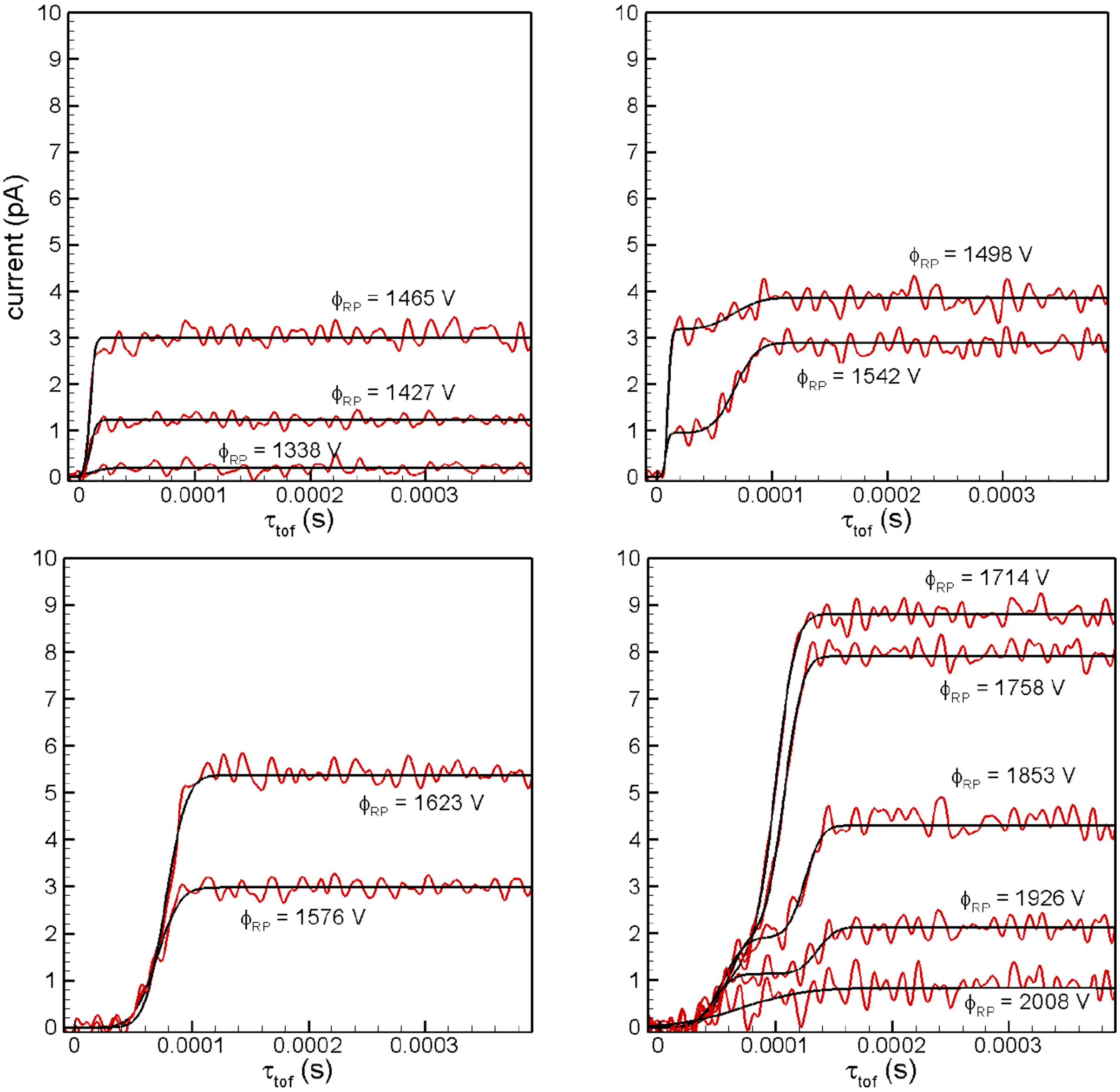

Figure 2.7: Time-of-flight spectra at different retarding potentials (see black dots in Fig 2.6) for $I_B = 230$ nA, 21 °C.

2.4 Analysis and discussion

2.4.1 Determination of the velocity and potential of the jet in the breakup region

References [[48]] and [[37]] demonstrate a method for obtaining the nominal velocity and potential of the jet in the breakup region. The technique is based on the natural dispersion of the droplets' mass-to-charge ratio induced by the breakup, and assumes that the variations of potential and droplets' velocities in the unsteady breakup region are much smaller than the voltage drop along the cone-jet and the velocity gained by the liquid along the jet. Under these conditions all droplets produced by the breakup are emitted at approximately the same nominal potential ϕ_J and velocity v_J. Thus, if the retarding potentials and mass-to-charge ratios of many i droplets emitted from the breakup region are available, ϕ_J and v_J can be obtained from the linear regression

$$\phi_{RP,i} = \frac{1}{2} v_J^2 \zeta_i + \phi_J, \tag{2.6}$$

This model is tested in Fig. 2.8 by plotting the average mass-to-charge ratio of the droplet distributions in Fig. 2.7 versus their retarding potentials. The droplets in the high-ζ population, with standard deviations given by the horizontal bars, follow (2.6) well, suggesting that they are indeed emitted from a region in which the variations of potentials and velocities are small. This common region for the majority of the droplets in the beam can only be the jet breakup. Henceforth this population will be referred to as main droplets. The y-intercept and the slope of the linear fitting yield the nominal potential and velocity of the jet, $\phi_J = 1547$ V and $v_J = 547$ m/s. ϕ_J coincides with the retarding potential at the maximum of P_1, marked in the figure by a red point. Thus, the ions forming the P_1 peak are emitted from the breakup region as well. This explains the sharp transition between ions and droplets in the retarding potential curves: since the kinetic energy per particle charge of ions is insignificant compared to that of droplets when both are emitted from the same small region, the retarding potentials of the latter must always be larger than the retarding potential of ions. On the other hand, the droplet population with low-ζ does not conform to (2.6), suggesting that they are not emitted directly from the breakup region or, if they are, undergo processes that modify their retarding potentials or their mass-to-charge ratios. Coulomb explosions and ion emission from droplets in flight are mechanism that may explain the anomalous $\phi_{RP}(\zeta)$ relation, and Section 2.4.3 discusses this possibility. Figure 2.8 also shows the charge-to-mass ratio of the jet, $\zeta_J = \rho Q/I_B$, as an orange bar over the fitting. Most of the main droplets have a mass-to-charge ratio higher than the jet. This large departure from conservation of mass and charge in the breakup, which requires $< \zeta_D > \approxeq \zeta_J$, may be explained by the natural angular segregation of droplets by mass-to-charge ratio induced by the beam's space charge, which concentrates the droplets with higher ζ towards the axis [37]. However, the substantial presence of ions and low-ζ droplets in the same angular location suggests that other phenomena may contribute to the drastic disappearance of the large fraction of the main droplets with $\zeta_D \lesssim \zeta_J$.

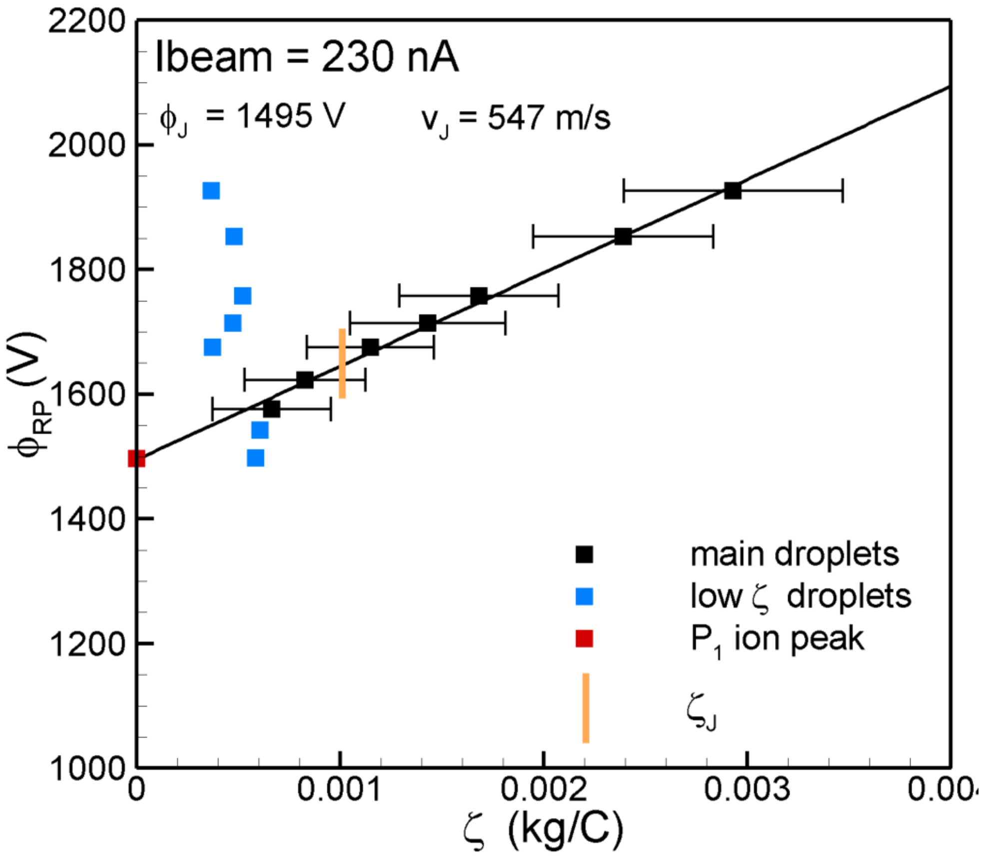

Figure 2.8: Average mass-to-charge ratio vs. retarding potential of droplet populations and ion peak P_1 from spectra in Fig. 2.13. Main droplets and P_1 ions are emitted from the jet breakup.

Figure 2.9 shows the linear regression for the main droplets of the 300 nA, 400 nA and 450 nA beams, at 21 °C. The linear model fits well the points, and the y-intercepts are near the retarding potential of the maxima of the P_1 peaks. The low-ζ droplets are not shown to avoid crowding the chart, but their phenomenology is identical to that shown in Fig. 2.8. All beams studied at 21 °C display the same patterns of main droplets and P_1 ions being emitted from the breakup region, the reduced presence of main droplets with $\zeta_D \lesssim \zeta_J$, and low-ζ droplets that do not follow the breakup equation (2.6). Table 2.2 lists the velocity of the jets at the breakup and the voltage drop along the cone-jet, $\phi_E - \phi_J$, together with other jet parameters discussed in sections 2.4.2 and 2.4.3. Reference [Gamero2008PoF] shows that the voltage drop along the cone-jet is independent of ϕ_E. This work also reports values for $\phi_E - \phi_J$

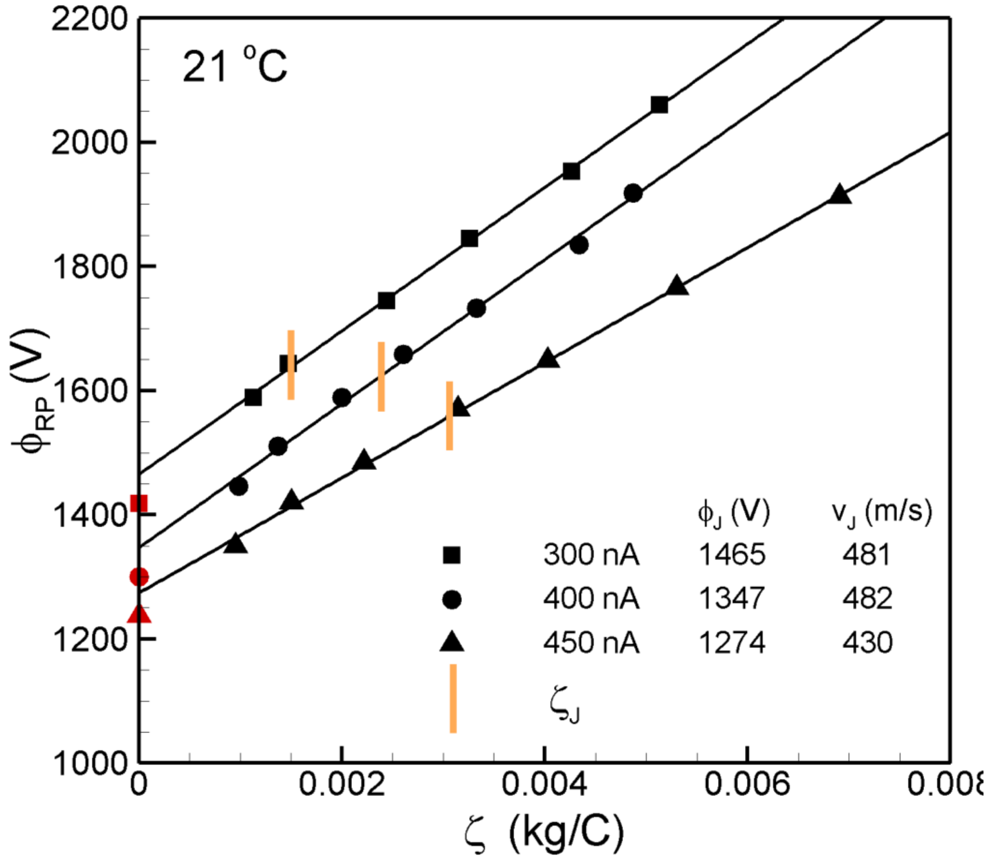

Figure 2.9: Average mass-to-charge ratio vs. retarding potential of main droplets and ion peak P_1, for several beam currents at 21 °C.

and v_J for electrosprays of EMI-Im. The $\phi_E - \phi_J$ values agree well with those in Table 2.2, but the jet velocities are substantially higher. Reference [Gamero2008PoF] does not employ RP-TOF in tandem, and can not use (2.6) to determine ϕ_J and v_J. Instead, it identifies the P_1 peaks as ions emitted from the breakup, and in the absence of better information estimates the jet velocity as $[2(\phi_E - \phi_J)/\zeta_J]^{1/2}$. This estimate neglects dissipation and the generation of surface in the jet, and as a result yields a larger velocity.

2.4.2 Self-heating effects and universal jet radii

Table 2.2 lists the flow rates and currents of the EMI-Im beams characterized at 21 °C. These quantities are also given in dimensionless form, $\tilde{Q} = \rho K Q/(\gamma \varepsilon_0)$ and $\tilde{I} = I_B/(\varepsilon_0 \gamma^2/\rho)^{1/2}$, for

Table 2.2: Relevant parameters of EMI-Im electrosprays at 21C: flow rate Q; beam current I_B; dimensionless flow rate $\tilde{Q}$ and beam current $\tilde{I}$; nominal mass-to-charge ratio ζ_J and velocity v_J of the jet in the brekup; nominal jet radius R_J, and value normalized with Gañán-Calvo's characteristic length $\tilde{R}_J$; Rayleigh limit radius $R_{Ray}(\zeta_J)$ of droplet with mass-to-charge ratio ζ_J; potential drop along the cone-jet $\phi_E - \phi_J$; normal electric field on the jet's surface $E^o_{n,J}$; jet's viscosity J and electrification Ψ parameters

Q (nl/s)	I_B (nA)	$\tilde{Q}$	$\tilde{I}$	ζ_J (g/C)	v_J (m/s)	R_J (nm) (nm)	$\tilde{R}_J$	$R_{Ray}(\zeta_J)$ (nm)	$\phi_E - \phi_J$ (V)	$E^o_{n,J}$ (V/nm)	J Ψ	Ψ
0.153	230.	612.	86.3	1.01	547.	9.42	0.273	17.	196.	0.802	0.00057	1.54
0.233	265.	933.	99.5	1.33	531.	11.8	0.277	20.5	242.	0.76	0.000714	1.73
0.297	300.	1190.	113.	1.5	481.	14.	0.292	22.2	274.	0.8	0.000848	2.28
0.375	325.	1500.	122.	1.75	462.	16.1	0.297	24.6	304.	0.786	0.000971	2.52
0.464	350.	1860.	131.	2.01	501.	17.2	0.285	26.9	331.	0.731	0.00104	2.33
0.562	375.	2250.	141.	2.28	503.	18.9	0.285	29.2	354.	0.711	0.00114	2.42
0.629	400.	2520.	150.	2.39	482.	20.4	0.291	30.2	392.	0.732	0.00123	2.77
0.743	425.	2980.	160.	2.66	448.	23.	0.302	32.4	449.	0.742	0.00139	3.21
0.905	450.	3630.	169.	3.06	431.	25.9	0.308	35.6	455.	0.726	0.00156	3.46

easier comparison with the literature. The $\{\tilde{Q}, \tilde{I}\}$ points are well fitted by $\tilde{I} = 2.39\tilde{Q}^{1/2}$+28.4, in agreement with the well-established scaling law $\tilde{I} \simeq \alpha\tilde{Q}^{1/2}$ except for the large positive y-intercept of 28.4. The value $\alpha = 2.6$ is a good fit for measurements of a large group of liquids [51], while a numerical solution finds $\alpha = 2.5$ for a liquid of similar dielectric constant (tributyl phosphate, $\varepsilon = 8.91$) [46]. The large positive y-intercept is associated with significant self-heating due to ohmic and viscous dissipation typical of fluids with high conductivities, which increases the conductivity of the fluid along the transition region of the cone-jet. If corrected for this effect by using a conductivity averaged over the transition region, the values of $\tilde{Q}$ would be larger than in Table 2.2, resulting in a reduction of the y-intercept [40].

The dimensionless flow rates at which EMI-Im can be electrosprayed are very high compared to others liquids, see for example Fig. 7 in Ref. [Ganan2018]. In our experiments we find that the minimum stable flow rate at room temperature is $\tilde{Q}_{MIN} \approxeq 460$. This is to be expected for cone-jets of highly conducting liquids with an elevated viscosity, a condition that can be evaluated in terms of $Re_K = \left[\rho\varepsilon_o\gamma^2/(\mu^3 K)\right]^{1/3}$, a dimensionless number frequently used in the literature of cone-jets. Its value for EMI-Im at 21 °C is $Re_K = 8.53 \times 10^{-3}$. Reference [Gamero2019b] shows that the minimum flow rate for tributyl phosphate, a fluid with similar dielectric constant but Re_K values at least one order of magnitude larger than EMI-Im, scales as $\tilde{Q}_{MIN} \simeq 1.87 Re_K^{-1.1}$. This relation yields $\tilde{Q}_{MIN} = 353$ for $Re_K = 8.53 \times 10^{-3}$, a value similar to that of EMI-Im.

Table 2.2 also lists the nominal radius of the jet, $R_J = \left[Q/(\pi\, v_J)\right]^{1/2}$, and it dimensionless form normalized with Gañán-Calvo's characteristic length $\tilde{R}_J = R_J/r_G$, $r_G = \left[\rho\varepsilon_o Q^3/(\gamma K)\right]^{1/6}$ [52, 50]. Besides the nanometric radii of these jets, the near constancy of $\tilde{R}_J$ for all flow rates is noteworthy: while Q changes by a factor of 4.9, $\tilde{R}_J$ changes by a factor of 0.13. References [Gamero2019,Gamero2010] show that the geometry of the transition region of the cone-jet, when made dimensionless with r_G, remains nearly invariant to changes of the flow rate. The near constancy of the dimensionless jet radii in Table 2.2, $\tilde{R}_J \simeq \beta = 0.29$, extends this result valid for the transition region, to the jet's breakup, suggesting that the condition triggering the breakup is also driven by the physics and processes of the transition region.

2.4.3 Equipotential jet breakup, droplet radii and the effects of Coulomb explosions and ion evaporation

The broad mass-to-charge ratio distributions of droplets, the failure of the low-ζ droplets to conform to the breakup condition (2.6), the perplexingly high retarding potentials of some high-ζ droplets, and the potential presence of Coulomb explosions and ion evaporation from droplets in flight are important topics. A detailed investigation of these problems requires accurate modeling of the breakup at typical jet conditions, a numerical effort that is beyond the scope of this thesis. Instead, the following discussion will provide a basic explanation of the observed phenomenology and may guide future analytical work.

At low flow rates, $\tilde{Q} \lesssim \varepsilon$, the break up produces droplets with narrow distributions of diameters and mass-to-charge ratios. At higher flow rates an additional class of droplets with smaller diameters and mass-to-charge ratios, referred to as satellites, appears. Numerical models and visualization of experiments show that satellite droplets form in the pinching region of main droplets, where charge accumulates due to the higher curvature and electric field. This process is associated with the increasing nonlinearity of the breakup, triggered by a sufficiently high value of the Reynolds number. At still higher flow rates the atomization transitions to a regime with significantly broader distributions, without a clear separation between main and satellite droplets. The latter breakup regime has been associated with the onset of lateral oscillations, induced by the destabilizing effect of increasing electrification [113, 37, 48, 39]. The dimensionless Taylor number

$$\Psi = \frac{\sigma^2 R_J}{\varepsilon_0 \gamma} \simeq \frac{\alpha^2 \beta^3}{4} \tilde{Q}^{1/2}, \tag{2.7}$$

approximately twice the ratio between the electrostatic stress and the capillary pressure, is a measure of the electrification of the jet. The pressure in the fluid is negative for $\Psi > 2$, a condition happening at the Rayleigh limit of droplets (2.5) and in all jets in Table 2.2, except for the two lowest currents. The large value of Ψ in EMI-Im jets is a direct consequence of the high flow rates needed to make the electrospray stable, and will also be characteristical of most highly conducting ionic liquids due to their low Re_K values and associated high $\tilde{Q}_{MIN}$.

Linear instability analysis is a standard technique for determining the initial growth rate of axisymmetric perturbation modes prescribed on the jet's surface [8]. A perturbation with a positive grow rate makes the jet unstable, and the wavelength λ of the perturbation yields the radius of the associated droplet, $R_D = (3\lambda R_J^2/4)^{1/3}$. The perturbation with maximum growth rate produces the most likely droplet, with critical radius R_D^*. For the simplest case of an uncharged and inviscid jet, the ratio between R_D^* and the radius of the jet is $R_D^*/R_J = 1.89$. This ratio changes when viscous effects and electrification are important, e.g. it is well known that viscosity has an stabilizing effect in the breakup, increasing R_D^*/R_J [8]. Reference [Gamero2002JFM] provides formulae for the growth rate as a function of λ, Ψ and the dimensionless parameter J

$$J = \frac{\rho \gamma R_J}{\mu^2} \simeq \beta \tilde{Q}^{1/2} Re_K^2 \tag{2.8}$$

for several electrification limiting hypothesis, namely equipotential breakup, constant volumetric charge and charge bounded to the surface. Note the correspondence between J and the more common Ohnesorge number, $Oh = J^{-1/2}$. The equipotential breakup is the appropriate scenario for EMI-Im jets due to the small ratio between the electrical relaxation time $t_r = \varepsilon\varepsilon_0/K$, and the characteristic flow time during the breakup. The latter can be estimated by balancing the always important capillary pressure with inertia, $t_{\gamma\rho} = (\rho r_J^3/\gamma)^{1/2}$, or with the viscous stress, $t_{\gamma\mu} = \mu r_J/\gamma$. The ratios of times for both cases are

$$\frac{t_r}{t_{\gamma\rho}} = \frac{\varepsilon}{\tilde{Q}^{3/4}}, \qquad \frac{t_r}{t_{\gamma\mu}} = \frac{\varepsilon Re_K}{\tilde{Q}^{1/2}}, \tag{2.9}$$

In the case of EMI-Im, the very large values of the dimensionless flow rate and the low Re_K make the electrical relaxation time always much smaller than the characteristic flow time. Therefore the surface charge must be near equilibrium throughout the breakup, shielding the fluid from external fields. For a equipotential breakup the initial growth rate $\sigma(x, J, \Psi)$

of a perturbation with wave number $x = 2\pi/\lambda$, is found by eliminating y from [48]

$$\sigma\frac{\rho R_J^2}{\mu} = y^2 - x^2 \tag{2.10}$$

$$\begin{aligned} &2x^2\left(x^2+y^2\right)\frac{\mathrm{I}_1'(x)}{\mathrm{I}_0(x)}\left[1-\frac{2xy}{x^2+y^2}\frac{\mathrm{I}_1(x)\mathrm{I}_1'(y)}{\mathrm{I}_1'(x)\mathrm{I}_1(y)}\right]-\left(x^4-y^4\right) \\ &= J\left\{x(1-x^2)\frac{\mathrm{I}_1(x)}{\mathrm{I}_0(x)}-\Psi\frac{x\mathrm{I}_1(x)}{\mathrm{I}_0(x)}\left[1+\frac{x\mathrm{K}_0'(x)}{\mathrm{K}_0(x)}\right]\right\}. \end{aligned} \tag{2.11}$$

The wavelength $\lambda^*(J,\Psi)$ associated with the maximum growth rate yields the radius of the critical droplet

$$\frac{R_D^*(J,\Psi)}{R_J} = \left(\frac{3}{4}\frac{\lambda^*}{R_J}\right)^{1/3}. \tag{2.12}$$

Figure 2.10 shows R_D^*/R_J as a function of Ψ, for several values of J and equipotential breakup. Note that for the case of inviscid breakup and marginal electrification, $J \to \infty$ and $\Psi \to 0$, R_D^*/R_J approaches the expected value of 1.89. Increasing values of the Taylor number make the critical droplet smaller, while strong viscous effects (decreasing J) make the critical droplet larger, especially when the importance of electrification is small. For the very large values of Ψ typical of EMI-Im jets the effect of J on the breakup is reduced, the destabilizing effect of electrification dominates over the stabilizing effect of viscosity, and R_D^*/R_J may fall substantially below 1.89. Note also that for moderate and highly electrified breakup R_D^*/R_J asymptotes fast to a single curve for sufficiently low values of J, with the curves for $J = 0.1$ and $J = 0.0001$ being nearly identical for $\Psi \gtrsim 0.5$. Clearly the breakups of most highly conducting liquids are described by this asymptote.

The mass-to-charge ratio of the jet can be expressed in terms of Ψ

$$\zeta_J = \frac{\rho}{2\varepsilon_0^{1/2}\gamma^{1/2}} \frac{R_J^{3/2}}{\Psi^{1/2}}, \tag{2.13}$$

which makes it possible to write the maximum stable radius of a droplet with mass-to-charge ratio ζ_J as

$$\frac{R_{Ray}(\zeta_J)}{R_J} = \frac{3^{2/3}}{\Psi^{1/3}}. \tag{2.14}$$

This relation is plotted in Fig 2.10, and provides an interesting corollary: in an equipotential breakup with the very strong viscous and electrification effects typical of EMI-Im jets, the critical droplet charged with the mass-to-charge ratio of the jet is at, or very near, the Rayleigh limit. A droplet of critical radius with $\zeta_D < \zeta_J$ is unstable and should undergo a Coulomb explosion, while one with $\zeta_D > \zeta_J$ is stable; similarly, a droplet with $\zeta_D = \zeta_J$ is stable if its diameter is smaller than R_D^*, and unstable otherwise.

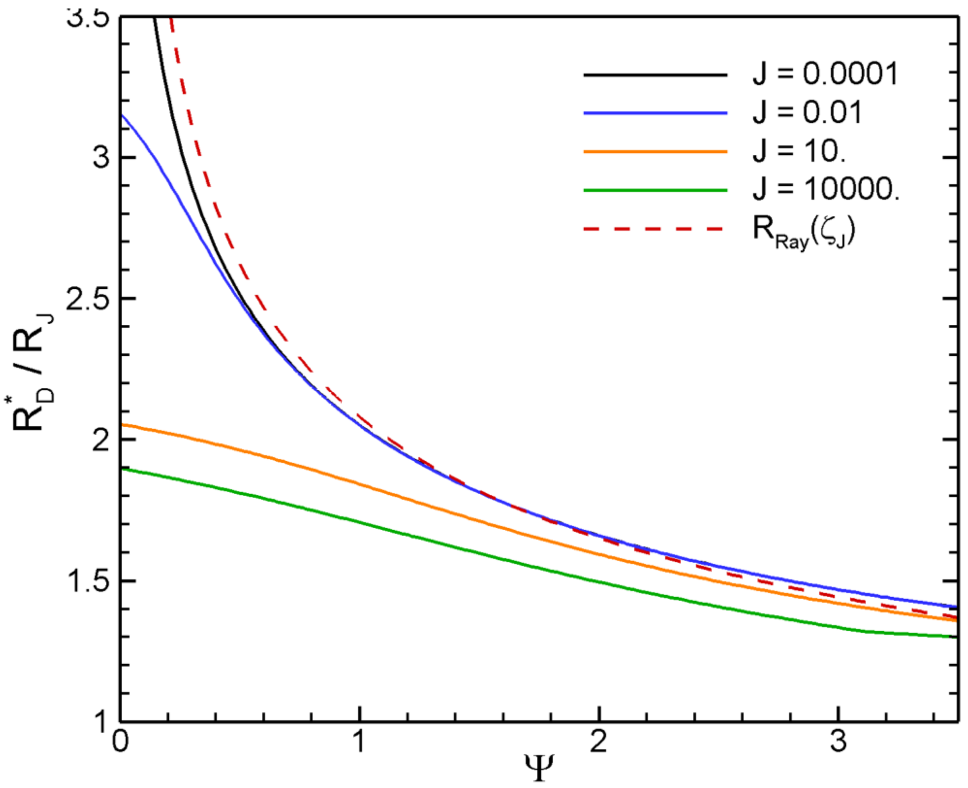

Figure 2.10: Critical droplet radius R_D^* normalized with the radius of the jet, as a function of the Taylor Ψ and Ohnesorge numbers, $Oh = J^{-1/2}$; and Rayleigh limit of the droplet with the mass-to-charge ratio of the jet.

To understand the effects of Coulomb explosions and ion emission from droplets we notice that the inherent randomness and nonlinearity of the breakup causes a variability in both the diameter of the droplets, and in the mass-to-charge ratio of droplets with the same diameter. However the equipotential condition requires these two variables to be distributed in a band around the constraint

$$\phi_c \cong \frac{q_D}{4\pi\varepsilon_0 R_D} \quad \longrightarrow \quad \zeta_D \cong \frac{\rho}{3\varepsilon_0\phi_c} R_D^2, \tag{2.15}$$

where the characteristic potential ϕ_c can be approximated by the potential of the most likely droplet, i.e. that with the critical radius and mass-to-charge ratio ζ_J, $\phi_c = \rho R_D^{*2}/(3\varepsilon_0\zeta_J)$.

Thus, in an equipotential breakup, the radius of a droplet scales with its mass-to-charge ratio as

$$\frac{R_\phi}{R_D^*} = \left(\frac{\zeta}{\zeta_J}\right)^{1/2}. \tag{2.16}$$

The constraint imposed by the Rayleigh limit (2.5) can similarly be written as

$$\frac{R_{Ray}(\zeta)}{R_D^*} = \frac{R_{Ray}(\zeta_J)}{R_D^*}\left(\frac{\zeta}{\zeta_J}\right)^{2/3}, \tag{2.17}$$

where the ratio $R_{Ray}(\zeta_J)/R_D^*$ is one for the lowest beam currents and slightly smaller than one for the highest beam currents, as illustrated by the ratio between functions (2.14) and (2.12) in Fig. 2.10. Finally when the electric field on the droplet exceeds a critical value E_{IFE} promoting ion field emission, charge from its surface is rapidly emitted at constant droplet radius until it reduces the electric electric field just below E_{IFE}. The relation for the radius of a droplet and its mass-to-charge ratio at constant electric field E_{IFE} is

$$\frac{R_{IFE}}{R_D^*} = \frac{E_{IFE}}{E_D^*(\zeta_J)}\frac{\zeta}{\zeta_J}, \tag{2.18}$$

where $E_D^*(\zeta_J)$ is the electric field of the droplet of critical radius with mass-to-charge ratio ζ_J. Figure 2.11 plots (2.16), (2.17), and (2.18) with $E_{IFE} = 1.2eV$, for the 230 nA beam; the plots for all other beam currents are similar due to the nearly coincidence between R_D^* and $R_{Ray}(\zeta_J)$ for all EMI-Im jets. The randomness of the breakup produces droplets with different mass-to-charge ratios, with diameters given by (2.16). Droplets with $\zeta_D/\zeta_J > 0.98$ have radii smaller than their associated Rayleigh limit and are stable; droplets with $0.64 < \zeta_D/\zeta_J < 0.98$ have diameters over the Rayleigh limit, are unstable and break into fragments, probably one with the larger mass fraction, and higher ζ and ϕ_{RP} than the original droplet; and several smaller fragments with lower ζ and ϕ_{RP} than the original droplet; and droplets with $\zeta_D/\zeta_J < 0.64$ evaporate ions at constant radius. Among the ion evaporating droplets, those with $\zeta_D/\zeta_J > 0.42$ reach the ion evaporation curve with a radius above the Rayleigh limit and undergo Coulomb explosions; and droplets with $\zeta_D/\zeta_J < 0.42$ reach the ion evaporation limit with a stable $\{\zeta_D, R_D\}$ value.

This analysis is consistent with the experimental observations: a) an equipotential breakup, with its cuadratic $\zeta_D(R_D)$ dependence, produces droplets with broad mass-to-charge ratio distributions, in agreement with the TOF spectra; b) the experiments show that a large number of droplets produced at the breakup remain intact during flight. Most of these main droplets have mass-to-charge ratios larger than ζ_J; c) a small fraction of the droplets with mass-to-charge ratios smaller than ζ_J reach the collector, suggesting that they are unstable and generate other droplets that do not fulfill the breakup equation (2.6). Two new types of droplets with low-ζ are indeed observed in the beams: one at low retarding potentials likely are fragments of Coulomb explosions, and one at the largest retarding potentials. This last droplet population is striking, because despite its very low mass-to-charge ratios (it is the droplet population with lowest ζ) it has the highest retarding potentials, even exceeding the emitter potential by several hundred volts. We can only explain this population as droplets that are produced at the breakup with a mass-to-charge ratio ζ_0, fly several hundred volts $\Delta\phi$ while evaporating a significant amount of charge at constant radius, and end up at the ion evaporation limit with a larger mass-to-charge ratio ζ_f. In this scenario the retarding potential of these ion-evaporating droplets is approximately given by $\phi_J + (\zeta_f/\zeta_0)\Delta\phi$. We cannot think of an alternative mechanism that can augment the retarding potential of such low-ζ droplets several hundred volts above the potential of the emitter. Furthermore, the ions emitted from these droplets in flight should appear within a few hundreds volts below the maximum of the P_1 peaks, which is indeed observed in the retarding potential curves in the form of a low energy tail.

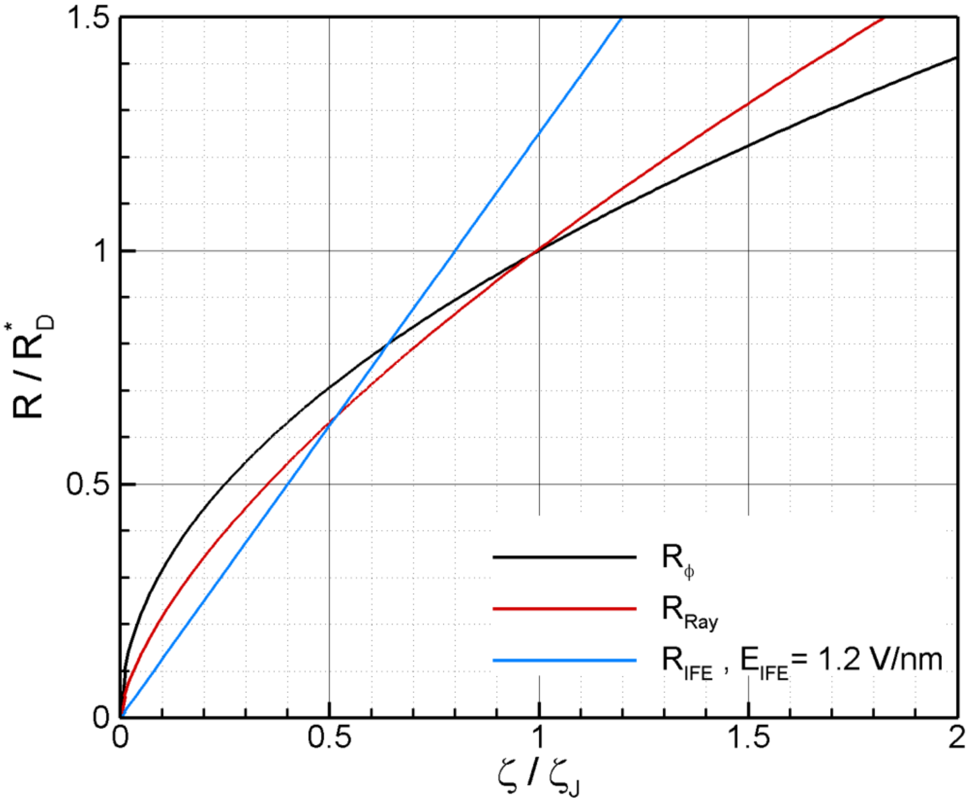

Figure 2.11: Droplet radius normalized with the critical droplet radius $R_D^*(J,\Psi)$, for a beam current of 230 nA at 21 °C and three different mechanisms: equipotential breakup R_ϕ; Rayleigh limit R_{Ray}; and ion evaporation limit R_{IFE}, with $E_{IFE} = 1.2eV$.

When ion field evaporation from droplets becomes more intense, either because the critical droplet is smaller and more charged or its temperature is higher, the ion emission constraint (2.18) has a smaller slope and intersects the equipotential diameter and Rayleigh limit curves at higher values of the normalized mass-to-charge ratio. Under such conditions only the droplets with the highest mass-to-charge ratio remain unchanged during flight, while most others evaporate a large fraction of their charge and Coulomb explosions may be suppressed. The EMI-Im beams at 50 °C exhibit this behavior. At constant beam current increasing the temperature of the fluid promotes ion evaporation because the electrical conductivity increases significantly with temperature, increasing the electric field normal to the surface of the cone-jet; and the larger temperature increases the number of ions than can overcome the energy barrier restricting emission. Figure 2.12 shows retarding potential curves for several beam currents at 50 °C. At the largest beam currents the curves are similar to those measured at 21 °C, except for the higher current values of all ionic peaks relative to the maximum of the droplet distribution. Starting at 320 nA and increasing at lower beam current, the region $\phi_{RP} \gtrsim 1850$ V separates from the central droplet zone, forming a separate population at the lowest beam current. Furthermore the area of the central droplet region (this is where the main droplets preferentially appear) becomes smaller compared to the area of the new droplet population, almost disappearing at the lowest stable beam current of 180 nA. Although retarding potential analysis does not yield the mass-to-charge ratio distributions, it is apparent that the increasingly dominating droplet population at $\phi_{RP} \gtrsim 1850$ V is formed by droplets that have emitted ions, and that most droplets become ion emitters at the lowest beam currents. Figure 2.13 shows TOF spectra for the 255 nA beam, measured at the retarding potentials indicated by black dots in Fig. (2.12), and a chart with the average mass-to-charge ratios and standard deviations of the droplet populations. The phenomenology up to the maximum of the droplet region, $\phi_{RP} = 1755$ V, is similar to that described at 21 °C, with only ions appearing under most of the P_1 peak, and a combination of ions and droplets in the overlap region followed by a single family of droplets up to $\phi_{RP} = 1755$ V. At larger retarding potential the phenomenology changes: the average charge-to-mass ratio of the droplets decreases, reaching a minimum value for all droplet populations at the highest retarding potential, 2171 V. These droplets must have evaporated a fraction of their charge. Note also the very broad distribution at the turning point, $\phi_{RP} = 1844$ V, likely indicating a coexistence of the two types of droplets (main droplets and ion evaporating droplets). As the retarding potential increases the standard deviations decreases, probably reflecting a diminution of main droplets and a constraining of the ion emitting droplets: only those with the smallest mass-to-charge ratios and therefore the smallest radii can evaporate a fraction of their charge large enough to sufficiently increase their retarding potentials.

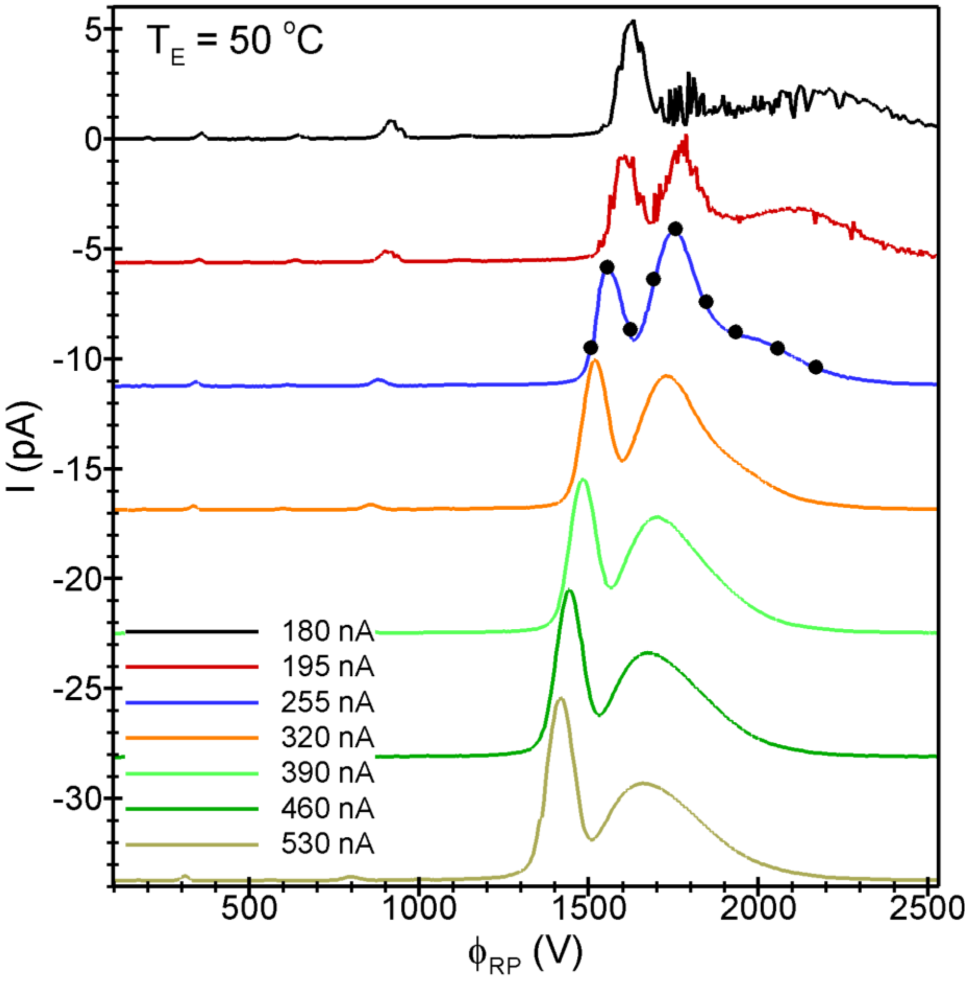

Figure 2.12: Retarding potential curves for several beam currents at 50 °C.

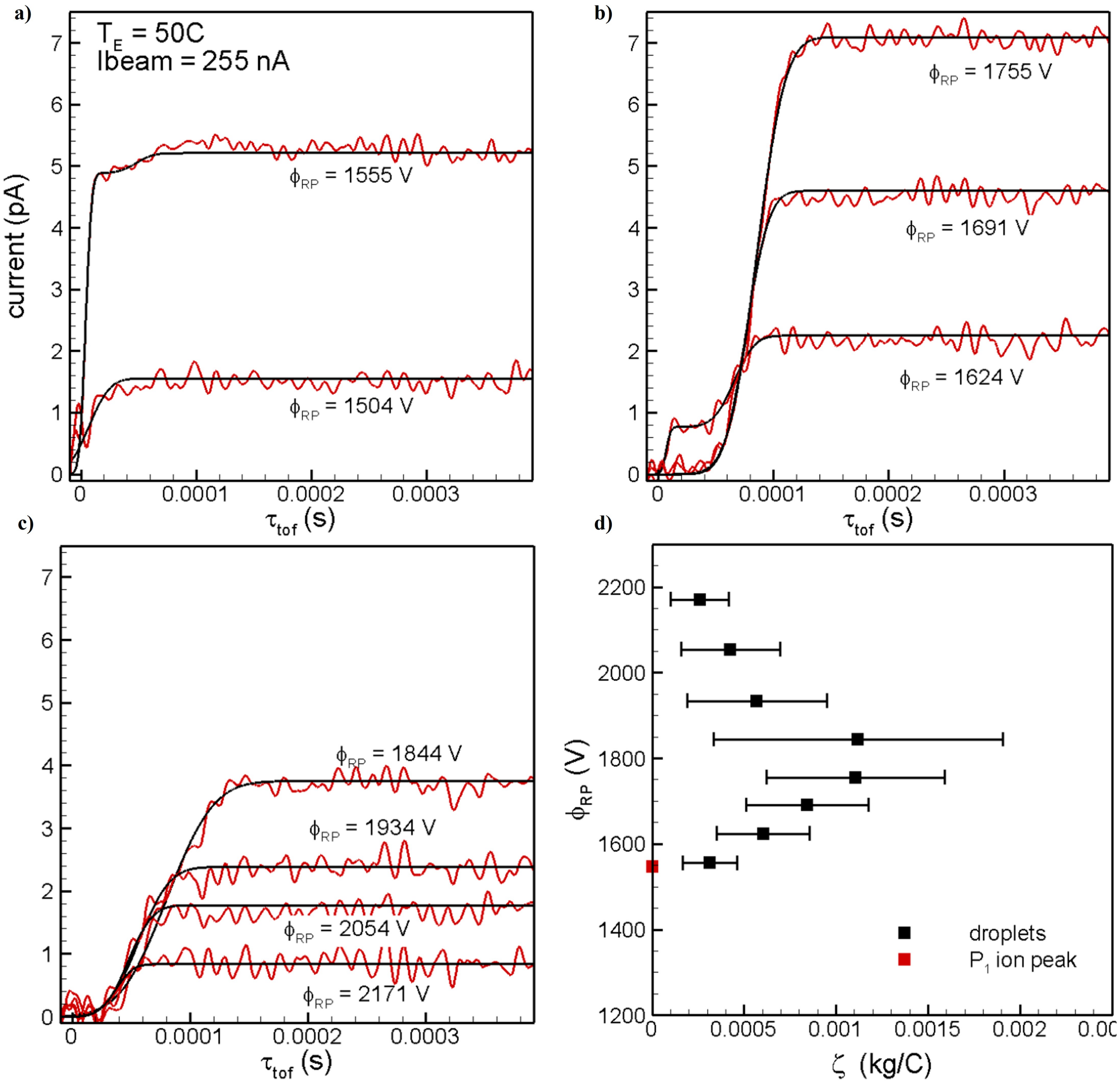

Figure 2.13: a-c).TOF spectra for a 255 nA beam at 50 °C. d) average mass-to-charge ratios with standard deviations of the droplet populations.

2.5 Conclusions

Electrosprays of highly conducting liquids ($K \gtrsim 0.5$) produce beams of charged nanodroplets and molecular ions. The natural breakup of its jet, Coulomb explosions, ion field evaporation and spontaneous desolvation of molecular ions shape the distributions of particles in the beam. Retarding potential and time-of-flight analysis in tandem provides a wealth of experimental information, including the velocity and electric potential of the jet in the breakup region [48, 37]. The radius of the jet, derived from the computed velocity, remains nearly independent of the flow rate when normalized with Gañán-Calvo's characteristic length [52]. This is a well-known property of the much smaller transition region between the cone and jet [39, 46], and its extension far downstream suggests that the breakup may be triggered by the local behavior of the transition region. Experimental values of the velocity and electric potential at a point of the jet are ideal validation parameters for numerical models of the cone-jet, and much needed due to the difficult probing of this nanometric system. The velocity and electric potential in the breakup are also key initial conditions for any model of the expansion of electrospray beams [37].

Due to the much smaller electric relaxation time compared to flow times, the jet breakup of highly conducting liquids is nearly equipotential. When combined with the very high values of the Taylor number Ψ, and less importantly with the high Ohnesorge number ($Oh = J^{-1/2}$) of highly electrified and viscous nanojets, the breakup produces critical droplets significantly smaller than the value $R_D^*/R_J = 1.89$ for inviscid jets without electrification [48]. Furthermore the critical radius $R_D^*(J, \Psi)$ is at, or slightly above, the Rayleigh stability limit for a droplet with the mass-to-charge ratio of the jet ζ_J. Since the randomness of the breakup produces droplets with radii and mass-to-charge ratios other than R_D^* and ζ_J, and the equipotential breakup makes these values to be distributed near $R_D \propto \zeta_D^2$, most droplets with mass-to-charge ratios larger than ζ_J have radii smaller than their Rayleigh limit, are stable and remain intact during flight. The $\{\zeta, \phi_{RP}\}$ values of these main droplets make it possible to obtain the velocity and potential of the jet. On the other hand most droplets with mass-to-charge ratios smaller than ζ_J are unstable and undergo Coulomb explosions to produce fragments with smaller mass-to-charge ratios. These fragments appear in the experiments as droplets with low mass-to-charge ratio that do not conform to the breakup condition (2.6). The smallest droplets with the lowest mass-to-charge ratios evaporate charge at constant radius, may reach the ion field emission limit with a charge smaller than its Rayleigh limit, and remain stable. They form the droplet population with the lowest mass-to-charge ratios and highest retarding potentials, significantly in excess of the emitter potential.

Ions carry an important fraction of the beam current. The ion fraction is a weak function of the flow rate and increases with temperature, in qualitative agreement with both the scaling of the electric field normal to the surface of the cone-jet and the field emission equation [46, 75]. We have identified in the retarding potential curves EMI$^+$ ions joined to up to four EMI-Im molecules. The retarding potential distribution shows a concentration of the ion emission in the breakup region, followed by emission from droplets in flight up to a few hundred volts below the breakup region. Some of these solvated ions lose one or two EMI-Im molecules in flight [99], giving rise to additional isolated peaks in the retarding potential curve.

Although this chapter describes the phenomenology for the ionic liquid EMI-Im, the findings can be extended to other highly conducting liquids on the bases of the dimensionless numbers $\tilde{Q}$, Re_K and ε that parameterize the state of the cone-jet, and the ion solvation energies regulating the emission of ions from the liquid matrix. The following generalizations for electrosprays of highly conducting ionic liquids emerge: a) the Re_K numbers of these liquids are always much smaller than one due to their high viscosities and conductivities; b) due to the dependence of the minimum dimensionless flow rate on Re_K [45], these liquids operate at $\tilde{Q} \gg 1$; c) the breakup is invariably nearly equipotential due to the high values of $\tilde{Q}$ and low value of Re_K; d) the Taylor numbers are near one or larger than one due to the high values of $\tilde{Q}$; e) because of the large Taylor number, small J parameter, and the equipotential breakup, the critical droplet radius normalized with the jet radius follows the small J limit shown in Fig. 2.10. Accordingly, the jet breakup phenomenology of highly conducting ionic liquids is similar to that of EMI-Im, with the possible exception of ion emission effects which also depend on the solvation energies specific to the ion/liquid matrix pair. In the case of highly conducting liquids of reduced viscosity, which may be able to operate at significantly lower dimensionless flow rates, the jet breakup phenomenology will be different due to the lower jet electrification and a departure from the equipotential breakup limit.

Chapter 3

Microfabrication of microfluidic electrospray thrusters

3.1 Introduction

As introduced in chapter 1, electrospray propulsion is a natural fit for the micropropulsion required by SmallSats because it is a soft ionization technique that does not involve the formation of a plasma. A single electrospray emitter efficiently converts electric power into beam kinetic power while operating at mW levels, and MEMS fabrication techniques can be used to create the arrays of hundreds of emitters needed to deliver the thrust requirements operating at the electric power levels available in CubeSats and larger smallsats. Successful miniaturization of electrospray emitter arrays requires an intersection of MEMS fabrication expertise with detailed knowledge of the fundamentals of electrosprays. There have been several attempts at miniaturizing actively fed emitter arrays, i.e., designs in which the flow of propellant between a reservoir and the emission tips takes place through fully encased channels, driven by an imposed pressure difference [73, 74, 85, 91]; these emitter arrays operate in either a droplet or a mixed droplet-ion emission modes. However, these attempts did not implement the high and well-matched hydraulic resistances needed to evenly distribute the propellant among every emitter at the flow rates required for operation in the cone-jet mode and failed shortly after testing. Suzuki et al. tried to increase the hydraulic resistance by doing submicrometer SiN capillaries [121] in order to increase the hydraulic resistance but failed to provide long operation times. Recent attempts using novel technologies such as 3D microlithography and two photon-lithography making photoresist-based emitters have also been unsuccessful to operate [86, 65, 129, 72]. These designs for actively fed emitter arrays have focused on implementing the required hydraulic resistance through the radius and length of the emitter. However, the necessary length of the out-of-plane emitters (perpendicular to the substrate), even at the small diameters made possible by two-photon lithography, required by the needed hydraulic impedance, is outside the capabilities of existing manufacturing technologies. It would unlikely survive the vibration tests needed for space qualification. An alternative and more successful approach is that of passively fed emitter arrays, typically made of porous materials, and in which the flow of propellant is driven by capillarity dependent on the porous sizes of the emitter electrode and the small suction pressure at the emitter tip generated by the electric potential applied to the emitter[15]. The latest generation of electrospray thrusters of these characteristics has been developed at MIT using passively fed emitter tips, etched in porous borosilicate glass, operating in pure ionic emission [82, 112]. However, they report a loss of propulsion efficiency over time due to non-uniformities and large pores introduced by the randomness degree of the microfabrication process, which leads to non-uniform current emission that generate erosion on the extractor grid or shorts between emitters and extractor. Actively fed emitter arrays operating in droplet mode present advantages such as the protection that fully encased channels provide to the propellant, as well as the continuous elimination of neutralized counterions that flow out of the system with the atomized propellant. Recently, Grustan-

Gutierrez& Gamero-Castaño [57] introduced the successful idea of implementing adequate hydraulic impedance by detaching it from the geometry of the out-of-plane emitter. Expanding this approach, this chapter demonstrates a scalable microfabrication and assembly process to produce compact silicon-based multi-emitter electrospray sources. Silicon emitter arrays with different emitter numbers are microfabricated to demonstrate the scalability of the process, that are individually fed by fractal-like etched microchannels perpendicular to the out-of-plane emitters. The electrospray sources are compact, and its components, an emitter array electrode, an extractor electrode, and a supporting micromachined glass substrate, are permanently bonded and precisely aligned using anodic bonding. The uniformity and synchrony of emission in each emitter part of the array are demonstrated together with a fast and good response to the applied pressure in the propellant reservoir. The electrospray thruster heads are tested using the ionic liquid EMI-Im as a propellant, which electrospray has been studied in detail in the previous chapter [41], and exhibit excellent life-performance extending its operation for up to 100 hours and counting. The thrust generated, current emitted by the emitter array, current intercepted, and the operational flow rates are studied in detail.

3.2 Design and Microfabrication

The designed and microfabricated electrospray source includes the three main elements shown in Figure 3.1: an emitter electrode consisting of a patterned double side-polished Si wafer with an array of emitters etched on the topside, and microfluidic channels etched on the backside, and extractor electrode microfabricated in a second double side-polished Si wafer; and a micromachined borosilicate glass wafer used as a substrate to bond and align the emitter array and extractor, as well as to seal the microfluidic channels. The three components, microfabricated independently, are designed with matching features to allow accurate alignment and their permanent integration into a single thruster head element.

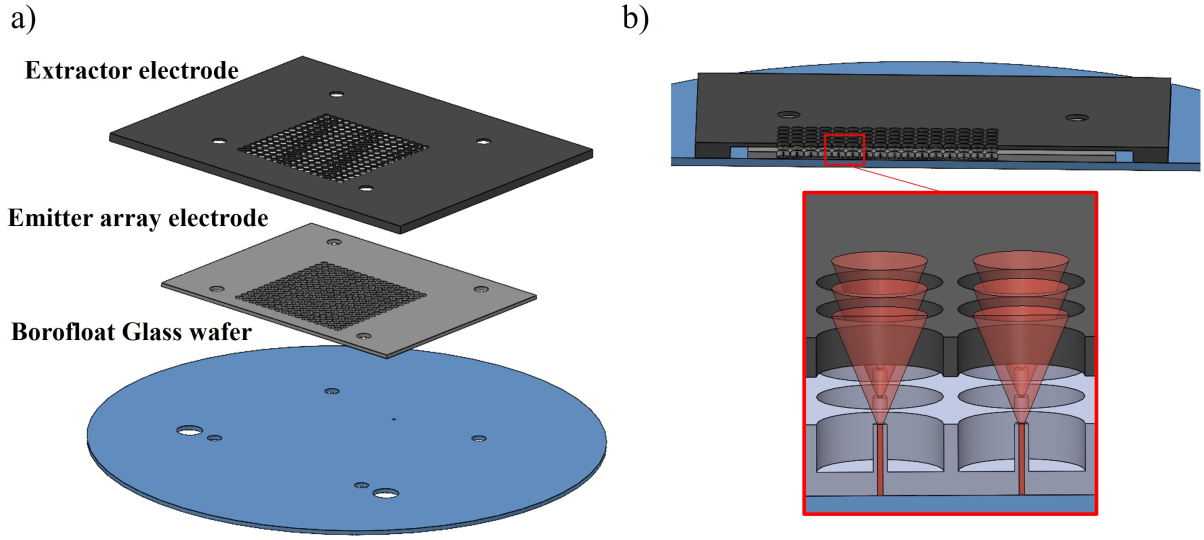

Figure 3.1: a) Exploded view of the components of the electrospray source; micromachined glass wafer, emitter array electrode, and extractor electrode b) Section view of the assembled electrospray head thruster showing the side gap and top gap between the emitter array electrode and the extractor electrode granting voltage isolation between them.

3.2.1 Microfabrication of the emitter array electrode

The emitter array electrode is the main component of the thruster head and the most challenging to fabricate. It comprises an array of silicon emitters whose inner hole goes through all the silicon wafer thickness matching individually fractal-like etched microchannels perpendicular to the out-of-plane emitters. Figure 3.2 shows the schematic of the microfabrication process of the emitter array electrode.

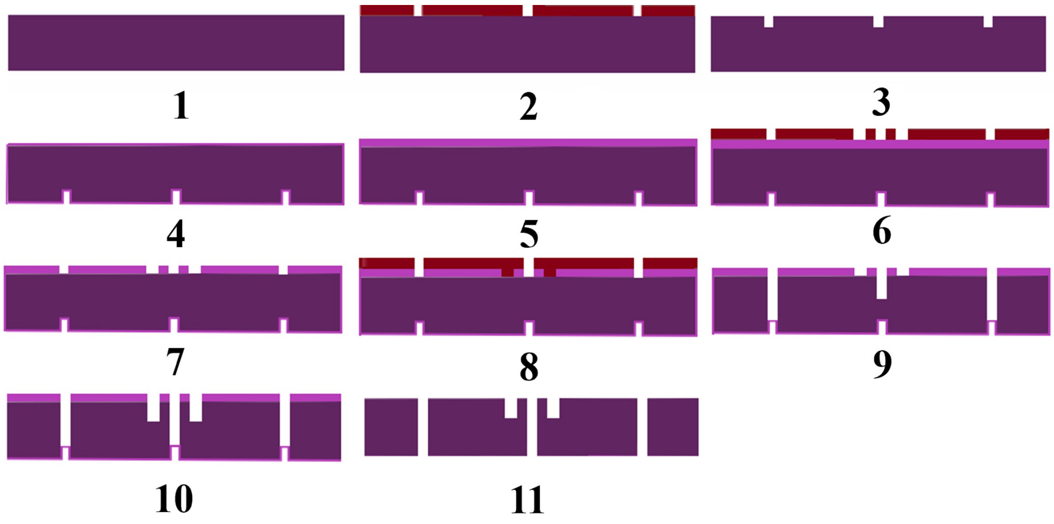

Figure 3.2: Schematic of the microfabrication process of the emitter array electrode.

First (1), the Si wafer undergoes an RCA cleaning (5:1:1, H_2O : 27% NH_4OH : 30%H_2O_2) to guarantee a clean surface followed by a dehydration process to remove water physisorbed. This step is repeated before each lithography and etching during the fabrication. (2) The microfluidic channel pattern and the alignment marks are transferred to the backside of the wafer with photolithography using an AZ positive photoresist, shown in Figure 3.3 ;

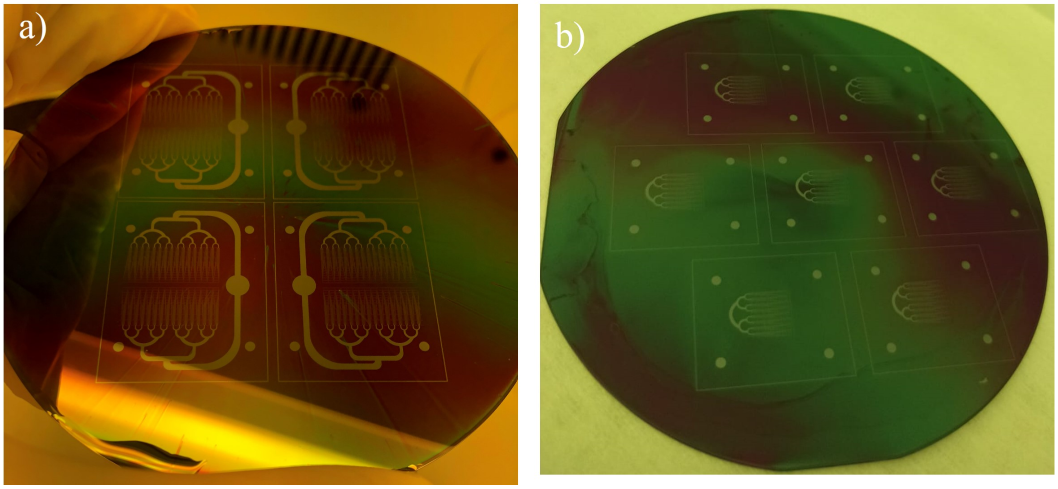

Figure 3.3: a) 4 inch Si wafer with 64 microfluidic pattern b) 4 inch Si wafer with 256 microfluidic pattern

(3) the microfluidic channels are then etched using inductively-coupled plasma reactive-ion etching (ICP-RIE) with an optimized Bosch recipe shown in Table A.3. The etching of the process is stopped at a specific depth using a previous calibration of the etch rate in order to implement the desired hydraulic resistance, targeting in most of the electrodes a microchannel depth of 20μm-30μm. The channels are individually inspected through microscopy and profilometry after the etching, as shown in Figure 3.4.

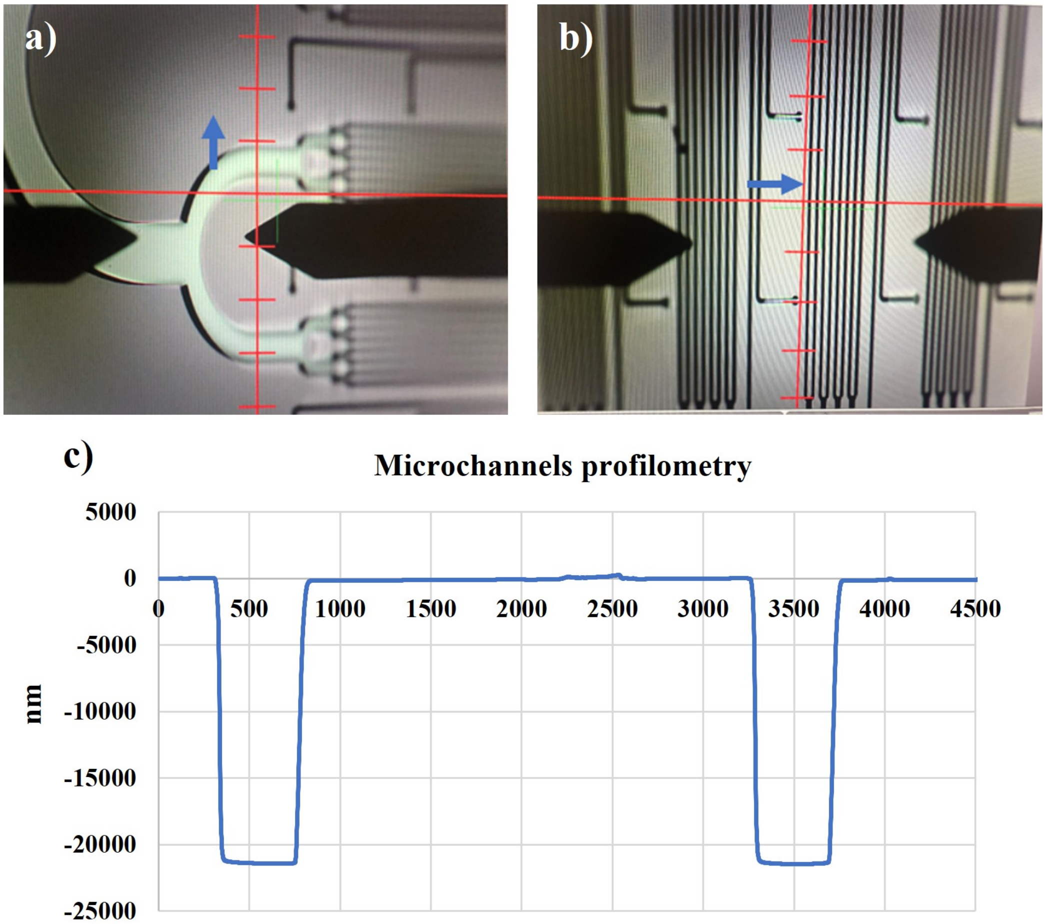

Figure 3.4: a-c) profilometry inspection of the etched microchannels

(4) The photoresist is stripped, and the wafer undergoes a dry thermal oxidation process to grow a 1μm layer of SiO_2. The SiO_2 layer is used to protect the microfluidic channels and provide a stopping layer for the last etching step. Thermal oxidation can be done with two different processes: wet oxidation and dry oxidation.

$$\mathrm{Si} + 2\mathrm{H_2O} \rightarrow \mathrm{SiO_2} + \mathrm{H_2}$$

$$\mathrm{Si} + \mathrm{O_2} \rightarrow \mathrm{SiO_2}$$

A common mathematical model to estimate oxide thickness is the Deal-Grove model [21], which is given by:

$$t = \frac{X^2 + AX}{B} \tag{3.1}$$

Where t is the processing time, X is the oxide thickness, and A and B are the parameters determined for each oxidation condition (wet or dry oxidation, temperature, wafer types, etc.). Simplifying this, the film thickness is proportional to $X \approx \sqrt{Bt}$, because B is completely related to the oxide diffusion rate into silicon. As temperature increases, given that we are over the temperature threshold allowing oxygen diffusion, B becomes smaller, and the oxidation rate increases. Wet oxidation is usually much faster than dry oxidation, but the obtained oxide films have more defects and higher porosity than dry oxide films. For the stopping etching layer needed in the emitter array electrode, as shown in the following steps, a dry oxidation layer is preferred over the wet oxide layer. Deal-Grove provided oxidation rates for both processes based on the temperature. The 1 μm SiO_2 layer is grown with dry oxidation for 10 hours at 1200ºC with an oxygen pressure of ~760 torr.

After the thermal oxidation, (5) a 3 μm layer of SiO_2 is deposited on the top side of the wafer (opposite to the microchannels side) using plasma-enhanced chemical vapor deposition (PEVCD). The gases used for plasma deposition of SiO_2 are the following:

$$\mathrm{SiH_4} + \mathrm{N_2O} \rightarrow \mathrm{SiO_2}\ (+2\mathrm{H_2} + \mathrm{N_2})$$

The optimized recipe for this deposition and its deposition rate is shown in Table A.1 in the appendix section. The final SiO_2 thickness is inspected using ellipsometry technique. The deposited SiO_2 will act as a mask for the final etching step due to its high resistivity and etching selectivity, being resistant to silicon plasma etching agents. To etch the mask, (6)the emitter array pattern, where each emitter is a cylindrical tube with different external diameters tested and 40 μm inner diameter, together with alignment marks, is transferred using lithography with an AZ photoresist. The external diameters tested during the fabrication are 100, 80, and 70 μm. Backside alignment is used in this lithography to match the center hole of the emitters with the end of the microfluidic channels in the backside of the wafer. Previous to the lithography, the deposited SiO_2 layer is pretreated with HDMS to increase the adhesion of the photoresist. Figure 3.5 shows the result of the lithography for different external emitter diameters.

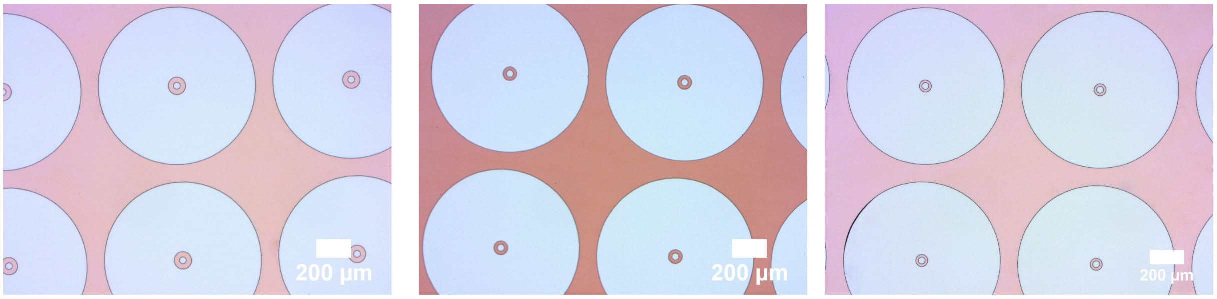

Figure 3.5: Emitter array lithography backside aligned with the microlfuidic channels ends with 100, 80 and 70 μm external diameters and 40 μm inner diameter

(6) The emitter pattern and its surrounding well is then etched on the SiO_2 deposited layer using reactive ion etching with a SiO_2 etch recipe, Figure 3.7. The optimized recipe for the etching is shown in Table A.2 in the appendix.

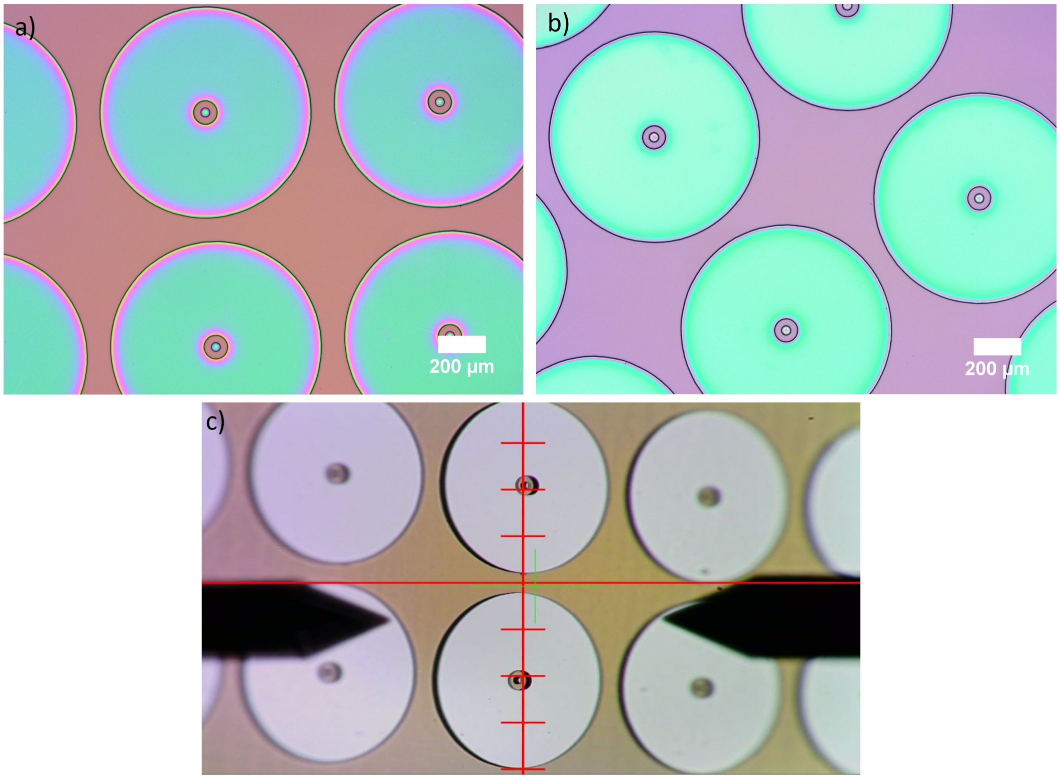

Figure 3.6: a-b)Gradual etching of the SiO_2. c)Profile view from profilometer of the SiO_2 etched mask.

(7) the photoresist is stripped, and another lithography is performed (8), exposing only the inner hole of the emitter and the alignment holes using front-side alignment. This mask will be used to etch 50 to 75 % the inner hole depth depending on the initial thickness of the silicon wafer used;

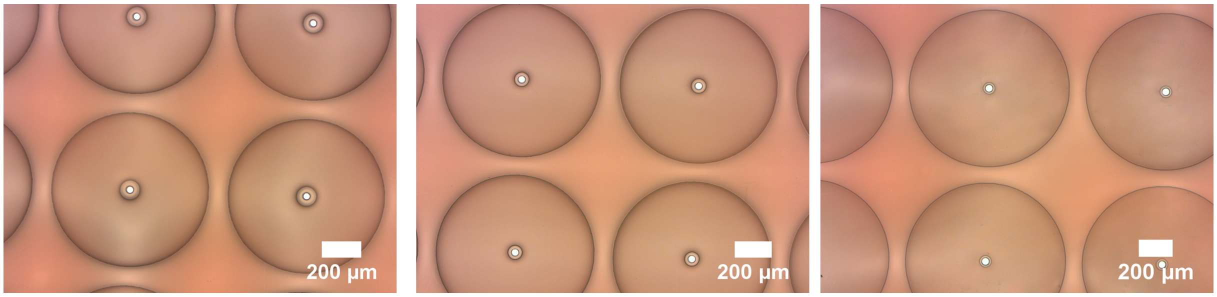

Figure 3.7: Photolithography mask covering the SiO_2 mask with an opening matching the inner hole of the emitters with different external diameters.

The exposed inner hole undergoes etching together with the alignment holes using deep reactive ion etching with the silicon etch recipe (9). This etching required several attempts in order to calibrate the etching rate of the 40 μm hole opening. After the etching, the photoresist is stripped, exposing the SiO_2 mask with the inner hole of the emitter halfway etch through as shown in Figure 3.8

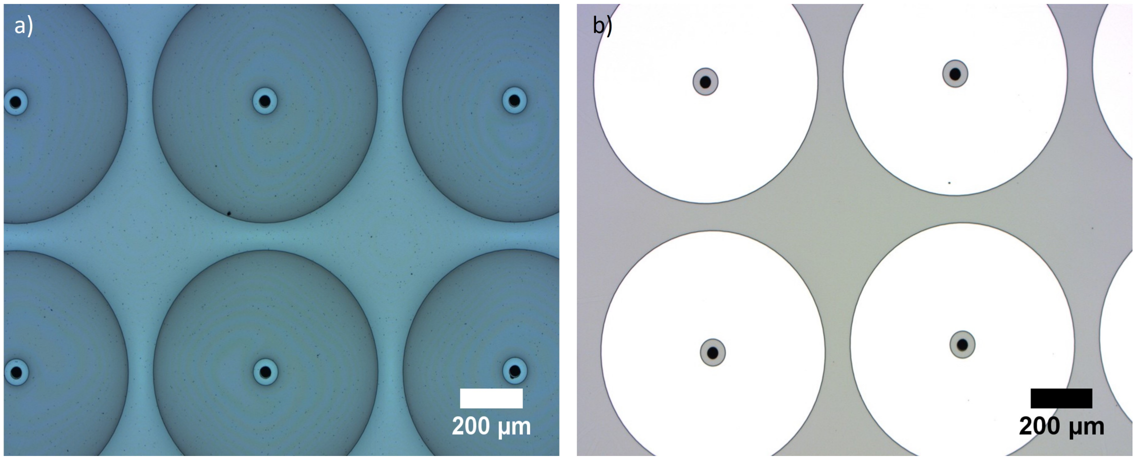

Figure 3.8: a) Photoresist after the inner hole etch b) SiO_2 mask exposed after the etching of the inner hole and the stripping of the photoresist.

(9) The photoresist is stripped, and the SiO_2 mask with the geometry of the emitter and the surrounding well undergoes the last RIE process (10), which finishes the central hole etch, connecting each emitter to the end of each microfluidic channel, and defines the emitter height and the surrounding well depth, which is set at 275 μm; Figure 3.9 a-b. shows optical images of the final silicon etch step. Figure 3.9 c-d. shows optical pictures of an over etch well that helps to see how the microchannels connect the emitters. In Figure 3.10 a SEM image of an etched emitter still with the SiO_2 is shown together with details of the etch profile of the Bosch process. The sidewall profile directly under the mask is a reversed taper. It becomes vertical, and gradually tapers as the aspect ratio or etch depth increases. Several calibrations were pursued to minimize this tapper profile.

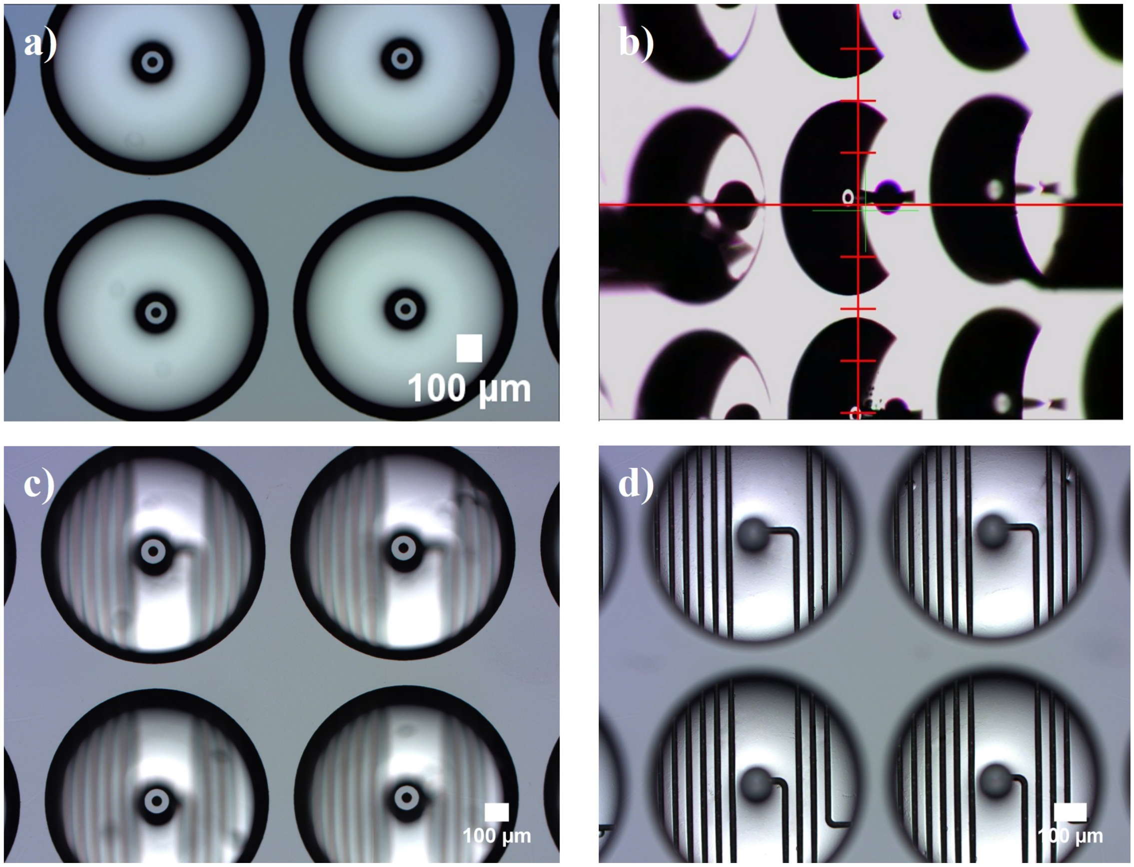

Figure 3.9: a) Optical image from the top of the well and emitter after the final Si etch step. b) Side view of the array from the profilometer. c-d) over etched well displaying the match of the microfluidic channels of the backside with the emitters on the front side of the Si wafer.

Figure 3.11 shows SEM pictures of the etch through of the inner hole of the emitters matching the end of the microchannels perfectly and stopped by the SiO_2 dry oxidation thermal layer, note that the SEM pictures are taken outside the cleannroom and before RCA clean, displaying some thermal grease remains.

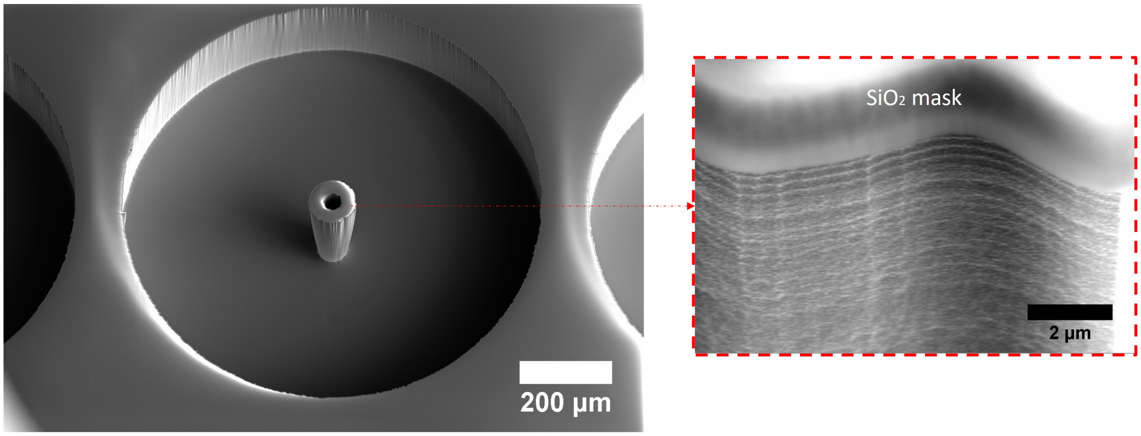

Figure 3.10: SEM image of an emitter, part of the array, after the final Silicon etch step with the SiO_2 mask, and details of the etch-passivation etch marks typical of the bosh process.

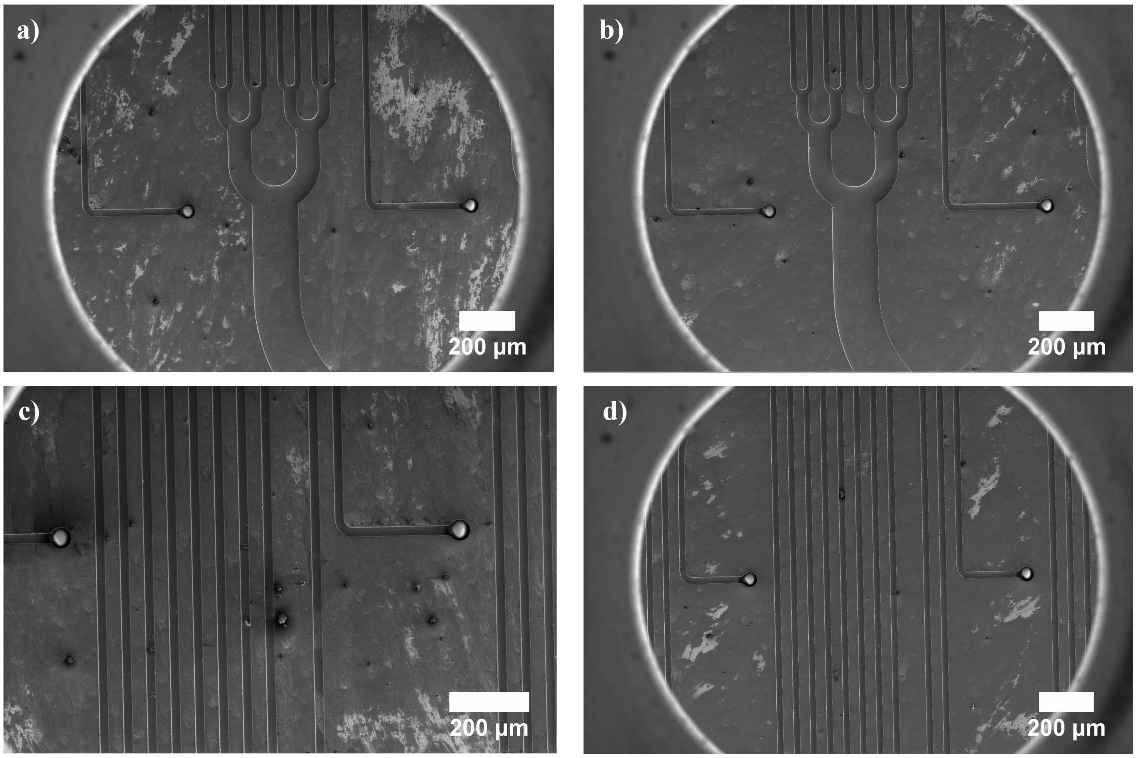

Figure 3.11: SEM pictures of the etch through of the inner holes of the emitter array matching the end of the microchannels in the back side of the wafer with the SiO_2 dry oxidation stopping layer.

(10) To remove the oxide layer, the wafer is soaked in a buffered oxide etch bath (6:1 volume ratio of 40% NH_4F in water to 49% HF in water) for 1h 10 min to completely remove the

SiO_2 mask. The complete etching of the SiO_2 mask takes longer on the top side of the emitter array electrode due to the extra 3 μm PECVD layer of SiO_2. Figure 3.12 shows the etch process of SiO_2 thermal oxide layer on the microchannels side, and Figure 3.13 shows the etch process for the SiO_2 thermal oxide layer and PECVD SiO_2.

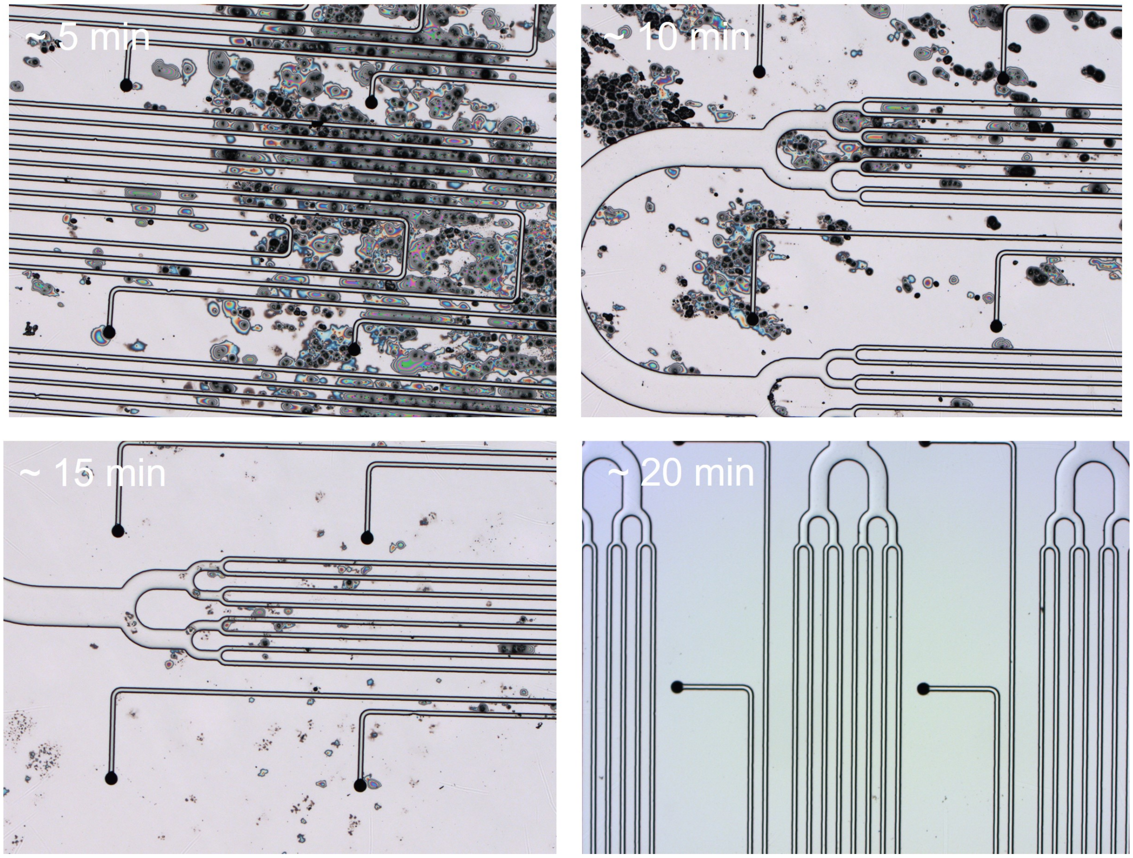

Figure 3.12: Etching rate of the SiO_2 thermal oxide layer on the microchannels side of the emitter array electrode, using BOE.

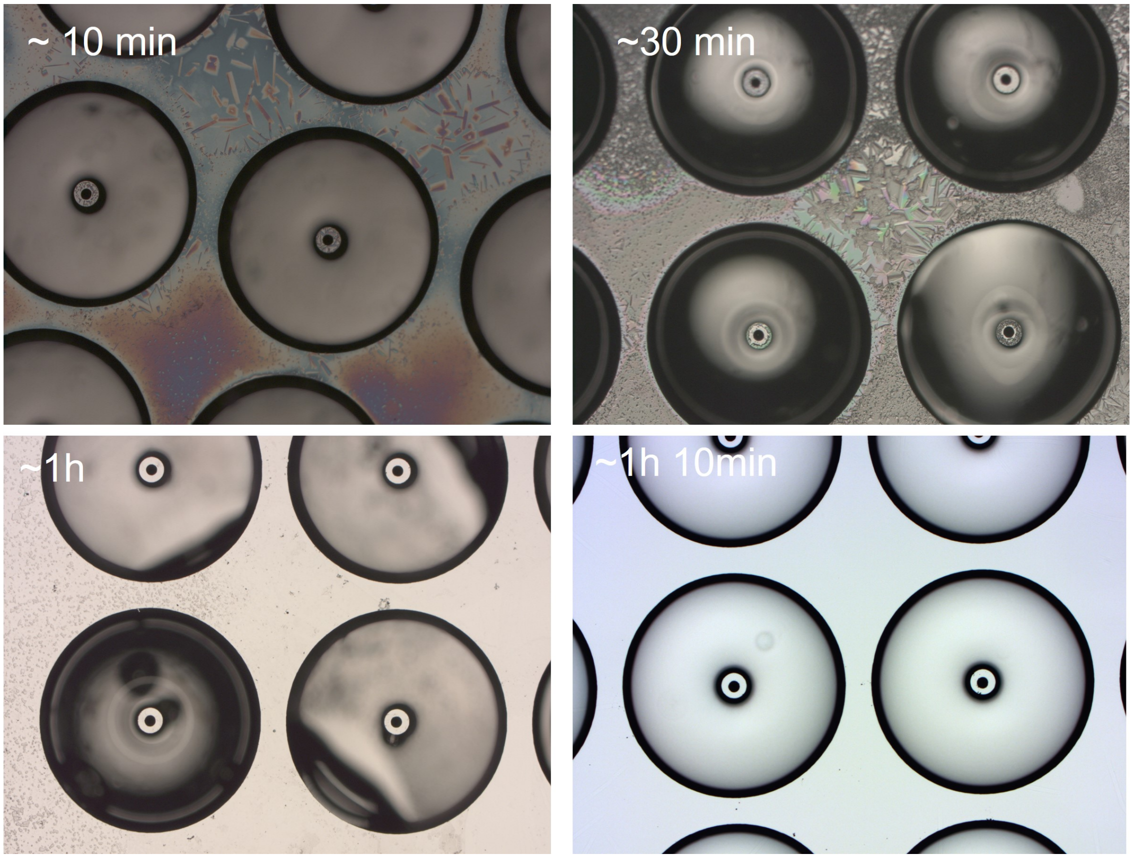

Figure 3.13: Etching rate of the SiO_2 thermal oxide layer and PECVD layer on the emitters side of the emitter array electrode, using BOE.

With the final wet etch of the SiO_2, the emitter array electrode fabrication is concluded. It is essential to realize an extensive optical microscope inspection to check that all the microfluidic channels are nicely etched and connected. Also, all the ends of the microchannels must be connected to the inner hole of the emitters. The same microscope inspection has to be carried out on the emitter array side of the electrode. If one single emitter of the array is broken or defective, the propellant will short the electrospray source during operation. In Figure 3.14 a-b) SEM pictures of the silicon emitters on the top side of the emitter array electrode, after the SiO_2 etch are shown. Figure 3.14 c-f) shows optical pictures of some areas of the microchannels without SiO_2 and with etching through. In Figure 3.15 photographs of the top side and backside of emitter array electrodes for a 64 emitter array and a 256 emitter array are shown.

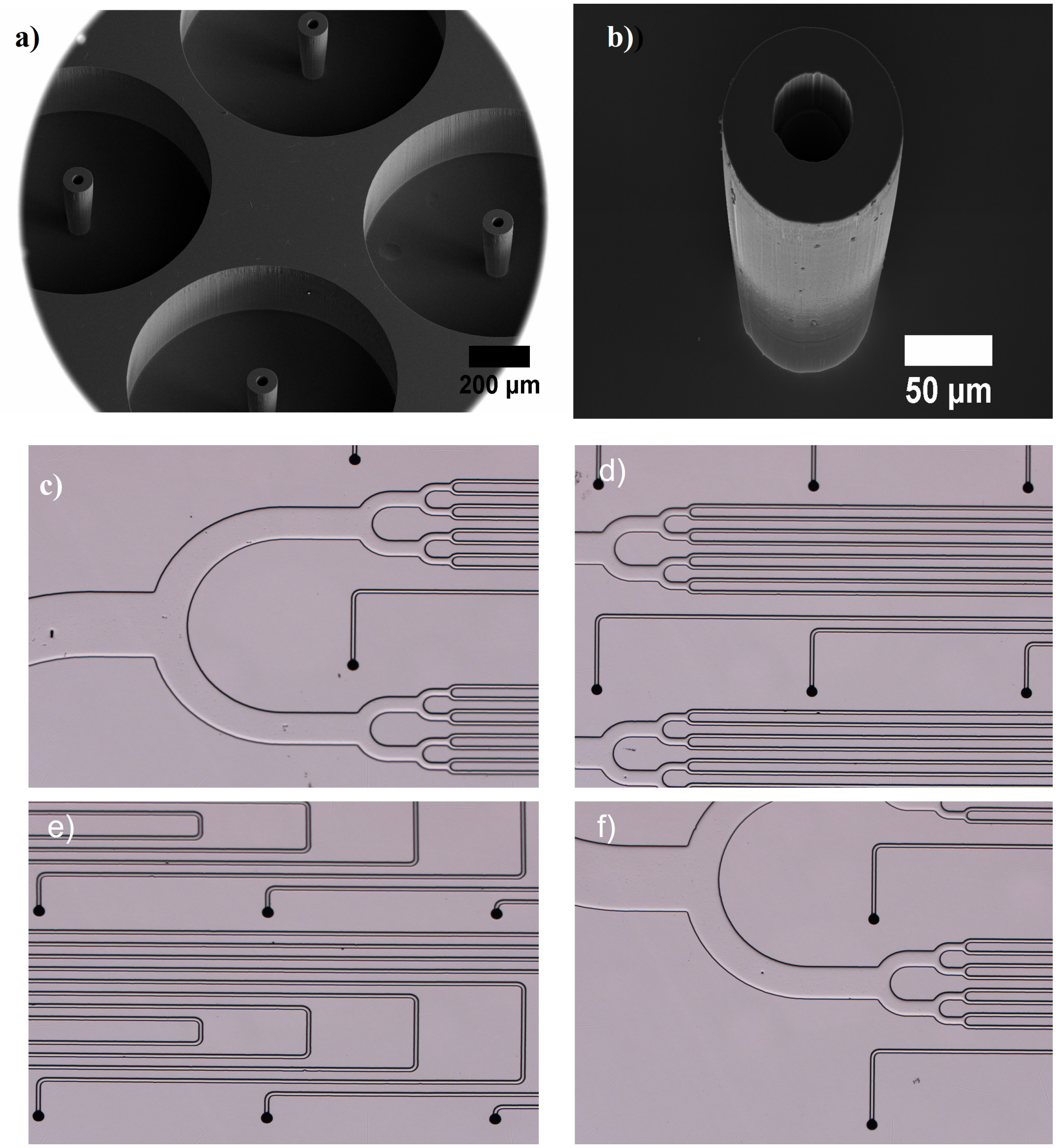

Figure 3.14: Etching rate of the SiO_2 thermal oxide layer and PECVD layer on the emitters side of the emitter array electrode, using BOE.

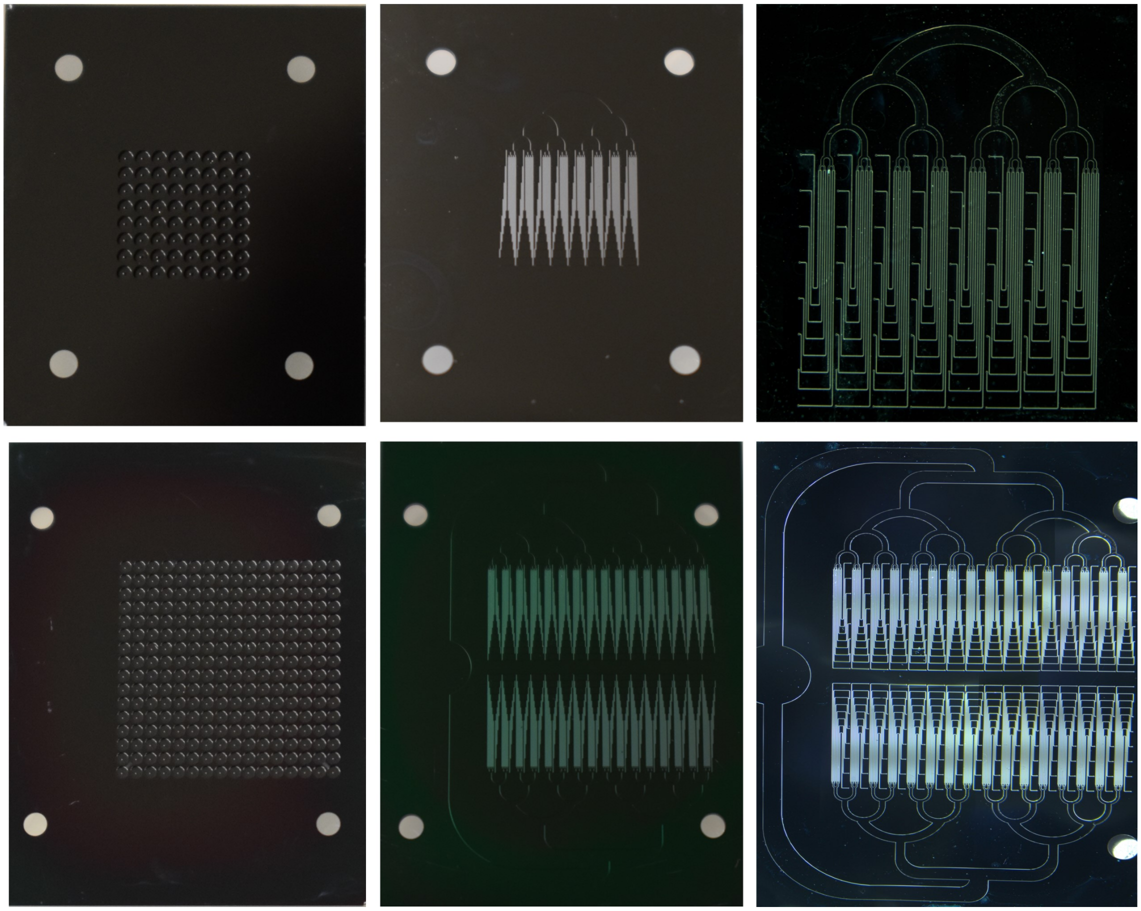

Figure 3.15: 64 and 256 fabricated emitter array electrodes. (a) photograph of the top view of the 64-array emitter electrode with the emitters and the surrounding well. (b) photograph of the backside view of the 64-array emitter electrode with the microfluidic channels. (c) Amplified view of the 64 emitter microchannel arrays. (d) photograph of the top side view of the 256-emitter array electrode with the microfluidic channels (e) photograph of the back side view of the 256-array emitter electrode with the microfluidic channels.

The emitter array electrode is successfully fabricated with a wafer thickness of 500 μm, 450 μm and 400 μm.

3.2.2 Microfabrication of the extractor electrode

For the fabrication of the extractor electrode, we use double side silicon polished wafer with a 1 mm thickness. Figure 3.16 a. shows the schematics of the microfabrication process.

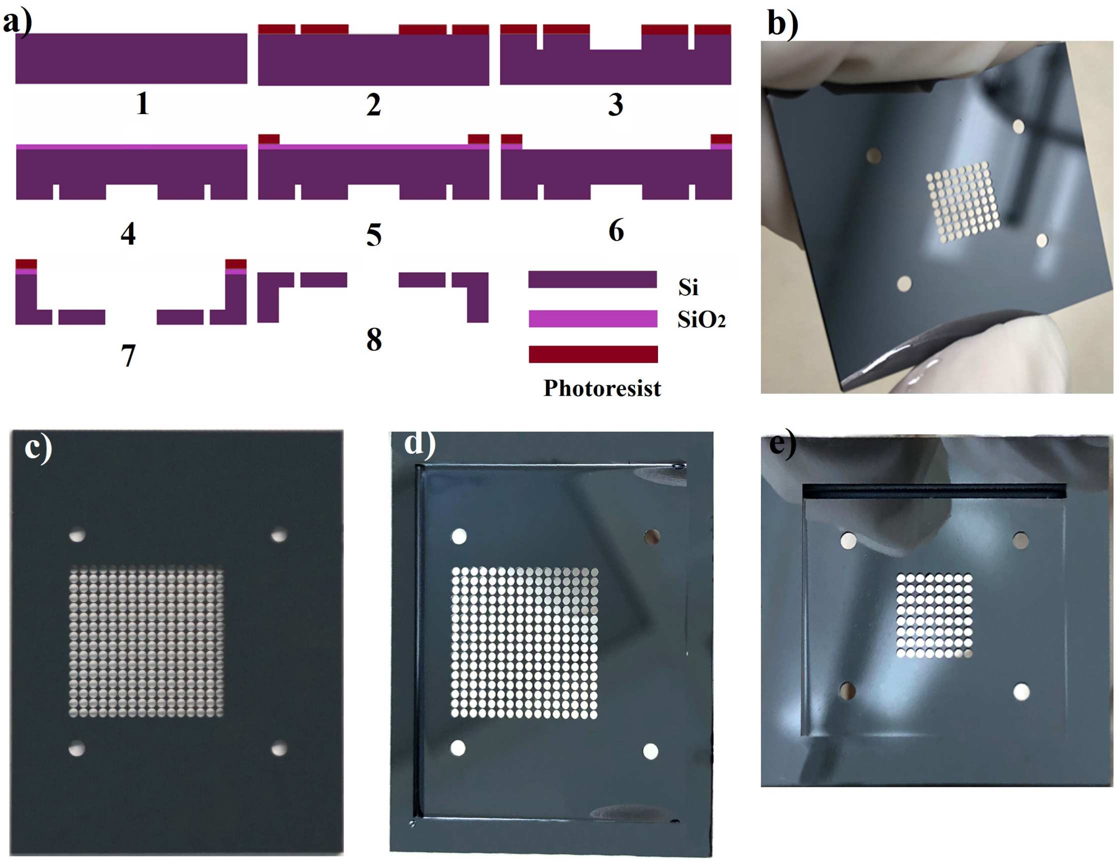

Figure 3.16: a. Schematic of the fabrication of the extractor electrode. b and e) top and back side view of the extractor for a 64 emitter electrospray source. c-d) top and back side view of the extractor for a 256 emitter electrospray source.

To micromachine the circular openings and the alignment holes, matching the number of emitters in the emitter array electrode and centered with the center holes of the emitters, the designed pattern is transferred on one side of the double-side polished Si wafer using an AZ positive photoresist and photolithography (Figure 3.16 .a.2). The pattern is then etched using DRIE with a modified standard Bosh recipe until a 250 μm depth is reached (Figure 3.16 .a.3). The photoresist is stripped, and the wafer is then flipped, and a 4 μm layer of SiO_2 is deposited using PEVCD (Figure 3.16 .a.4). The SiO_2 deposited layer will act as a mask for the final etch. The SiO_2 mask is patterned with lithography (Figure 3.16 .a.5) and etched using a SiO_2 etch recipe leaving a SiO_2 layer in the frame (Figure 3.16 .a.6). The exposed silicon is then etched with a modified slow Bosh process (the etching area is extensive) to guarantee an uniform profile along with the extractor (Figure 3.16 a.7.). The photoresist is then stripped, and the SiO_2 of the frame is removed with BOE (Figure 3.16 .a.8). The length of this final etch will dictate the distance between the extractor and the emitter array electrode as follow:

The gap between the emitter and extractor electrode = Depth of final etch in extractor electrode – thickness of emitter electrode. This distance can be tailored to minimize the voltage required and intercepted current during the operation of the electrospray source. Figure3.16b-e. shows photographs of the top and bottom side of a finished extractor electrode for a 256-emitter array and a 64-emitter array.

3.2.3 Micromachined Borofloat glass, anodic bonding and integration of all the components

For the sealing of the microfluidic channels of the emitter array electrode, the alignment and the bonding of the extractor electrode all together in a compact thruster head, a borofloat glass wafer is used as a bonding platform. The borosilicate wafer has a small orifice, a connection hole, and four laser micromachined alignment holes that match the alignment holes on the emitter array electrode and extractor array electrode. The small orifice will be used for the insertion and bonding with a hard resist of a fused silica tube that will feed the propellant from an external reservoir to the flow-resistive channels of the emitter array electrode. The connection hole will connect the emitter electrode to the voltage source. The borofloat glass undergoes first a dehydration and RCA process, and then the emitter electrode is anodically bonded to it, sealing the resistive flow microchannels as shown in schematic Figure 3.17.

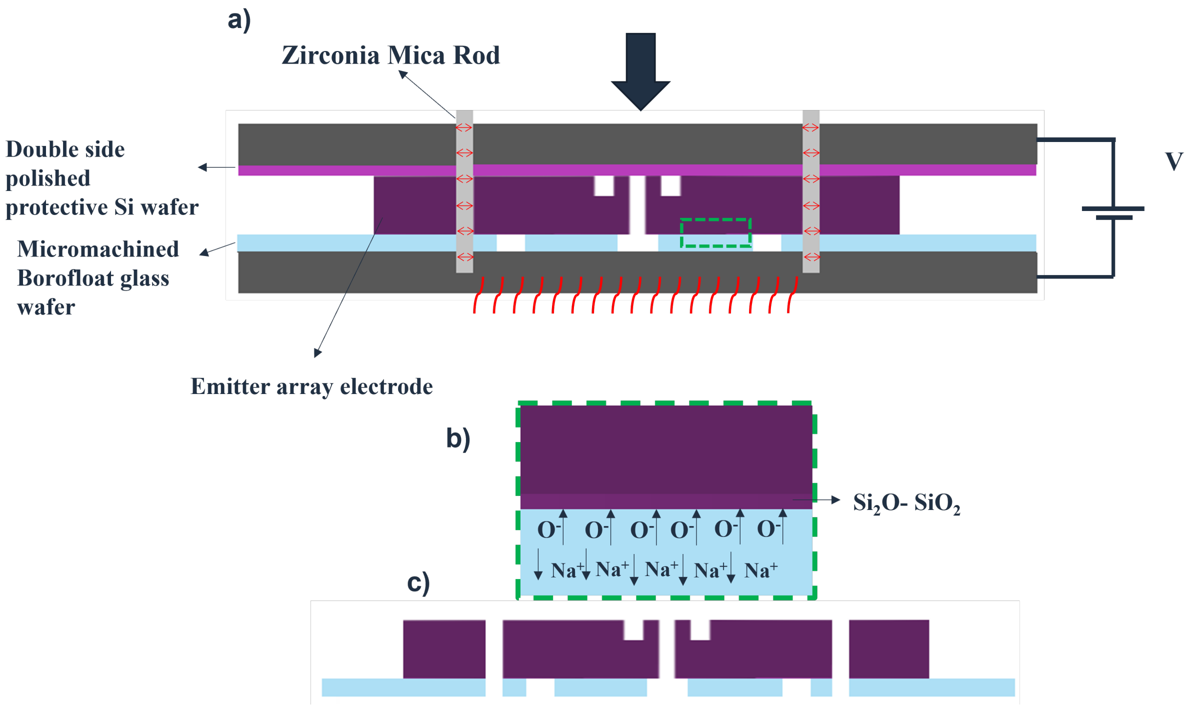

Figure 3.17: a)Schematics of the custom set up used for bond anodically the emitter array electrode to the glass wafer aligned using Zirconia mica rods.b) Depletaion layer that generates the permanent bonding. c) Final result after the bonding.

The anodic bonding is carried out at 350ºC and 1000 V for one hour while compressing the emitter electrode, protected with a double side polished wafer on top, towards the borofloat glass wafer. Zirconia mica rods are used through the alignment holes of the borofloat glass wafer and emitter array electrode to precisely align both components. The coefficient of thermal expansion of the rods is used to reduce the tolerance with the alignment marks while bonding. At 350ºC, together with the electric field generated, diffusion of sodium ions(Na$^+$) from the glass interface in contact with the silicon move towards the backside of the glass connected to the cathode. That creates a depletion region (Figure 3.17.b.) where the electric field is high, drifting the oxygen ions (O$^-$) towards the interface reacting with the silicon and forming a thin oxide layer between both surfaces, siloxane (Si-O-Si) and SiO$_2$, that ensures an irreversible bonding between the emitter array electrode and the borofloat wafer. P-type silicon (doped with boron, leaving silicon atoms with a vacant location on its outer shell, called a ”hole”) is used for the microfabrication of the emitter array reducing the energy necessary to drift the oxygen anions of the glass towards the silicon lowering the temperature and electric field needed during anodic bonding to generate the thin silicon oxide bonding layer [89]).

Figure 3.18.a-b. shows the results of a 64 emitter microchannels array and a 256 emitter microchannels array anodically bonded and aligned to the glass wafer.

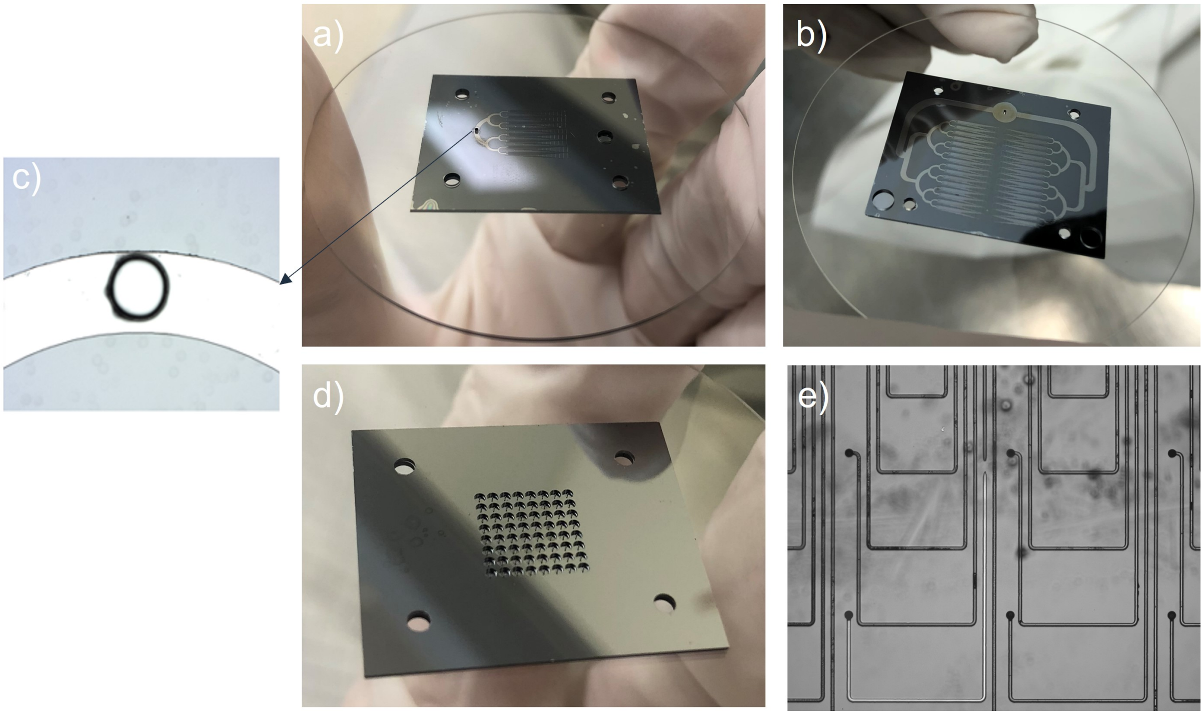

Figure 3.18: a-b) Photographs of the microchannels side of a 64 for emitter array electrode and a 256 emitter array electrode anodically bonded to the glass wafer.c) Optical Picture of the orifice to insert the fused silica line matching the main microfluidic channel. d) Top side of the emitter array electrode shown in a), showing the emitter array. e) Test of the sealing of the channels with a discontinued microchannel.

Figure 3.18c. shows the etched orifice in the glass wafer aligned with the beginning of the microchannels branch that is used to insert a fused silica line to feed the propellant. The sealing of the microchannels is tested and validated by flowing ionic liquid to a sealed microchannel array with a discontinued microchannel. In Figure 3.18e., the discontinued microchannel is shown without liquid overflowing from its neighbor’s channels, proving an excellent bonding.

After bonding the emitter array electrode with the borofloat wafer, the extractor electrode is also aligned, and its frame is anodically bonded to the glass wafer, leaving a gap with the emitter electrode, and electrically isolating both electrodes through the glass as shown in schematic Figure 3.19.

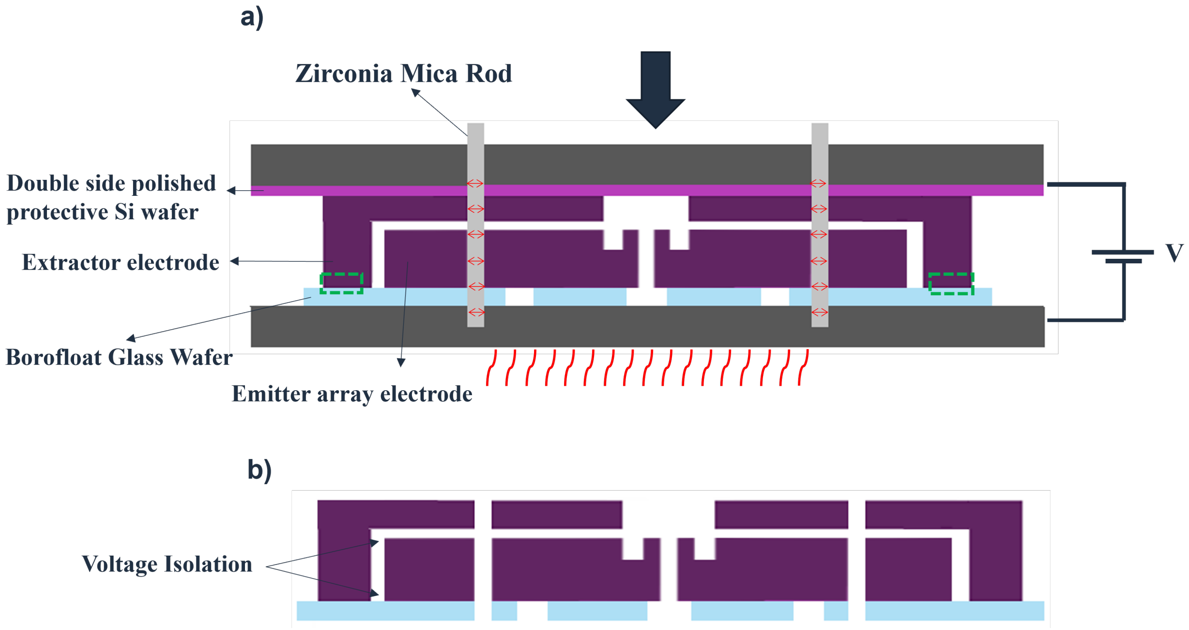

Figure 3.19: a) Schematic of the anodic bonding of the extractor electrode to the glass wafer aligned with the emitter array electrode.b) Schematic of the compact electrospray thruster head bonded.

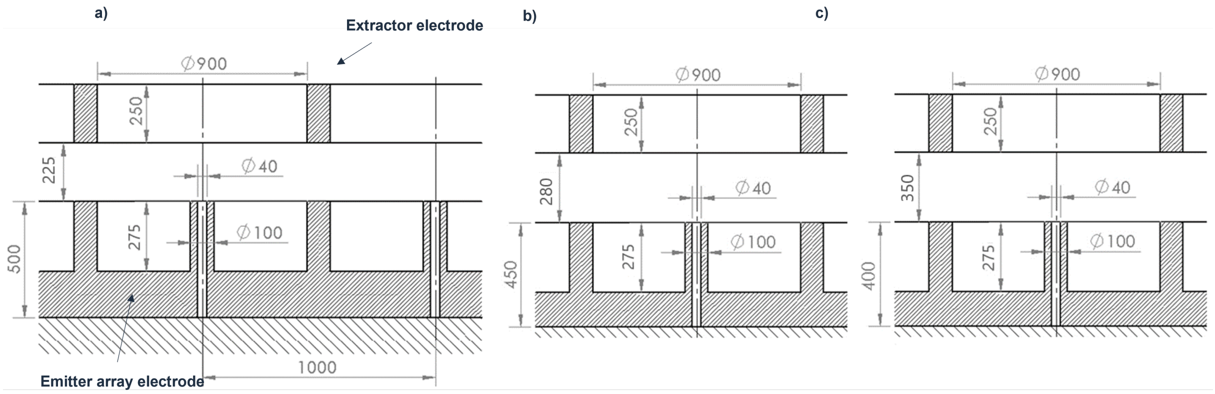

Figure 3.20: Layout of the emitter array section aligned and bonded with the extractor electrode, displaying different wafer thicknesses used to fabricate the emitter array electrode and with a fixed depth of the extractor to 750 μm. All distances are in μ, and the distance between emitters is always 1mm. a) Gap between emitter array electrode fabricated with a 500 μm wafer with extractor electrode. b) Gap between emitter array electrode fabricated with a 450 μm wafer with extractor electrode. b) Gap between emitter array electrode fabricated with a 400 μm wafer with extractor electrode.

Figure 3.21 shows photographs of the top side and backside of all the components integrated and bonded into a compact electrospray thruster head for a 64 emitter array and a 256 emitter array. Figure 3.23 shows a SEM picture of the gap between emitters and extractor together with optical images focusing the emitters and the extractor detailing a precise alignment into the micrometer range. The gap between the emitter array electrode and the extractor array electrode is defined, as aforementioned, by the etching depth of the extractor and the thickness of the wafer used to microfabricate the emitter array electrode as shown in Figure 3.20.

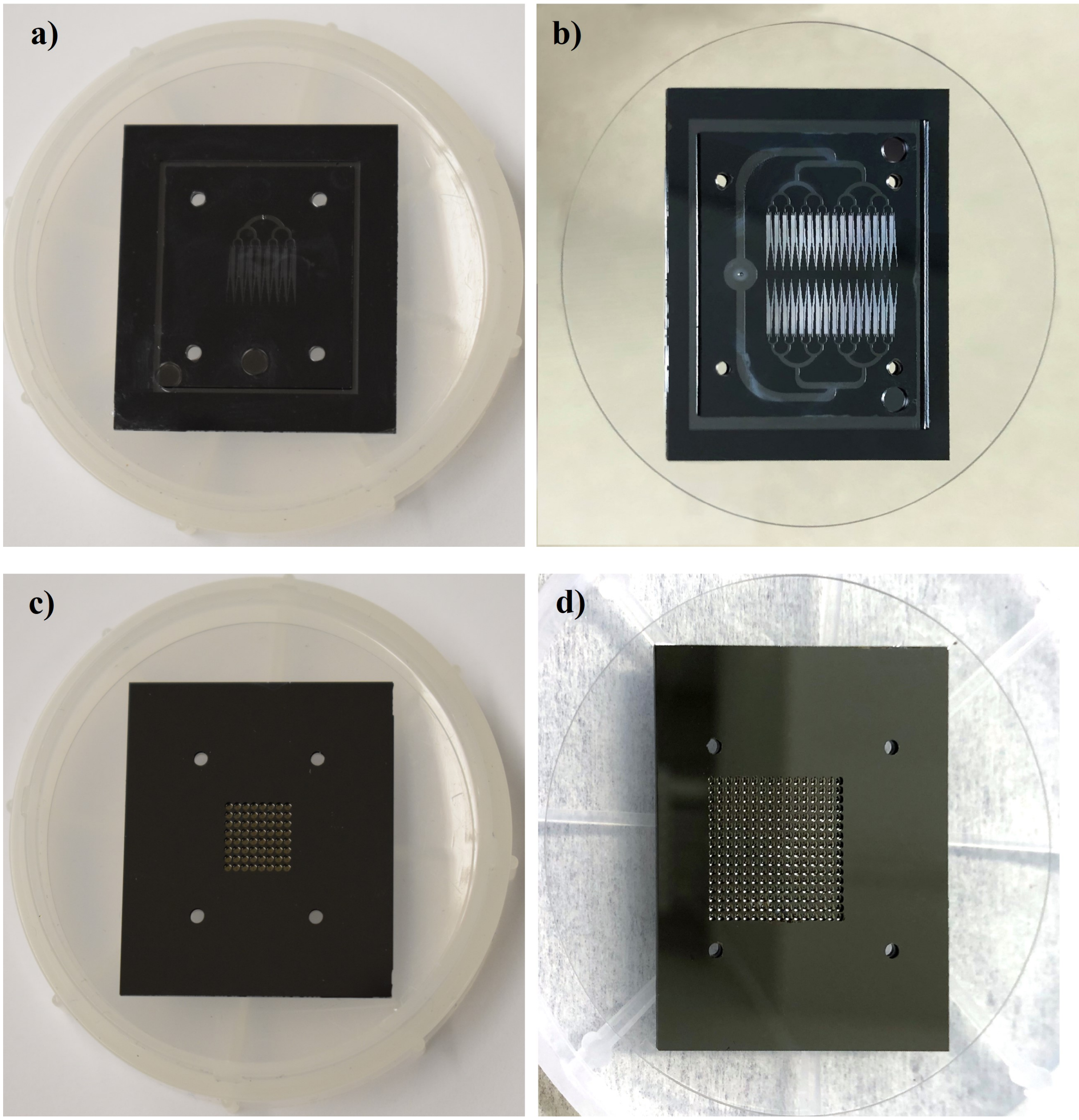

Figure 3.21: Completed 64 and 256 emitter electrospray thruster head. a-b) Microfluic channels side view. c-d) emitter array and extractor view.

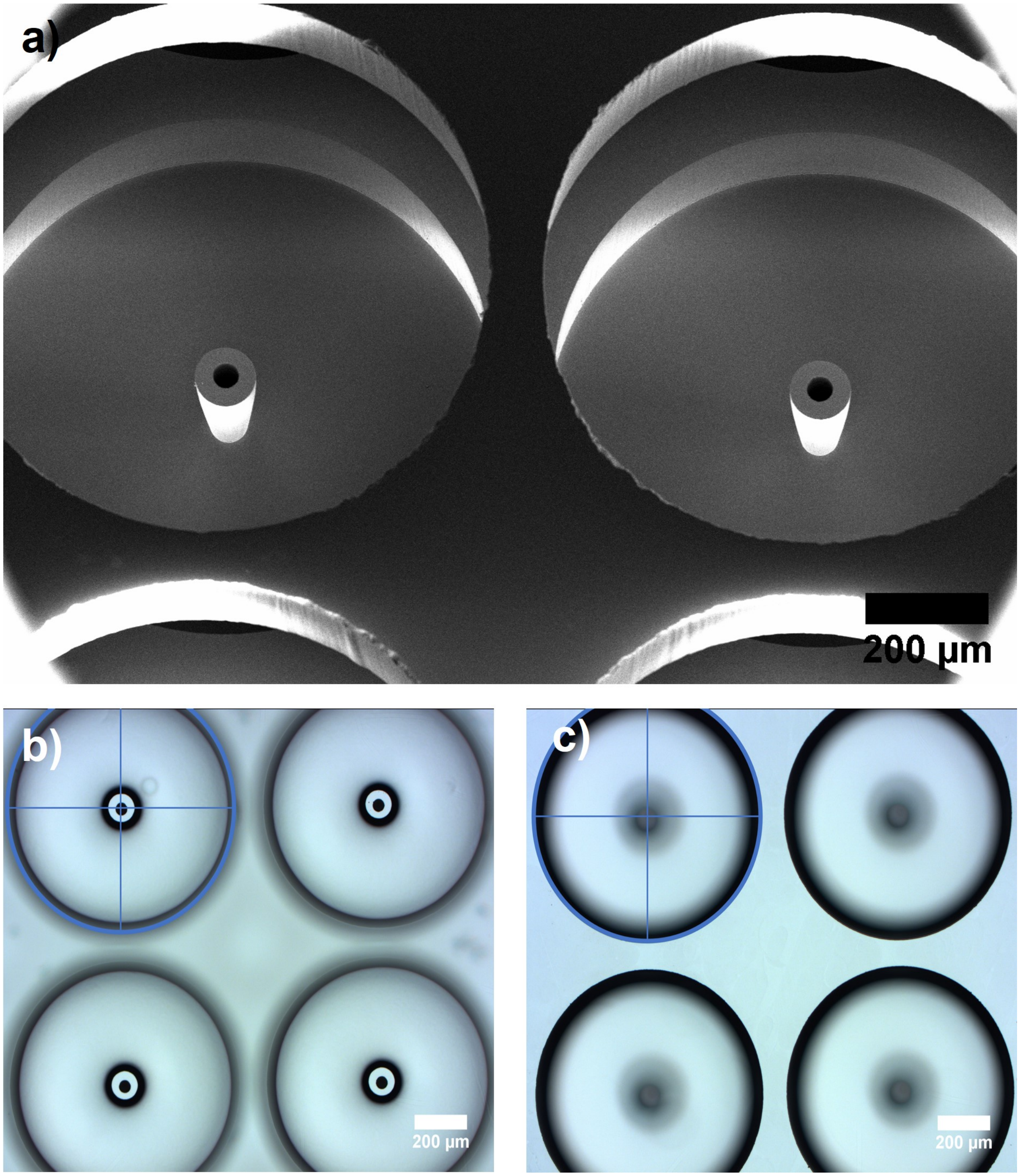

Figure 3.22: a) SEM image showing of the extractor electrode and the emitter array. b-c) Optical images focusing the emitter array and the extractor electrode aligned and bonded.

Following the same microfabrication approach as the one shown for the 64 and 256 emitter array, a single emitter source is also microfabricated to demonstrate the scalability of the process.

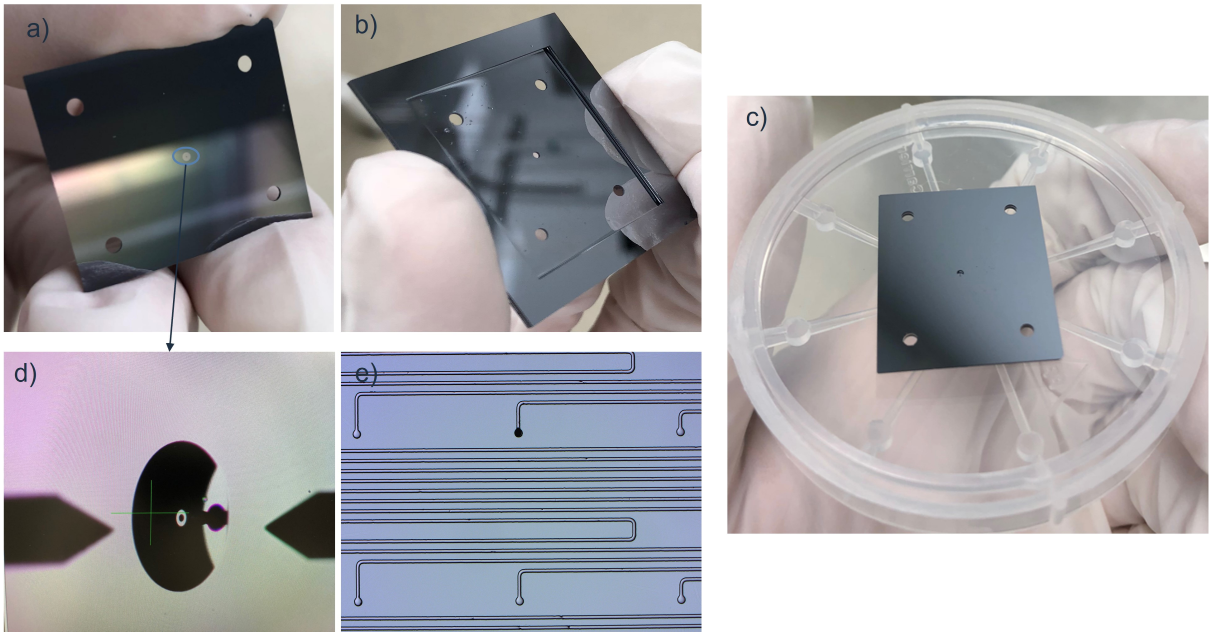

Figure 3.23: Assembly process of a single emitter source. a) Single emitter electrode b) Extractor electrode c) Emitter electrode and extractor electrode aligned and bonded to the glass wafer. d) Profile view of the etched emitter. e) Etch through of the single emitter in one single microchannel

3.3 Testing, results and discussion

The three different emitter arrays are tested to characterize the scalability of the thruster head and the microfabrication process, as well as the sensitivity to basic geometric parameters such as the distance between the emitters and the extractor and the depth of the microfluidic channels. In particular a single-emitter, two 64-emitter array, and a 256-emitter array are tested. After bonding the fused silica line for the propellant feeding, the thrusters are mounted on a Delrin machined fixture as shown in Figure 3.24 and assembled on a vacuum flange for testing.

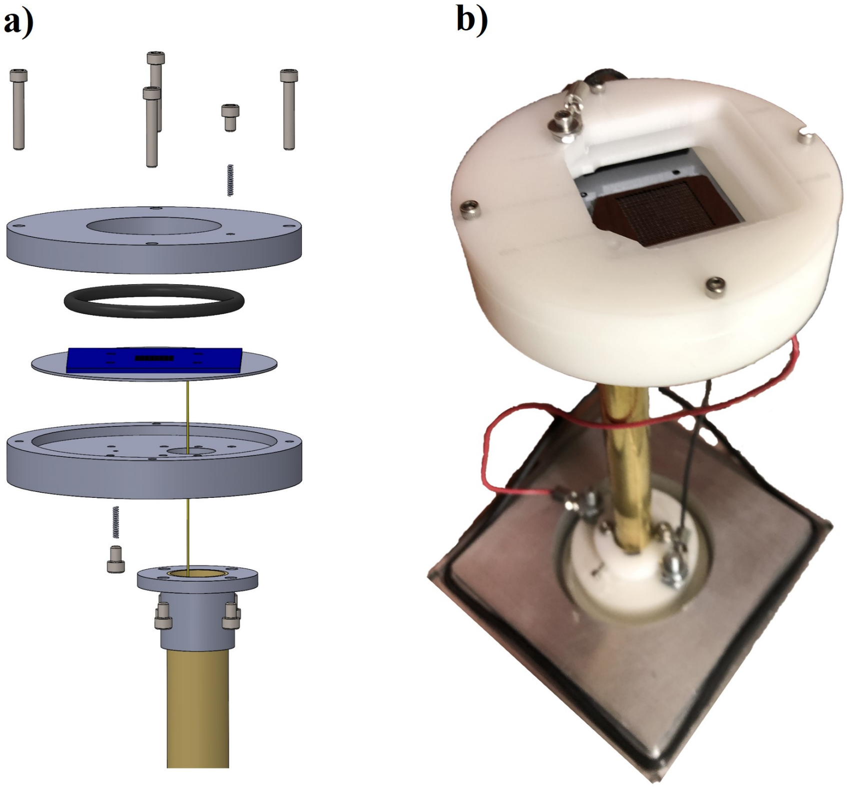

Figure 3.24: a) Schematic exploded view of the assembly b) 256 emitter array assembled with the vacuum flange.

The electric contacts to the emitter and extractor electrodes are made with cobalt-nickel alloy corrosion-resistant springs compressed by screws attached to copper wires. The fused silica line feeding the propellant to the thruster head is passed through the flange using an Upchurch fingertight fitting. The flange of the thruster head assembly is mounted on a stainless-steel vacuum chamber served by a turbo molecular pump backed by a mechanical pump. During testing, the background pressure, measured with a Kurt J Lesker 423 cold cathode gauge, is maintained below 5 x 10-6 torr. Figure 3.25 shows a schematic of the testing and a photograph of the vacuum chamber used and the thruster assembly inside the chamber.

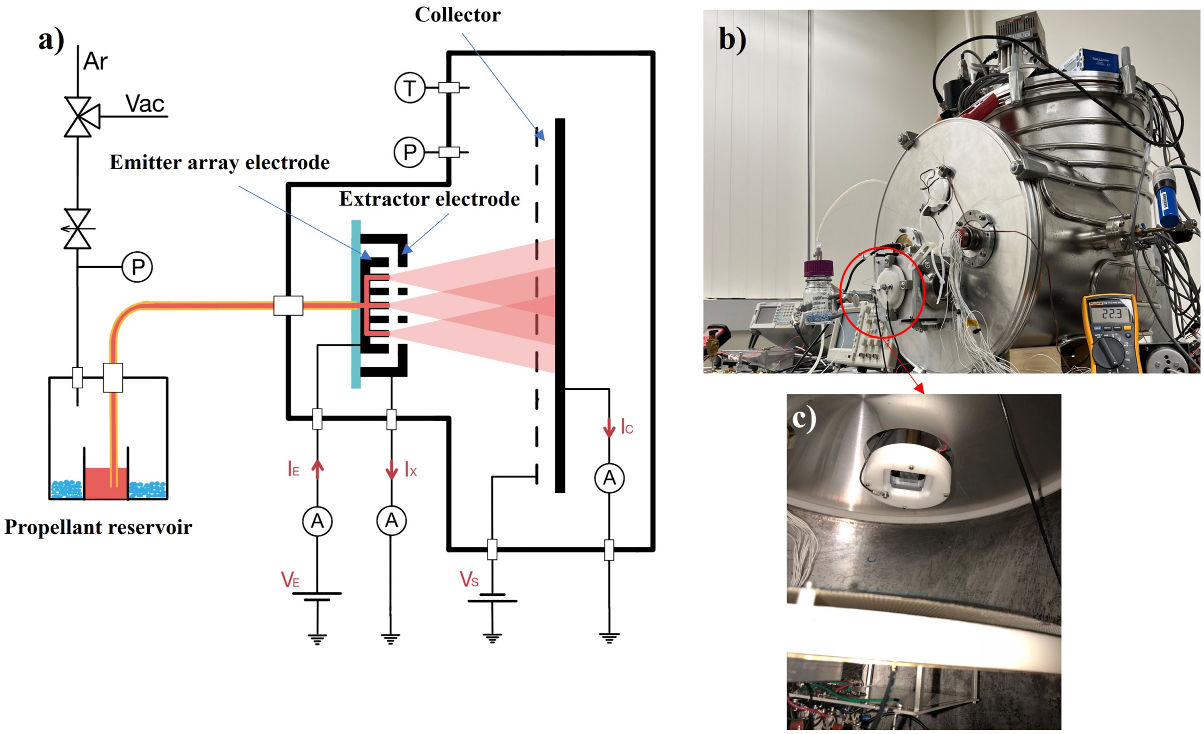

Figure 3.25: a) Schematic of the testing b) vacuum chamber and assembly used. c) 256 emitter head trhuster inside the vacuum chamber facing the collector.

The free end of the fused silica tube is inserted into a pressure-tight tank and submerged in a vial filled with propellant. For all the tests of microfabricated electrospray head thrusters, the propellant EMI-Im studied in chapter 2 is used. EMI-Im is hydrophilic, and to eliminate potential water absorption, the propellant reservoir is kept under vacuum for 24 hours before the start of testing, after which the reservoir is pressurized as needed using argon. As a precaution, the vial sits over a bed of drierite desiccant for absorbing water vapor molecules that may have entered the system. Pressurized argon, a mechanical pump, a pressure gauge, and a manifold of valves are used to accurately control the pressure P in the propellant tank and feed the desired flow rate of EMI-Im to the thruster head. The flow rate of propellant is given by

$$Q = \frac{P}{\mu R_H} \tag{3.2}$$

Where R_H is the hydraulic resistance, the total hydraulic resistance of each thruster head R_H is calculated as the sum of the hydraulic resistance of the microchannels, the hydraulic resistance of the fused silica line, and the hydraulic resistance of the emitters. The hydraulic resistance of the microchannels is calculated with:

$$R = \frac{12\mu L}{hw^3}\left[1 - \frac{192w}{h\pi^5}\sum (2k+1)^{-5}\tanh\left(\frac{(2k+1\pi h)}{2w}\right)\right]^{-1} \tag{3.3}$$

and the hydraulic resistance of the fused silica line and emitter is given by:

$$R = \frac{8\mu l}{\pi r^4} \tag{3.4}$$

Where μ is the EMI-Im viscosity, L, w and h are the length, width and the depth of the microchannels, l and r account for the length and radius of the fused silica line and the emitters. The viscosity of EMI-Im exhibits a strong dependence on temperature; the experimental fitting $\mu = 0.00021392e^{692.46./(T-160.11)}$ is used to evaluate the viscosity of EMI-Im. The temperature of the flange holding the thruster head is monitored with a thermocouple and logged during the experiments.

The three different emitter arrays are tested to characterize the scalability of the thruster head and the microfabrication process, as well as the sensitivity to basic geometric parameters such as the distance between the emitters and the extractor and the depth of the microfluidic channels. In particular, a single-emitter, a 64-emitter array, and a 256-emitter array are tested. In all cases, the arrays are square with a pitch of 1 mm between emitters, and the height, inner diameter, and outer diameters of the emitters are 275 μm, 40 μm and 100 μm; Table 3.1 shows the parameters (emitter-extractor gap, microfluidic channel depth, radius of fused silica line, length of fused silica line, hydraulic resistance) between the three thruster heads tested, including the dimensions of the fused silica line needed to compute the hydraulic resistance of the system.

Table 3.1: Design parameters of the assembled microfabricated electrospray head thrusters

	Single emitter thruster head	**64 emitter thruster head**	**256 emitter thruster head**
Emitter-Extractor Gap (μm)	280	225	350
Channels depth (μm)	28	28	20
Dry mass (g)	4.224	4.144	5.08
Fused silica line length (cm)	72	48.5	83
Fused silica line radius (μm)	25	75	125
Total Hydrualic resistance (Pa $\cdot$ s)/m3	$2.065 \cdot 10^{17}$	$2.064 \cdot 10^{15}$	$1.4276 \cdot 10^{15}$

Note that the hydraulic impedance shown in Table 3.1 is calculated considering the viscosity of EMI-Im at 21ºC.

The emitter and extractor electrodes are connected to the output and return of a high voltage power supply, with the return terminal also connected to the ground of the facility. The potential of the emitter is designated by V_E. The currents out of the emitter and into the extractor electrodes are measured with shunt resistors. The shunt resistor for the extractor current is placed between the extractor and ground, and the small voltage difference referenced to ground is measured with an op-amp in the standard non-inverting amplifier configuration. The shunt resistor for the emitter current is placed in series with the high voltage output, and the voltage difference is transferred and referred to the facility ground using an ISO121 isolation amplifier. The beam of charged droplets and ions resulting from electrospraying the propellant is collected by a large brass plate connected to the ground through a third shunt resistor for measuring the current with a fast-response electrometer. This collector, electrostatically shielded by a screen biased at -10 V to suppress secondary electron emission, is used to measure the time-of-flight spectra of the particles in the beam. The emitter and extractor currents, the pressure, and the temperature signals are logged in a computer using a LabView application and a NI data acquisition card.

As the pressure driving the propellant is increased from 0 torrs with the voltage applied between the extractor electrode and emitter array electrode, the emitter array starts to produce current at increasing pressure depending on its total hydraulic resistance. Right at the first initial flow at starting feeding pressures, the emitter current is intermittent, indicating that a number of emitters are turning on, but the flow is insufficient to operate above the minimum flow rate as the pressure is further increased up the emitter current increases in a stepwise manner, suggesting that rows of emitters are successively turning on. Finally, the emitter current stabilizes, and further increase of the pressure causes a monotonic increase of the current in the form $I \propto Q^{0.5}$, a well-established scaling law for electrosprays operating in the cone-jet mode. Figure 3.26 shows pressure-current ramps for the different electrospray thrusters heads assembled, validating its good performance and quick response to the applied pressure in the propellant reservoir.

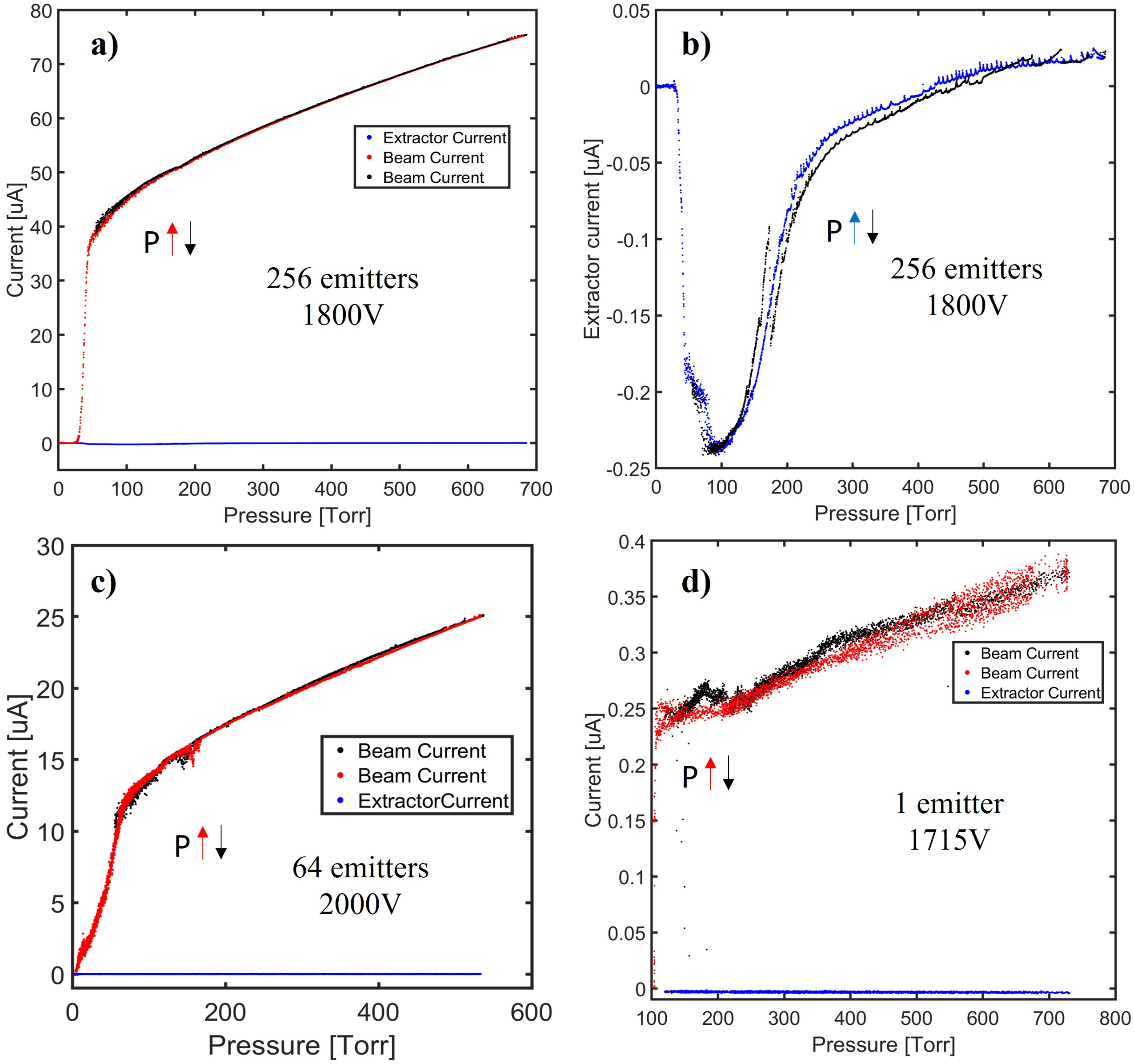

Figure 3.26: P-I curves for the electrospray thrusters heads tested. a) P-I curve for the 256 emitter array electrode operated at 1800V. b) extractor current amplified from a) c) P-I curve for the 64 emitter array operated at 2000V d) P-I curve for the single emitter electrode operated at 1715 V.

The extractor current measured during the P-I ramps demonstrates perfect isolation between the emitter array electrode and the extractor electrode together with an almost null interception of the beam generated. At all the applied pressures, with the largest emitter-extractor gap (350 μm for the 256 emitter source), the extractor current is below 0.5% of the total beam current. Figure 3.26b. highlights the evolution of the extractor current of the P-I curve of the 256 emitter electrode. Note that the current measured is negative, associated with the secondary emissions generated in the collector grid by the impact of high energy ions and small droplets generated by the electrospray cone jets. The emission of secondary species (SSE) in colloid thrusters operated in vacuum facilities during ground testing are well-reported [125]. The negative current decreases as the pressure (hence flow rate) increases. The hypothesis is that as the flow rate increases, the beam angle does so, as recently reported [43]. Some positive droplets or ions start to be intercepted by the extractor (accounting for less than 0.5% of the beam), compensating for the negative current coming from SSE. But it could also be that at the minimum flow rates (the maximum negative current match the minimum flow rate), the ion emission is larger, hence more SSE when hitting the collector grid, and as we increase the flow rate, the beam density increases, shielding the SSE to reach the extractor.

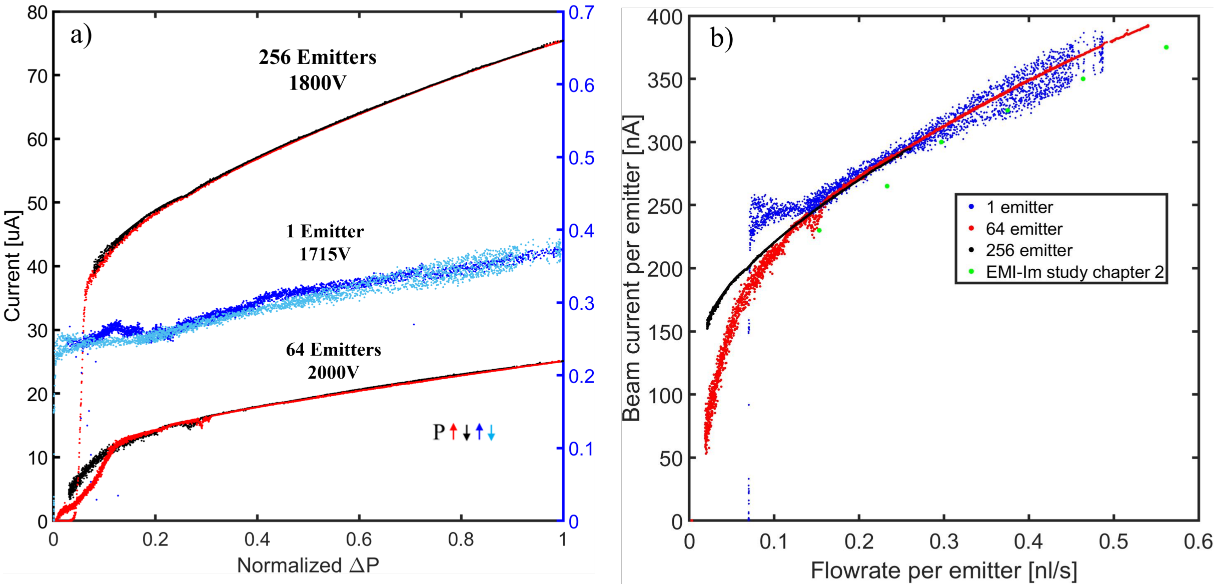

Figure 3.27: a) Emitter current as a function of the normalized ΔP driving the propellant for the tested thrusters b) Total flow rate and beam current per emitter. Flow rate is obtained using pressure ramps shown at Figure 3.26

Figure 3.27a. shows the three P-I curves for the tested thrusters for the normalized ΔP driving the propellant together with the flow rate-beam current per emitter. Figure 3.27b.

shows the flow rate per emitter, obtained by computing the total flow rate divided by the number of emitters of each thruster. The total flow rate is computed using Eq 3.2 taking into account that R_H is also calculated at each data point, accounting for the temperature variation. The perfect match of the flow-rate per emitter-current of the three thrusters heads (including the single emitter) validates perfect synchrony in the beam emission of each emitter part of the emitters array behaving as expected in a cone-jet for the ionic liquid EMI-Im. The curves are validated with the data obtained in chapter 2 for an electrospray cone-jet of EMI-Im (flow-rate vs. current), accounting that the voltage and temperature on those experiments differ from those in the thruster testing.

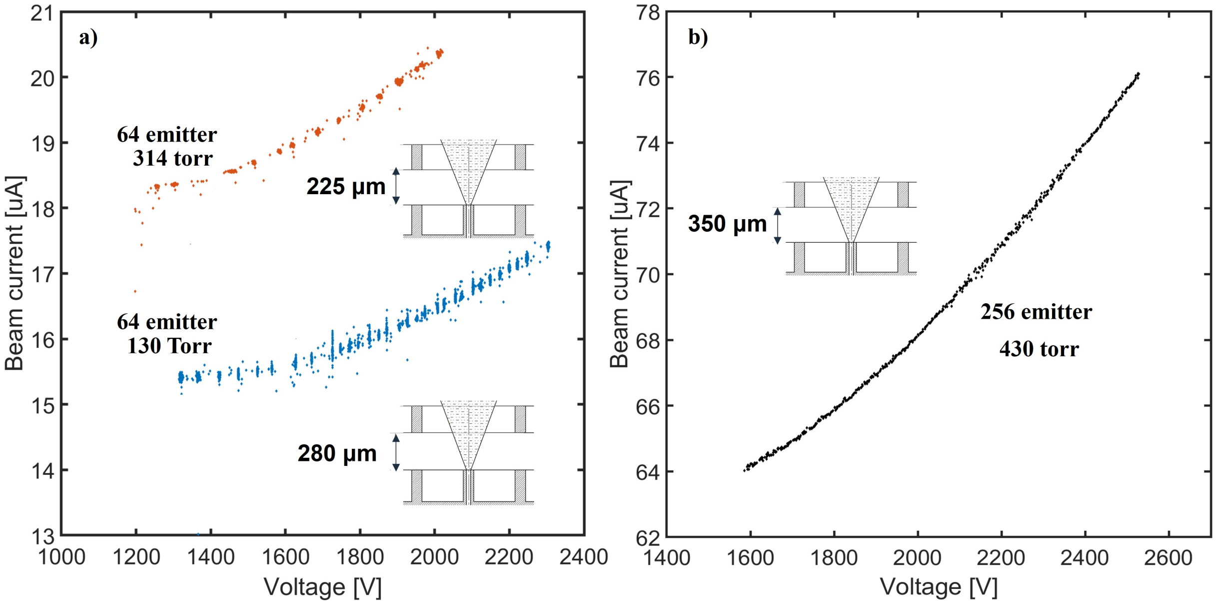

Figure 3.28: a) Voltage-Beam current ramp for two 64 emitter sources operating at 314 Torr and 130 Torr propellant pressure fixed with a 225 μm gap and 280 μm gap between emitters and extractor electrode. b) Voltage-Beam current ramp for a 256 emitter source operating at 430 Torr propellant pressure fixed and with a 225 μm gap and 280 μm gap between emitters and extractor electrode.

Figure 3.28 shows the increase of the beam current with the voltage operation at a fixed propellant reservoir pressure. For the safety of the sources, the test increases 1000V from the minimum voltage to trigger electrospray on the emitter arrays, which is found experimentally by ramping down the voltage until the current emission drops significantly. However, the excellent voltage isolation could allow up to 4000V of operating voltages. For this test, another 64 emitter source is used with a higher gap than the ones reported in table 3.1 It is observed how the different gaps between the emitter and extractor electrode affect the minimum voltage to activate the electrospray. As expected, the minimum voltage required to operate the source diminishes as the gap lowers. The voltage ramps are done increasing 1000V from the minimum voltage. With that voltage ramp window a 10 to 15 % beam current increase is observed.

3.3.1 Life Time performance test

Electric propulsion systems are designed to operate over extended periods of time, often several years, due to their low thrust values and the total impulse required by typical maneuvers. Demonstrating a long lifetime operation is perhaps the most challenging step in the development of electric propulsion systems. Several life-limiting mechanisms have been identified in ESP, such as the partial interception of the beam by the extractor and accelerating electrodes, the disruption of the nominal flow by bubbles of vapor and gas, and the electrochemical degradation of the emitter electrode. After succeeding and demonstrating the good performance of the microfabricated sources in this thesis, in terms of pressure-current and voltage-current response, it is key for real applications to demonstrate that the sources can operate optimally for several hours. To do so, we operated the 64 emitter source continuously at a fixed propellant pressure of 142 torr monitoring beam current, extractor current, and temperature. We were expecting, as an optimal outcome, that the beam current would remain steady, with minimal variation only caused due to temperature variations. However, as Figure 3.29 shows, as we were adding hours of operation, the beam current started to linearly decrease.

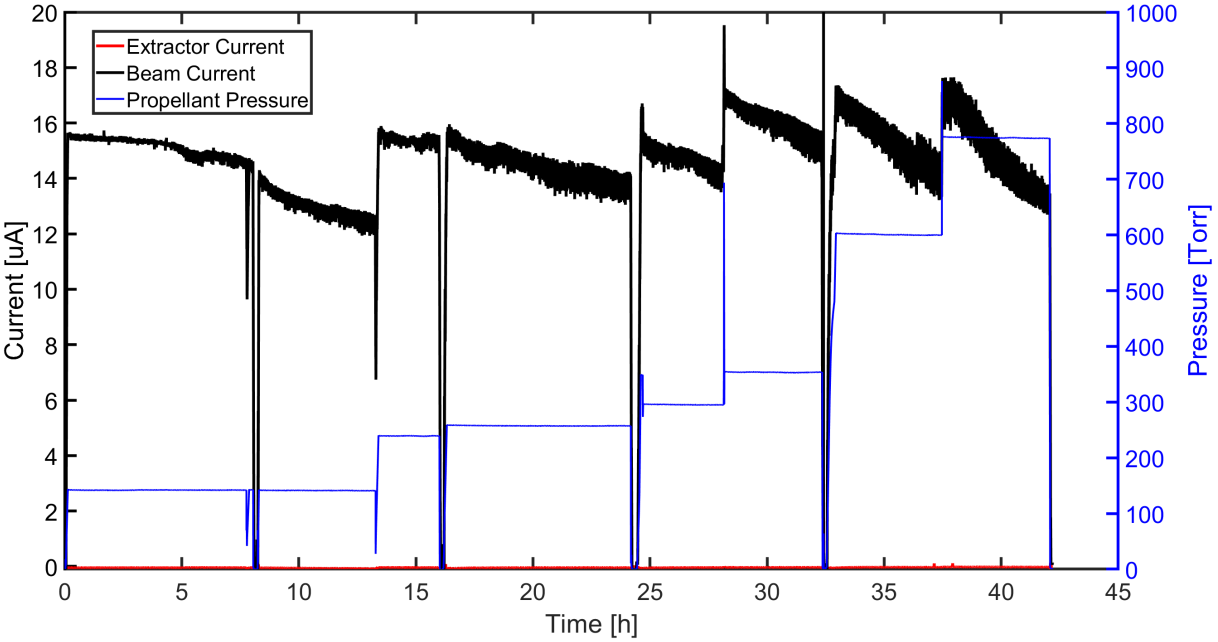

Figure 3.29: 64 emitter source 42 hours test, beam current and pressure of the propellant reservoir is highlighted.

Figure 3.29 shows a 42 hours performance test done in the 64 emitter source. Note that the test was taken in cycles of 8 hours, where at the end the pressure is dropped to 0 to turn off the firing of the thruster head. The vacuum facility used is not automated and could not stay running overnight due to risk protocols. At a fixed 142 torr pressure, the current of the beam decreases an 18% of the initial current, with very little temperature change, after 12 hours of operation. To maintain the initial beam current emission, the propellant pressure is steadily increased over the test days until at a point at which the fall of the current is accelerating, and the propellant pressure can not be increased anymore, and the test was interrupted for diagnostics.

Analyzing the extractor current, shown in Figure 3.30, it is possible to conclude that the decrease in the beam current does not come from a short between the emitter array and the extractor electrode. A connection between both or a broken emitter would cause a complete saturation of the electronics that measure the currents. The only explanation is that either there is clogging on the channels creating an increase of R_H and more intermittent-noisy emission or deposition on the area of the break up of the jets clogging the emitters due to electrochemical reactions, as reported with other ionic liquids.

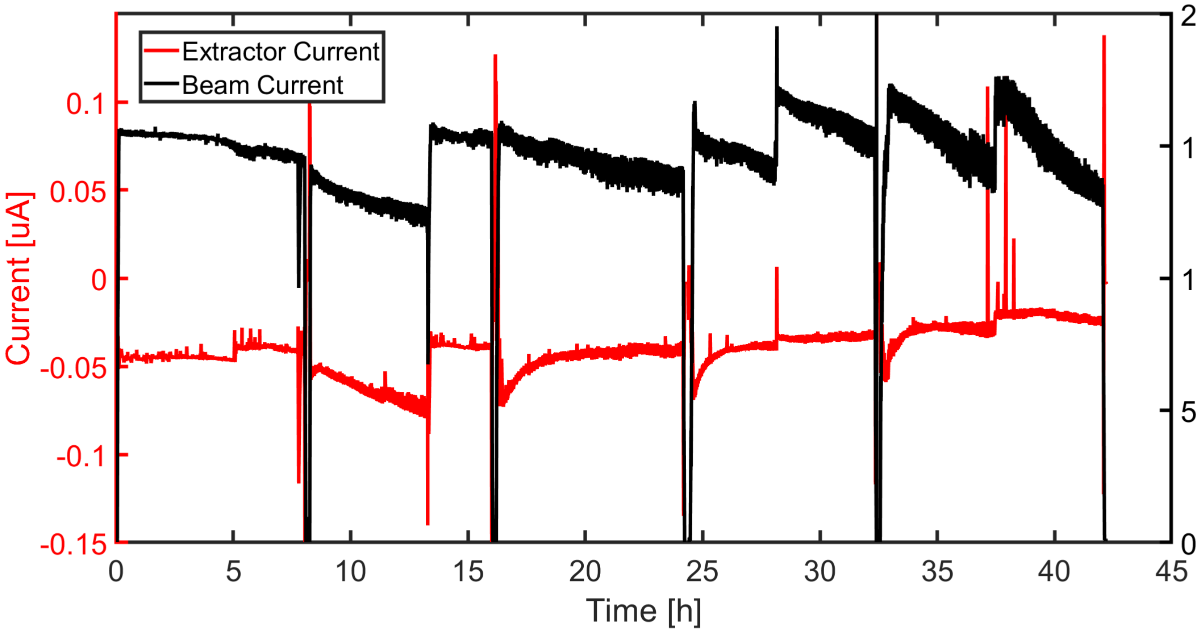

Figure 3.30: Beam current and extractor current from Figure 3.29

SEM inspection of the 64 emitter source after the performance test confirmed that the decrease of current over time is due to electrochemical deposition of the ionic liquid caused by a build up a charge of the counter ion over time, forming a thin film on top of the emitters that end up clogging it. The evolution of the film that ends up clogging the emitters is shown in Figure 3.31.

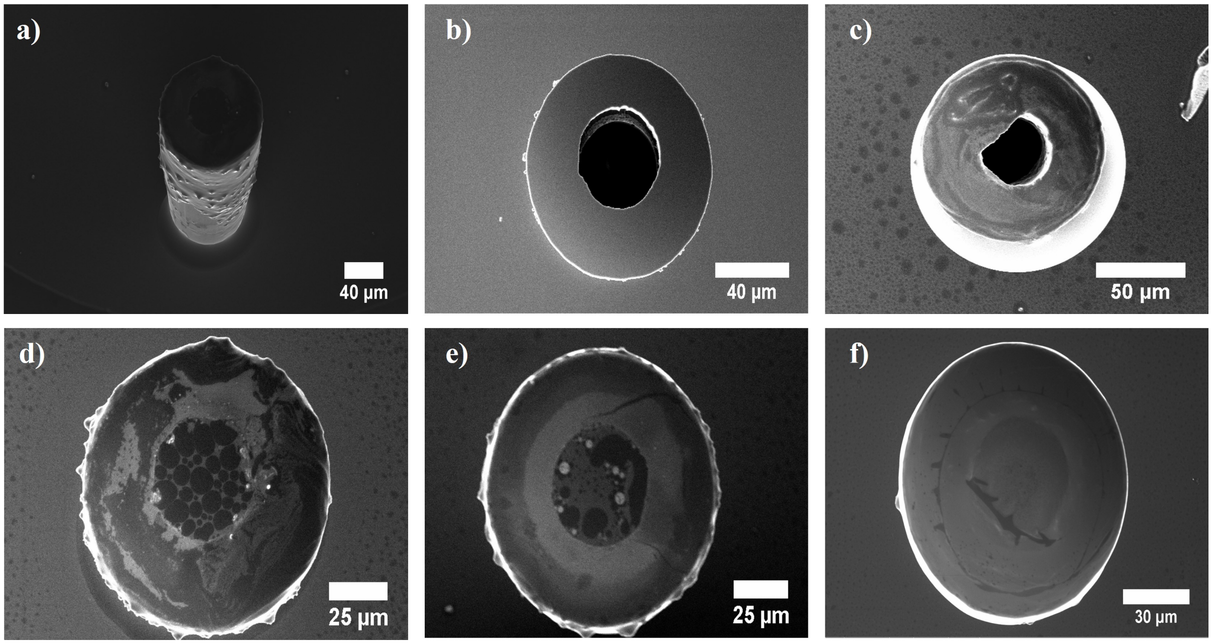

Figure 3.31: a-f)Evolution of the electrochemical film deposition that clogs the emitters

Electrochemical degradation of EMI-Im on the silicon emitter array

Electrochemical reactions in ionic liquids electrosprays are electronic charge transfers between the liquid and the contact electrode, in this case, the emitter array. These reactions occur when a potential difference between the electrode and the ionic liquid bulk is strong enough to overcome its electrochemical window in the liquid-electrode interface. In the case of the emitter array, the current flow through the power supply changes the surface charge of the emitter array, with an equal change of opposite polarity on the ionic liquid side, wetting the emitter wall through ionic conduction. In this interface, the electrical double layer is formed as more current is drawn or supplied to the electrode, the potential difference in the interface increases. The nanometric size of the double layer generates extremely high electric fields even at very small potentials overcoming the electrochemical window of the ionic liquid, generating electron transfer across the double layer as shown in Figure 3.32. Those electrochemical reactions generate precipitates that were reported to adhere to the emitter when electrospraying ionic liquids in the pure ionic regime, such as EMI-BF4 at the minimum flow rate, in some emitter materials such as stainless and tungsten generating a substrate on its surface degradation or clogging them.

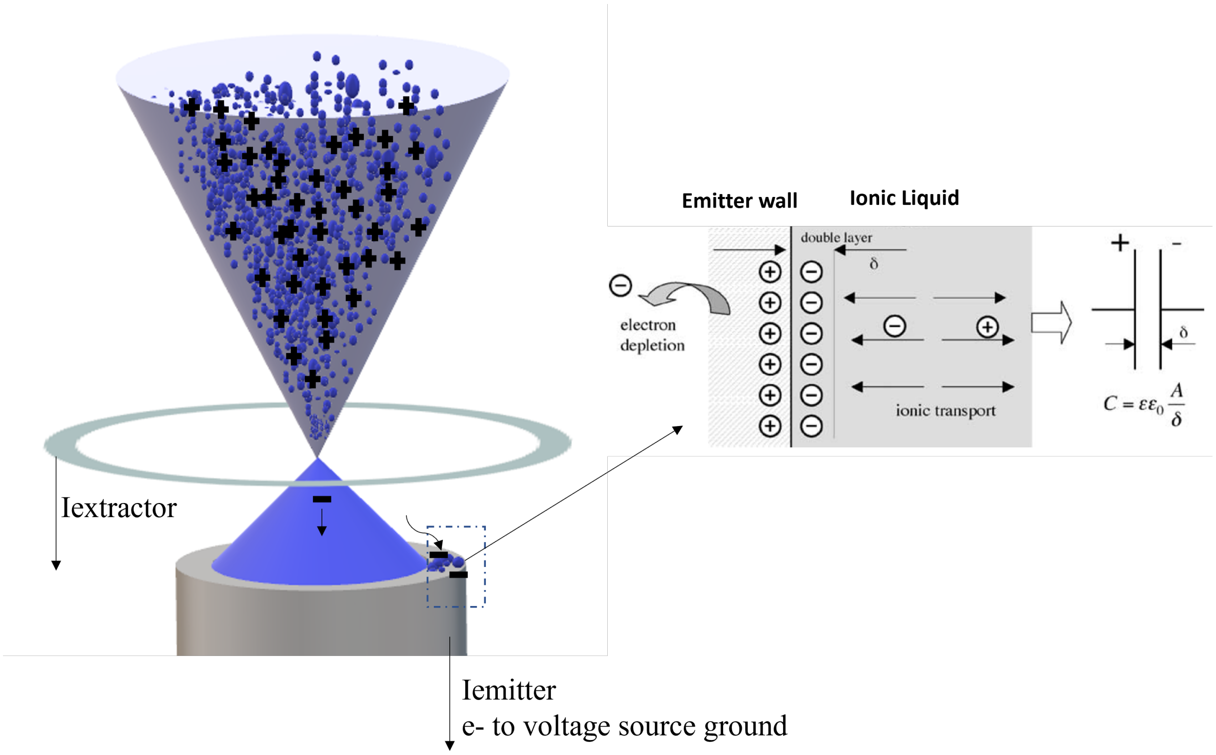

Figure 3.32: Schematics of the electrochemical system during electrospray of an ionic liquid.

The solution that Lozano's group proposed at MIT is to cancel the electrochemical reactions by alternating the voltage polarity of the emitter electrode [96]. The double-layer acts as a parallel plate capacitor:

$$C = \varepsilon\varepsilon_0 \frac{A}{\delta} \tag{3.5}$$

The time it takes to the potential to reach the electrochemical window is dependent on the current supplied to the double layer capacitor:

$$I = CdV/dt \tag{3.6}$$

When the voltage difference generated on the interface is higher than the electrochemical window $V_w^{\mp} = V_w^{+} + V_w^{-}$ the electrochemical reactions inside the double layer start. The time that the potential takes to reach the electrochemical window can be obtained from:

$$t_w^{\mp} = \varepsilon\varepsilon_0 \frac{V_W^{\mp}}{I}\frac{A}{\delta} \tag{3.7}$$

It has been experimentally proven that the time to reach the electrochemical potential window is especially short when operating in a pure ionic regime. In a pure ionic regime, there is a larger and faster build-up of charge due to the counter ion left behind when operating in DC. The fast alternation of polarity using AC used at MIT was proven to be able to discharge the double layer before $t_w^{\mp}$ is reached, increasing the operational time significantly. However, they still see a degradation over time that ends up shorting their extractor electrode and emitter array.

In solvent-based electrosprays and electrosprays in con-jet mode with a significant droplet emission, most of the neutralized counterions and their reaction products are supposed to leave the solution along with emitted liquid droplets in a self-regulated process producing none or almost no degradation. The fact that we did not see any degradation on the single fused silica emitter source used to study EMI-Im in chapter 2 pointed that the effect of the material of the electrode is relevant in these electrochemical film depositions. Note that to make conductive the chamfered fused silica line in chapter 2, we deposited a thin film of Iridium. Experiments with needles of platinum on pure ionic regime still reported degradation of the liquid, but no apparent deposition was left behind[96]. The colloid thruster developed by Busek with JPL for the LISA Pathfinder mission was also made out of platinum capilaries electrosprayin EMI-Im, and no clogging was reported [69].

Cancelling the electrochemical deposition with gold and platinum

The literature and the knowledge acquired during the testing of EMI-Im in chapter 2 suggested that a coating of a novel metal could perhaps suppress the film deposition and the clogging of the emitters. At this point, a microfabrication step on the emitter array electrode was added to analyze if a noble metal interface between the silicon and the IL could cancel the electrochemical deposition. Step 12 is shown in Figure 3.33..

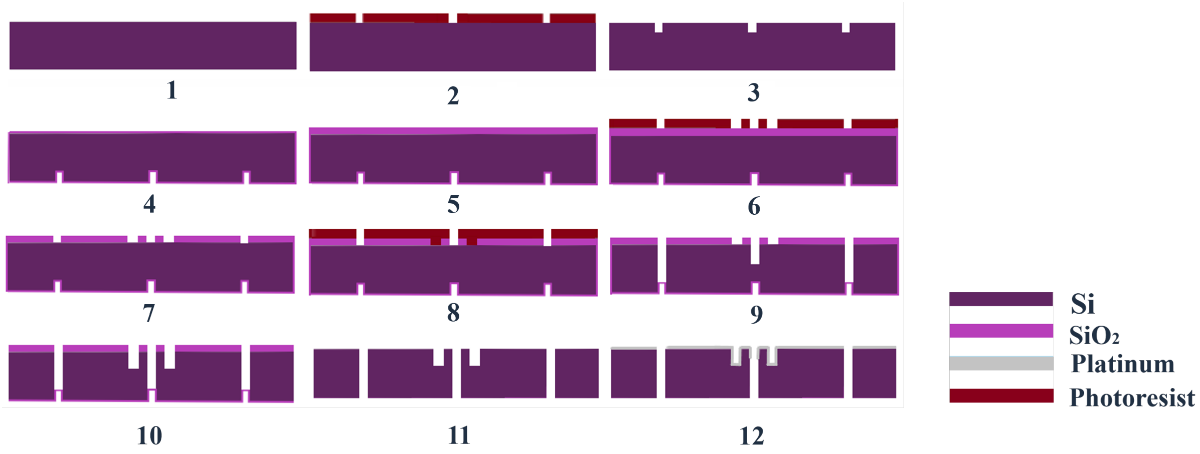

Figure 3.33: schematic of the emitter array electrode microfabrication process to add a nobel metal

For the deposition of the gold and platinum on the emitter array electrode, the back with the channels is protected with a double side polished Si wafer. A glass mask is then used to cover the electrode exposing only the area of deposition interest. A high voltage DC sputtering process is then used to generate plasmas and sputtering deposition of gold and platinum to externally coat the emitter arrays and internally coat a few micrometers of depth the inner hole of the emitter array. During the anodic bonding of the 64 emitter array coated with gold, a migration and oxidation of silicon through the surface of the gold film was observed, damaging the coating and ruling out gold as a reliable interface to coat the emitter arrays. These were reported at high temperatures, but the effect seems to be triggered during anodic bonding [68]. Figure 3.34 shows the results of the coating before and after the bonding process together with SEM-EDX pictures of the degradation of the coating.

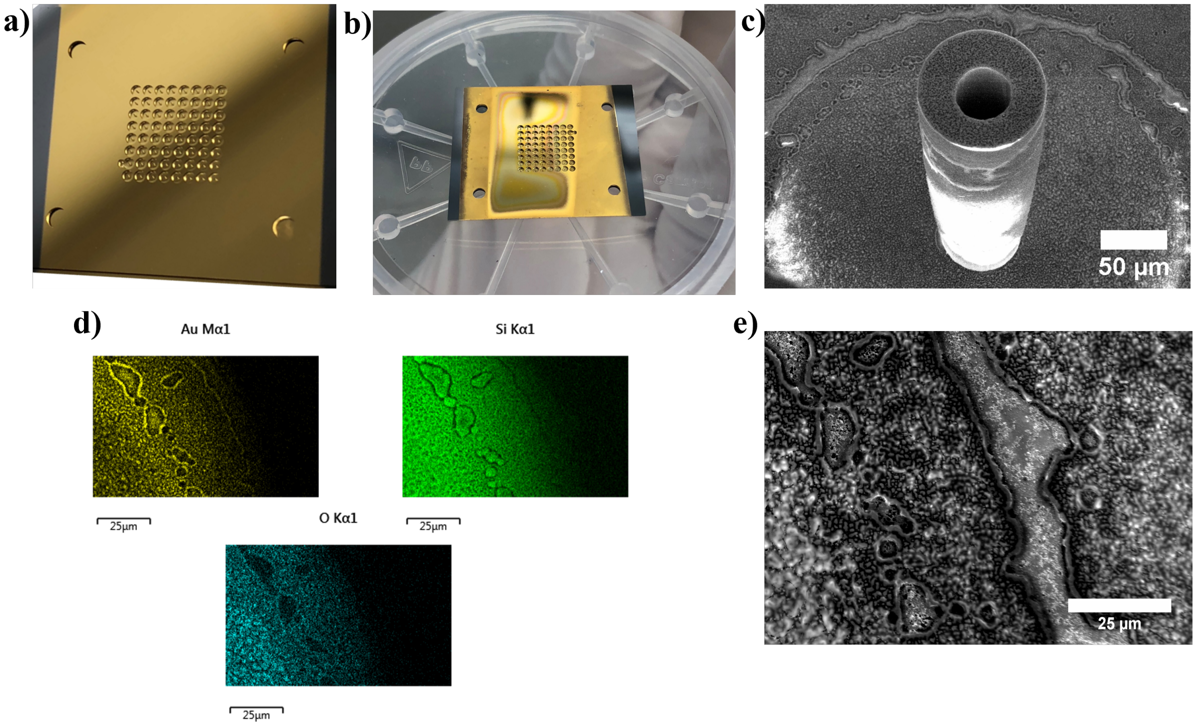

Figure 3.34: a)64 emitter array electrode coated with gold before the anodic bonding. b) 64 emitter array electrode with gold coating clearly damaged after the anodic bonding c) SEM image of one of the emitters after the coating and anodic bonding showin anoxidized material d-e) SEM-EDX results displaying a diffusion and oxidation of the silicon on the gold layer

The platinum sputtering coating showed excellent results. One concern was the adhesion between the platinum and silicon without an intermediate sputtering layer. However, the anodic bonding increases the adhesion of the Pt film substantially by forming a thin layer of Pt-Si due to diffusion of silicon on the first nanometers of platinum [97]. Figure3.35 shows an SEM figure of the PT-Si interface after coating just 40 nm of platinum.

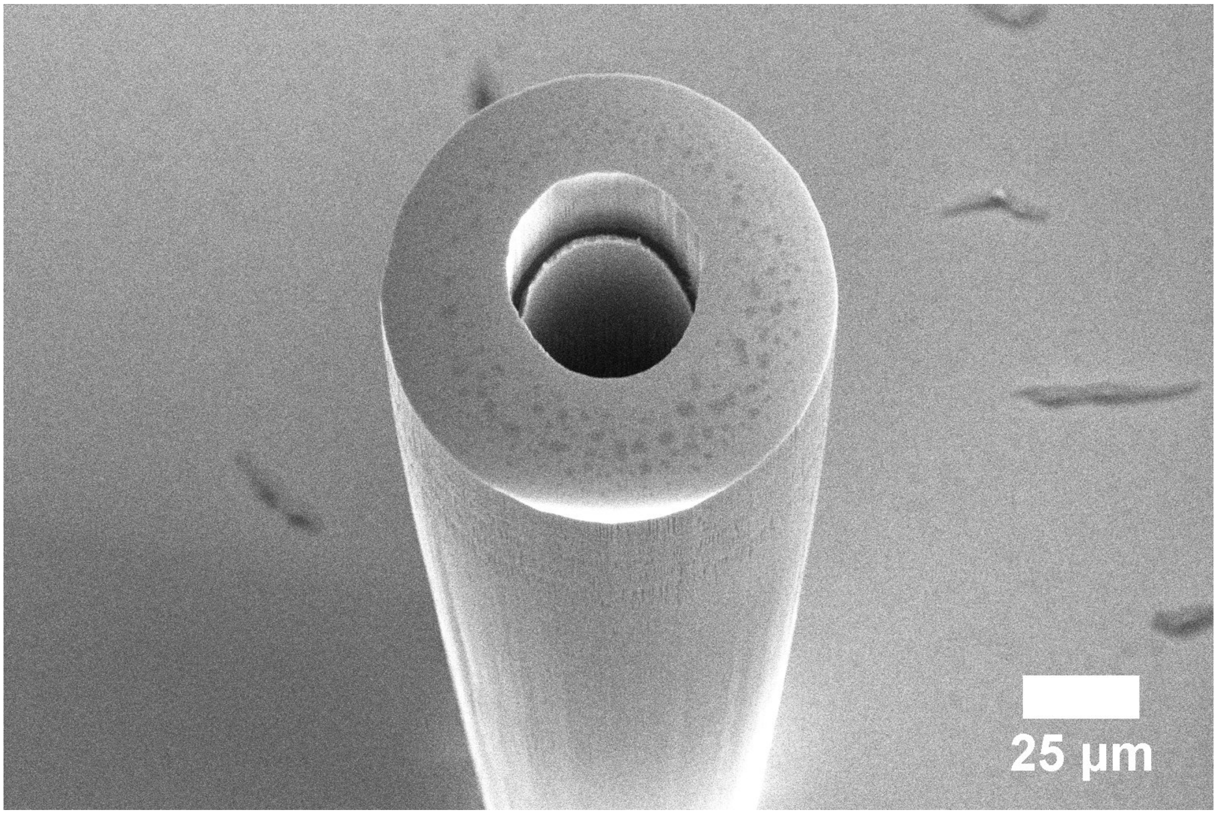

Figure 3.35: si diffusion observed in a 40 nm platinum layer after anodic bonding

When increased to 100 nm. The diffusion can not be observed anymore on the surface as shown in Figure 3.36

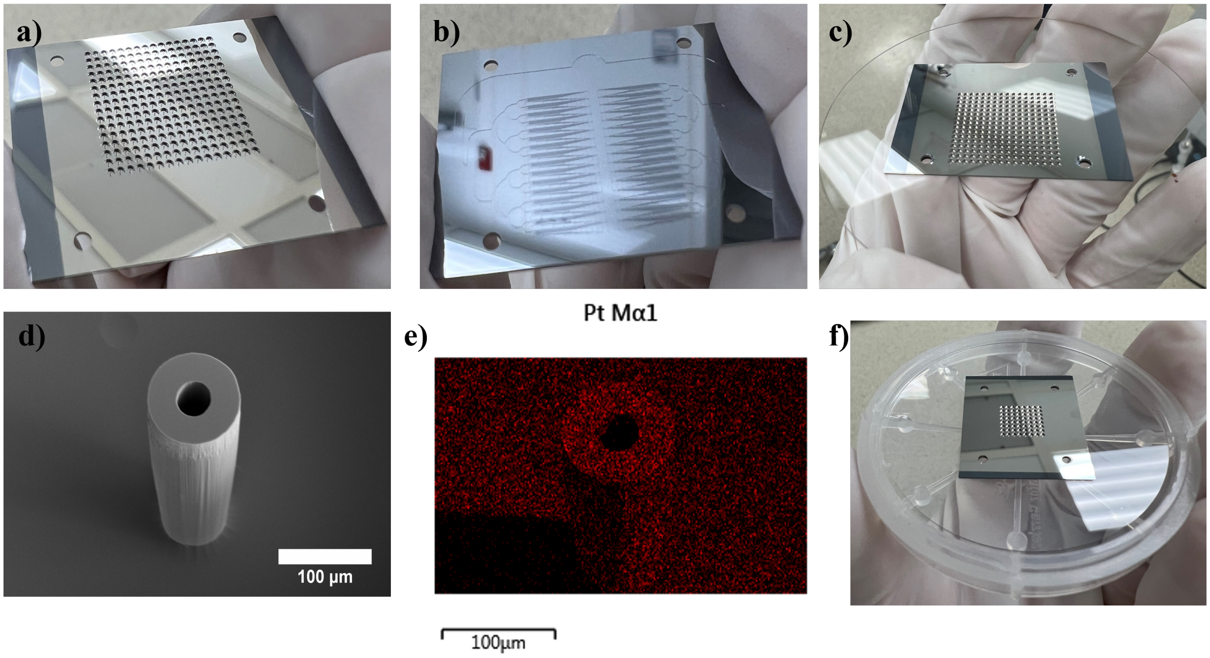

Figure 3.36: a) 256 emitter source with a 100 nm platinum coating. b) back of the coating without source without any deposition or impurities. c) source after the first bonding. d) SEM detail of the 100 nm coating e) EDX scan of the emitter. f) 64 emitter source bonded wih 100 m Pt coating

After the platinum deposition and complete bonding, the 256 emitter electrospray source is assembled, and a performance test is performed. Figure 3.37 shows a 86 hours performance test where the current emission is steady at a fixed pressure. As observed in Figure 3.37a. during the first 8 hours, different Pressure ramps are done to evaluate the response of the thruster showing an excellent response. After that, the pressure is fixed at 430 torrs during 70 hours, with small 1 torr deviations due to the nature of the valve manifold used to regulate the pressure. On the last day of the test, another pressure-current ramp is performed, fitting the values of the first day P-I curve perfectly and proving that the hydraulic resistance is not compromised due to electrochemical depositions and only depends on the temperature. The current emission of the beams is steady overall in the performance test. This demonstrates that the platinum coating inhibits the deposition of the neutralized counter ions and clogging of the emitters when electrospraying EMI-Im. The extractor current is also analyzed in

Figure 3.37b., showing values of negative current below 0.05% of the total current, being negative due to the secondary emission generated.

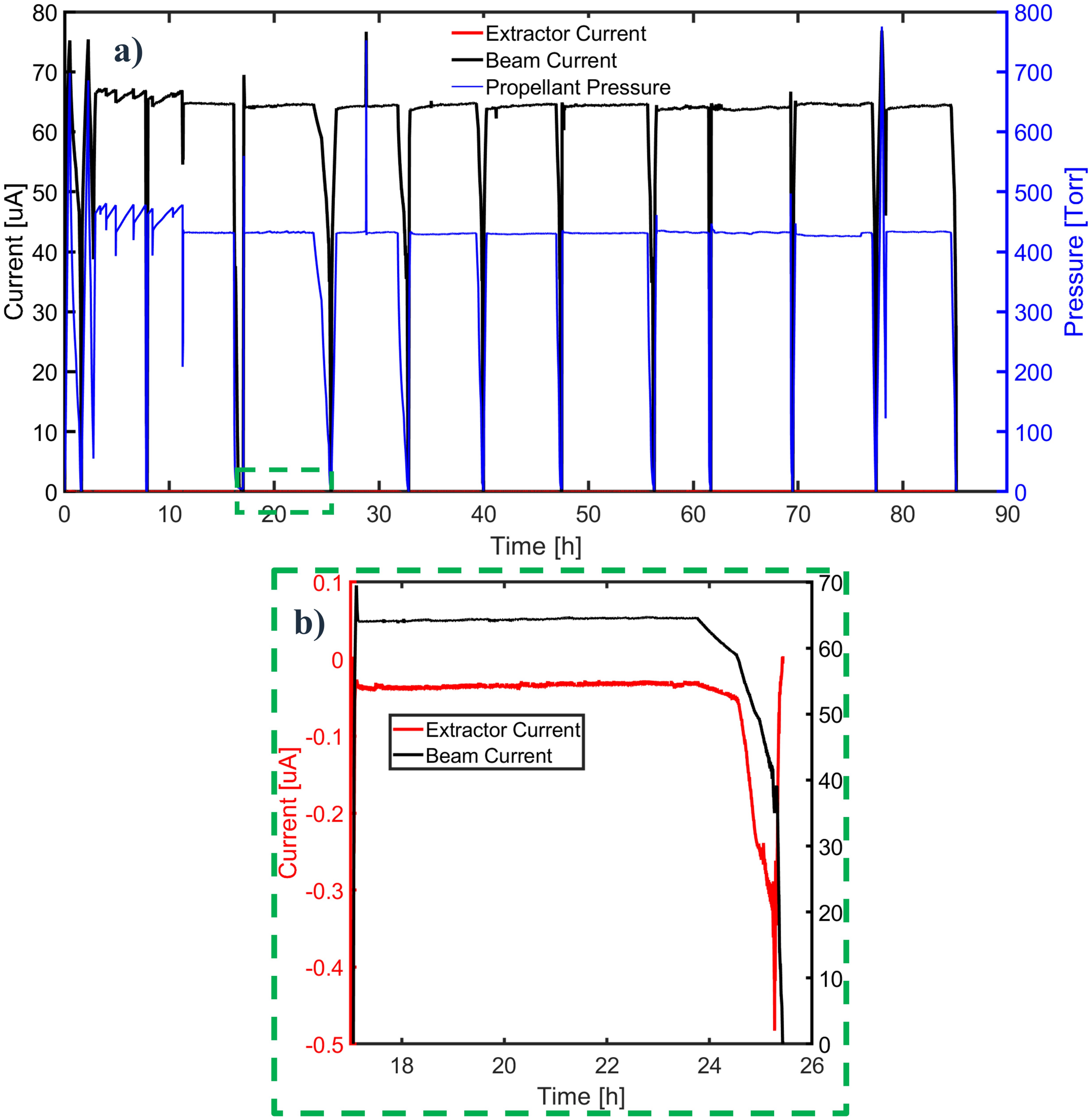

Figure 3.37: 86 hours performance test of a 256 emitters electrospray source. a) Pressure-Beam current over time b) Extractor current and beam current of one day test highlighted in a)

The LabView-DAQ data recording system used in the experiment measures the temperature at each data point. The total hydraulic resistance is then computed at each point taking into account the viscosity dependence on temperature of EMI-Im ($\mu = 0.00021392e^{692.46./(T-160.11)}$). Using Poiseuille law (Eq. 3.2) then is possible to compute the flow rate at each value of pressure during the performance test as shown in Figure 3.38.

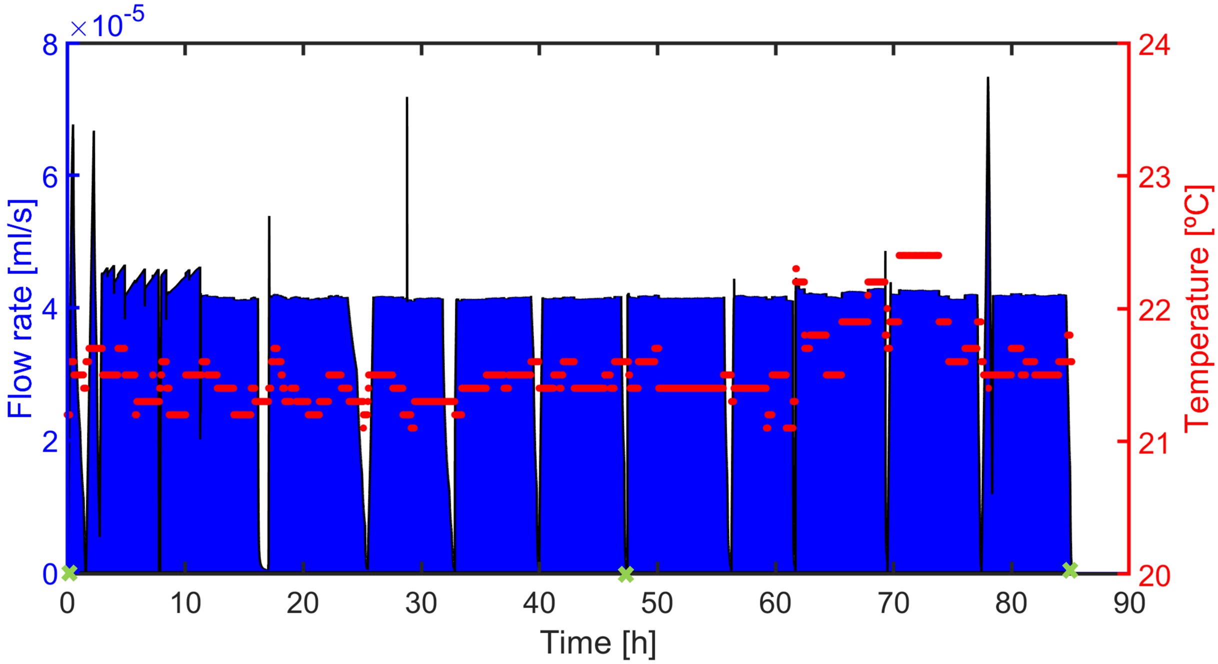

Figure 3.38: Flow rate computed using P from Figure 3.37 and the temperature measurement. Green crosses are measurements of weigh in the propellant reservoir.

By multiplying this flow rate at each point with the density value of EMI-Im, which is also dependent on temperature by $\rho =$ (1544-T$*$1.0008) the mass flow rate can be obtained. By doing the integration of the propellant mass flow rate over time, the total mass of propellant consumption over time is calculated as shown in Figure 3.39. To validate the calculation of the mass flow rate of the 256 emitter source during the performance test, three propellant weight measures were taken with an analytical balance to compare the computed propellant consumption with the real one. One measurement of the propellant weight was done before starting the test, one in the middle of the test and one at the end (shown as green crosses in figure 3.38 and also highlighted in Figure 3.39).

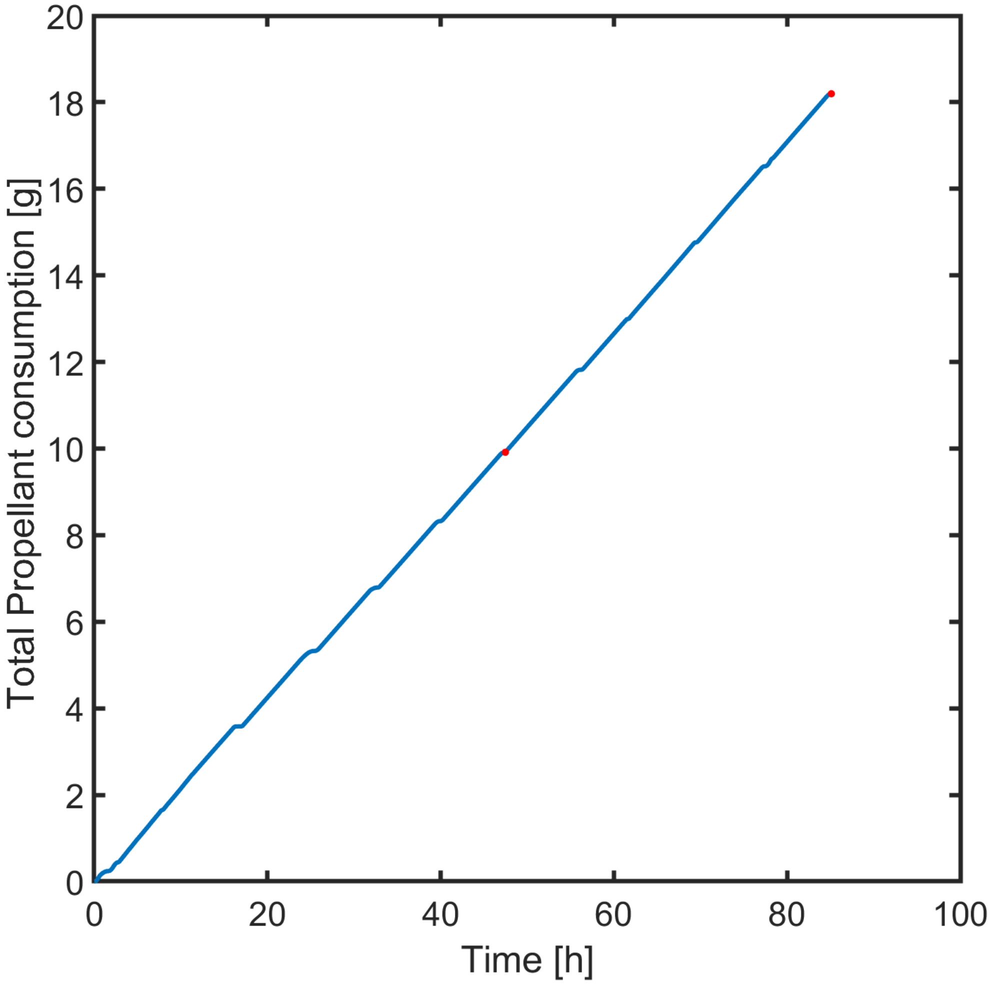

Figure 3.39: Computed propellant mass consumption over time. The highlighted points are used to compare it with real propellant consumption measurements.

$$\frac{9.9139\ g\ computed}{10.3543\ g\ measured}\ x100 = \ 95.76\% \tag{3.8}$$

$$\frac{8.2825\ g\ computed}{8.5638\ g\ measured}\ x100 = \ 96.71\% \tag{3.9}$$

The small error (both cases below the 5% threshold) obtained on the computed mass flow rate over the real measurements of propellant consumption validates the hydraulic resistance calculation of the electrospray thruster head.

At this point, the platinum coating has proven to prevent the deposition of the oxidized counterion on the surface of the emitters, and the calculations of the hydraulic resistance based on the initial design of the microchannels to feed the emitter array are validated. This provides a method that allows to tailor and predict the system's hydraulic resistance on the initial design and microfabrication steps, and customize at optimal flow rates to operate in a cone-jet mode different ionic liquids. The 85 hours lifetime test proves the reliability of the microfabricated sources done in this dissertation, reporting (at the moment this dissertation is written) the longest lifetime optimal operation of a silicon-based, microfabricated emitter array electrospray source actively feed. The lifetime test of the 256 emitter source with platinum was interrupted not because of a failure on the source but to be analyzed and run a 1000 hours uninterrupted performance test by our collaborators at the NASA Jet Propulsion Laboratory. They are also conducting direct measurements of the thrust delivered by the source, perhaps the most important outcome of a propulsion system.

3.3.2 Thrust measurements of the microfabricated electrospray sources

[1] Recalling again the scaling laws of electrospray, introduced in chapter one and chapter two, we know that the current of an electrospray can be approximated as :

$$I_B \cong f(\varepsilon)(\gamma K Q)^{1/2} \tag{3.10}$$

---

[1] Real thrust measurements on this section are performed at NASA Jet Propulsion Laboratory by Dr. Colleen Marrese-Reading and Steven Arestie at their facility. Results and figures of the setup used of the measurements are shared in this thesis with their permission.

Where I_B is the beam current, ε is the propellant's dielectric constant, γ is the propellant surface tension, K is the propellant electrical conductivity, and Q is the propellant flow rate. In our case, I_B is obtained by direct measurement of the current of the emitter's beam generated by the fabricated thrusters at known Q.

The average droplet charge to mass ratio can be obtained also with the scalling laws by:

$$< \frac{q}{m} >= \frac{I_B}{\rho Q} \cong \frac{f(\varepsilon)}{\rho} \left(\frac{\gamma K}{Q} \right)^{1/2} \tag{3.11}$$

where ρ is the propellant density. It is possible then to relate the scaling laws of electrospray to the basic propulsion equations to approximate the I_{sp} and thrust generated by an electrospray thruster. The Thrust was already defined as:

$$T \cong \rho Q u_{ex} \tag{3.12}$$

Which is basically the mass flow rate multiplied by the exhaust velocity. Assuming no energy disipation, the quinetic energy of the droplet is equal to the electric potential when it is from the end of the cone-jet.

$$qV_A = \frac{1}{2} m v^2 \tag{3.13}$$

where V_A is the acceleration voltage, equal at the voltage difference between electrodes (the voltage applied to the emitter array) minus a loss associated with the break up of the cone-jet. This voltage loss is analyzed in detail in chapter 2 with retarding potential analysis. The thrust can be then approximated using the average charge to mass ratio of the droplets, calculated at each current by Eq 3.11, with the acceleration voltage.

$$T \cong \rho Q u_{ex} = \rho Q \sqrt{2 < \frac{q}{m} > V_{acc}} \tag{3.14}$$

and the I_{sp} can also be written as:

$$I_{sp} \cong \frac{1}{g_0} \sqrt{2 < \frac{q}{m} > V_{acc}} \tag{3.15}$$

However, Eq 3.12 overestimate the calculated thrust since the exhaust velocity is assumed to be completely on the x-axis. The repulsion between positively charged droplets on the breakup region of the jet, where the charge density is the highest, lead to the beam opening angle θ as shown in Figure 3.40. The modeling of the angle of the beam is extremely complex and dependent on the geometry of the emitter and extractor array. The most accurate way to do then the thrust measurements in the microfabricated electrospray sources would be to use a thrust stand. At our facility in UCI, we lack the capability for those direct measurements, but the collaborators of this project at NASA JPL have an outstanding facility for direct thrust measurements of electrospray thrusters.

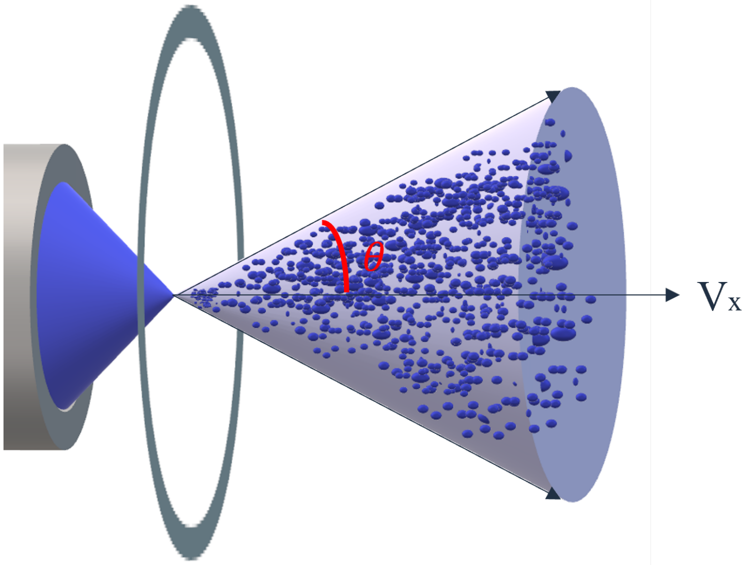

Figure 3.40: Schematics of the beam opening angle

Two microfabricated electrospray sources were delivered at NASA JPL for thrust measurements. A 64 emitter source and the 256 emitter source described in the lifetime performance test. Figure 3.41 shows the set used for the thrust measurements at JPL by Dr. Colleen Marrese-Reading and Steven Arestie.

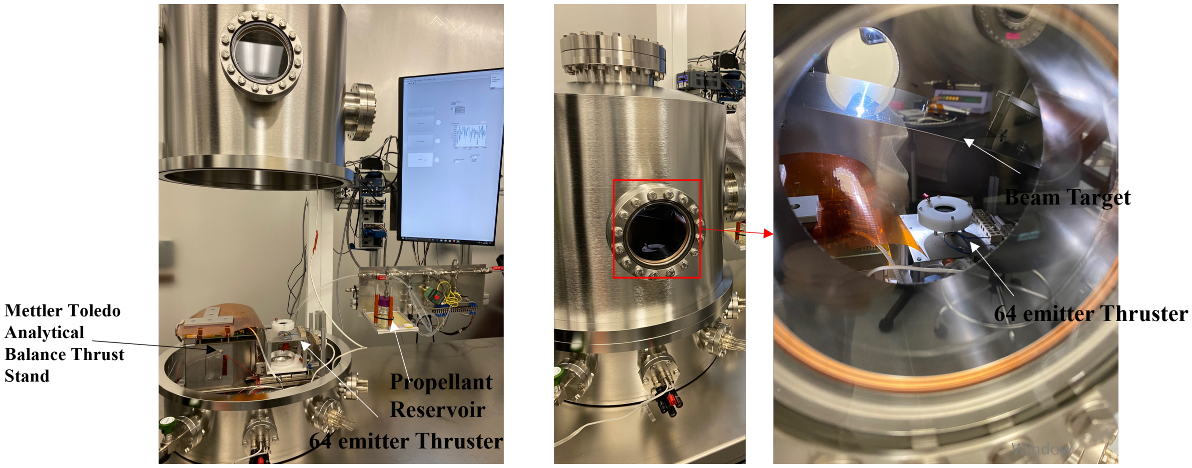

Figure 3.41: Set up used in NASA Jet Propulsion Laboratory to test the electrospray thruster fabricated in this thesis with a 64 emitter source assembled for testing.

The thruster is mounted in a vertical orientation on a vacuum chamber located in a 100 class cleanroom facility, spraying up to a beam target. The propellant flow rate is controlled with applied pressure on the liquid reservoir, as the testing described at UCI, using nitrogen. The thruster is mounted on a Mettler Toledo analytical balance to measure thrust with a 2μN accuracy. Figure 3.42 shows the 256 emitter head thruster assembled.

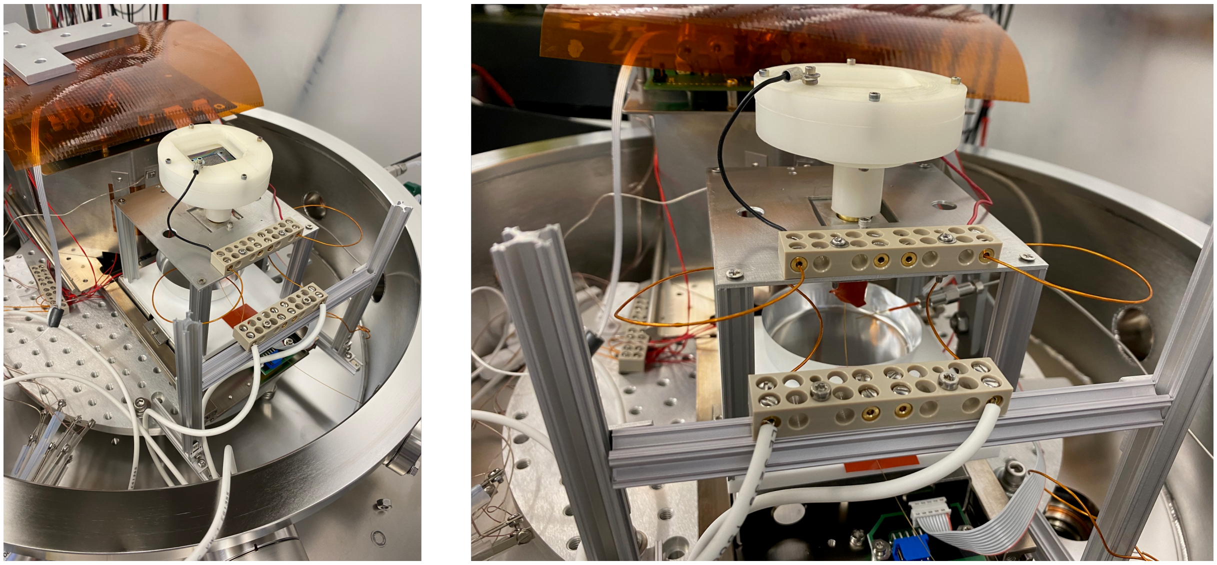

Figure 3.42: Set up used in NASA Jet Propulsion Laboratory to test the electrospray thruster fabricated in this thesis with a 64 emitter source assembled for testing

Figure 3.43 shows the results of the thrust measurements of the 256 emitter source with the pressure on the propellant reservoir, beam current and voltage applied on the emitter array.

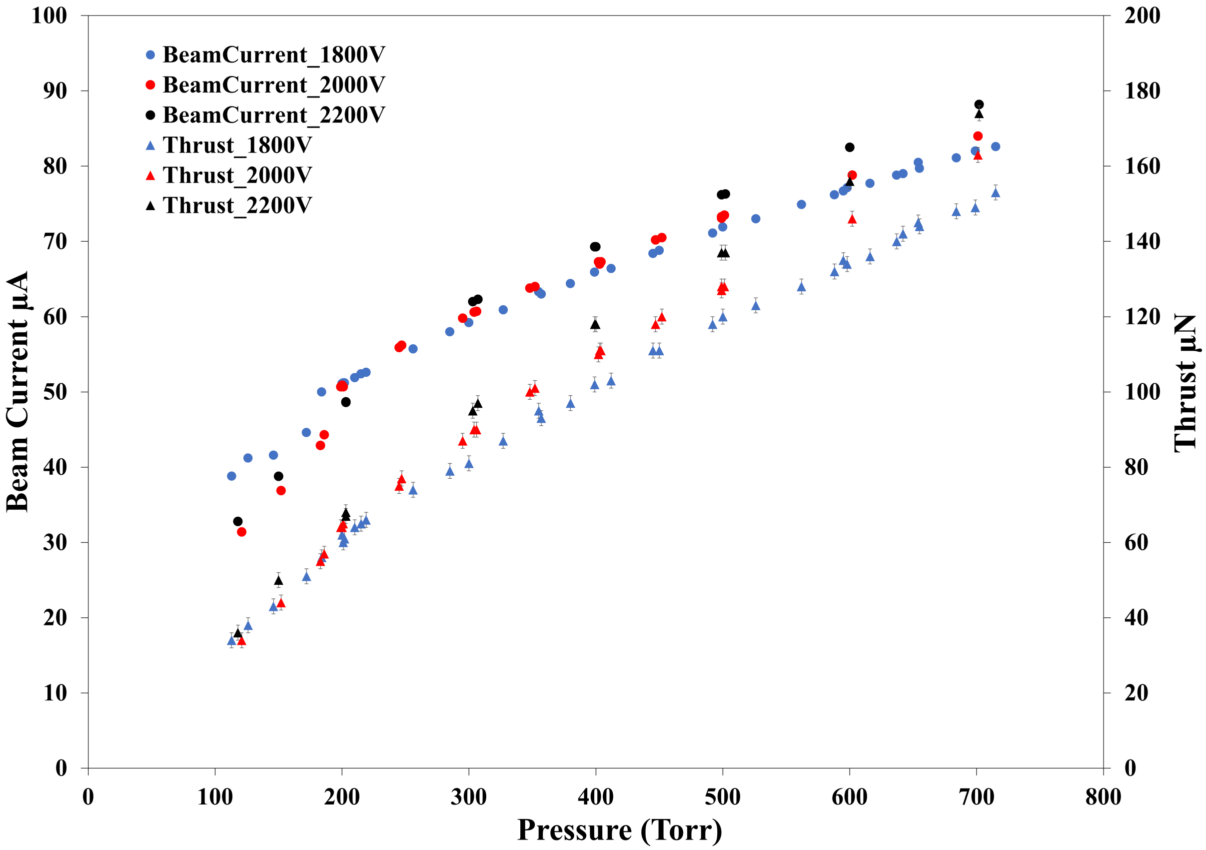

Figure 3.43: Thrust measurements of the 256 emitter array electrospray at different beam currents and emitter voltages

The results show an excellent performance, demonstrating the ability of the microfabricated electrospray sources to deliver significant thrust, scaling with the beam current and acceleration voltage as explained in equations 3.11 and 3.14. The maximum thrust measured is 174 μN ±2, more than three times higher than the maximum thrust delivered by the BUSEK-JPL colloid thruster demonstrated on the ST7 mission [152], and the highest thrust reported in a microfabricated colloid thruster actively fed. That maximum is reached at a beam current of 88.2 μA (344 nA per emitter) and an emitter array voltage of 2200V. More beam current was not tested to avoid pressurizing the propellant reservoir above 760 torrs. However, it is proven that the same thruster could increase the maximum thrust at least 25% more by operating the emitters at currents up to 450 nA and higher voltages. More research finding the maximum operating voltages, at which the voltage isolation of the sources is not compromised, could also help to boost the delivered thrust. A set up at JPL is currently getting ready for the 1000 hours performance test of the 256 emitter source.

3.4 Conclusion

This chapter has demonstrated a scalable microfabrication method of silicon micro-emitters for a compact microfluidic electrospray propulsion system. The fabricated sources are compact, and its components, an emitter array electrode, extractor electrode, and a supporting micromachined glass substrate, are permanently bonded and precisely aligned using anodic bonding. The number of emitters, the hydraulic resistance of the microfluidic system, and the gap between the extractor electrode and the emitter electrode can be tailored during the initial design and fabrication steps to achieve desired pressures and voltage operations. The good performance, uniformity, and synchrony of emission in each emitter part of the array are demonstrated together with a fast and good response to the applied pressure in the propellant reservoir. A key performance issue is identified and addressed by adding a platinum layer on top of the emitter array, avoiding the deposition of the neutralized counter ion during operation. The performance test realized and the one undergoing at the moment demonstrates the largest operational lifetime of a microfabricated electrospray source with capillary-like emitters actively fed. The thrust measurements show thrust values up to 174 μN with room for higher values. Overall it is demonstrated that the design, fabrication, and performance of the sources shown in this chapter could lead to a real primary propulsion solution for smallsatellites.

Chapter 4

Jet initiation in polymer solutions

4.1 Electrospray to Electrospinning

[1] The previous chapters show that electrospray propulsion uses liquids with very high conductivities and low vapor pressures to produce tiny droplets with a very high charge-to-mass ratio that do not evaporate in vacuum. However, when electrospraying polymer-based solutions, the conductivity is usually low due the nature of the polymer electrosprayed and the vapor pressure high due to the solvents typically used, leading to fast evaporation of the electrospray droplets into polymer micro-nano particles accelerated towards a collector. Another interesting difference is that the collector and the extractor in electrospray deposition are usually the same. In electrospray propulsion, the extractor electrode is surrounding the emitter to avoid interception of the beam and to accelerate droplets and ions into the free space. However, in the electrospray of polymer solutions, the extractor electrode usually

---

[1] Portions of this chapter are reprinted or adapted from A. Cisquella-Serra, Marco Magnani, Alvaro Gual-Mosegui, Sunshine Holmberg, Marc Madou, Manuel Gamero-Castaño "Study of the electrostatic jet iniation in near-field electrospinning" J. Colloid Interface Sci., vol. 543, pp. 106–113, 2019.https://doi.org/10.1016/j.jcis.2019.02.041. With permission of Elsevier Publishing.

faces the emitter and intercepts all the particle beam. Figure 4.1 shows an electrospray of a polymer solution facing and electrode and the nanoparticles collected.

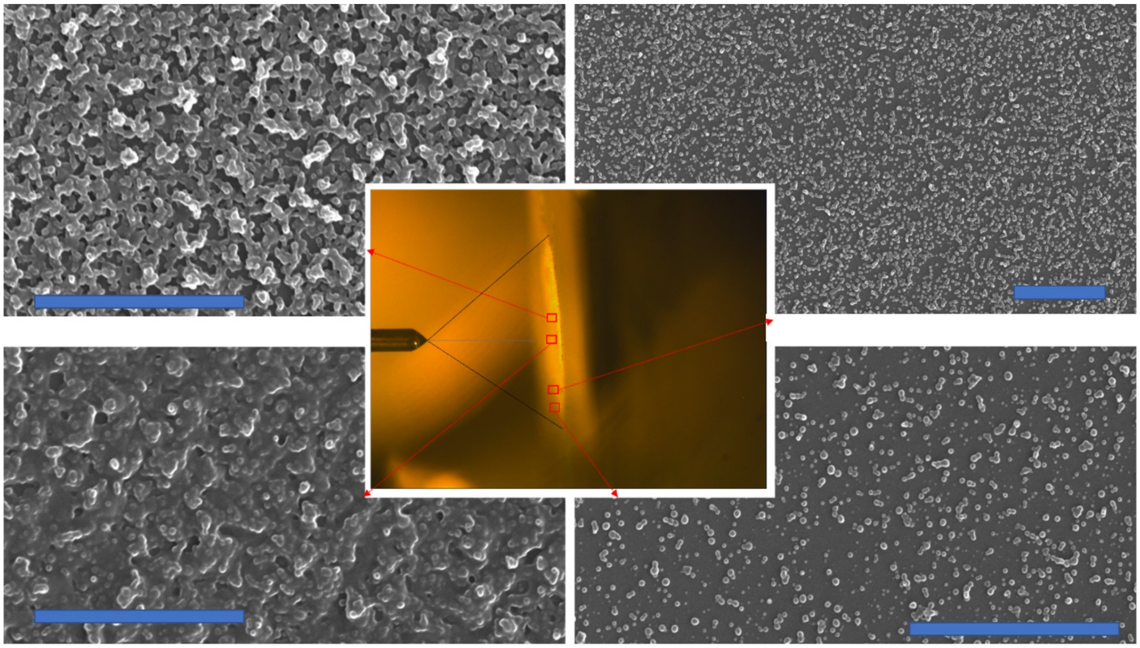

Figure 4.1: Electrospray deposition of SU-8 nanoparticles. Scale bar is 5 μm.

In Figure 4.1 a solution made with dimethylformamide, SU-8 photoresist and tetrabutylammonium tetrafluoroborate (a salt to increase the conductivity of the solution), is electrosprayed at 3000V collecting the particles in the extractor electrode, which is a silicon wafer electrode. It can be observed that the density of particles is dependent on the angle of the axysimetric beam, having higher dentity in the x axis (0 degrees half angle) and decreasing as the beam angle increases. Which is expected and follows the basic electrospray principles. The electrospray of SU-8 nanoparticles can generate thin films of a few nanometers by using very shorts deposition times that can be patterned using photolithography skipping a spin coating process as shown in Figure 4.2.

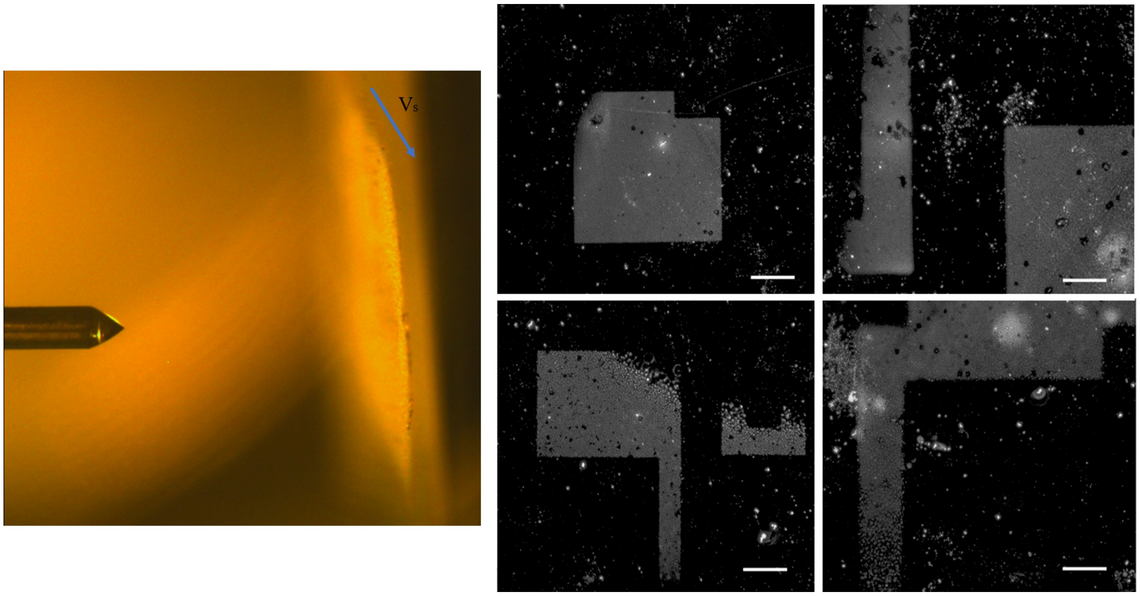

Figure 4.2: Electrospry thin film deposition of SU-8 and obtained patterns after lithography

By modifying the total time at which the electrospray is operating, the thin films can be scaled up to 3D structures, as shown in Figure 4.3

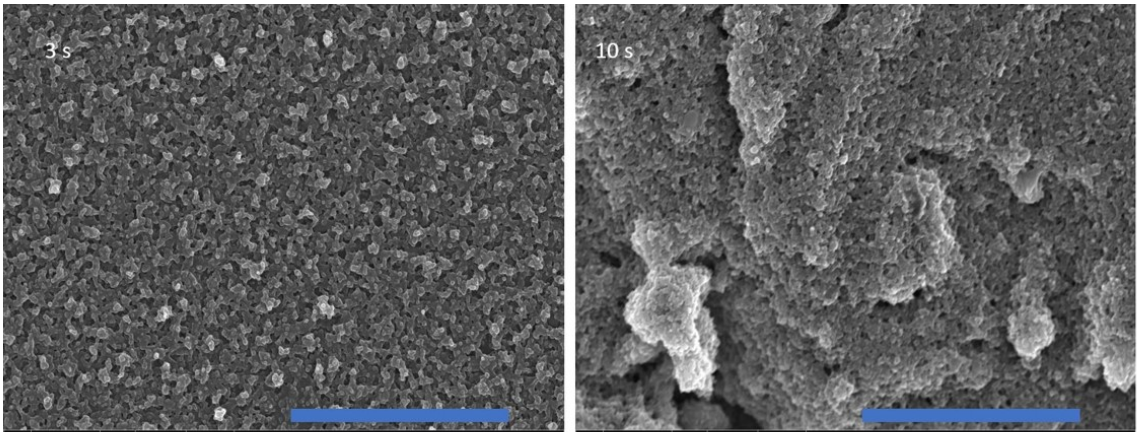

Figure 4.3: Pattern obtained after a 3 second deposition and a 10 second deposition. Scale bar is 5 μm.

Electrospray deposition can be a fascinating tool for a plethora of applications. However, the interest in this dissertation is to understand its ability to produce long micro and nanofibers. As mentioned in the introductory chapter, the molecular weight of the polymer solution plays an important role. It separates the electrospray jet to break into small nanodroplets to break into continuous nanofibers. For example, in the solution used in the electrospray shown in Figures 4.1 the concentration of SU-8 can be increased, but the jet will still break into droplets due to its low molecular weight. However, if we add to the solution a polymer of high molecular weight such as Polyethylene oxide (MW= 4,000,000), the disintegration of the jet due to polymer entanglement is inhibited, as shown in Figure 4.4. The ability of electrospray jets to generate polymer fibers is called electrospinning.

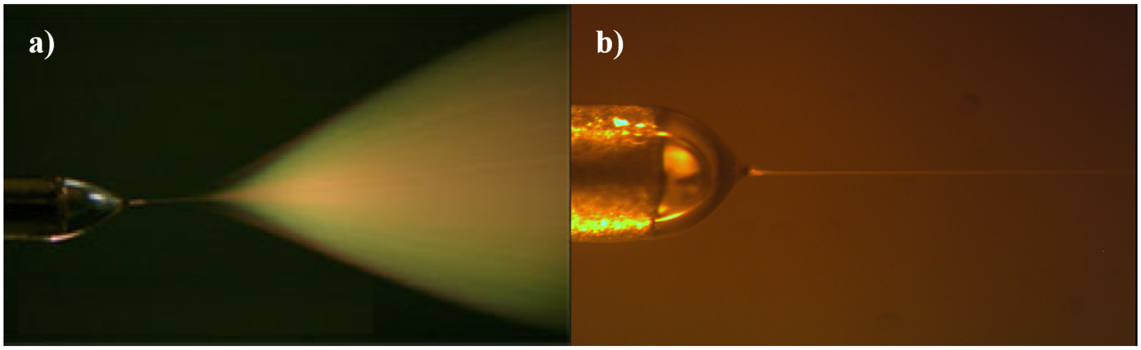

Figure 4.4: a)Electrospray jet breaks into a beam of droplets b) The jet disintegration is inhibited, and a polymer fiber is ejected

As mentioned in the introduction, electrospinning is the technique for producing long micro and nanofibers from a polymer liquid solution [111] by applying an electric field that overcomes the surface tension of the solution. An electrospray and its jet naturally develop from a liquid drop under the influence of a strong electric field, which induces the external stress required to balance the high capillary tension resulting from the jet's curvature [53],[46]. An important feature of electrosprays is that the diameter of the base of the jet only depends on the physical properties of the fluid (surface tension, electrical conductivity, and density) and its flow rate. In addition the electric field acting on the charge migrated to the surface accelerates the jet, thinning it down for as long as it remains stable. Thus, by operating with the appropriate combination of fluid properties and electric field strength, jets with diameters ranging from several micrometers to tens of nanometers can be generated regardless of the diameter of the nozzle feeding the fluid, and the associated fibers can be drawn into intricate microarchitectures.

With Nearfield electrospinning, controlled patterns made of sub-micron fibers of polymers can be produced, by avoiding the bending instabilities typical of far field electrospinning, and can be integrated with other microfabrication processes such as lithography to generate more complex patterns[5][32]. As mentioned in chapter 1 most of the research on NFES has focused on the analysis of the properties of the generated fibers and fiber patterns[64] [139], while the physics behind NFES has received less attention. In our experience succesful NFES operation is largely based on the user's familiarity with the technique and trial and error practices, probably due to the lack of a fundamental understanding of the processes involved. For example, a key step in NFES is the initiation of the jet. Lin and collaborators, in their landmark article originating the field, initiate the jet by simply increasing the voltage difference between a metallic needle holding a pendant drop, and a facing grounded plane [120]. This is the standard way of initiating electrosprays, for which the jet's onset or critical voltage V_0 scales with the surface tension γ of the fluid and the radius R of the liquid drop as $\mathrm{V}_0 \approx (2\gamma R/\varepsilon_\mathrm{O})^{1/2}$, where ε_O is the permittivity of vacuum. However, this standard initiation method in NFES typically results on undesired outcomes such as the discharge and deposition of most of the drop or multiple fibers, and a lack of control on the deposition of the fiber due to bending instabilities of the jet. To overcome this problem mechanical initiation methods have been developed based on piercing the drop with a sharp glass or metal needle before or coinciding with the application of an electric field, and dragging the attached fluid bridge to the deposition plate[5][90][10]. Mechanical initiation is difficult to reproduce and leads to large variations in the diameter of the fibers[151]. Furthermore, some studies point to the need of critical electric fields one order of magnitude higher in NFES than in traditional electrospinning, e.g. 10^6V/m versus 10^5V/m[10], which is paradoxical because the electric field required to initiate the jet should only be a function of the properties of the fluid, and not of the dimensions of the emitter and collector. It is apparent that a better understanding is needed to rationalize why the simpler standard initiation usually fails in NFES; devise conditions compatible with standard initiation if possible; obtain reliable laws for the diameter of the jet and fibers; and generally, optimize NFES on the basis of first principles. In this chapter the jet initiation phenomenon in NFES is deeply analized. A physical model is elaborated to compute the shape of the liquid meniscus in the presence of an electric field, and for predicting the critical voltage for given fluid properties and geometry of the emitter and collector electrodes. The results of the model compare well with experimental data obtained with a SU-8 based solution which, upon UV exposure and pyrolysis of the collected fibers, yields to glassy carbon wires[32]. This will be explained on detailed in the next chapter Carbon MEMS.

4.2 Materials preparation and experimental methods

The jet initiation experiments are carried out with a polymeric solution made by mixing SU-8 2002 from MicroChem. Inc. MA, USA, with 0.75 wt. % of high molecular weight (MW= 4,000,000) polyethylene oxide (PEO) from Dow Inc. (WSR-301), and 1 wt. % tetrabutylammonium tetrafluroborate (TBF). The SU-8/PEO/TBF blend is diluted with 30 vol. % of N,N-Dimethyleformamide. This polymer solution is electrospunnable and pyrolizable[5]. The properties of the resultant fibers after pyrolysis yield glassy carbon wires, which have been recently analyzed[32]. While the SU-8 component, after crosslinking with UV light and performing pyrolysis, produces the glassy carbon phase, the PEO component provides the viscoelastic properties needed for electrospinning. The ratio SU-8/PEO is critical, since an excess of PEO will not allow carbonization of the fiber during pyrolysis due to the oxygen content. Figure 4.5 shows a sketch of the experimental set up used in the characterization of jet initiation.

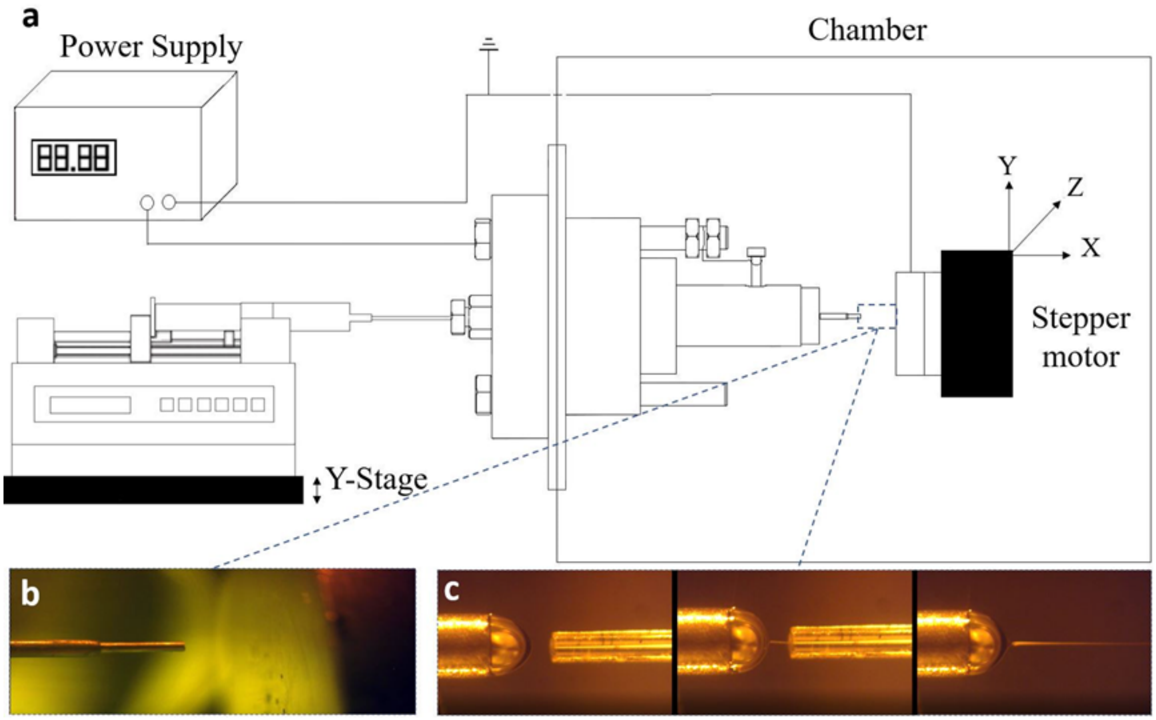

Figure 4.5: (a) Schematic of the experimental setup used for the analysis of jet initiation; (b) jet initiation in the emitter/plate configuration; (c) jet initiation in the emitter/rod/plate configuration.

The polymeric solution is stored in a syringe protected from ultraviolet light to avoid crosslinking of the SU-8. A stainless steel capillary tube attached to the tip of the syringe channels the solution to the emission site, which takes place at the end of the capillary tube itself. The outer and inner diameters of the tube are 710 μm and 533 μm. The end of the line used as emitter is mounted inside a chamber that provides mechanical rigidity. A syringe pump drives. the solution to the emission site, and is turned off once the fluid emerges and forms a visible meniscus. The size of the liquid meniscus, held at the tip by surface tension, can be modified by adjusting the height difference Δh between the pump and the emission site. The chamber has windows that allows the observation of the meniscus with a microscope housing a camera. Most experiments were recorded with a high-speed digital camera, and some with a standard digital camera. Ultraviolet filters placed on the windows avoid crosslinking of the SU-8. A brass disk with a diameter of 38 mm is used as a collector. It is mounted perpendicular to the emitter on an X, Y, Z stage that, actuated with stepper motors, allows for incremental positioning with a resolution of 26,5 μm. The emitter is connected to a high voltage power supply, and the collector is grounded. The jet initiation experiments are done for two geometries: the simpler emitter/plate configuration; and placing a fused silica rod between the emitter and the disk, referred to as emitter/rod/plate configuration. The rod has a diameter of 340 μm, a typical length of 2.23 mm, and a dielectric constant of 3.77 (Polymicro Technologies, LLC). All the experiments are performed at atmospheric pressure and room temperature, between 22ºC and 24ºC.

Figure 4.6.a shows the evolution of the liquid meniscus in a typical jet initiation experiment, as the emitter potential is increased up to the value that triggers the formation of the jet. Although the experiment corresponds to the emitter/rod/plate configuration, the basic phenomena is common to the emitter/plate configuration. At zero potential the meniscus is spherical, with a shape that results from the balance of surface tension and the pressure head of the fluid. As the voltage increases the electrical stress pulls out the meniscus, while the surface retains the spherical shape. The displacement of the meniscus increases modestly up to a potential of 960 V, at which point a very modest increase in potential suffices to double the displacement: at 980 V the meniscus accelerates forward and touches the surface of the rod immediately before releasing the jet and pulling back. The last photograph in Figure 4.6.a shows the final, stationary state of the meniscus and jet at 980 V. Figure 4.6.b shows images of the meniscus during the sudden displacement leading to the ejection of the jet, taken with the fast camera under near identical conditions: during a transient of a few hundred milliseconds the spherical tip of the meniscus turns into a conical shape before ejecting a jet. This minimum voltage that triggers an abrupt transition from a spherical to a conical meniscus from which the jet forms is observed in all experiments, and defines the critical voltage.

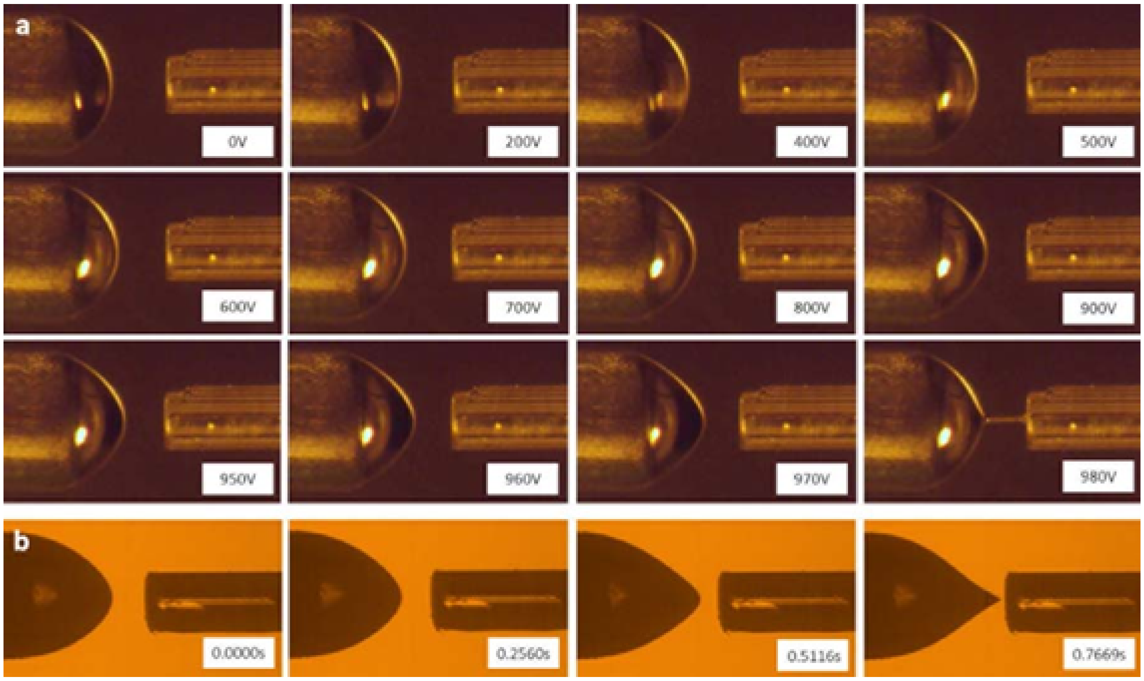

Figure 4.6: Evolution of the liquid meniscus at increasing potential in the emitter/rod/plate configuration : (a) photographs at increasing voltage, up to the ejection of the jet; (b) high speed imaging of the fast evolution from spherical to conical meniscus preceding jet ejection.

4.3 Jet initiation model

A model is next formulated based on the work by Pantano et al.,[103] to compute the position of the free surface and the electric field surrounding the meniscus, and ultimately to determine the critical voltage leading to the emission of the jet. Figure 3 shows a sketch of the axisymmetric model domain.

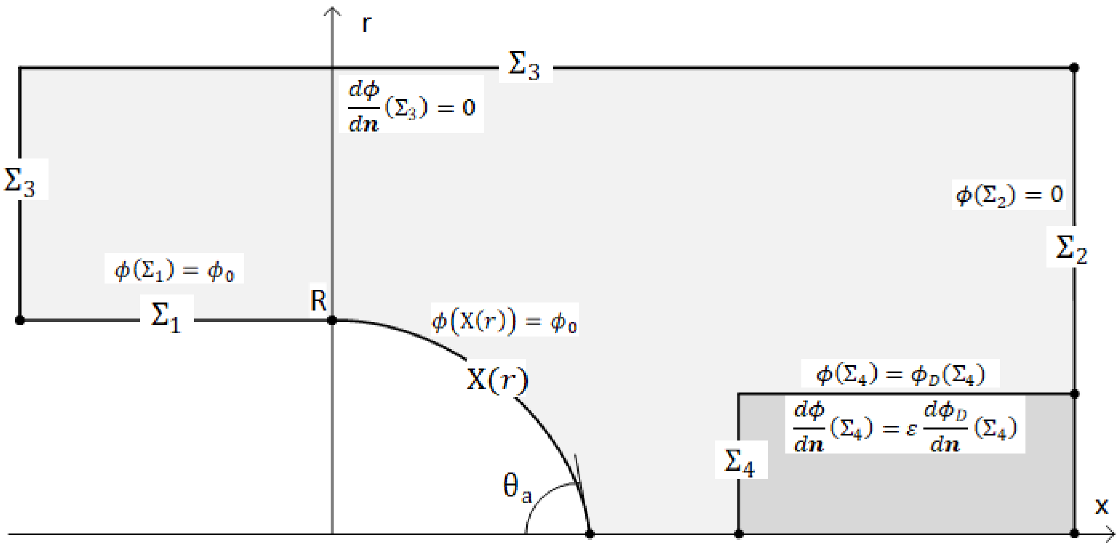

Figure 4.7: Computational domain and boundary conditions.

A hydrostatic liquid meniscus is attached to an emitter electrode, and has a free surface *X(r)* determined by a balance between surface tension, pressure and electric stress. An electric field surrounds and acts on the meniscus, induced by a voltage difference ϕ_o applied between the emitter and a ground electrode, and in some cases influenced also by the presence of a dielectric rod. The domain is enclosed by a surface Σ_3 , while Σ_1 , Σ_2 and Σ_4 are the surfaces of the emitter, ground electrode and dielectric rod respectively. We next introduce the equations of the model in nondimensional form using R, γ/R and ϕ_o/R as the length, pressure and electric field scales; symbols topped with a tilde denote nondimensional variables. The position of the surface is given by the augmented Young-Laplace equation and boundary conditions:

$$-\frac{\tilde{r}\tilde{X}'' + \tilde{X}' + \tilde{X}'^3}{\tilde{r}\left(1 + \tilde{X}'^2\right)^{\frac{3}{2}}} - \tilde{P} = \frac{\varepsilon_0 \phi_o^2}{2\gamma R} \tilde{\mathbf{E}}_S(\tilde{r})^2 \tag{4.1}$$

$\tilde{X}\,(1) = 0, \qquad \tilde{X}'\,(0) = -\tan^{-1}(\theta_a)$

P is the pressure in the liquid (constant throughout due to the hydrostatic assumption), and $\mathbf{E}_S\left(r\right) = \mathbf{E}\left(r, X\left(r\right)\right)$ is the electric field on the surface. One end of the surface is attached to the rim of the emitter, while the angle θ_a between the surface and the axis is imposed at the axis. The hydrostatic assumption requires a null electric field inside the fluid, and therefore an equipotential meniscus and an electric field that is normal to the surface. The electric field is derived from the electric potential, $\tilde{\mathbf{E}} = -\nabla\tilde{\phi}$, which fulfills the Laplace equation with boundary conditions:

$$\nabla^2\tilde{\phi} = 0 \tag{4.2}$$

$$\tilde{\phi}\left(\Sigma_1\right) = \tilde{\phi}_S\left(r\right) = 1 \qquad \tilde{\phi}\left(\Sigma_2\right) = 0, \qquad \frac{d\tilde{\phi}}{d\mathbf{n}}\left(\Sigma_3\right) = 0$$

i.e. constant potential at the surface of the liquid, emitter and plate, and symmetry conditions at the outer boundary.

The solution of the equations is a function of three dimensionless numbers: the dimensionless pressure $\tilde{P}$, the Taylor number $\Pi_T = \frac{\varepsilon_0\phi_o^2}{2\gamma R}$, and the angle θ_a; and of geometric factors. For example, the spherical menisci in Fig. 2(a) are readily computed by solving this model with the appropriate values of ϕ_o, the pressure head P, and using $\theta_a = 90^o$. However a main goal of the model is to determine the potential of the emitter that initiates the jet or, equivalently and as illustrated by Figure 4.6, makes the meniscus pointed. Therefore three additional relations are needed to fix the values of $\tilde{P}$, Π_T and θ_a for the jet initiation condition. To this end we seek two closure relations by first approximating the surface near the axis with a second order polynomial

$$\tilde{X}\left(\tilde{r} \to 0\right) = \tilde{X}_0 - \frac{\tilde{r}}{\tan\theta_a} + \frac{\tilde{X}_0''}{2}\tilde{r}^2 + O(\tilde{r}^3) \tag{4.3}$$

which, inserted in the Young-Laplace equation, yields the following condition valid near the axis (terms of order $\tilde{r}^2$ and higher are neglected):

$$\frac{\cos\theta_a}{\tilde{r}} - 2\sin^3\theta_a \tilde{X}_0'' - \tilde{P} = \Pi_T \tilde{E}_S(\tilde{r})^2 \tag{4.4}$$

In a pointed surface, $\theta_a < 90^o$, the dominant capillary pressure term $\cos\theta_a/\tilde{r}$ is singular at the axis and must be balanced by the electric stress. Thus the electric field near the axis must follow the power law:

$$\tilde{E}_S\left(\tilde{r} \to 0\right) = \frac{E_r}{\sqrt{\tilde{r}}} \tag{4.5}$$

where the parameter E_r is to be obtained from the solution. After inserting this expression in (9) and balancing separately the dominant terms, and terms of order one, we obtain the two closure equations for the Taylor number and the dimensionless pressure:

$$\Pi_T = \frac{\cos\theta_a}{E_r^2} \tag{4.6}$$

$$\tilde{P} = -2\sin^3\theta_a \tilde{X}_0'' \tag{4.7}$$

We impose a tip angle as the third closure relation defining jet initiation, and consider two significant values: the limit $\theta_a \to 90^o$ associated with the initial stage of the fast transition from spherical to conical meniscus (we use $\theta_{a,S} = 89.95^o$ to obtain numerical solutions); and the angle of a Taylor cone, $\theta_{a,T} = 49.29^o$. Although $\theta_{a,T}$ is the solution for a highly idealized configuration (a semi-infinite, equipotential cone in which surface tension fully balances the electric stress, i.e. with zero pressure jump across the surface), experimental electrosprays exhibit angles near $\theta_{a,T}$ [19].

Next other elements of the model and the numerical method are sumarized. First, we are interested in understanding the effect of a nearby dielectric rod in the initiation of the jet. The model incorporates this by solving an additional Laplace's equation for the potential inside the rod, $\nabla^2 \phi_D = 0$, while enforcing the usual jump conditions across the uncharged surface of a dielectric: $\phi\left(\Sigma_4\right) = \phi_D(\Sigma_4)$ and $\frac{d\phi}{d\mathbf{n}}\left(\Sigma_4\right) = \varepsilon \frac{d\phi_D}{d\mathbf{n}}\left(\Sigma_4\right)$, where ε is the dielectric constant of the rod. Second, we solve the Laplace equation using the Boundary Element Method, BEM [3]. Since only the electric field at the free surface is needed to solve (Equation 4.1), the BEM technique, based on solving algebraic equations for the values of ϕ and/or $\frac{d\phi}{d\mathbf{n}}$ at nodes on the surfaces of the domain, is more efficient than methods discretizing the Laplace equation on a grid of higher dimensionality. We discretize the surfaces using constant elements except for the one ending at the vertex of the meniscus, where the electric field is singular. In this element the electric field varies according to Equation 4.5, and the BEM method provides an equation for E_r. Due to the non-linear nature of the Young-Laplace equation, the system of Equations 4.1- 4.2,Equation 4.6 and 4.7 is solved iteratively as illustrated in Figure:

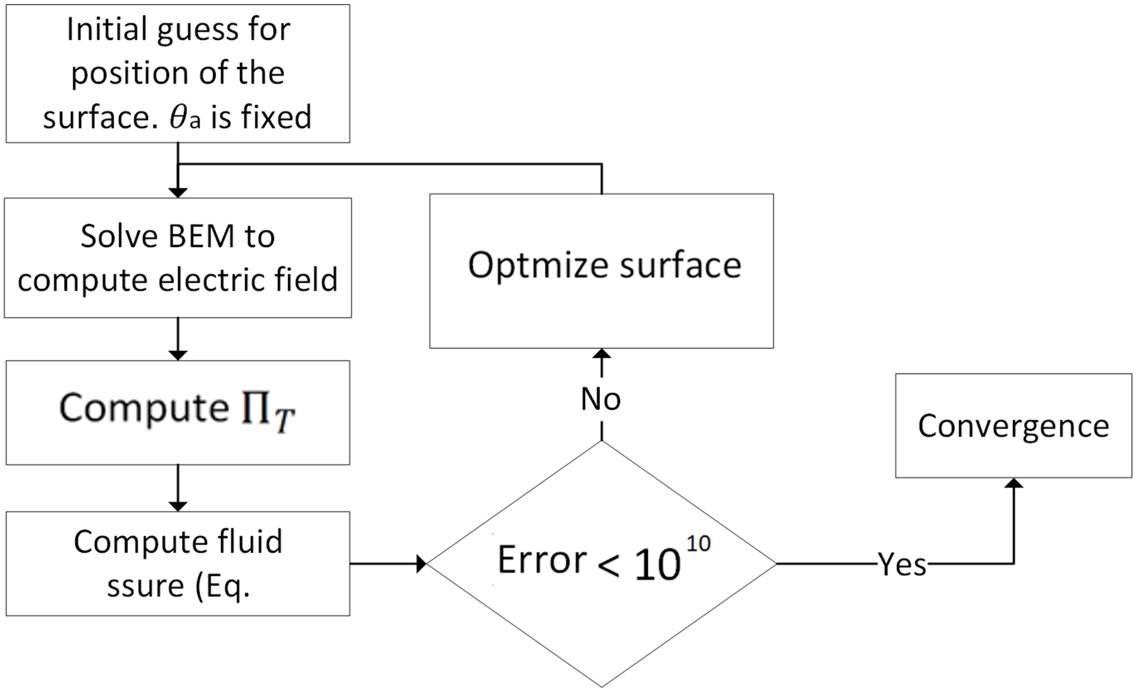

Figure 4.8: Algorithm for solving the model. Starting with an ad-hoc spherical meniscus, an iterative scheme is used to progressively modify the free surface until convergence

The value of the angle θ_a is set together with an initial guess for the position of the free surface; the electric field is computed next; the Taylor number and the dimensionless pressure are obtained using equations (4.6) and (4.7); the integral of the square of the residue of (4.1) is computed next. If the error is smaller than a desired tolerance the solution is accepted, otherwise a new position of the free surface is computed using the least-squares weighted residual method on the Young-Laplace equation, i.e. we find the position of the surface that minimizes the integral:

$$\int_0^1 \left\{ \frac{\tilde{r}\tilde{X}'' + \tilde{X}' + \tilde{X}'^3}{\left(1+\tilde{X}'^2\right)^{\frac{3}{2}}} + \left[\tilde{P} + \Pi_T \tilde{E}_S(\tilde{r})^2\right] \right\}^2 dr \tag{4.8}$$

for a known function $\tilde{P}+\Pi_T\tilde{E}_S(\tilde{r})^2$. The new free surface is used to compute the electric field and subsequent steps with the iterative algorithm that ends when the solution converges. The solution of the model provides the position of the free surface $\tilde{X}(\tilde{r})$, the Taylor number

Π_T, and the dimensionless pressure $\tilde{P}$ at jet initiation. The surface tension is needed to obtain the onset voltage from the Taylor number. The surface tension is not tabulated for this custom-made polymer solution, and is determined from a measurement of the shape of the meniscus as a function of the pressure head in the absence of an electric field. In this case most of the meniscus surface approximates well a sphere of radius R_C, and surface tension is balanced by the pressure head $\frac{2}{R_C}\gamma = \rho g \Delta h$, where g is the gravity acceleration and the density ρ is calculated with a mass-volume correlation, ρ =0.983 g/ml . Figure 5 shows photographs of the meniscus for several values of the height of the liquid column, the circumferences fitting the menisci and used to compute R_C, and the linear fitting of the $\{\frac{2}{R_m}, \rho g \Delta h\}$ measurements which yields $\gamma = 0.046 N/m$. The technique was tested with deionized water, for which we obtain $\gamma_{water} = 0.066 N/m$, i.e. a value 8.3% smaller than the one tabulated at 25ºC.

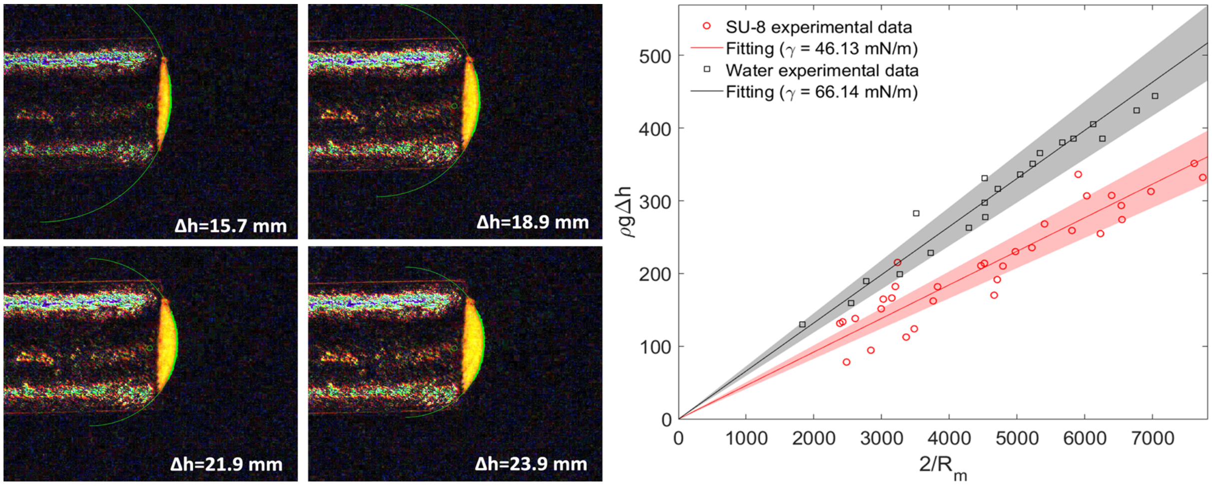

Figure 4.9: Correlation between the height of the liquid column and the radius of curvature of the meniscus in the absence of electric field, used to obtain the surface tension of the fluid

4.4 Results and discussion

Figure 4.10 shows photographs of the meniscus during the fast transition from spherical to conical shape preceding the ejection of the jet, taken with a high speed camera. Rows (a) and (b) are for the emitter/plate configuration, and (c) and (d) are for the emitter/rod/plate case. In rows (a), (b) and (c) the meniscus evolves towards the conical shape within milliseconds, and makes contact with the collector before releasing the jet. Upon contact the meniscus discharges reducing the electric stresses on the surface, and falls back while leaving behind a liquid bridge attached to the collector. Conversely the meniscus in row (d) becomes fully conical and releases a jet without contacting the collector, before discharging and receding back.

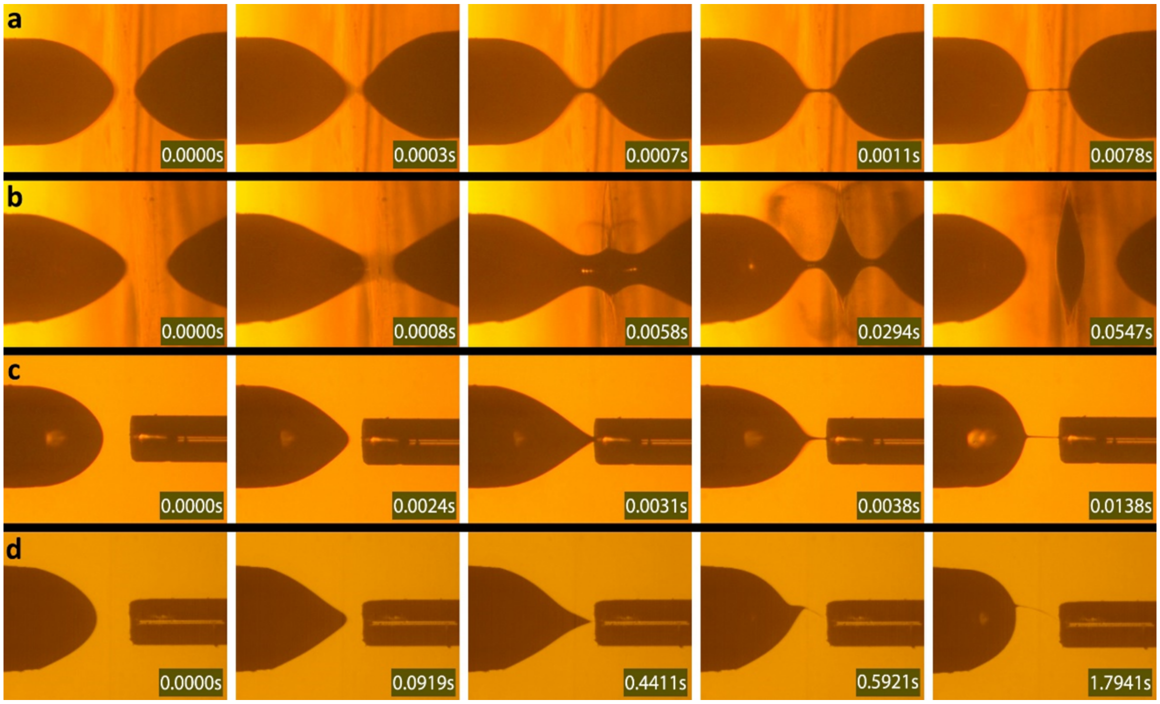

Figure 4.10: High speed photographs of the liquid meniscus transitioning to a conical shape and the jet formation. (a) and (b) are for the emitter/plate configuration, and emitter potentials of 500 V and 1000 V respectively. (c) and (d) are for the emitter/rod/plate configuration and emitter potentials of 1100V and 1500 V respectively

Two features are relevant to NFES: although (a), (c) and (d) result on liquid bridges that remain attached to the collector and can be used for patterning, there are clear differences on the diameters of the jets. When the meniscus touches the collector the initial diameter of the jet must be comparable to the contact area, and the jet thins down from this initial diameter as the meniscus recedes. On the other hand the diameter of the free-forming jet in (d) is miniscule by comparison. In this case the diameter is likely associated with that for the minimum flow rate that an electrospray operating in the con-jet mode can sustain, $d_{\min} \approx \left(\frac{\gamma\varepsilon_0^2}{\rho K^2}\right)^{1/3}\left(\frac{\gamma^2\rho\varepsilon_0}{\mu^3 K}\right)^{-1/6}$,[] a natural property that makes it possible to produce jets and fibers with diameters down to a few nanometers;K and μ stand for the electrical conductivity and the viscosity of the fluid. Secondly, although the conditions in row (b) initially produce a liquid bridge, it eventually collapses leaving behind a pool of fluid on the collector.

The collapsing of the meniscus and the resulting inability to produce a liquid bridge is a phenomenon that happens frequently in the emitter/plate configuration, and seldom occurs in the emitter/rod/plate case. Figure 4.11 shows the ability to produce a liquid bridge in each configuration, calculated as the percentage of successful tries, as a function of the emitter voltage.

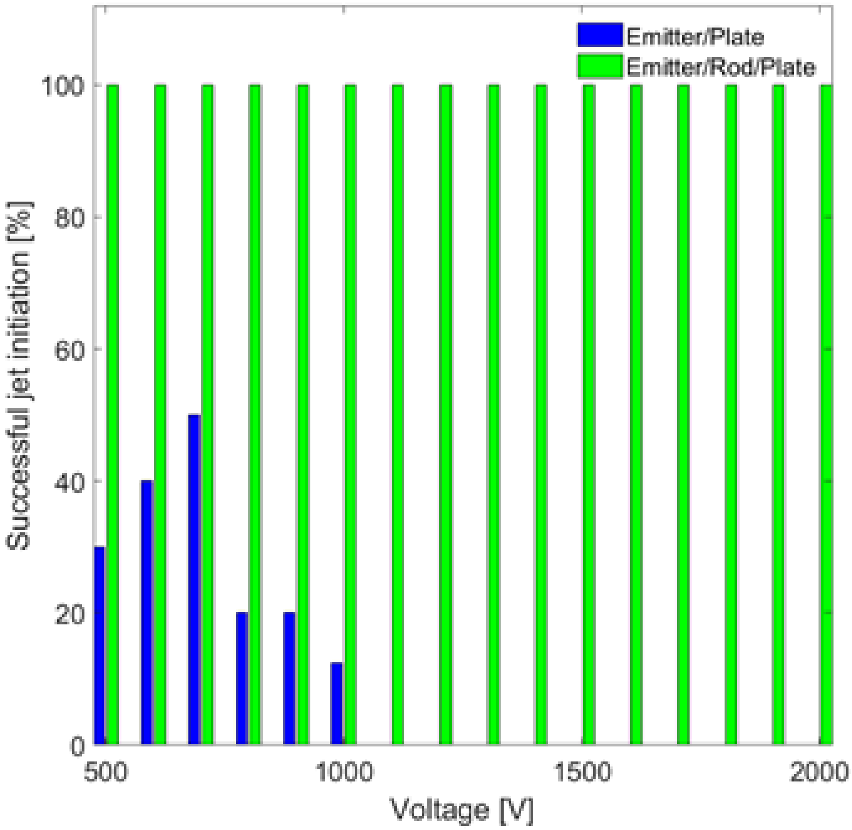

Figure 4.11: Percentage of successful jet initiations for the emitter/plate and emitter/rod/plate configurations, as a function of the emitter potential. The statistical value is obtained from 15 experiments at each condition

At each voltage the collector is slowly moved towards the emitter until either the liquid bridge forms, or the meniscus collapses. While the emitter/rod/plate experiments always produce a permanent liquid bridge, the emitter/plate configuration exhibits a lower success rate, becoming zero at emitter potentials exceeding 1000 V. The behavior of the emitter/plate configuration is consistent with the perceived difficulties in using the standard jet initiation method in NFES, and which motivated the development of initiation techniques that are mechanically aided.

The different ability of the configurations for producing liquid bridges is rationalized by the fields plotted in Figure 4.12.

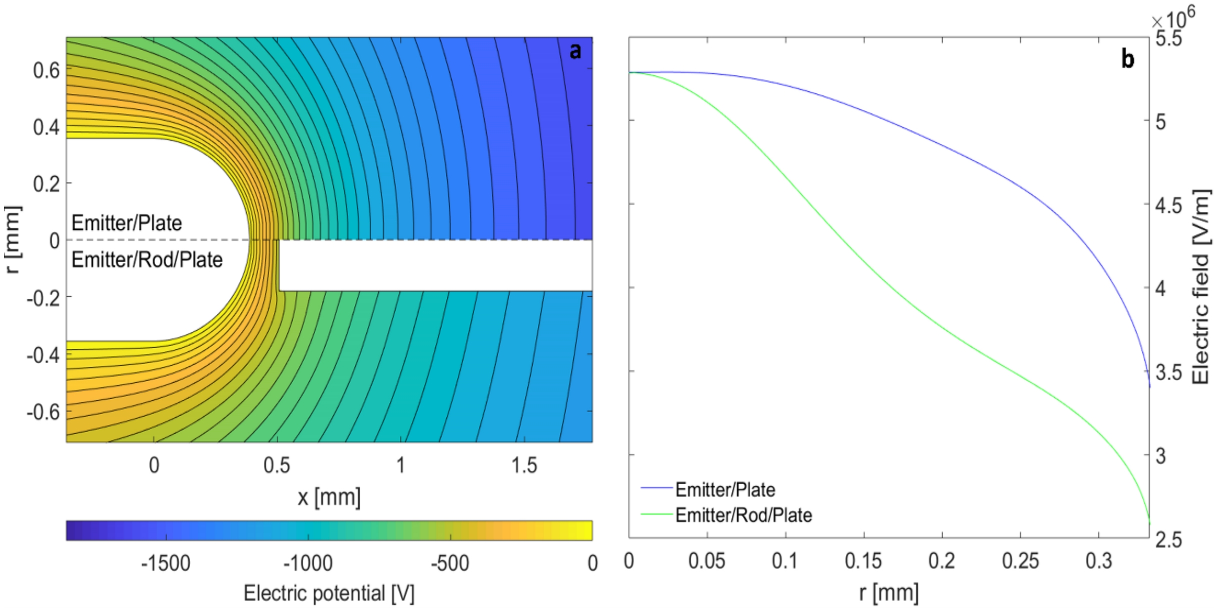

Figure 4.12: Electric potential field surrounding the meniscus for the emitter/plate and emitter/rod/plate configurations at jet initiation, for a tip angle of 89.95^o. The gaps between emitter and grounded plate are identical (2.73 mm). Contour lines are 50 V apart; (b) electric field on the meniscus surface for both configurations.

The model is solved to find the potential field at jet initiation for both configurations, using $\theta_{a,S} = 89.95^o$ for the tip angle and a gap between emitter and plate of 2.726 mm; the length of the rod is 2.23 mm. The model yields onset voltages of 1893 V for the emitter/plate configuration, and 1407 V for the emitter/rod/plate case. Figure 4.12.a shows how the dielectric rod changes the potential contours, making the field around the meniscus less spherical. Furthermore, the rod is able to induce an electric field near the axis identical to that of the emitter/plate configuration, but at a significant lower voltage difference between the emitter and the grounded plate (1407 V vs 1893 V). Figure 4.12.b shows the electric field at the surface: both configurations have a common value of 5.34x106 V/m near the axis, before diverging as $r^{-1/2}$ for $r \rightarrow 0$ (the plots do not show the divergence due to the smallness of the region where this occurs). At larger values of r the two electric fields separate, with the one for the emitter/plate configuration being significantly larger and nearly spherical along a significant fraction of the meniscus. Thus, while the deformation of the meniscus required to balance the electric stress is localized near the axis in the emitter/rod/plate configuration, the deformation for the emitter/plate case is more intense everywhere else. The larger deformation is more likely to lead to collapse as the electric pulling is intensified to reach the jet emission condition. Note also that the stress scales as the square of the electric field, and therefore the differences in Figure 4.12.b are magnified in the stress. The convergence of the electric fields for both configurations near the axis is an interesting feature of ‘ Figure 4.12.b. Since the inclusion of the dielectric rod makes the geometries quite different and introduces a dependency on the dielectric constant, the convergence near the axis suggests that the electric field at the tip at jet initiation is determined by local properties alone. In fact, the dominant balance in Equation 4.4 requires a dimensional field near the axis $E_S\left(r \rightarrow 0\right) = \left(\frac{2\gamma\cos\theta_a}{\varepsilon_0 r}\right)^{1/2}$, i.e. a field solely determined by the tip angle and the surface tension, and which does not depend on other factors such as the radius of the emitter, the gap between emitter and collector, or the dielectric constant of the rod. The common shape of the field near the axis in configurations with equal tip angle separates at increasing distance from the axis, responding to the particular values of the emitter-collector gap and the presence of the dielectric rod.

The evolution from a spherical to a conical meniscus and the subsequent ejection of a jet illustrated in Figure 4.6 is similar for both configurations. Furthermore if the collector is sufficiently close, the tip of meniscus contacts the collector before releasing the jet, creating also a liquid bridge as the meniscus recedes. We term *non-contact jet* mode and *contact jet* mode these two different ways of creating a liquid bridge in our configurations. Figure 4.13 shows for the emitter/rod/plate configuration the instant just before the jet is initiated in both *contact jet* and *non-contact jet* modes, at increasing value of the emitter voltage.

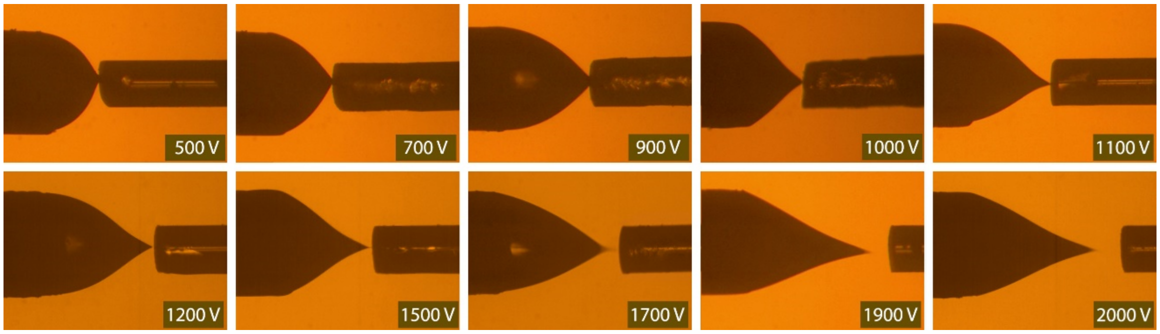

Figure 4.13: Instant just before the jet is formed in the emitter/rod/plate configuration. In each case the collector is moved towards the emitter at fixed voltage. From 500V to1100V the meniscus touches the rod before releasing a jet *(contact jet mode)*. From 1200V to 2000V the jet is released from a free-standing conical meniscus *(non-contact jet mode)*

Each photograph is for an experiment in which the emitter voltage is kept fixed, and the collector is slowly moved towards the emitter until the jet is released. For a dielectric rod 2.23 mm long, the contact jet mode occurs at or below a voltage of 1100V, while the non-contact jet mode is observed at 1200V and higher potentials. The formation of the liquid bridge is more uniform and controllable in the contact jet mode. In this case, after the initiation has happened, the conical meniscus recedes back to a spherical shape, while in the non-contact jet mode the shape after discharging sometimes remains non-symmetrical, probably due to the larger deformation the meniscus undergoes, preferential evaporation in the solution mixture, and its viscoelastic properties.

Figure 4.14 compares the relation between the onset voltage and the gap separating meniscus and collector, found in both experiments and with the model, for the emitter/plate and the emitter/rod/plate configurations. Although the gap between the rim of the emitter and collector is a more direct choice to define the onset voltage law, the experimental onset voltage is less repeatable when using this distance.

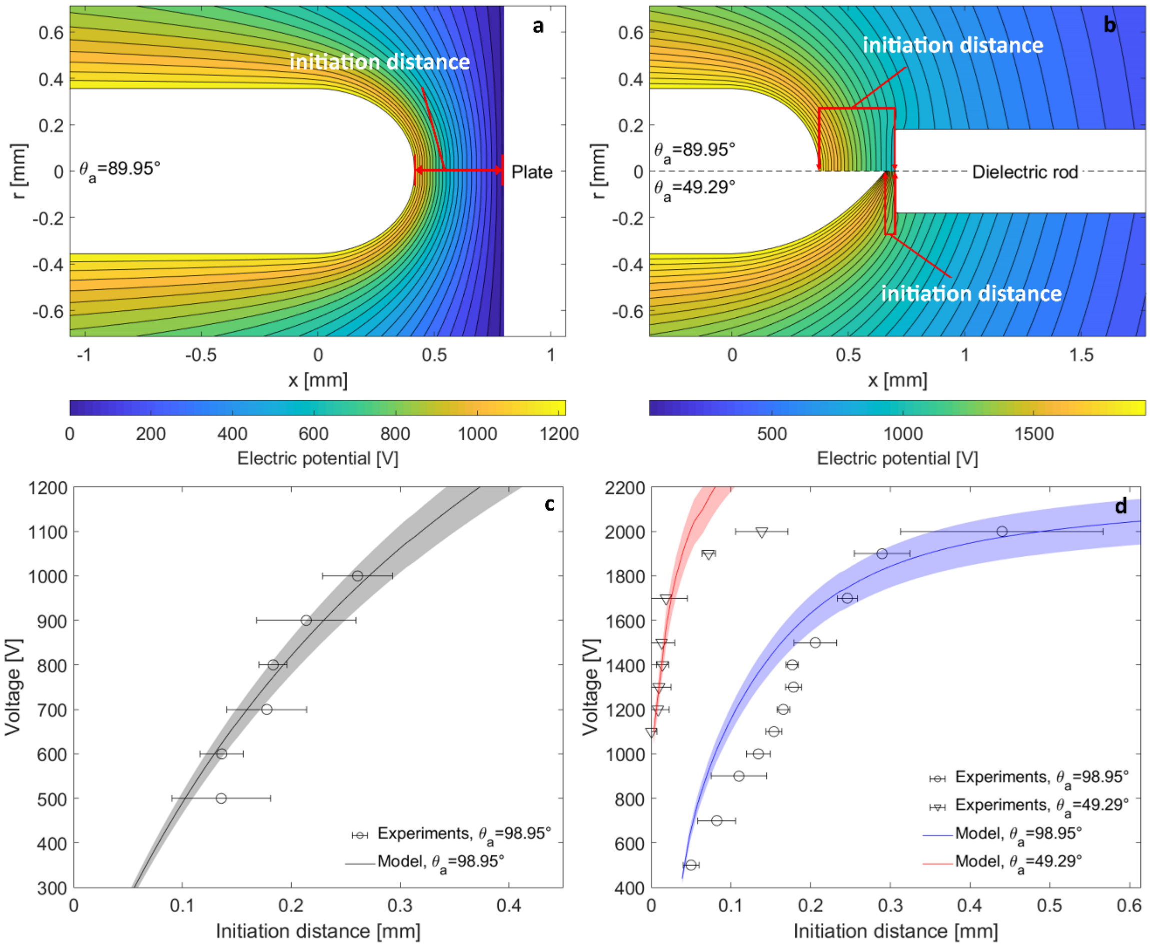

Figure 4.14: Comparison of the experimental and model onset voltage laws for the emitter/plate (a) and (c), and emitter/rod/plate configurations (b) and (d); (a) and (b) show typical potential fields and the definitions of the initiation distances; (c) and (d) show the onset voltage laws (emitter potential vs gap between meniscus and collector at jet initiation). The envelopes of the shaded areas correspond to a surface tension ±10% of the nominal value γ=0.046 N /m

This is due to the viscous nature of the solution, which makes it difficult to control the size and shape of the meniscus at zero electric field, and introduces a large uncertainty when establishing the position of an effective emitter rim. The emitter/rod/plate configuration considers both closure equations for the tip angle, $\theta_{a,S} = 89.95^o$ and $\theta_{a,T} = 49.29^o$. The emitter/plate configuration does not consider $\theta_{a,T} = 49.29^o$ because it only operates reliably in contact jet mode, i.e. if the meniscus fully evolves into a cone before touching the collector the probability for creating a lasting liquid bridge is small. Changes on the properties of the solution due evaporation of the solvent, when the meniscus is stretched into a conical geometry with higher surface area may be also affecting the final outcome. Figures (a) and (b) show contour plots for the electric potential and the definition of the initiation distance for both tip angles. The experimental initiation distance for $\theta_{a,S} = 89.95^o$ is defined as the gap between the spherical meniscus and the collector just before the meniscus abruptly turns conical, while for $\theta_{a,T} = 49.29^o$ we use the shortest gap recorded with the high speed camera once the meniscus turns conical. Figure 10(c) for the emitter/plate configuration shows a good agreement between the experimental onset voltage and the calculated one using $\theta_{a,S} = 89.95^o$ as the criterion for jet initiation. Figure 10(d) for the emitter/rod/plate configuration also shows a good agreement for both tip angles, although $\theta_{a,S} = 89.95^o$ yields a better agreement at the largest initiation distances. The model also captures well the onset voltage at which the tip of the cone just touches the rod, $V_{ON} = 1040V$ from the model and between 1100 V and 1200 V in experiments, as shown by the $\theta_{a,T} = 49.29^o$ solution. The model cannot compute onset voltages lower than 1040 V because the meniscus would need to cross the surface of the rod.

4.4.1 Metal tip initiation

As a supplementary part of the study, we changed the glass-fused silica tip for a metal one to focus the electric field on the meniscus and we analyzed the outcome. Surprisingly, the jet initiation was always unsuccessful. That highlights the magnitude of the effect of the collector for an optimal initiation on NFES. When changing the glass tip for the metal one it was observed that the initiated jet creates a discharge when making contact with the collector, burning the polymer meniscus as shown in Figures 4.15 a and b). After several attempts, a polymer coating was on top of the metal tip, and then the fiber initiation was possible, as shown in Figure 4.15 c. That demonstrates that having an insulator or semiconductor material as a collector in NFES is crucial to avoid the current conduction through the jets, self-heating, and electrical discharges. The conductivity of the polymer solution may also play an significant role in this phenomenon, besides affecting the voltage to trigger the jet initiation. However, a more exhaustive study of this phenomenon has to be pursued.

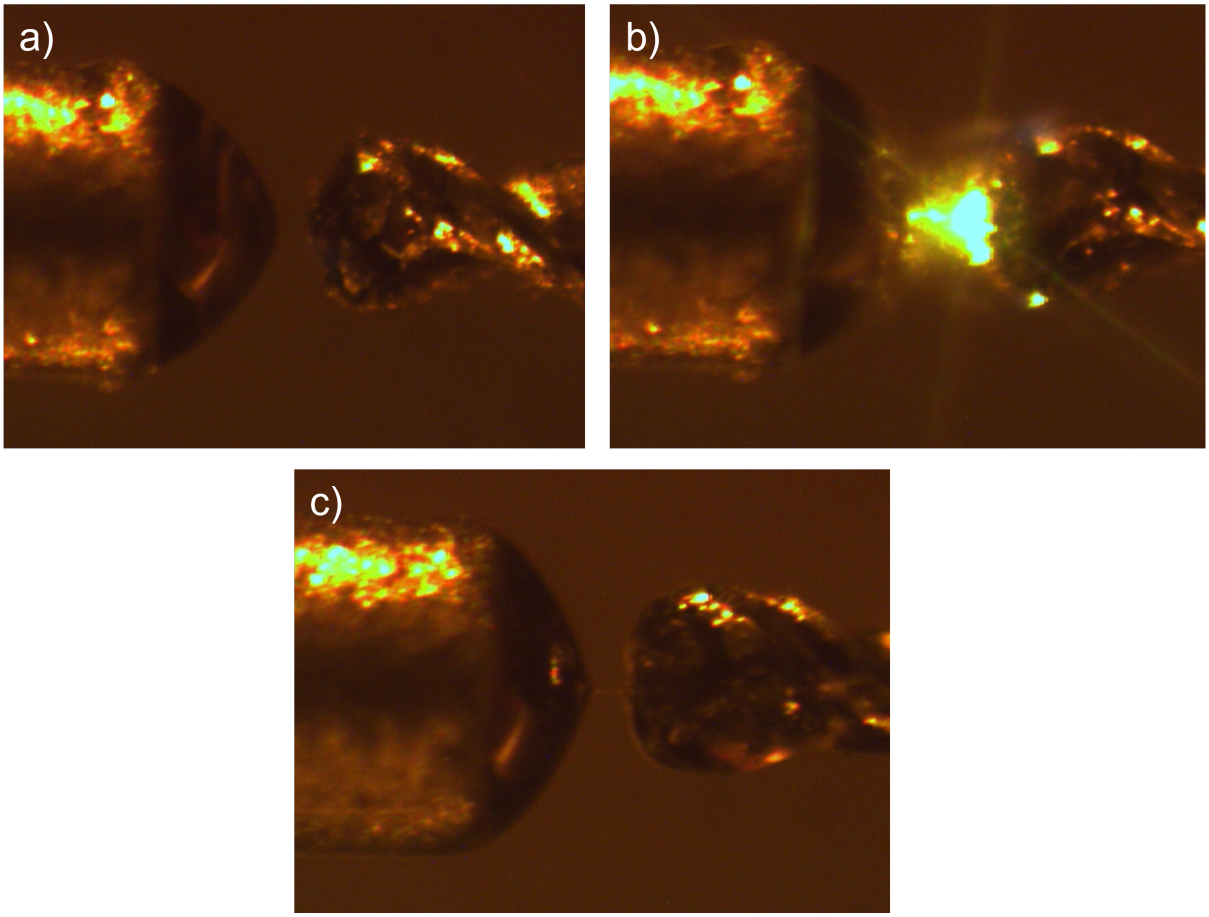

Figure 4.15

Chapter 5

Controlled Joule-Heating of Suspended Glassy Carbon Wires for Localized Chemical Vapor Deposition

5.1 Introduction

[1]The work described regarding the jet initiation on near-field electrospinning has straightforward applications. The polymer solution analyzed was previously optimized and demonstrated to be carbonizable into glassy carbon. Using Near-Field electrospinning, these jets can be precisely positioned on a SU-8 lithography pattern and carbonized through the C-MEMS process, obtaining suspended carbon fibers. Previous to carbonization, the suspended SU-8 fiber must be exposed with UV light to crosslink the SU-8 molecules to stand the pyrolysis process. The SU-8 lithography structure and the SU-8 based fibers lose their non-carbon

---

[1] Portion of this chapter are reprinted or adapted from A. Cisquella-Serra, M. Gamero-Castaño, L. Ferrer-Argemi, J. Wardini, and M. Madou, "Controlled joule-heating of suspended glassy carbon wires for localized chemical vapor deposition," Carbon N. Y., vol. 156, pp. 329–338, 2020.https://doi.org/10.1016/j.carbon.2019.09.069. With permission of Elsevier Publishing.

atoms undergoing a volume shrinkage during the carbonization process resulting in a monolithic carbon structure with excellent ohmic contacts. Figure 5.1a. shows a schematic of the process, and Figure 5.1b-c shows a suspended SU-8 based fiber on a lithography structure before and after pyrolysis.

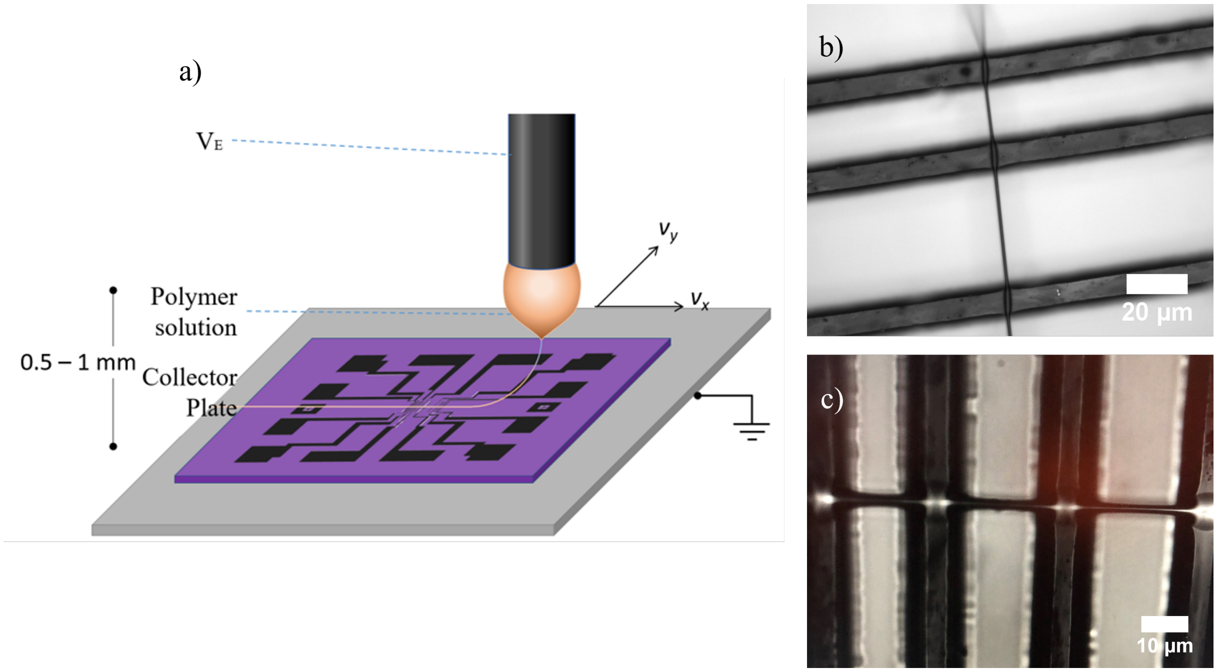

Figure 5.1: a) Schematic of the fiber deposition on a lithography pattern b) Fiber suspended in a lithography scaffold before pyrolysis.

With Near-Field electrospinning different fiber diameters can be obtained. As previously mentioned, the non-contact mode provides fibers of lower diameter but is more difficult to control. Most of the fibers suspended in this chapter are initiated using near-field electrospinning in contact mode providing fibers with 500 nm to 3 μm diameter range after pyrolysis .The pyrolysis ramp for optimal carbonization of the suspended fibers requires 2 hours of oxygen purge by flowing nitrogen on the pyrolysis furnace, a heating ramp of 4^{o}C/min until 300^{o}, 1 hour at 300^{o}, a second heating ramp of 10^{o}C/min until reaching 900^{o}C and 1 hour steady at 900^{o}C. Figure 5.2a. shows an SEM picture of a fabricated carbon electrode with suspended carbon fibers of different lengths and c-d) two suspended carbon fibers with different diameters.

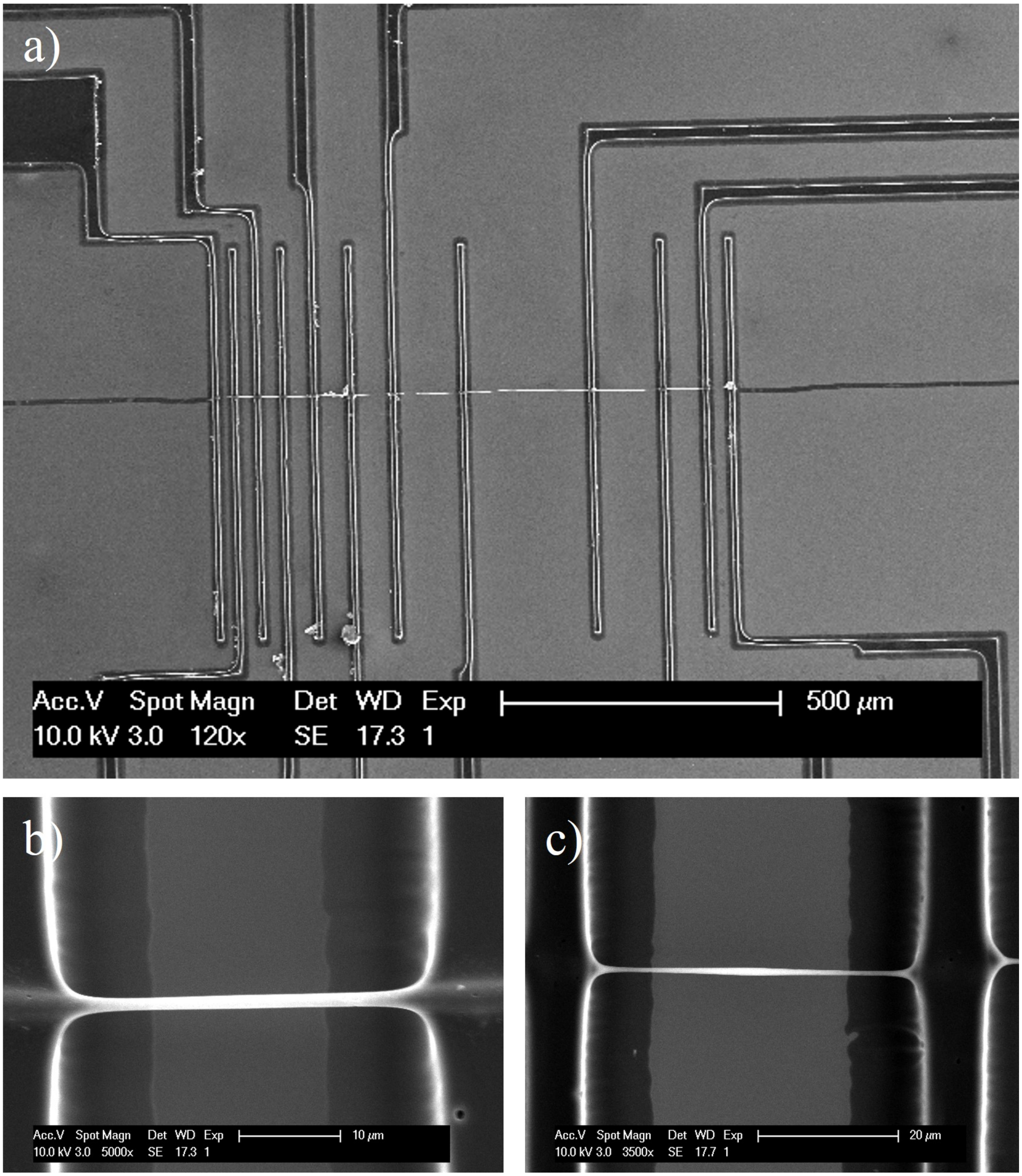

Figure 5.2: a) Overview of a suspended carbon fiber in a carbon scafold with different gaps b) Two suspended glassy carbon wires with different diameters.

A critical aspect of these suspended fibers is to think about their applications. Several suspended nano and microstructures are used in various sensors due to their excellent surface area to volume ratio granting good gas sensitivity and very little power consumption [144, 62]. However, it is fundamental to understand its electrical and thermal properties prior to its applications. The properties were of suspended glassy carbon wires were deeply analyzed in a collaborative project with Dr.Laia Ferrer Argemi at ENTER Lab at UCI [32, 33] . It was also observed, as previously reported, that in vacuum conditions suspended glassy carbon fibers could be heated at extreme temperatures through joule heating and generate nanogaps on the suspended fiber of the order of a few nanometers [115]. Figure 5.3 shows two nanogaps generated by Joule-Heating on suspended glassy carbon fiber coated with 20 nm os SiO_2. The nanogap highlighted on the figure has a lenght of 120 nm.

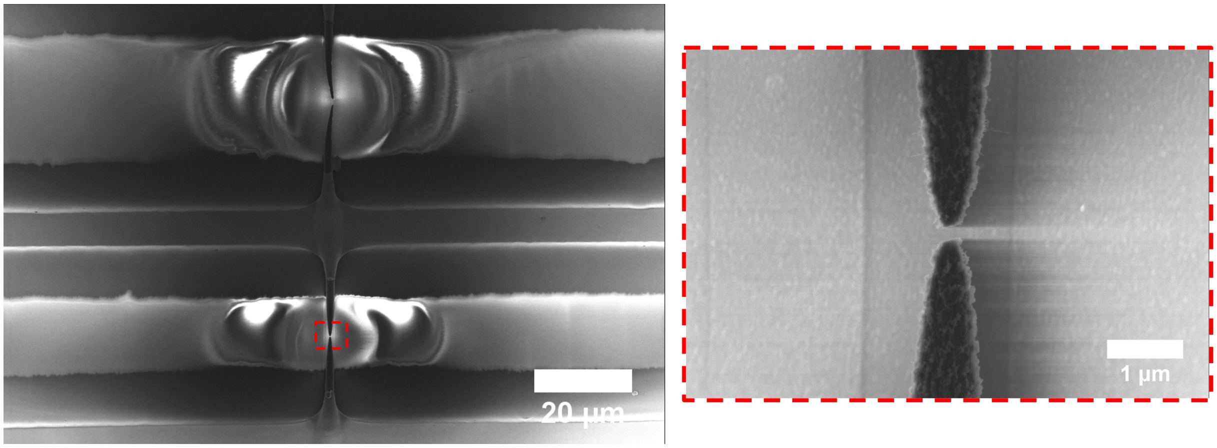

Figure 5.3: a) Overview of a suspended carbon fiber in a carbon scafold with different gaps width b) Fiber suspended in a lithography scaffold before pyrolysis.

Joule heating on glassy carbon wires was also demonstrated to initiate local chemical deposition (CVD) from a suitable precursor. For example, several transition metal oxides semiconductors (TMOS) can be deposited from heat's triggered decomposition of Metallo-organic precursors. This application is explored in detail in this chapter, where it will be demonstrated controlled localized chemical vapor deposition of WO_{3-x} on suspended glassy carbon fibers. The temperature required for the deposition of WO_{3-x} is generated by passing current through the fiber, which causes Joule heating. The deposition starts in the midpoint of the wire, and extends to its ends as the current is increased. The thickness and length of the coating are functions of the imposed current. The evolution of the coating can be monitored in real time by measuring the voltage vs current characteristic of the wire. WO_{3-x} coatings with thickness from 71 nm to 1.4 µm are deposited in glassy carbon wires with diameters between 780 nm and 2.95 µm. The coatings are uniform and polycrystalline. The suspended glassy carbon wire is a generic platform for the deposition of many transition metal oxide (TMO) coatings, and opens the door to carbon-TMO structures for applications including catalysis and gas sensing.

5.1.1 Carbon-TMOs composites

Transition metal oxides (TMOs) have attracted considerable attention in applications such as gas sensing (enabled by their chemo-resistivity) and the catalysis of the oxygen reduction reaction (ORR) and the hydrogen evolution reaction (HER) [133] [81]. Molecular hydrogen is a promising clean energy source, but the high cost of Pt-based catalysts handicaps large-scale applications. TMOs and other nonprecious-metal oxides could be economical alternatives to platinum but are limited by either their poor electronic conductivity or their inadequate catalytic performance. Recent research suggests that the catalytic and sensing performances of TMOs can be improved when combined with carbon materials such as graphene [147] [95], graphene oxide [110], carbon nanotubes (CNTs) [4], and pyrolytic carbon fibers. Zhang et al. [149]hybridized TiO_2 with graphite-like carbon layers to show that the semiconductor/graphite contact results in efficient separation of electron-hole pairs leading to higher photocatalytic activity under UV irradiation. Similarly, Woan et al. [136]demonstrated photocatalytic enhancement of TiO_2 by combining it with CNTs in a CNT-TiO_2 composite. Coating a suspended glassy carbon wire (GCW) with ZnO in a hydrothermal process led to lower limit of detection and higher sensitivity for NO_2 gas sensing than a single ZnO wire of the same dimensions [94]. Also carbon-SnO_2 hybrid structures have shown better electrochemical performance as anodes in lithium-ion batteries than pure SnO_2[[137], [79], [148]].

Nearly stoichiometric tungsten trioxide $WO_{3\text{-x}}$ is a TMO suitable for electrochromic devices [22], gas sensing [119] and HER catalysis [100]. Furthermore, the insertion of this TMO in a carbon matrix enhances its catalytic performance. For example Wu et al. [134] and Chen et al. [11] have synthetized composites of carbon fibers and tungsten oxide by preoxidizing and carbonizing a polymer matrix with embedded tungsten particle precursors. Both composites exhibit good HER performance, which the authors associate with the reduction of WO_3 by carbon during the carbonization step generating oxygen vacancies. However, the synthesis of these composites is difficult to control and reproduce. Local chemical vapor deposition (LCVD) of TMOs on suspended carbon nanowires is explained in this chapter to learn how to design, fabricate and test novel TMO compositions on carbon fibers. The fabrication of these test structures includes the steps described above: first, near-field electrospinning is used to suspend an SU-8 precursor fiber on a photopatterned SU-8 scaffold; pyrolysis of the SU-8 yields a monolithic carbon structure including a GCW of known diameter and length suspended on a glassy carbon (GC) scaffold with excellent ohmic contact. The well-defined geometry and transport properties of the GCW make it possible to accurately control its temperature profile by Joule heating, which in turn enables LCVD of TMOs. Joule heating has been used in the past to change the microstructure of the suspended carbon wires [71], to weld fibers [140], and to fabricate nanogaps [115].Glassy carbon is an ideal substrate for TMOs due to its low chemical reactivity and high thermal stability: glassy carbon is a low reactive carbon allotrope [59] [61] which does not graphitize even at very high temperatures (e.g. 2500ºC) [77]. As a demonstration for the utility, in this chapter the local chemical vapor deposition of $WO_{3\text{-x}}$ on a suspended GCW by controlled Joule heating is described bellow.

5.2 Experimental Methods

Figure 5.4 illustrates the fabrications steps for suspending a GCW on a glassy carbon scaffold, and depositing a layer of WO_3 on its surface by LCVD. Sections 5.2.1-5.2.2 describe the preparation of the sample, the annealing of the glassy carbon, the measurement of the GCW's temperature coefficient of resistance, and the deposition of the tungsten oxide. The scaffold design, shown in Figure B.1 in the appendix, is lithographically patterned from SU-8 2025 on a silicon wafer with a 1 μm thick thermal oxide layer [33][32] Next, near-field electrospinning in contact-jet mode [14] is used to suspend an SU-8 2002 based polymer fiber on the desired section of the scaffold Figure 5.4.a. Upon carbonization, the scaffold and suspended wire become a monolithic glassy carbon structure Figure 5.4.b. The carbonization is carried out in a nitrogen atmosphere, using a heating ramp from room temperature to 300 °C of 4 °C/min, followed by a one-hour halt at 300 °C, a second heat ramp up to 900 °C of 10 °C/min, and a final halt of one hour. The space between the walls of the scaffold fixes the length of the GCW, which is accurately determined by photolithography.

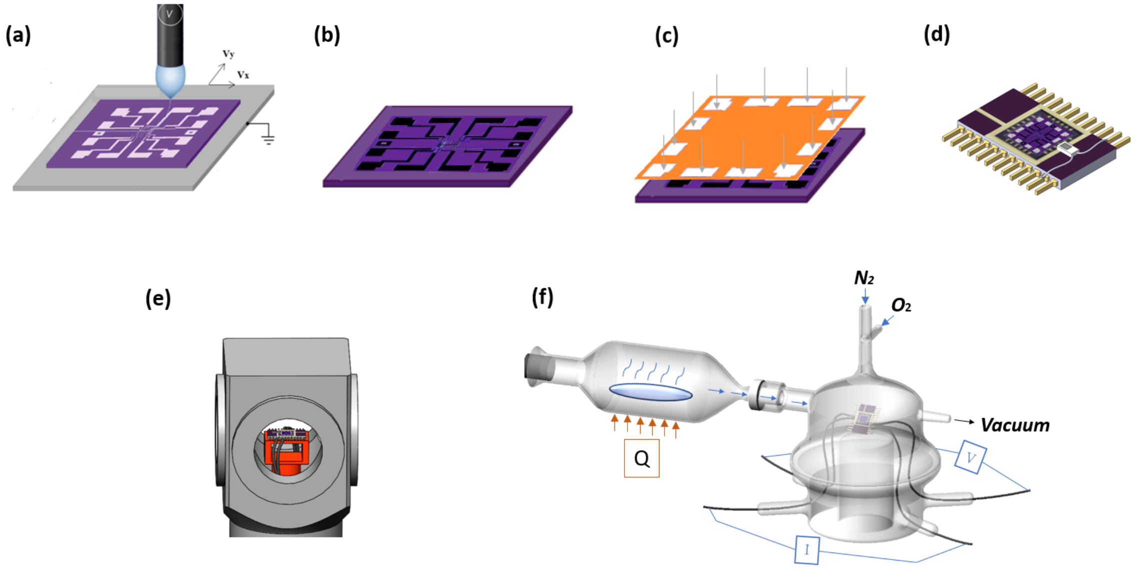

Figure 5.4: Figure 1. Schematics of the microfabrication steps for performing LCVD on a suspended GCW: (a) deposition of a polymer fiber on a SU-8 patterned scaffold using near-field electrospinning; (b) pyrolyzed carbon monolithic structure with suspended GCWs; (c) e-beam deposition of silver pads for electrical contacts; (d) integration of the carbon monolith in a ceramic package including an RTD sensor; (e) annealing and measurement of the temperature coefficient of resistance of the GCW; (f) LCVD of WO$_3$-x on GCW.

On the other hand, although progress has been made on the understanding of near-field electrospinning [14], the diameter of the deposited fiber cannot be accurately predetermined. In our set up we can obtain GCWs with diameters between 200nm and 3 μm. Based on our experience we choose the polymer blend solution and operational parameters such as the emitter voltage and the collector speed to aim at a fiber diameter, but we do not have the control or reproducibility to accurately predetermine it. Furthermore the dimensions of the GCW are different from those of the deposited fiber due to the loss of non carbon atoms during the pyrolysis. The shrinkage of SU-8 photolithography structures during carbonization is well known and reported in the literature [101], and the change in dimensions can be predicted accurately. The dimensions of the suspended GCW are accurately determined with a SEM. We select GCWs with diameters near one micron to simplify their characterization. The final glassy carbon structure on the SiO_2/Si substrate is mounted on a ceramic package and wire-bonded to the package's gold contact pins Figure 5.4.d. To ensure good electrical connections with the gold pins a 500 nm thick layer of silver is deposited by e-beam evaporation on selected areas of the carbon structure Figure 5.4.c. The silver contact pads are deposited using a stencil copper mask fabricated with dry film lithography [55] [87].

5.2.1 Annealing and measurement of the temperature coefficient of resistance

In order to perform localized chemical vapor deposition it is paramount to have a detailed knowledge of the temperature dependence of the resistivity of the GCW. Furthermore, this dependence must not change significantly as the GCW is heated both when measuring its temperature coefficient of resistance (TCR), and when performing LCVD. To avoid this unwanted variation of the TCR, caused by changes in the microstructure of the glassy carbon during heating [118], the GCW must be annealed to minimize those changes. The annealing is carried out for 6 hours at 370ºC in a vacuum furnace, JANIS VPF-800 Figure 5.4.e. Afterwards, we measure the electrical resistance R at different sample temperatures to compute the TCR of the GCW:

$$TCR = \frac{1}{R_0}\frac{dR}{dT} \tag{5.1}$$

where R_0 is the resistance at the reference temperature T_0, set at 295 K. The temperature dependence of the resistance $R(T)$ of the annealed GCW is characterized by measuring its current vs. voltage $I(V)$ response, using a 4-probe configuration in a current driven setup to avoid the influence of contact resistances [132] [88].The current, kept very low to avoid significant Joule heating, is injected with a Keithley 6221 current source and the resulting voltage difference across the GCW is measured with a precision Keysight 34465A multimeter. The sample is placed inside a vacuum chamber with a base temperature adjusted with a Lake Shore 330 temperature controller, and the temperature of the sample itself is measured with a platinum resistance temperature detector (RTD) attached to the sample with thermal paste. The $R(T)$ characteristic of the GCW in the temperature range of interest is nearly linear and has a negative slope, which is used to compute a single value of the TCR, equation (1), for the temperature range within which LCVD is performed.

5.2.2 Localized Chemical Vapor Deposition

The sample is placed inside a custom glass reactor with four sealed electrical outlets and connected in a 4-probe configuration to avoid contact resistances Figure 5.4.f. The reactor is divided into the actual CVD chamber (700ml), and a pre-heating chamber (435 ml) containing the precursor solution and equipped with a flexible heater. The precursor consists of a solution of $W(CO)_6$ in Acetone/DMF (1:1) and is heated at reduced pressure, leading to its evaporation and transport to the CVD chamber. With the precursor flowing into the CVD chamber, an increasing voltage (V_D)is applied to the sample using the 4-probe configuration as shown in schematic Figure 5.5.

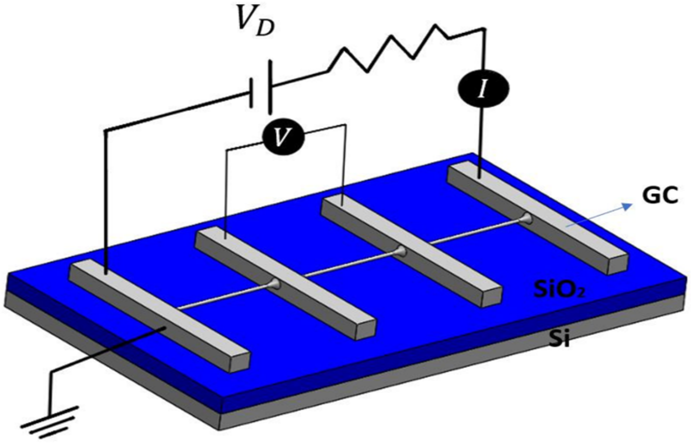

Figure 5.5: Schematics of the 4-probe voltage driven set-up used to perform LCVD. The current and voltage at the terminals of the GCW are measured to obtain its resistance.

The current and voltage at the terminals of the GCW are measured to compute its resistance and to estimate the average temperature increase with respect to T_0 using the TCR value:

$$\Delta T_{avg} \cong \frac{\Delta R}{TCRR_0} \tag{5.2}$$

5.3 Results and discussion

5.3.1 Process parameters required for LCVD of WO3-x

We have deposited tungsten oxide coatings on suspended GCWs with thicknesses ranging from 70 nm to 1.4 μm. The LCVD process conditions studied include the CVD chamber pressure, the pre-chamber temperature, and the molarity of the precursor solution. Optimal conditions for the reactor include a chamber pressure of 60 mbar, a pre-chamber temperature of 90 ºC, and a saturated $W(CO)_6$ solution. The decomposition and oxidation of $W(CO)_6$ to $WO_{3\text{-}x}$ at low pressures is well known [18][78]. Both molecular oxygen in the gas phase and the evaporated acetone [104] used as solvent for the precursor contribute to the oxidation of $W(CO)_6$to $WO_{3\text{-}x}$. Coatings of $WO_{3\text{-}x}$ were obtained at chamber pressures as high as 160 mbar as long as the O_2 partial pressure remains sufficiently low to avoid oxidizing the GCW during Joule heating. At chamber pressures above 160 mbar oxidation of the GCW leading to its thinning and even complete burning was observed as shown in Figure 5.7. Lower pre-chamber temperatures do not produce a sufficient vapor flux from the solution, while higher pre-chamber temperatures result in evaporation rates too fast to enable controlled LCVD.

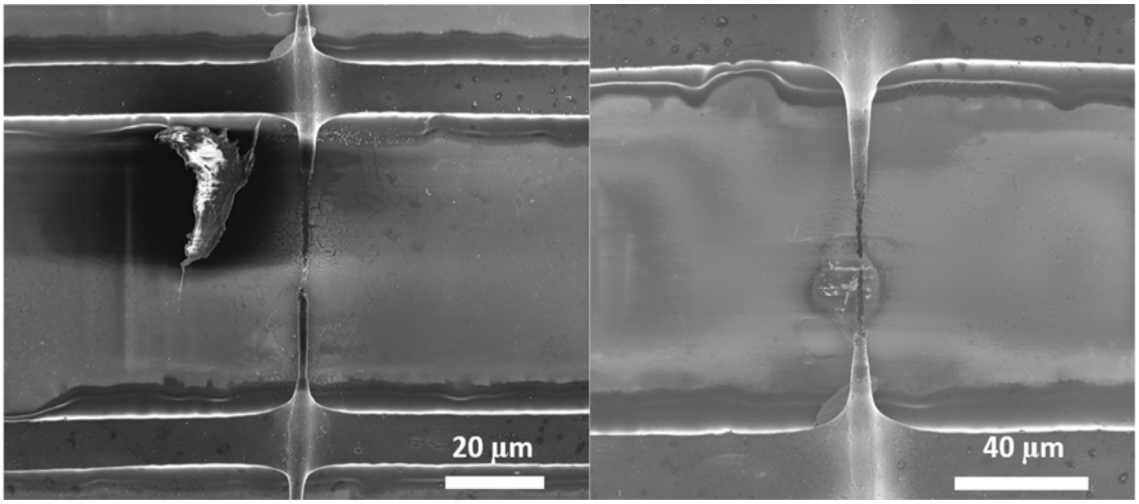

Figure 5.6: GCWs after LCVD process at pressures above 160 mbar. The GCW appears burnt or thinned

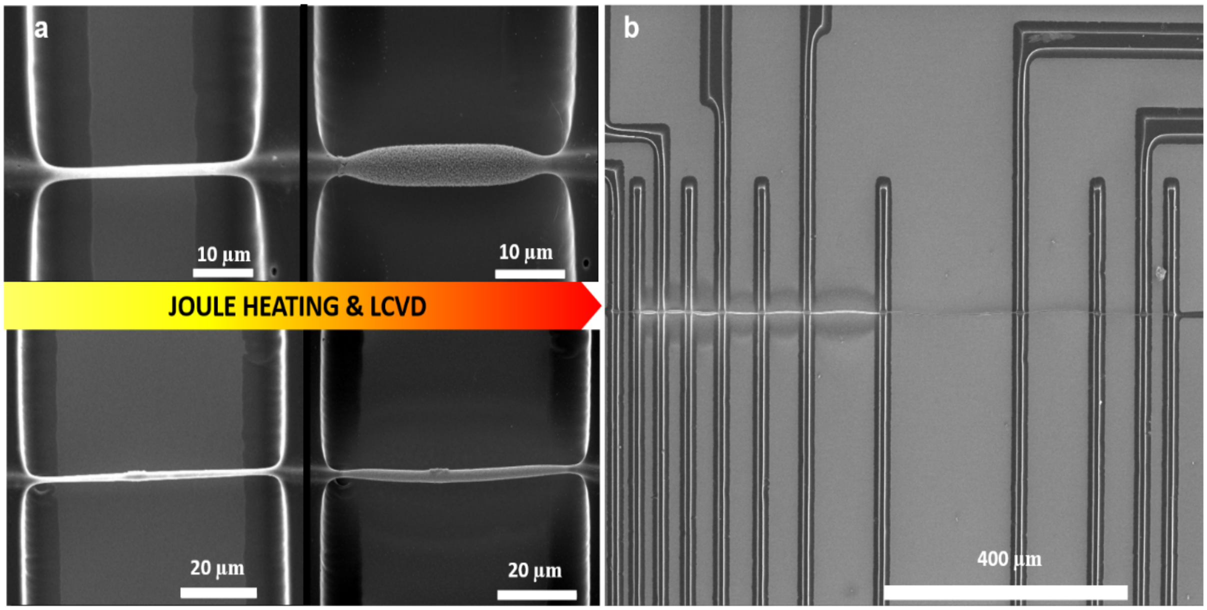

Figure 5.7: a) SEM pictures of suspended GCWs before and after the LCVD process; b) overview of multiple fibers suspended from scaffolds, illustrating how they can be locally coated (bright fibers) or left uncoated (darker fibers) without contaminating the carbon scaffold.

Figure 5.7a. shows two suspended GCWs with different lengths and diameters, before and after LCVD. The formation of the WO_{3-x} coating is restricted to the length of the GCW and does not extend to either the glassy carbon scaffold or the SiO_2 surface of the substrate. Note also the different thicknesses of the coatings. Figure 5.7b. shows how in the same chip can be coated with different thicknesses, while other fibers remain uncoated. The scaffold connections and the resulting independent control of the current injected through each fiber make this possible.

5.3.2 coating formation and temperature profiles

In Figure 5.8 we show the voltage vs. current characteristics of several GCWs labeled A to F, during the deposition of $WO_{3\text{-x}}$, as well as SEM images of the final state of the GCWs. The $V(I)$ curves reflect the LCVD process path, and also depend on the geometry of the glassy carbon wire. The different$V(I)$ curves are chosen to illustrate the different stages of the coating process. In the actual experiments we recorded and analyzed these paths to understand how the deposition takes place. Note also that the control variable in the experiments is the voltage V_D driving the 4-point configuration , while the resulting values of V and$I$ plotted in Figure 5.8 are defined at the terminals of the GCW of interest (i.e. a section of the glassy carbon wire limited by two consecutive walls of the scaffold). The diameter, the length, the resistance at room temperature and the TCR of each GCW are given in Table 1. The $V(I)$ curve for fiber A illustrates a typical LCVD experiment: at first, an increase in Iresults in an almost linear increase of V, with only a slight deviation from linearity due to Joule heating and the negative value of the TCR. The quasi linear $V(I)$ trend then transitions into a plateau around the point $\{1.46$ mA, 1.64 V$\}$. Joule heating at this point raises the temperature at the middle of the GCW to the value required to initiate the deposition of $WO_{3\text{-x}}$. The flattening of the $V(I)$ curve indicates that the deposition of $WO_{3\text{-x}}$ decreases the overall resistance of the suspended wire. Since the deposition is progressing from the middle of the GCW towards its contacts with the scaffold, this indicates that the equivalent resistivity of the coated section must be lower than the resistivity of the uncoated GCW. The SEM image of the final state of the sample shows a thick coating covering fiber A, which is uniform in diameter except for a progressive thinning near the contacts. The $V(I)$ curve for fiber B is similar up to the start of the plateau, at which point the voltage V_D driving the 4-point configuration is kept constant. This results in a decrease of the voltage V across the fiber, and a slight increase of I. The SEM image of the sample B shows a very thin coating only in the middle of the fiber. The $V(I)$ curve for fiber C is carried out slightly differently: once the plateau is reached, instead of fixing $V_D$we increase its value by 1.1 V. The start of the plateau is discernable in this case, resulting in a thin coating slightly thicker than for fiber B, but which neither extends to the contacts with the scaffold. The $V(I)$ curve for fiber D is similar to that of fiber A (initial quasi linear ramp followed by and extended plateau) and produces a relatively thick coating that extends to near the contacts. The resistance at room temperature of fiber D is significantly higher than those of fibers A, B and C, the slope of its $V(I)$ curve is accordingly larger, and the increased Joule dissipation ($\sim RI^2$) requires a lower current to reach the critical temperature needed for CVD. The $V(I)$ curve for fiber E extends to form a broad plateau, but at the current value of 1.92 mA it starts increasing to later decrease again, at which point the experiment was terminated. The SEM image of this sample reveals a thick coating that also covers the contacts with the scaffold. Finally, the $V(I)$ curve for fiber F (which has the highest R_0) features the typical initial quasilinear ramp, an extended plateau, a second linear increase, and a final erratic decrease. The SEM image of this fiber shows a thick coating extending all the way to the contacts with the scaffold, and the disappearance of the coating at several points as locally the temperature becomes high enough to melt the coating. The end of the plateau coincides with the coating of the fiber reaching the contacts, at which point the coated fiber behaves like a single resistor (V and I are proportional with a significant positive slope).

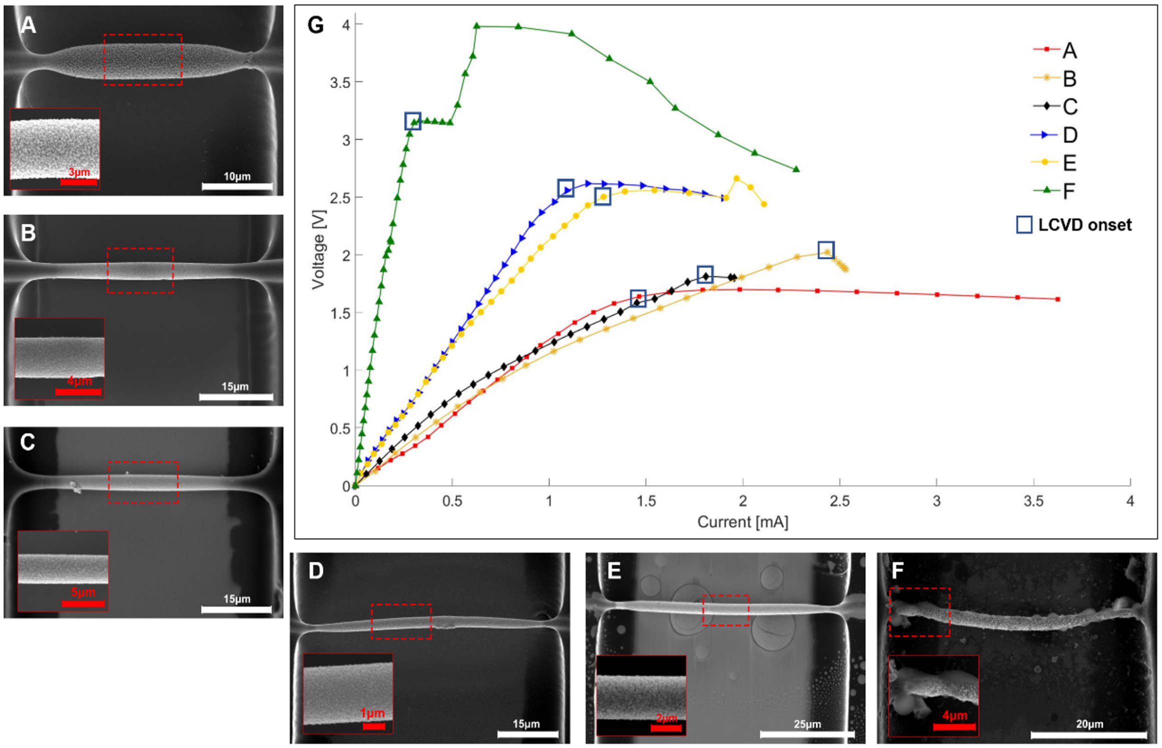

Figure 5.8: a) SEM pictures of suspended GCWs before and after the LCVD process; b) overview of multiple fibers suspended from scaffolds, illustrating how they can be locally coated (bright fibers) or left uncoated (darker fibers) without contaminating the carbon scaffold.

	GCW A	GCW B	GCW C	GCW D	GCW E	GCW F
Diameter (μm)	1.27	2.95	1.39	1.83	1.66	0.78
Length (μm)	31.37	46.16	50.16	60.33	63.75	52.382
$R_0(\Omega)$	1273	1387	1718	3422	3475	13472.57
$TCR(K^{-1})$	0.0013	0.00052	0.00055	0.00094	0.00106	0.00053
Coating thickness (μm)	1.42	0.07	0.12	0.29	0.48	-
$R_{after}(\Omega)$	4697	2192	-	5442	-	-

Table 5.1: Values of the diameter, length, resistance at room temperature R_0 and TCR of different GCWs before WO_{3-x} deposition, together with the coating thickness and resistance at room temperature after deposition.

Since the temperature profile is a most critical parameter in the LCVD of $WO_{3\text{-x}}$, knowledge of the temperature profile along the suspended fiber is needed to understand the deposition process including the $V(I)$ curves in Figure 5.8. The temperature profile $T(x)$ can be estimated with the following one-dimensional equation and boundary conditions:

$$\frac{d^2T}{dx^2}+\frac{I^2R_o^{'}}{\kappa A}\left[1+TCR(T-T_o)\right]=0 \qquad \frac{dT}{dx}_{x=0}=0, \qquad (L/2)=T_o \tag{5.3}$$

In this model the GCW has a constant cross section A, length L, and a resistance per unit length $R_o^{'}$ at room temperature T_o. I is the electrical current flowing through the fiber. For simplicity we assume constant thermal conductivity κ and TCR; see Ferrer-Argemi et al. [33] for a more accurate GCW thermal model that retains the temperature dependence of these parameters. Equation 5.3 represents the balance between heat conduction and Joule heating: convection is negligible at the reduced pressure of the reactor, while radiation can be neglected at the temperatures typical of the LCVD process. We set the origin of the axial coordinate at the middle of the GCW (symmetry requires a zero heat flux at this point), while its ends remain at room temperature (in the actual configuration the scaffold acts as a thermal bath). The analysis is simplified by rewriting these equations in dimensionless form using the dimensionless temperature $\theta=(T-T_o)/T_o$ and the dimensionless coordinate $\tilde{x}=x/L$:

$$\frac{d^2\theta}{d\tilde{x}^2}+\Pi^2(1+T_oTCR\theta)=0 \qquad \left.\frac{d\theta}{d\tilde{x}}\right|_{\tilde{x}=0}=0 \qquad \theta\left(1/2\right)=0 \tag{5.4}$$

These equations show that the $\theta(\tilde{x})$ profile is just a function of the dimensionless number $\Pi=\sqrt{\frac{I^2R_o^{'}L^2}{\kappa AT_o}}$ and the product T_oTCR. The solution is

$$\theta\left(\tilde{x}\right)=\frac{1+e^{\sqrt{-T_oTCR}\Pi}-e^{\frac{1}{2}(1-2x)\sqrt{-T_oTCR}\Pi}-e^{\frac{1}{2}(1+2x)\sqrt{-T_oTCR}\Pi}}{\left(1+e^{\sqrt{-T_oTCR}\Pi}\right)(-T_oTCR)} \tag{5.5}$$

which has the following maximum at the middle of the GCW:

$$\theta_{\max}=\frac{\left(-1+e^{\frac{1}{2}\sqrt{-T_oTCR}\Pi}\right)^2}{\left(1+e^{\sqrt{-T_oTCR}\Pi}\right)(-T_oTCR)} \tag{5.6}$$

Figure 5.9 three temperature profiles obtained from with this model are illustrated. Curve 1 is the solution for $\Pi = 5.68$and $T_oTCR = -0.387$, i.e. for fiber A in Table 1 at the onset of LCVD, $I = 1.46mA$; we use $\kappa = 7$ to take into account the elevated temperature of the GCW. The profile is monotonic and has a maximum at its center with a value of $\theta_{\max} = 1.73$ or equivalently $T_{\max} = 539^oC$, which is within the range of the deposition temperatures for $WO_{3\text{-}x}$ [18][78]. If this maximum temperature is near the critical value triggering chemical vapor deposition, only as small section of the GCW around the midpoint will be coated with $WO_{3\text{-}x}$. Furthermore, from the description of Figure 5.8, we know that at the deposition temperature the central section of the GCW coated with $WO_{3\text{-}x}$ has a lower linear resistance than the uncoated fiber. The lower resistivity of the coated section reduces Joule heating in this area ($\sim I^2R$), lowering the temperature profile at fixed Π and quenching the deposition. This scenario is readily verified by modifying Equation 5.4 to account for the change in the linear resistance between the coated and non-coated sections:

$$\frac{d^2\theta}{d\tilde{x}^2}+\Pi^2\frac{R_o^{'}\left(\tilde{x}\right)}{R_o^{'}}(1+T_oTCR(\tilde{x})\theta)=0 \tag{5.7}$$

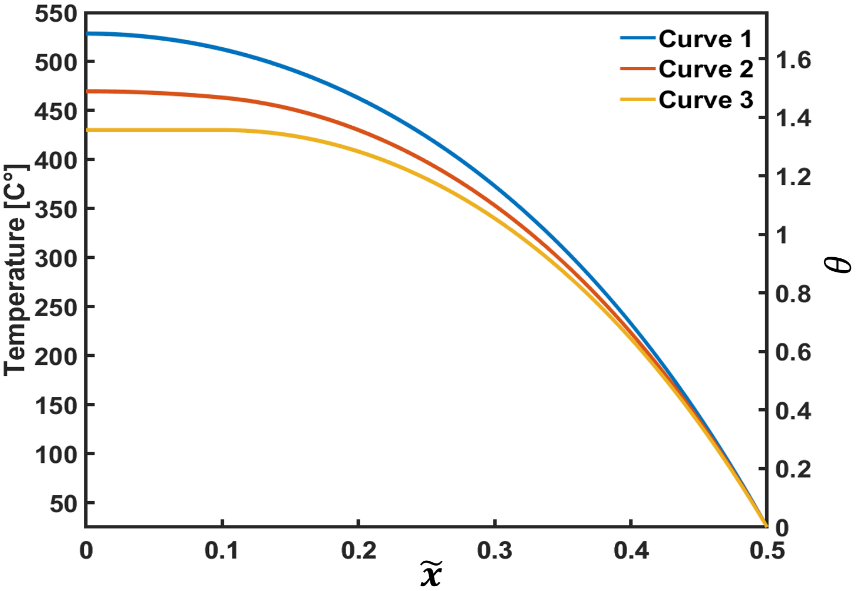

Figure 5.9: Temperatures profiles along the GCW, equation (7), for and , and different lengths of the coating : Curve 1 is for an uncoated GCW; Curve 2 is for a GCW with a coated section having a resistivity one third of the original GCW and extending 20% of the GCW length; Curve 3 is for a coated section with negligible resistivity and extending 20%.

Curve 2 in Figure 5.9 is the solution of this equation for $\Pi = 5.68$,$T_o TCR = -0.387$ and a coated section with one third of the resistivity of the original GCW extending over 20% of the GCW length. This temperature profile is always lower than Curve 1, the temperature profile for the uncoated GCW heated up by the same current. Curve 2 also has a maximum temperature at the center with values $\theta_{\max} = 1.53$ and $T_{\max} = 481^o C$. Curve 3 is for a coating with the same length in the limiting case of zero resistivity, and $\Pi = 5.68$, $T_o TCR = -0.387$. The temperature profile is flat in the coated region because of the absence of Joule heating in this section, and is lower than both Curves 1 and 2. Given that the deposition of $WO_{3\text{-x}}$ quenches the LCVD at constant Π (i.e. at constant current for a fixed GCW geometry), extending the coating towards the ends of the GCW requires a continuous increase of Π or, equivalently, of the current injected through the fiber. This model also explains the plateaus in the $V(I)$ curves shown in Figure 5.9: when the resistivity of the coated section is much smaller than that of the original GCW, the temperature profile in the coated region is flat and decreases monotonically in the non-coated section (see Figure 5.9, Curve 3). The profile in the non-coated section during further deposition is then the solution of Equation 5.4 with the origin of the coordinates shifted to the interface between coated and non-coated sections, and with the length of the non-coated section L_{nc} now playing the role of characteristic length, $\Pi = \sqrt{\frac{I^2 R_o' L_{nc}^2}{\kappa A T_o}}$. When the current injected through the GCW is increased slowly the interface between the coated and non-coated sections shifts towards the ends of the GCW at constant maximum temperature (due to the self-quenching character of the deposition), and therefore at constant Π, Equation 5.6. The voltage V across the GCW is the voltage drop along the non-coated section (the resistance of the coated section is comparatively small), and therefore proportional to $L_{nc}I$. Since Π is constant during deposition, $L_{nc}I$ and V must be constant as well, i.e. the deposition proceeds at constant voltage difference across the GCW.

The coating thickness increases with the ratio between the current passing through the GCW and the onset value I_{on} needed to start the deposition. For example, the ratio $D_c/D_o = 3.24$ between the diameters of the coated (D_c) and uncoated fiber (D_o) in Figure 3.A is obtained with a current ratio $I/I_{on} = 2.48$. The same values for Figure 5.8.B, Figure 5.8.C, and Figure 5.8.D are $D_c/D_o = \{1.04, 1.09, 1.32\}$, and $I/I_{on} = \{1.04, 1.17, 1.74\}$. We show in Figure 5.10 the profiles of the coated fibers A and B.

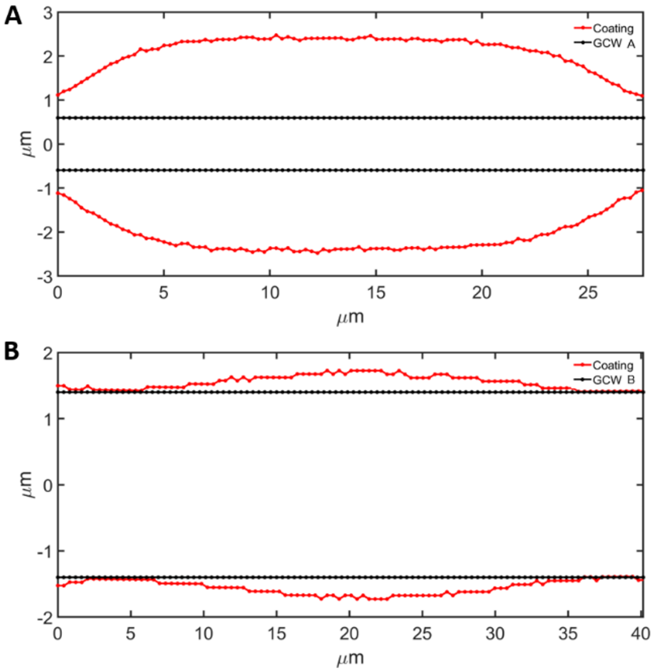

Figure 5.10: Profiles of the A and B GCWs (black), together with their profiles after deposition of $WO_{3\text{-x}}$ (red).

When the fiber is coated up to the contacts with the scaffold (e.g. fiber A), the thickness of the coating is uniform along most of its length, and decreases smoothly near the contacts. Furthermore, we observe that at very high values of I/I_{on} the coating may melt, and/or the scaffold area near the fiber may become hot enough to induce LCVD on the scaffold like shown in Figure 5.11 The foregoing experiments and analysis demonstrate that there is a one-to-one correspondence between the current passed through the GCW and the state of the coating for a given GCW and conditions in the CVD chamber. Therefore the current can be used to control the deposition. However, at this point we cannot determine a priori the value of the current that will produce a prescribed coating state for any GCW in general. To do this we would need to have a better deposition model. An alternative for producing a prescribed coating would be to monitor the coating and actuate the current until the desired coating is obtained.

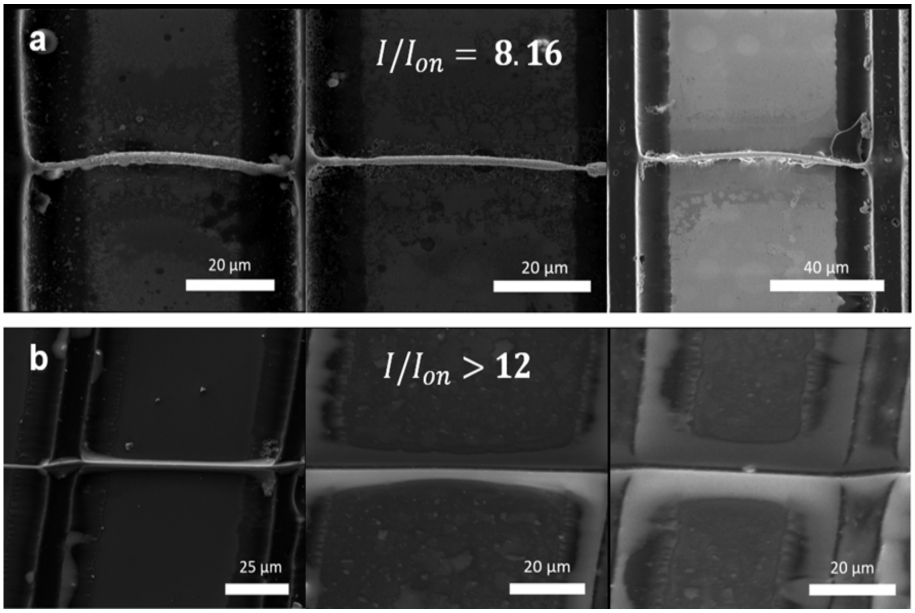

Figure 5.11: Local coating melting at high values of I/I_{on} during LCVD. In a) the coating has melted at some points along the fiver, while in b) the GCW appears stripped of coating which, after melting, has deposited in surrounding areas

5.3.3 Sample Characterization

The geometry and the Raman spectra of the GCW and the WO_{3-x} coating are measured before and after LCVD with a FEI MAGELLAN 400 XHR scanning electron microscope (SEM) and an InVia Confocal Raman Microscope respectively. In addition, cross sections of the coated GCW are characterized with SEM-EDX and a JEOL 2800 transmission electron microscope (TEM) to obtain elemental maps and the atomic arrangement. The cross-sections are cut with a FEI Quanta 3D SEM/FIB (focused ion beam) following a procedure detailed shown in Figure 5.12. Figure 5.12.a-d. shows SEM images of the steps to obtain the cross-sectional cuts of a coated GCW. Prior to making cross-sectional cuts of the GCWs, a protective Pt coating was deposited, first with the electron beam to minimize Ga+ ion implantation, then with the ion beam to preserve the structure during thinning of the GCW cross-section for TEM analysis. The FIB cuts were positioned far from the inspection point to prevent any ion-beam induced structural changes in the GCW. The cut GCWs were then mounted on a TEM grid and SEM-EDX was used to collect chemical maps on the cross-

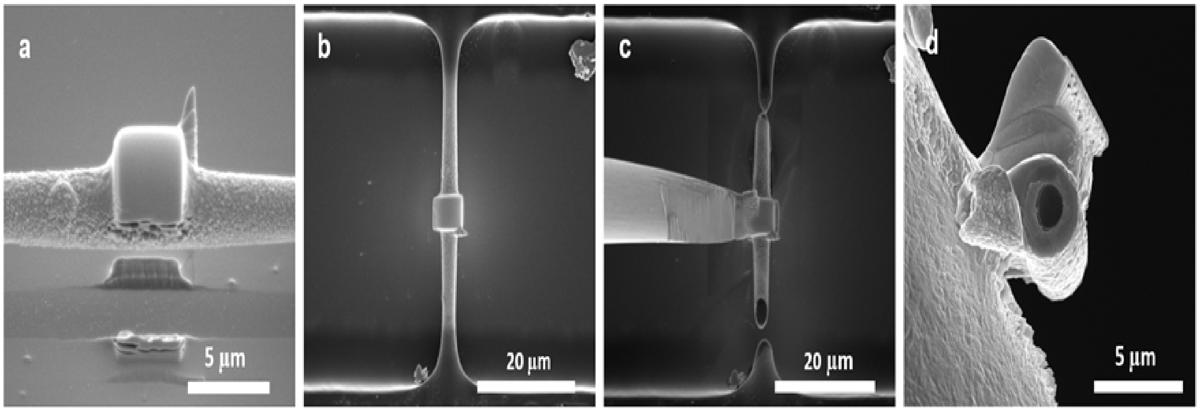

Figure 5.12: Procedure for making cross-sectional cuts of coated GCWs. a-b) A protective Pt layer is deposited with the electron/ion beam. c) The fiber is attached to an omniprobe and cut on either end to free it from the scaffold. d) The fiber is transferred to a TEM grid and the cross section is polished by ion beam to smooth the surface observation.

sections using a FEI Magellan 400 XHR SEM. The GCW cross-sections were then thinned to electron transparency (< 100 nm) with a final 5 kV polish to remove the ion-beam induced damage layer. The thinned cross-section was analyzed by bright-field TEM (BF-TEM), high-resolution TEM (HR-TEM), scanning TEM - secondary electron imaging (STEM-SEI), and selected-area electron diffraction (SAED) in a JEOL 2800 TEM at 200 kV.

The Raman spectroscopy is performed with a 532 nm excitation wavelength that is appropriate for both glassy carbon and WO_{3-x}, an 0.5% laser intensity and an exposure time of 5 seconds to avoid inducing microstructural changes in the sample [130]

Figure 5.13.a and Figure 5.13.b show SEM pictures of the surfaces of two WO_{3-x} coatings, which are formed by agglomerated nanoparticles of uniform size. Figure 5.13c-f show the cross-section of a GCW with a coating thickness of 1.05 μm and EDX elemental mappings. The SEM image Figure 5.13c shows a clear distinction between the glassy carbon core and the surrounding WO_{3-x} coating. The elemental mappings show a core of carbon matching the section of the GCW, while the surrounding area of the coating is composed of oxygen and tungsten proving the coating to be in the form of a tungsten oxide. The Quantitative

analysis of the elements at the mapping sections performed with EDX and its statistical error is shown in Table 2. Quantitative analysis in EDX is only used as an estimation due the error of quantification of light elements such oxygen, but the atomic % obtained suggest the formation of WO_{3-x} with an x value close to 0.25. This could be due oxygen vacancies or due the formation of a very thin interlayer of WC as is explained in the TEM results below. More details of the atomic quantification and the EDX spectrum are shown in the Figure S3 and table S1 in supplementary material.

Figure 5.13.g and Figure 5.13.h show Raman spectra of a non-coated GCW and a coated one respectively. The non-coated GCW shows the characteristic spectrum of glassy carbon with two Gaussian peaks associated with small graphite crystallites without long range translation symmetry (D band, 1300 - 1400 cm^{-1}), and in plane displacement of the carbons in the hexagonal sheets (G band, 1560-1610 cm^{-1}); the measured intensity ratio $I_D/I_G = 1.04$ is typical of glassy carbon [32].The spectrum for the GCW coated with WO_{3-x} shows two clear Raman shifts at 803.3 and 704.5 cm^{-1} that can be assigned to the O-W-O stretching modes, while 327.5 and 263.5 cm^{-1} correspond to the O-W-O bending mode [17]. The two peaks at 185.2 and 128.9 cm^{-1} correspond to the lattice mode [124]. This spectrum also features a very low intensity peak at 981.3 cm^{-1} corresponding to the stretching mode of the W=O bond typical of hydrated tungsten trioxide crystals[17], and which has also been observed in samples calcinated between 400 and 500 ^{o}C[128]. The lower peaks at 1350 and 1607.5 $cm^{-1}$are produced by the GCW substrate.

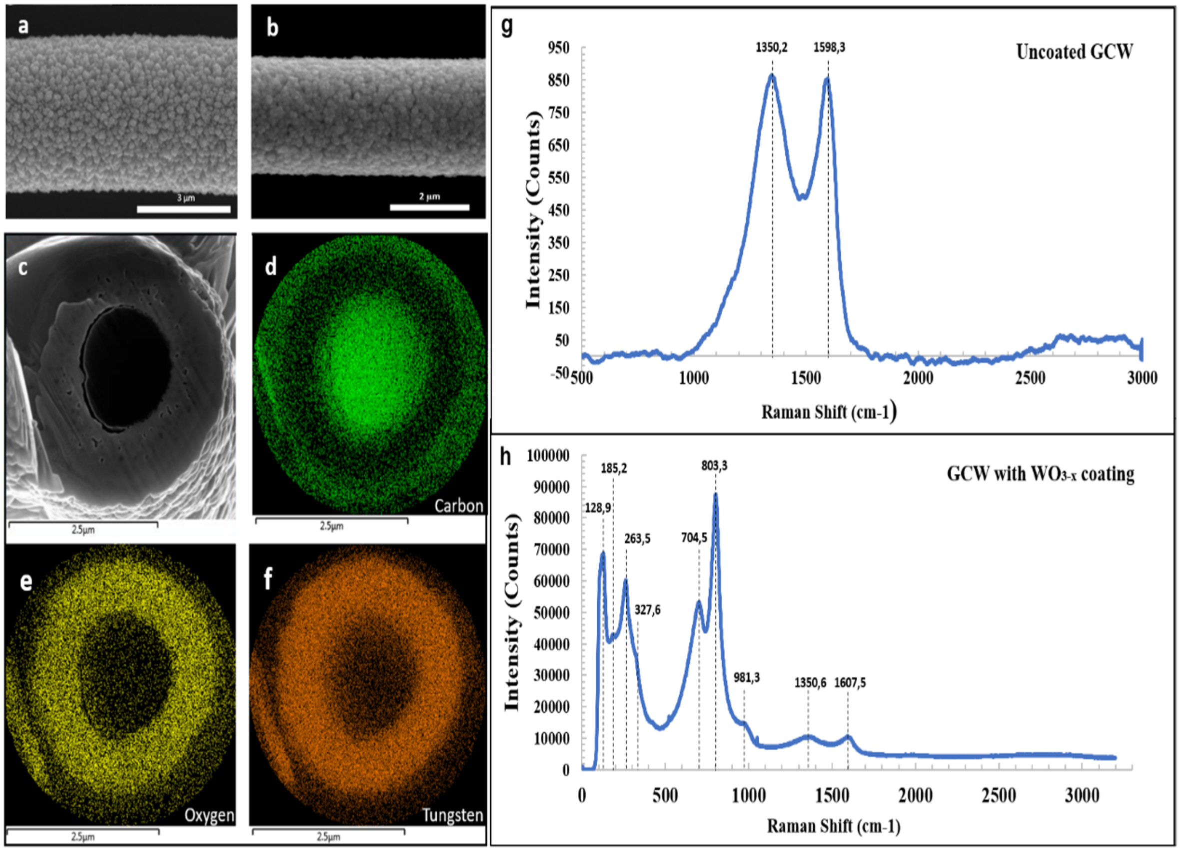

Figure 5.13: a & b) SEM images of the surface microstructure of typical coatings; c) SEM image of the cross section of a coated GCW; d-f) EDX elemental mappings of carbon, oxygen and tungsten of the cross section in c); g) Raman spectrum of an uncoated GCW; h) Raman spectrum of a GCW coated with $WO_{3\text{-x}}$.

Map Sum Spectrum	Line Type	Apparent Concentration	Weight %	σ(Weight %)	Atomic %
Carbon	K series	0.61	28.64	0.18	66.95
Oxygen	K series	0.81	13.82	0.12	24.26
Tungsten	M series	1.95	57.54	0.21	8.79
Total			100		100

Table 5.2: Information of the parameters used in the qualitative analysis performed by EDX and the Weight %, statistical error (σ) and Atomic%.

The TEM data presented in Figure 5.14 reveals the detailed microstructure of the cross section of a coated GCW, taken from a point near the midsection of the wire. The bright-field TEM image in Figure 5.14.a shows that the coating has a polycrystalline structure with an increasing crystallite size and density approaching the outer layer of the coating. The uniform contrast of the wire core indicates that it likely has the expected amorphous structure, which is confirmed in Figure 5.14.f with high-resolution TEM (HR-TEM) and selected-area electron diffraction (SAED). The transition from the amorphous GC to the crystalline WO_{3-x} is captured in Figure 5.14.b with a high magnification view of the region outlined in Figure 5.14.a. The 50nm GCW-WO_{3-x} interface displays nanoscale crystallites which become larger and more interconnected through the thickness of the interface away from the core. The dispersed bright regions in the coating indicate the presence of porosity. The Scanning TEM- secondary electron image (STEM-SEI) of the coating in Figure 5.14c is used to confirm that these regions are in fact voids rather than additional GC regions. HR-TEM images of the outer portion of the coating, the interface, and the amorphous GC are presented in Figure 5.14.d-Figure 5.14.f respectively. The SAED patterns displayed in the insets are taken from identically sized areas centered on the region presented in the corresponding HR-TEM image. The HR-TEM images of the coating regions in Figure 5.14.d and Figure 5.14.e shows lattice fringes and their corresponding SAED spot patterns confirm the polycrystalline nature of these regions. The measurements of the d-spacings from the SAED pattern in Figure 5.14.d for the bulk of the coating are shown in Figure 5.15 and correlate well with the monoclinic WO_{3-x}.Some d-spacing seem to be associated with the presence of $WO_{2.72}$(JCPDS Card No.732177)[124] and a few outliers may imply the presence of a third phase. Finally, HR-TEM of the GC core in Figure 5.14.f shows the characteristic tight fragments of curved carbon sheets formed by hexagonal and non hexagonal carbon rings [59][61], and the diffuse intensity of the SAED pattern also confirms the amorphous structure of this region.

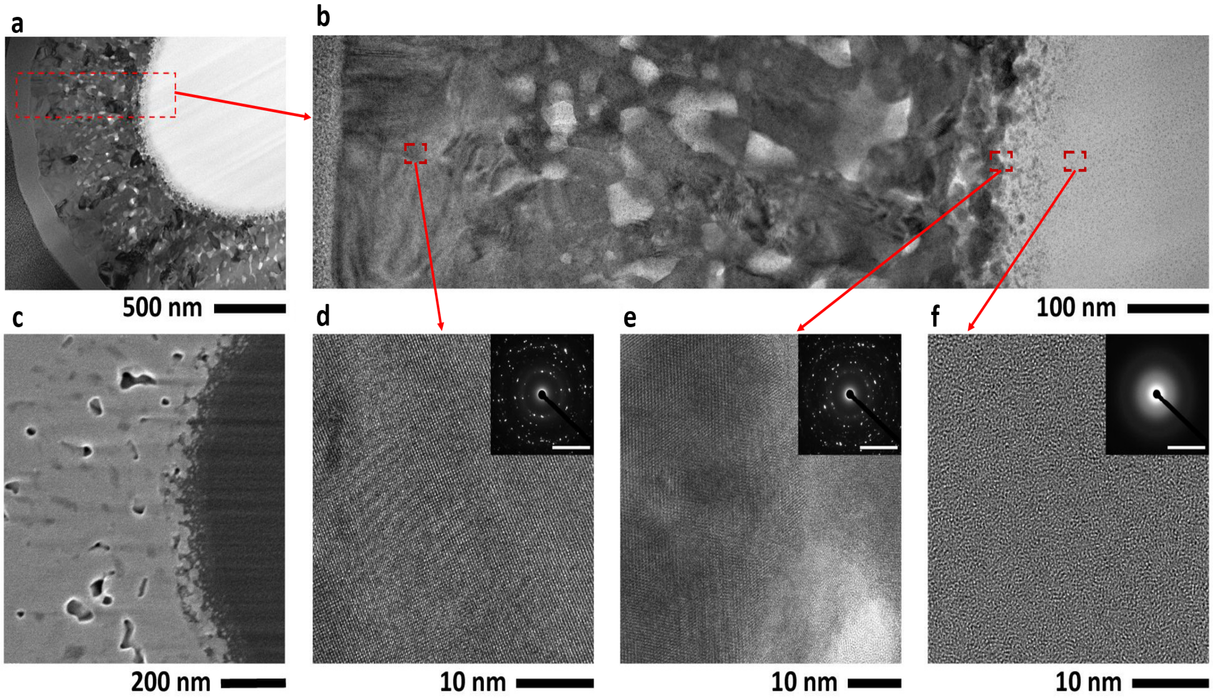

Figure 5.14: a) bright-field TEM image showing the polycrystalline tungsten oxide coating surrounding the amorphous carbon wire; b) magnified image of the area outlined in a); c) dark-field TEM image of the coating, interface and GCW showing isolated voids in the coating; d-f) HR-TEM images of the bulk of the coating, interface and amorphous GCW core.

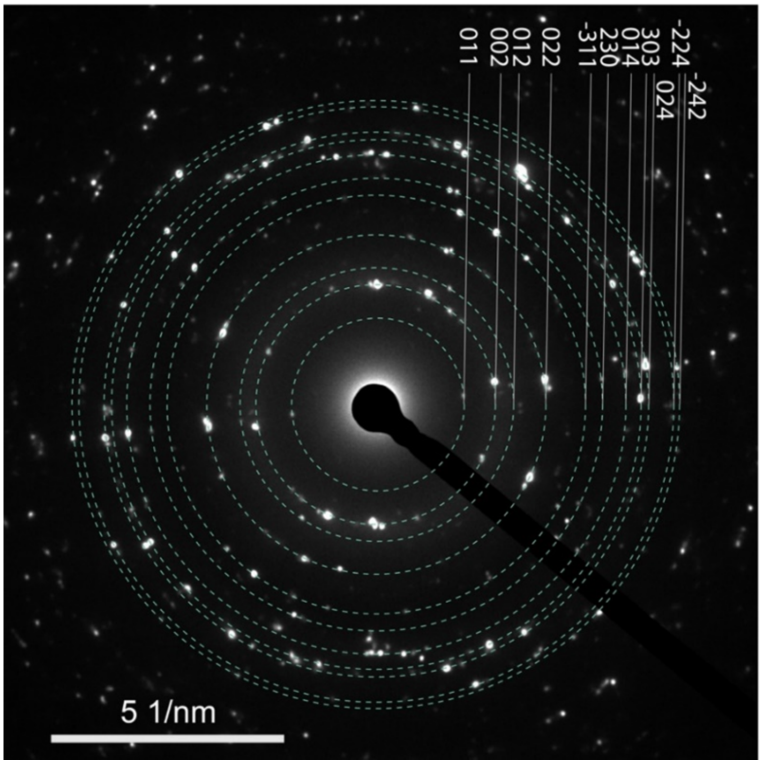

Figure 5.15: Indexed selected-area electron diffraction (SAED) pattern of the tungsten oxide coating (SAED pattern in Figure 5.14.d The dominant phase is monoclinic WO_3 (JCPDS Card No. 830951), based on the best match for the atomic plane d-spacings in combination with the corresponding plane Miller indixes shown in Table B.2 in Apendix XX

Figure 5.16 includes HR-TEM images of the bulk of the coating and the interface with the GCW, together with the measurement of lattice spacings. The measured spacing value of 0.38 nm and of 0.37 nm in the bulk of the coating correspond to $WO_{3\text{-x}}$ in the (002) and (002) plane (JCPDS Card No.830951)[124]. Furthermore, these lattice spacings remain constant everywhere in Figure 5.16a. In the interface, Figure 5.16b, although the atomic arrangement is crystalline everywhere except for the GC amorphous phase in the bottom right corner, we measure a variety of lattice spacings, as illustrated by the value of 0.44 nm in Figure 5.16c. We associate this non uniformity to a variation of the stoichiometry of the tungsten oxide, with a decrease in the concentration of oxygen closer to the GC core. Finally, closer to the amorphous GC core but still in the crystalline phase, Figure 5.16d, we observe a layer with a lattice spacing of 0.28 nm, a value reported for WC (JCPDS Card No.510939)[58]. The reduction of WO_{3-x} to WC is thermodynamically favored in the presence of carbon at low oxygen pressures[102][110] We think that as the coating thickness increases, the access of oxidizing agents to the coating-GCW interface decreases, promoting the reduction of WO_{3-x} by carbon from the GCW. This reduction of the oxide suggests that the stoichiometry of the WO_{3-x} coating can be controlled in our system by annealing the GCW and its coating in either vacuum or an oxygen-rich atmosphere.

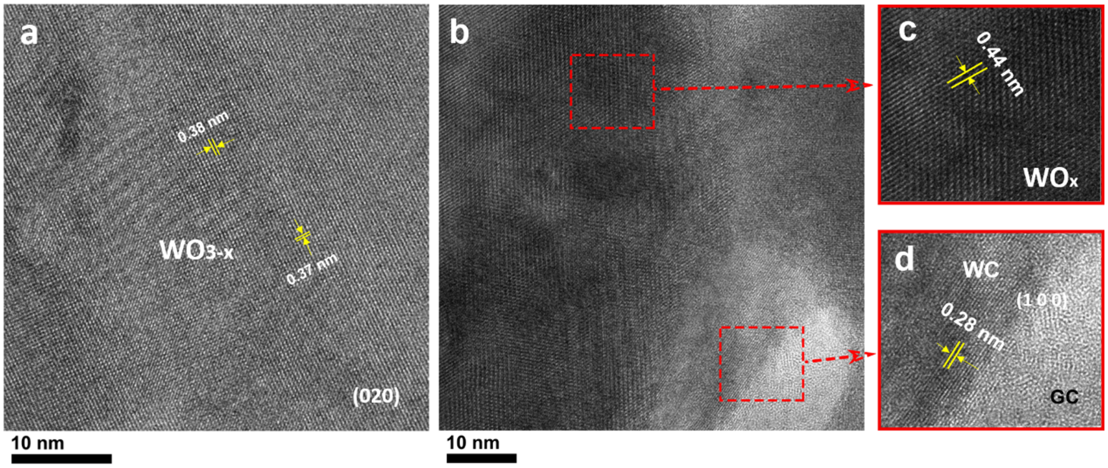

Figure 5.16: HR-TEM images with measurements of lattice spacings. a) Bulk of the WO_{3-x} phase; b) interface between coating and GCW; c) detail of the crystalline phase in the interface, away from the GCW; d) detail of the crystalline phase in the interface, near the GCW

The following steps would be to test applications of the coated GCWs. However, its parabolical coating geometry and the low surface for catalysis applications limit its use. An effort to scale up the process in a more extensive carbon fiber array would significantly increase its application outcomes.

Chapter 6

CVD farfield electrospinning

6.1 Introduction

The goal of the present chapter is to investigate whether the use of Joule heating to render these functional isolated carbon fibers can be extended to produce larger scale materials such as mats of carbon nanofibers, and eventually lead to an useful self-assembly manufacturing technique with high resolution at the nanoscale level. In particular, this chapter describes the deposition of WO_{3-x} on carbon nanofiber mats, created by far field electrospinning. WO_{3-x} deposition is studied again due its catalytic performance when combined with carbon nanofibers. These composites have previously been produced by hydrothermal methods and through the carbonization of a polymer matrix with embedded tungsten particle precursors. Both methods are difficult to reproduce and control[11, 138]. In the present manufacturing method Joule heating is again central to the process expecting to achieve a better coating uniformity in a large scale material than the one shown in chapter 5. The carbon nanofiber mats were fully characterized before and after the CVD process, and IR-Thermography was used to characterize the temperature field during Joule heating. The dominance of heat radiation over thermal conduction leads to uniform temperature fields on the mat, making it an ideal large-scale substrate that can be activated with layers of metal oxides and other coatings for different applications.

6.2 Experimental Methods

6.2.1 Sample preparation

Polyacrylonitrile (PAN) nanofibers are produced by electrospinning 1 ml of a 8% PAN/dimethylformamide solution. A grounded drum rotating at 500 rpm and facing the emitter is used to collect the fibers, ensuring sample uniformity in thickness and density. The resulting PAN nanofiber mats are first stabilized in air at 270 ºC for 6 hours[143], and then carbonized in a nitrogen atmosphere with the temperature ramp shown in Figure S1 (1000 ºC maximum temperature). The thickness of the resulting mats is typically 30 ± 3 µm, and the diameter of the carbon nanofibers range from 80 to 120 nm. The mats are then cut into rectangular samples, connected to copper leads with silver paste, and mounted on an acrylic structure to avoid mechanical stress when manipulating the sample as shown in Fig. 6.1.a. Figures 6.1.b and 6.1.c show SEM images of the carbon nanofiber mat after pyrolysis, illustrating the uniformity in density and diameter of the carbon nanofibers. The absence of beads in the fibers is typical of optimum far-field electrospinning.

6.2.2 IR Thermography

We do IR-Thermography of the samples before coating them to obtain a calibration curve of the sample temperature as a function of the electric power dissipated by the mat. The dissipated power is simply $P = IV$, where the voltage difference V between the electrodes

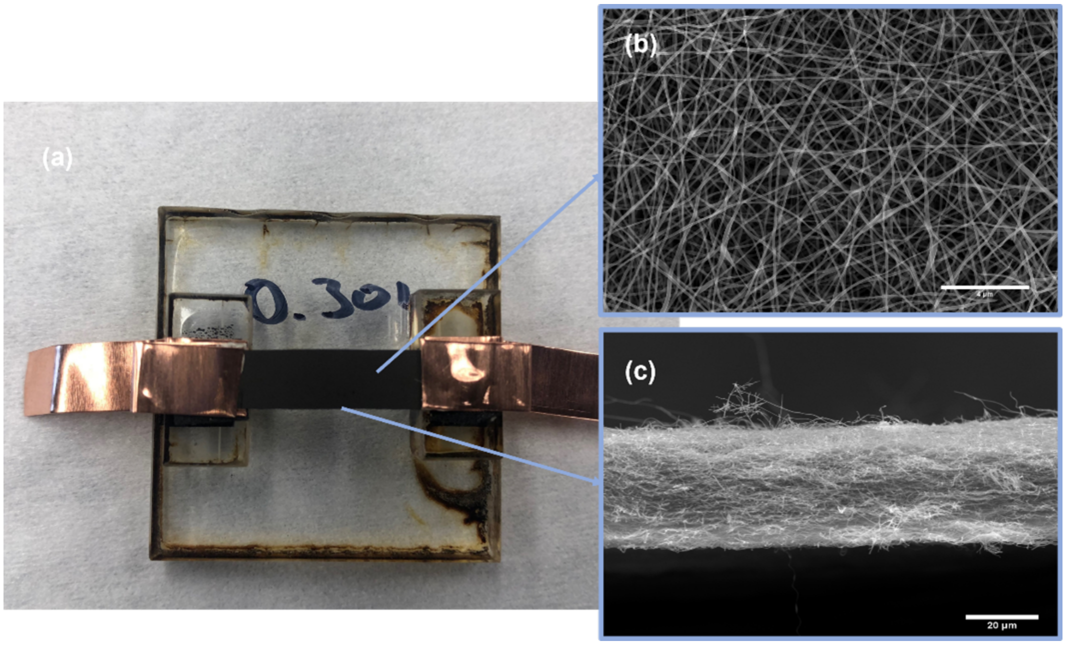

Figure 6.1: a) carbon nanofiber mat with rectangular shape connected to copper connections; b) SEM image of the carbon nanofiber mat; c) SEM image of the cross-section of the mat.

and the current I passed through are easily controlled and measured. The ability to impose a known temperature is key for CVD. The IR-Thermography is done in a vacuum chamber JANIS VPF- 800 with electrical connections and ZnSe windows for optimal imaging. The background pressure is maintained below 10^{-5} Torr with an Edwards T-station 75 turbopump. Thermograms of the carbon nanofiber mats are taken with an IR camera (FLIR A655sc-7 LWIR Science-Grade) while imposing a voltage difference between the copper electrodes and measuring the current passing through. In this way the temperature field on the mat is measured as function of the known Joule heating. The parameters inputted on the IR camera are the distance between the sample and the camera, the estimated emissivity of the material, the relative humidity and the atmospheric temperature[76]. The emissivity ε of the carbon surface was obtained by placing side by side a carbon nanofiber mat and a tape of known emissivity, on a surface of known temperature (see Figure S2), and executing an IR-Thermography calibration. The calibration yielded an average value $\varepsilon = 0.86$ with a standard deviation of 0.01.

6.2.3 Localized Chemical Vapor Deposition of WO_{3-x}

The CVD process is done inside a custom glass reactor with four electrical feedthroughs for powering the sample and induce Joule heating[13]. The reactor is divided into the actual CVD chamber (700ml) containing the carbon nanofibers mat sample , and a pre-heating chamber (435 ml) containing the precursor solution and equipped with a flexible heater. The precursor consists of a solution of $W(CO)_6$ in Acetone/DMF (1:1) which is heated at reduced pressure, leading to its evaporation in the pre-chamber and diffusion to the main CVD chamber. With the precursor diffusing into the CVD chamber, a voltage ramp is applied to the sample using a 4-probe configuration. The current and voltage at the terminals of the copper connections are measured to compute its resistance. Further details on the CVD process can be found in Ref. [13].

6.2.4 Sample Characterization

The surfaces of the carbon nanofiber mats were analyzed before and after the CVD process with a FEI MAGELLAN 400 XHR scanning electron microscope (SEM). SEM-Energy Dispersive X-Ray Analysis(EDX) is used to obtain elemental maps of the samples. Raman spectroscopy is done in carbon nanofiber mats without coating and with different coating thickness using an Invia Confocal Raman Microscope, to analyze both the degree of graphitization of the carbon nanofiber and the coating obtained after CVD. Raman spectroscopy is performed with a 532 nm excitation wavelength, appropriate for both pyrolytic carbon and WO3-x, 0.5% laser intensity and an exposure time of 5 seconds to avoid inducing microstructural changes in the sample. X-ray photoelectron spectroscopy (Kratos AXIS-SUPRA surface analysis instrument) was used to analyze the atomic composition of the CVD coatings.

6.3 Results and discussion

6.3.1 Thermal characterization of the pyrolyzed mats

Figure 6.2.a shows the temperature map of a mat measured with the IR camera, resulting from Joule heating when a voltage difference of 6.6 V is applied across the electrodes (P =0.594 W). The width, length and thickness of the mat are 15.9 and 7.8 mm, and 29 μm respectively. Postprocessing of the temperature map yields an average temperature of 513 K and a standard deviation of 20.7 K (see Figure S3). Figure 6.2.b shows the current passed through the mat and the dissipated power as a function of the imposed voltage difference. The current is not proportional to the voltage because the resistance of the carbon mat exhibits a significance dependence on temperature. Figure 6.2.c shows the average temperature as a function of the power dissipated in the mat, featuring a scaling $T \propto P^{1/4}$ that will be justified later in this section. Although the resistance of the mat at room temperature depends on its geometry, the experimental characterization shows that the relationship between average temperature and power density is independent of the aspect ratio of the rectangular mats. Figure 6.2.d shows the resistance of the mat as a function of the average temperature . The decreasing resistance at increasing temperature is a well-known property of carbon-based materials[7].

The self-heating of the mat and the resulting temperature field can be understood with a simple thermal model. Since the thickness of the mat is approximately uniform and much smaller than either its length or width, we consider a rectangular two-dimensional mat. A balance of heat conduction, radiation and ohmic generation yields the temperature equation

$$\frac{P}{W} = \frac{\dot{q}_{rad}}{\Delta z} - k\left(\frac{\partial^2 T}{\partial x^2} + \frac{\partial^2 T}{\partial y^2}\right) \tag{6.1}$$

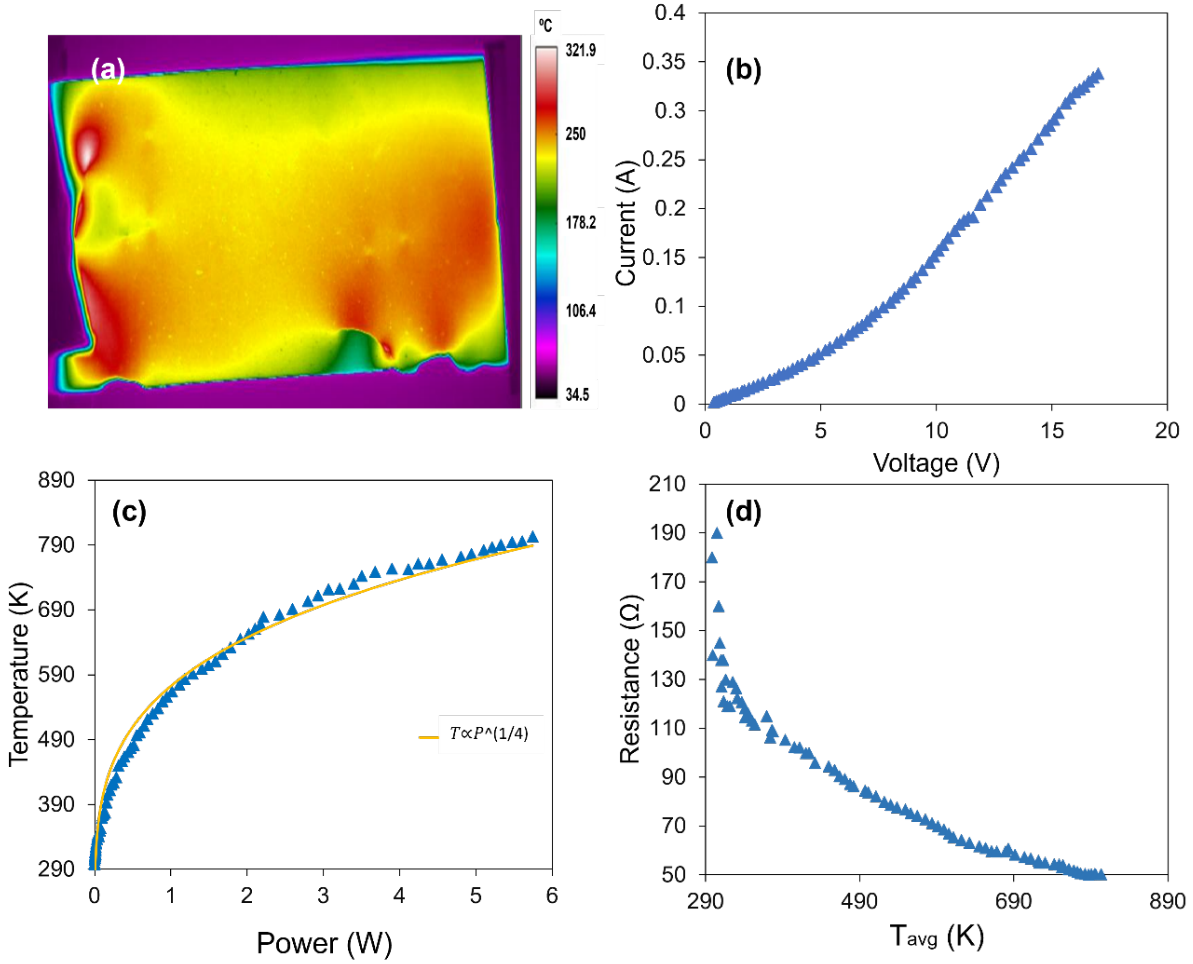

Figure 6.2: a) IR-Thermogram of the carbon nanofiber mat during the voltage ramp at an applied voltage of 6.6 V; b) $I(V)$ curve during Joule heating; c) average temperature of the mat computed from the IR-thermogram as a function of dissipated electric power; d) resistance of carbon mat as a function of average temperature.

with coordinates x and y aligned with the length and width of the mat respectively. P is the total ohmic power dissipated into the mat, W is the mat volume, Δz is the mat thickness and $\dot{q}_{rad}$ is the heat flux due to radiation. The mat radiates heat from both sides, and $\dot{q}_{rad}$ is given by

$$\dot{q}_{rad} = 2\varepsilon\sigma\left(T^4 - T_o^4\right), \tag{6.2}$$

where ε is the carbon nanofiber mat emissivity , σ is the Stefan-Boltzmann constant, and

T_o is the temperature of the surrounding chamber. Equation (6.1) requires appropriate boundary conditions. On the symmetry axes $x = L_x/2$ and $y = L_y/2$ the heat flux must be zero

$$\left.\frac{\partial T}{\partial x}\right|_{L_x/2,y} = \left.\frac{\partial T}{\partial y}\right|_{x,L_y/2} = 0. \tag{6.3}$$

The mat is clamped to a copper foil at $x = 0$. Due to the high electrical conductivity of copper dissipation is negligible. Furthermore we assume that the temperature in the electrode follows a linear profile between room temperature and the temperature of the mat at the interface, $T(0, y)$. The heat flux at the interface with the mat is then

$$k\left.\frac{\partial T}{\partial x}\right|_{0,y} = \frac{k_{Cu}}{L_{Cu}}\left(T(0,y) - T_o\right), \tag{6.4}$$

where k_{Cu} and L_{Cu} are the copper conductivity and the length of the electrode . At the non-clamped side of the mat, $y = 0$, the radiated heat is balanced by thermal conduction:

$$k\left.\frac{\partial T}{\partial y}\right|_{x,0} = \varepsilon\sigma\left(T(x,0)^4 - T_o^4\right). \tag{6.5}$$

Equation (6.1) and the boundary conditions (6.3)-(6.5) are discretized along the x and y coordinates to produce a system of algebraic and non-linear equations, which we solve using the Newton method. Figure S4 shows the flow diagram of the algorithm for solving the model equations. Once the temperature field is computed, the average temperature of the mat is readily obtained by integrating the field:

$$T_{avg} = \frac{4}{L_x L_y}\int_0^{L_y/2}\int_0^{L_x/2} T(x,y)dxdy. \tag{6.6}$$

Figure 6.3 shows several IR thermograms taken at different values of Joule heating (left inset in each figure), together with the associated temperature fields computed with the continuum thermal model (right inset), for two different carbon nanofiber mats: Sample 1, characterized in Fig. 6.3.a, has length and width of 15.9 and 6.6 mm, while Sample 2 in Fig. 6.3.b is 15.4x7.8 mm. The average temperatures are shown on the top of each map. The thermograms exhibit small temperature gradient, likely associated with variations in the thickness of the mat and other inhomogeneities resulting from the fabrication process. For all power levels the average temperatures obtained with IR thermography agree well with the average temperatures derived from the model. Note also that, similarly to the thermograms, the temperature fields computed with the model are homogeneous throughout most of the mat: temperature variations are always negligible along the y coordinate, and are only important along the x coordinate in a narrow section near the interface with the copper electrodes. The experimental and numerical results in Fig. 6.3 show that the temperature

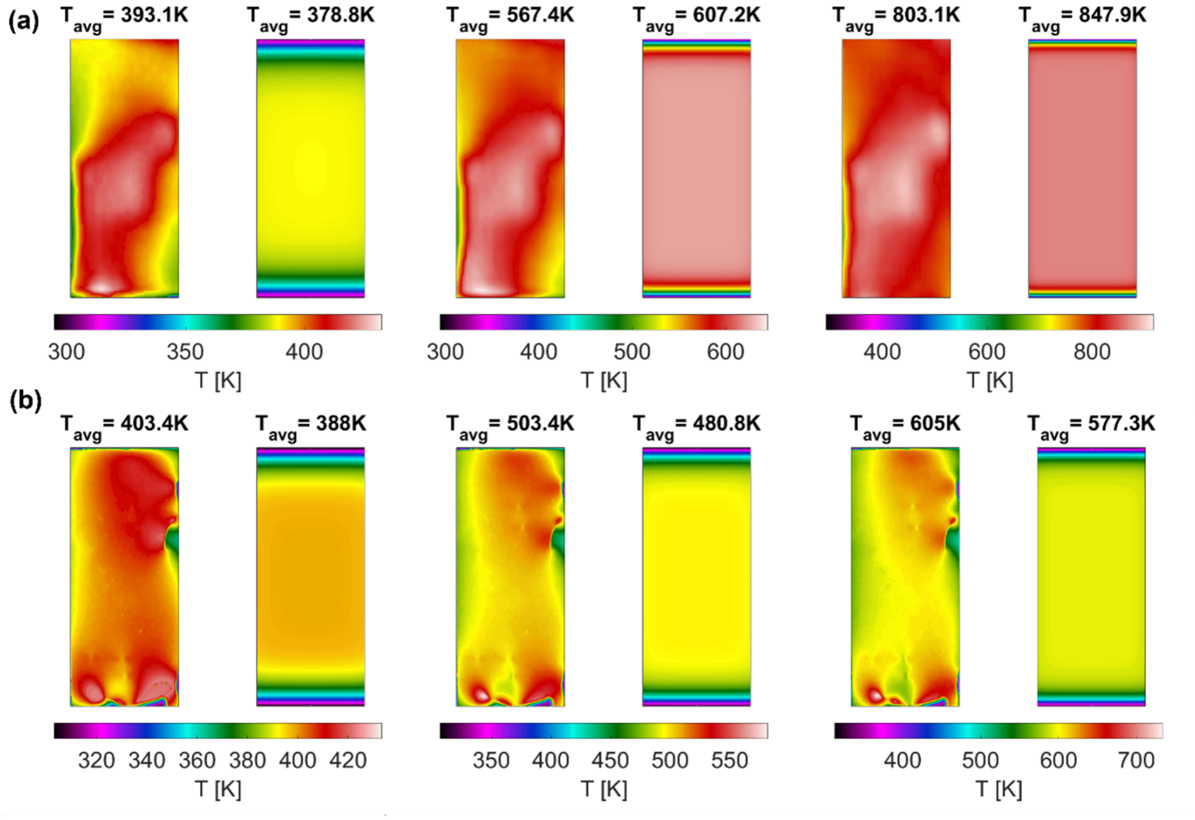

Figure 6.3: Comparison between measured (left) and computed (right) temperature fields for different values of the dissipated electric power, for two different carbon nanofiber mats a) and b)

field in the mat is relatively uniform, suggesting the dominance of radiation over thermal conduction in Eq. (6.1). In fact, the ratio between the two terms is of the order of the dimensionless number $\frac{k\Delta z}{2\varepsilon\sigma T_{avg}^3 L_x^2}$ which, for the mat characterized in Fig. 6.3, is already smaller than 0.01 at mat temperatures exceeding 400 K. In the limit of negligible conduction, Eq. (6.1) becomes a trivial balance yielding a mat temperature

$$T_{avg} = \left(\frac{P}{2S\varepsilon\sigma} + T_o^4\right)^{1/4}, \tag{6.7}$$

where S is the area of the mat. This result explains the correlation between temperature and Joule heating observed in Fig. 6.2.c, as well as the independency between the temperature vs. power density relationship and the aspect ratio of the mat.

Figure 6.4 compares the average temperature computed with the IR-thermograms with the two model predictions , equations (6.6) and (6.7), for the two carbon nanofiber mats characterized in Fig. 6.3. The average temperatures are plotted as a function of the power density. Sample 1 was characterized up to 610K, while Sample 2 was characterized at temperatures up to 803K. Both models are in good agreement with the temperature measurements. Figure 6.4 suggests that the model is slightly overestimating the radiative heat losses at low temperatures ($T < 600$ K), and underestimating heat losses in the electrode at high temperatures ($T > 600$ K, radiation from the electrode could start being significant they are not included by the model).

6.3.2 Joule heating-assisted CVD

In order to promote CVD of WO_x on the carbon fibers, the sample is introduced in the CVD chamber and heated by passing a current through (Joule heating). The temperature of the

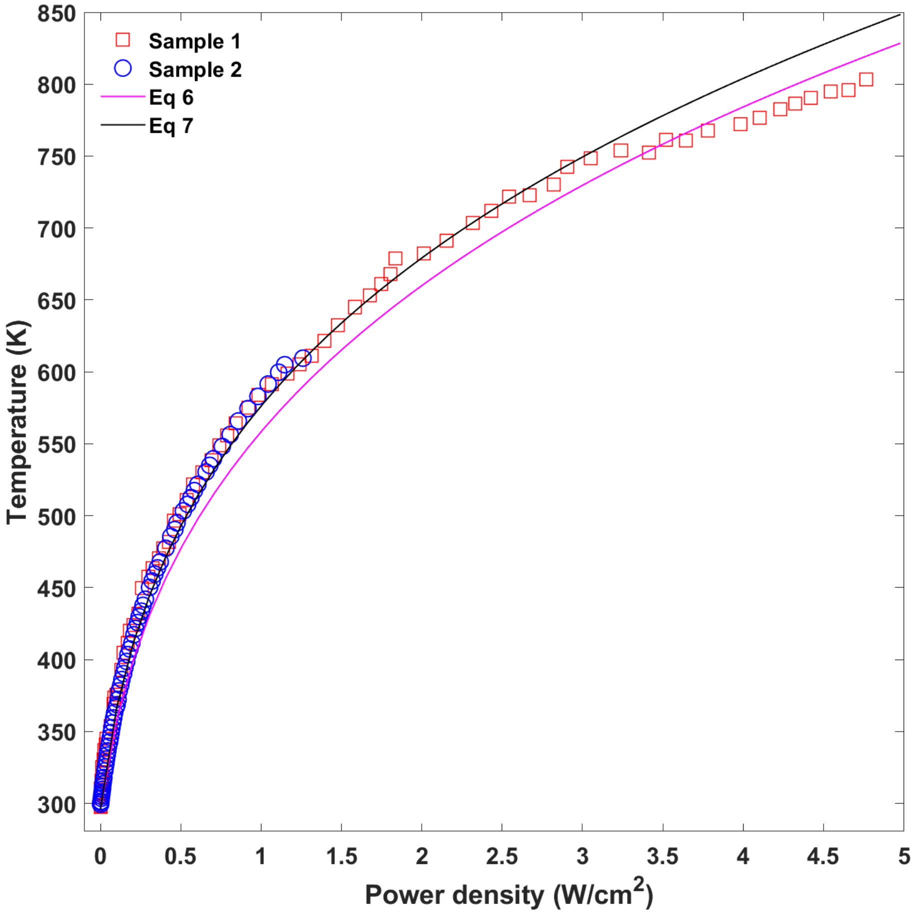

Figure 6.4: Average temperature vs dissipated power density for two mats with different areas. Comparison between measured and computed average temperatures.

deposition surface, a key parameter in CVD, is precisely controlled through the electric power dissipated and a calibration curve such as the one in Fig. 6.4. Figure 6.5.a is a schematic of the deposition process: the decomposition of the $W(CO)_6$ precursor is triggered on the surface of each carbon nanofiber when its temperature reaches a precise value, and a coating of WO_x grows around the nanofiber as the conditions are maintained. The evaporated acetone used as solvent in the precursor solution and molecular oxygen present in the chamber contribute to the formation of WO_{3-x}[127]. Figures 6.5.b and 6.5.c show SEM pictures of the carbon nanofibers, before and after CVD.

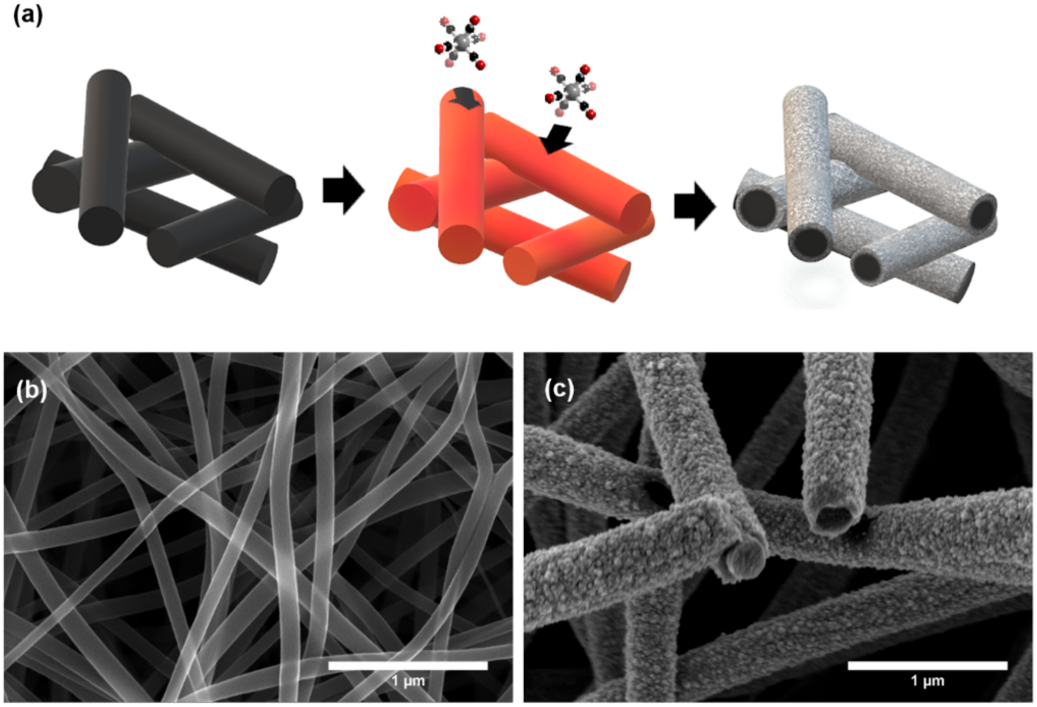

Figure 6.5: (a) Schematics of the process steps to obtain uniformly WO3-x coated carbon nanofibers by joule heating. (b) SEM pictures of carbon nanofiber matrix before and (c) after the WO3-x deposition by joule-heating.

The presence of a coating in all nanofibers in Fig. 6.5.c is evident; the cross sections of the coating and the nanofiber are visible in a fiber displayed near the center of this figure. Figure 6.6.a shows a typical $I(V)$ curve employed to promote CVD. The start of the deposition is identified as a small discontinuity in the $I(V)$ trend at $V = 5.96$ volts.[13] The power density at this point is 0.663 W/cm^2, and the associated mat temperature is 529 K. This value of the temperature is within the range reported for the deposition of WO_{3-x} from $W(CO)_6$.[126] The carbon nanofibers of the mat associated with Figure 6.6 (a) were characterized with an SEM. Figures 6.6 (b) and (c) show the surfaces of the nanofibers before the CVD process and right after CVD starts. While the original surfaces have a smooth and homogeneous appearance, the nanofibers resulting from light CVD contain bright nanoparticles sparsely distributed. The start of the deposition is characterized by the seeding of WO_{3-x} nanoparticles on the carbon nanofibers that will act as nucleation points of the coating that forms as the voltage and Joule heating are increased to continue the CVD process.

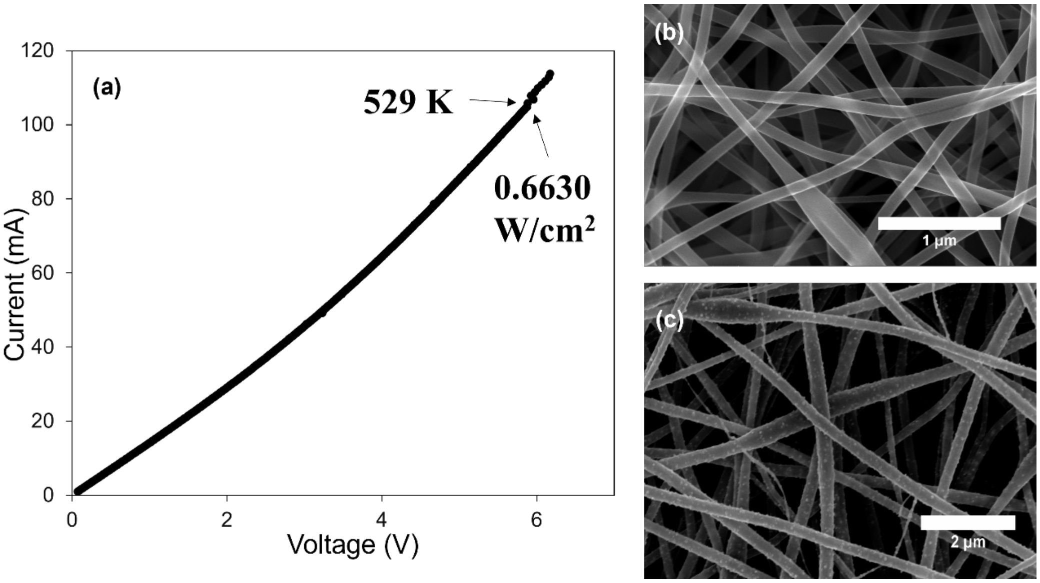

Figure 6.6: a) $I(V)$ curve of a carbon nanofiber mat during Joule heating, signaling the start of CVD; b) SEM pictures of the carbon nanofibers right before the onset of CVD; c) image of the nanofibers right after the onset of CVD.

Figure 6.7.a shows $I(V)$ curves for 5 samples, including 3 different mats sizes (16x10 mm, 25x6 mm and 25x4 mm). The voltage difference applied and the Joule heating are increased beyond the minimum value triggering CVD to increase the thickness of the WO_{3-x} coatings. Figure 6.7.b is a photograph of Sample 2 after CVD, showing the characteristic dark-blue color of partially reduced WO_{3-x} films[2]. Figures 6.7.c-6.7.f are SEM pictures of the coatings in Samples 2,3,4 and 5. The nanofibers in all samples are completely covered with uniform coatings of WO_{3-x} . The morphology of the coatings is that of a film of smaller nanoparticles. The thickness of the films range between 80 and 150nm. Figure S5 shows SEM images of the cross section of a carbon nanofiber with a coating approximately 70 nm thick and an overview of a coated mat.

The composition of the coatings was analyzed with Raman, XPS and EDX spectroscopy. Figures 6.8.a and 6.8.b show the Raman spectra of a carbon nanofiber mat before and after CVD. The Raman spectra of an uncoated sample is typical of stabilized and pyrolyzed PAN at 1000 ºC displaying a D band at 1340-1400 cm^{-1}, a G band at 1560-1600 cm^{-1} and a small

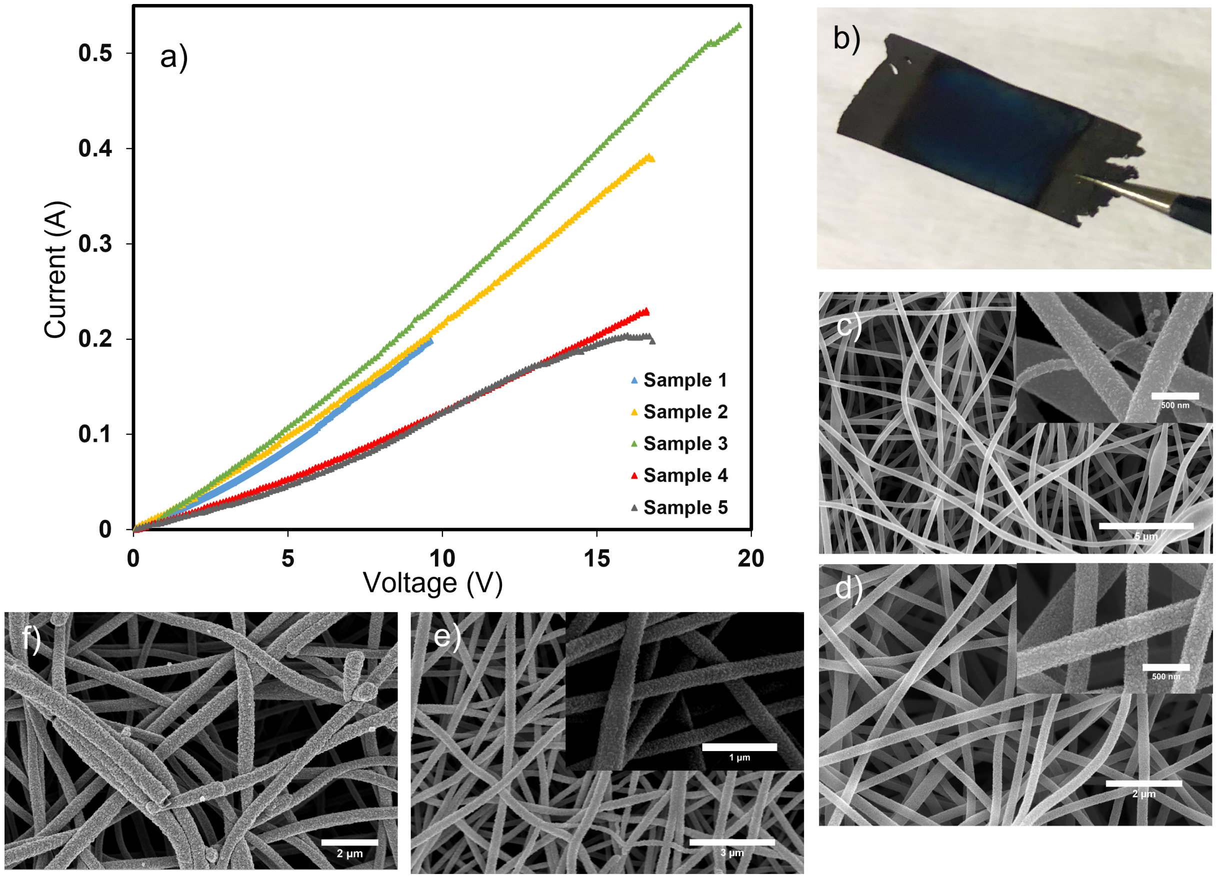

Figure 6.7: a) $I(V)$ curves of several samples during Joule heating-assisted CVD; b) Photograph of a mat exhibiting a the typical coloration of WO_{3-x} coatings; c)-f) SEM images of the coated nanofibers in different samples.

broad peak close to the 2D peak typical of pristine carbon[1]. The ID/IG ratio, an indicator of the degree of graphitization intensity, is 1.16. This value is typical for electrospun PAN fibers pyrolyzed at 1000 ºC[1]. The Raman spectroscopy of the coated carbon nanofiber mat displays the same D and G bands and ID/IG ratio, i.e. neither the heating nor the coating processes affect the degree of graphitization of the mats. This is to be expected because the temperatures reached during Joule heating for CVD are below the temperatures reached during pyrolysis[135]. The Raman spectra of the coated carbon nanofiber mat also contains the characteristic peaks of WO_{3-x}: peaks at 720 and 812 cm^{-1} correspond to the O-W-O stretching mode; the peak at 265 cm^{-1} corresponds to the O-W-O bending mode; and the peak at 132 cm^{-1} corresponds to the lattice mode[17, 124].

XPS spectroscopy confirms the final composition of the coating as WO_{3-x}. Figure 6.9.a shows the deconvolution analysis of tungsten including the W 4f doublets for W^{6+} and W^{5+}, together with the W 5p peak. The area ratio between the 4f7/2 and the 4f5/2 peaks is 0.75. The distance between the peaks of the fully oxidated W^{6+} is 2.15eV, while for the W^{5+} oxidation state the separation of the peaks is 2.18eV. The area of each peak has been corrected using the correspondent RSF value, which are 5.48 for the 4f7/2 peaks, 4.32 for the 4f5/2 peaks and 0.811 for the 5p3/2 peak. The close match of the area fractions for both the W^{6+} peaks and the W^{5+} peaks confirms the validity of the deconvolution. The deconvolution analysis of oxygen in Fig. 6.9.b includes the peaks for WO_3, WO_2 and chemisorbed oxygen species. The area ratio between the WO_3 and WO_2 peaks suggest a ratio of 0.73 between the two oxides. This is also confirmed by the 0.80 ratio of W^{6+} in the tungsten deconvolution . The higher ratio of W^{6+} compared to WO_3 may be due to the W-W bonds present in the substrate[12]. The elemental XPS mappings employed in the deconvolution analysis are shown in Fig. S6.

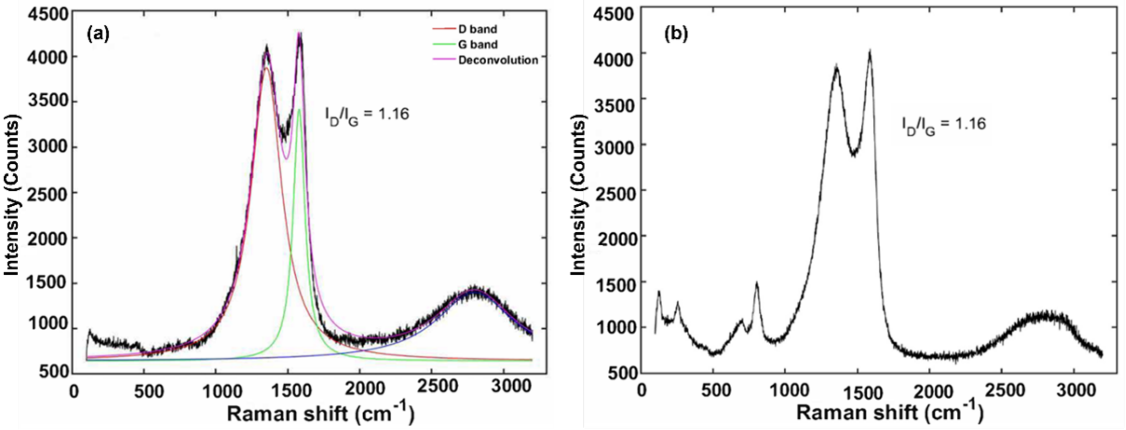

Figure 6.8: a) Raman spectrocscopy of a non-coated carbon nanofiber mat; b) Raman spectroscopy of a coated carbon nanofiber mat.

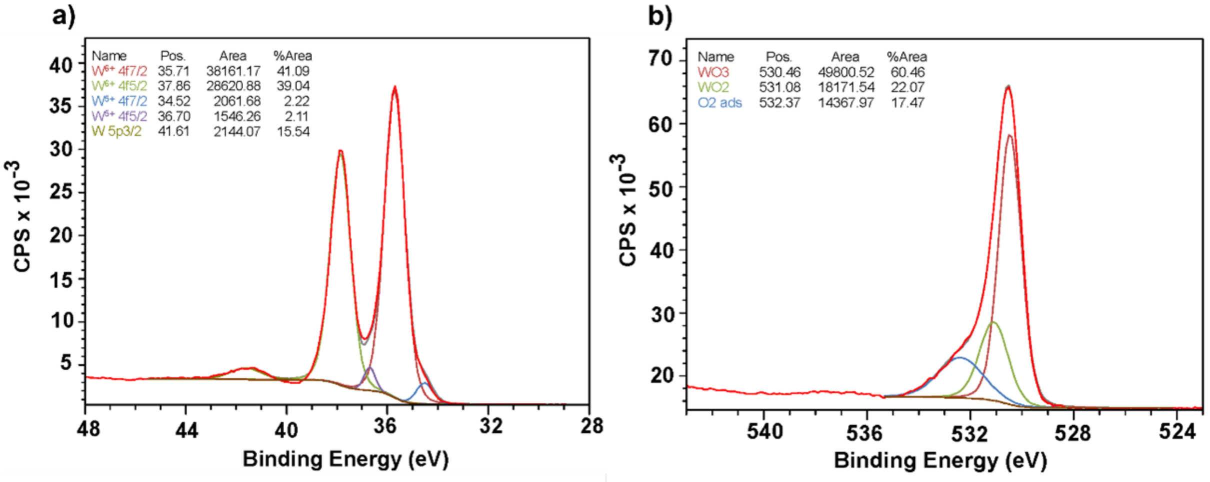

Figure 6.9: X-ray photoelectron spectroscopy of a coating showing main photoelectron lines of tungsten 4f (a) and oxygen 1s (b).

Chapter 7

Conclusions and future work

This dissertation has addressed four main objectives with dedicated studies that can be summarized as follows:

7.1 Experimental study of the the electrospray beam of the ionic liquid EMI-Im

In chapter 2 we have studied in detail the electrospray of EMI-Im to produce beams of charged nanodroplets and molecular ions. Retarding potential(RP) and time-of-flight (TOF) analysis were used in tandem, providing extensive experimental information, including parameters such as the velocity and electric potential of the jet in the breakup region, the radius of the jet, the ion and droplet contribution of the total current of the beam together with its charge to mass ratio. It is identified that ions carry an important fraction of the beam current and that the ion fraction is a weak function of the flow rate and increases with temperature. The study of more ionic liquids together with a better resolution of the retarding potential-TOF technique by increasing the lenght of the TOF without compromising the total measured current, could allow to study and select the best propellant for electrospray propulsion applications and understand more in detail the physics of these electrospray beams.

7.2 Microfabrication of electrospray thrusters

In chapter 3, we demonstrated a scalable microfabrication method of silicon micro-emitters for a compact microfluidic electrospray propulsion system, where the typical hydraulic resistance issue faced by several research teams is solved. The fabricated sources are compact, and its components, an emitter array electrode, extractor electrode, and a supporting micromachined glass substrate, are permanently bonded and precisely aligned using anodic bonding. We demonstrated the scalability and reliability of the process, fabricating and testing different head thrusters with a different number of emitters, varying hydraulic resistances of the microfluidic system, and different gaps between the extractor electrode and the emitter electrode. The excellent performance, uniformity, and synchrony of emission in each emitter part of the array are shown together with a fast response to the applied pressure in the propellant reservoir. A key performance issue is identified while operating the sources, the deposition of the neutralized counter on the silicon emitter clogging them, and is addressed and solved by adding a platinum layer on top of the emitter array. The 86 hours performance test demonstrates a large operational range, and the thrust measurements have shown thrust values up to 174 μN while operating the 256 emitter array source. Future improvements and follow-up experiments involve a 1000h hour lifetime tests. Another improvement will be increasing the emitter and channel density by using chromium masks or electron beam lithography in the etching steps, allowing further miniaturization of the system. As mentioned above, the ion fraction of the beam seems to respond more to the temperature than the flow rate. The design and incorporation of a MEMS heater attached to the borofloat wafer sealing the microfluidic channels could provide even higher I_{sp} capabilities.

C-MEMS process could be an ideal method to integrate a carbon based heater on the back of the glass wafer. As we have demonstrated in chapter 5 and 6, reproducible Joule-heating can be achieved at low power levels. Glassy carbon has previously shown good adhesion on glass [106]. Overall it is demonstrated that the design, fabrication, and performance of the electrospray sources shown in chapter 3 could lead to a real primary propulsion solution for small satellites.

7.3 Study of the fiber initiation in Near-Field electrospinning

In chapter 4, the initiation of the jet in near-field electrospinning, triggered by an applied electric field, is demonstrated to be reproducible and can be accurately predicted with a first principles, static model. The jet is formed as the initially spherical meniscus abruptly evolves into a conical shape when the applied potential reaches a critical value. Although this onset voltage is a function of all parameters in the model (including the gap between the emitter and grounded collector, the radius of the emitter and, in our studies, the presence of a dielectric rod), the electric field on the surface of the meniscus exhibits a more restricted dependency near the tip, $E_S\left(r \rightarrow 0\right) = \left(\frac{2\gamma\cos\theta_a}{\varepsilon_0 r}\right)^{1/2}$, i.e. it is only a function of the angle of the tip and the surface tension. We have studied two configurations, the basic emitter/plate geometry and one with a dielectric rod in between, and found that the electric field can be manipulated to facilitate the emission of the jet, and the subsequent deposition of fibers. A configuration with a metal conductor rod is also briefly studied. The emitter/rod/configuration focuses the electric field near the axis, reducing the area of the meniscus affected by strong electric fields, stresses and deformations, and preventing the collapse of the meniscus that often happens when significant stresses act on a larger area. Two different mechanisms are identified to create a polymer fiber between the meniscus and a collector, which are especially consistent in the emitter/rod/configuration: in non-contact jet mode the fiber is ejected from a fully conical meniscus that attaches to the collector; in contact jet mode the tip of the meniscus touches the collector before it can become fully conical, and leaves attached a fiber as the meniscus recedes upon discharging. Non-contact jet mode produces the thinnest fibers, with initial diameters that are likely to depend only on the properties of the fluid according to the law $d \approx \left(\frac{\gamma\varepsilon_0^2}{\rho K^2}\right)^{1/3}\left(\frac{\gamma^2\rho\varepsilon_0}{\mu^3 K}\right)^{-1/6}$[54]. Contact jet mode produces a bridge with an initial diameter of the order of the meniscus/collector contact region, similarly to mechanically aided fiber initiation strategies[5][10][151].A brief study with a metal tip is also conducted with a repeated outcome of unsuccessful initiation, explained by current discharges through the jet, pointing to an important role of the nature of the collector and the conductivity of polymer solution for success in operation NFES. The model and the experimental observations described in this work support the development of near-field electrospinning on the bases of first principles as shown in Figure 7.2.

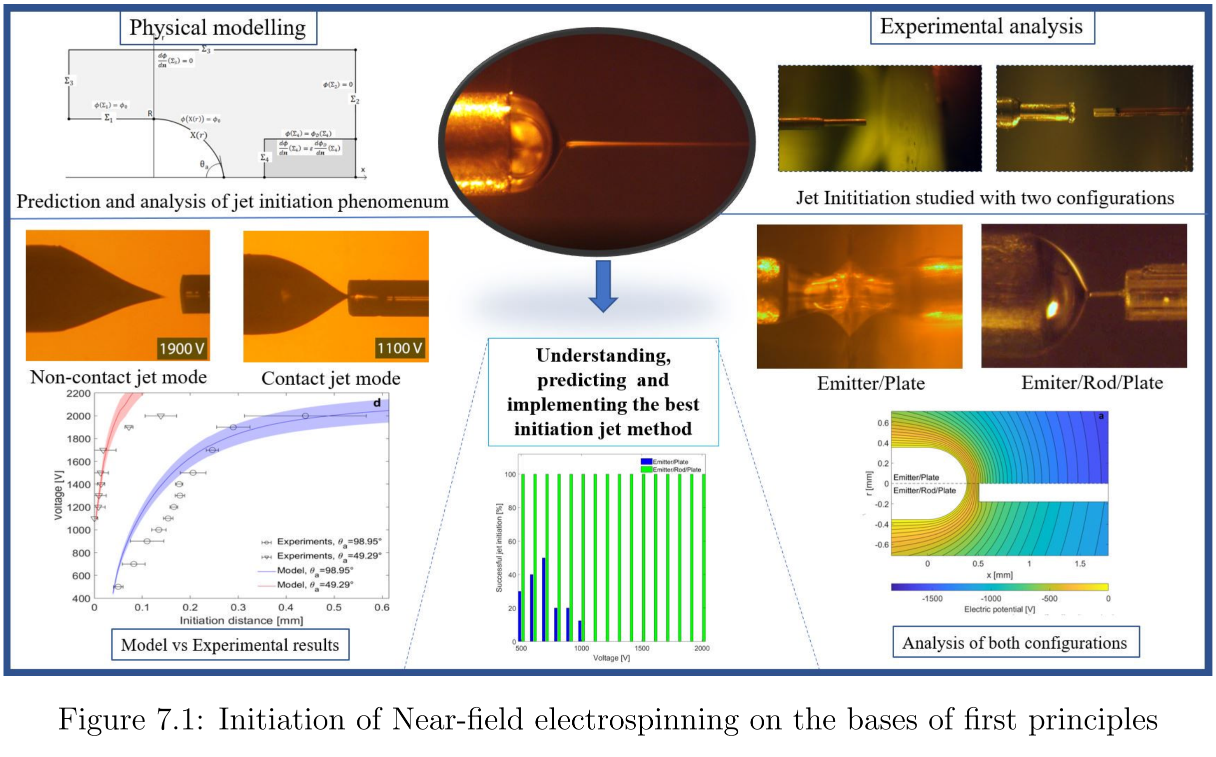

Figure 7.1: Initiation of Near-field electrospinning on the bases of first principles

7.4 C-MEMS-WO_{3-x} composites through Joule heating and CVD

In chapter 5 an optimized bottom up process to fabricate a GC/TMO microstructure consisting of a suspended GCW coated with WO_{3-x} is investigated. The coating is deposited by LCVD, activated by a temperature profile induced by Joule heating. The deposition of WO_{3-x} starts at the midpoint of the GCW, coinciding with the maximum of the temperature profile. Extending the coating towards the ends of the GCW requires increasing the current, while the voltage across the GCW remains constant. A thermal model shows that the consistency of the voltage at increasing current is due to the lower resistivity of the coated section at the deposition temperature; furthermore, the maximum of the temperature profile remains constant and shifts towards the ends of the GCW as the coating proceeds. Ultimately the length and thickness of the coating can be adjusted by imposing the current through the GCW and monitoring its voltage. We have demonstrated WO_{3-x} coatings with thickness ranging from 71 nm to 1.4 µm in glassy carbon wires with diameters between 780 nm and 2.95 µm. The stoichiometry of the coating (in terms of oxygen concentration) may be controlled by a post-annealing treatment in either an oxygen rich atmosphere or vacuum, favoring the oxidation of WO_{3-x} or its reduction by the carbon respectively. This is suggested by the full characterization of the coatings displaying a WC interface between the carbon and the WOx; the oxygen concentration seems to increase as the distance from the GC core. The nature of the suspended fiber integrated on the chip suggests the exploration of applications such as gas sensing but restricts other ones such as catalysis or electrochemical sensors. On top of that, the heat conduction nature along the fiber does not lead to uniform joule heating due to the heat sink of the GC wall where the fiber is suspended, leading to a non-uniform thickness along with the coating. This problem is solved in chapter 6 where we describe the optimization and scaling up of a process in larger carbon based materials such as carbon nanofiber mats. The Joule heating behavior of carbon nanofiber mats, fabricated by electrospinning of PAN and pyrolysis, shows a good correlation between power dissipated per unit area and temperature. The temperature distribution measured with IR thermography is uniform temperature throughout the mat, pointing to the dominance of radiation heat flux over conduction at temperatures below 800K, which are the ones of interest for CVD of many compounds. The uniformity of the temperature translates to uniform WO_{3-x} films deposited overall carbon nanofibers in the mat. Some results also suggest that joule-heating could significantly increase the degree of graphitization of the CNF mats, and even trigger field emission on some coated mats at large applied voltages. The future work involves testing the electrochemical performance of those carbon nanofiber composites for processes such as OER or HER and their photo-catalytic behavior. The process described suggests possible control strategies to generate oxygen vacancies in the coating that enhance electrochemical performance. Other target chemical precursors could be tried using the same technique to generate different carbon composites. A schematic figure of the achieved outcomes with Joule heating CVD on carbon fibers is shown in Figure 7.2

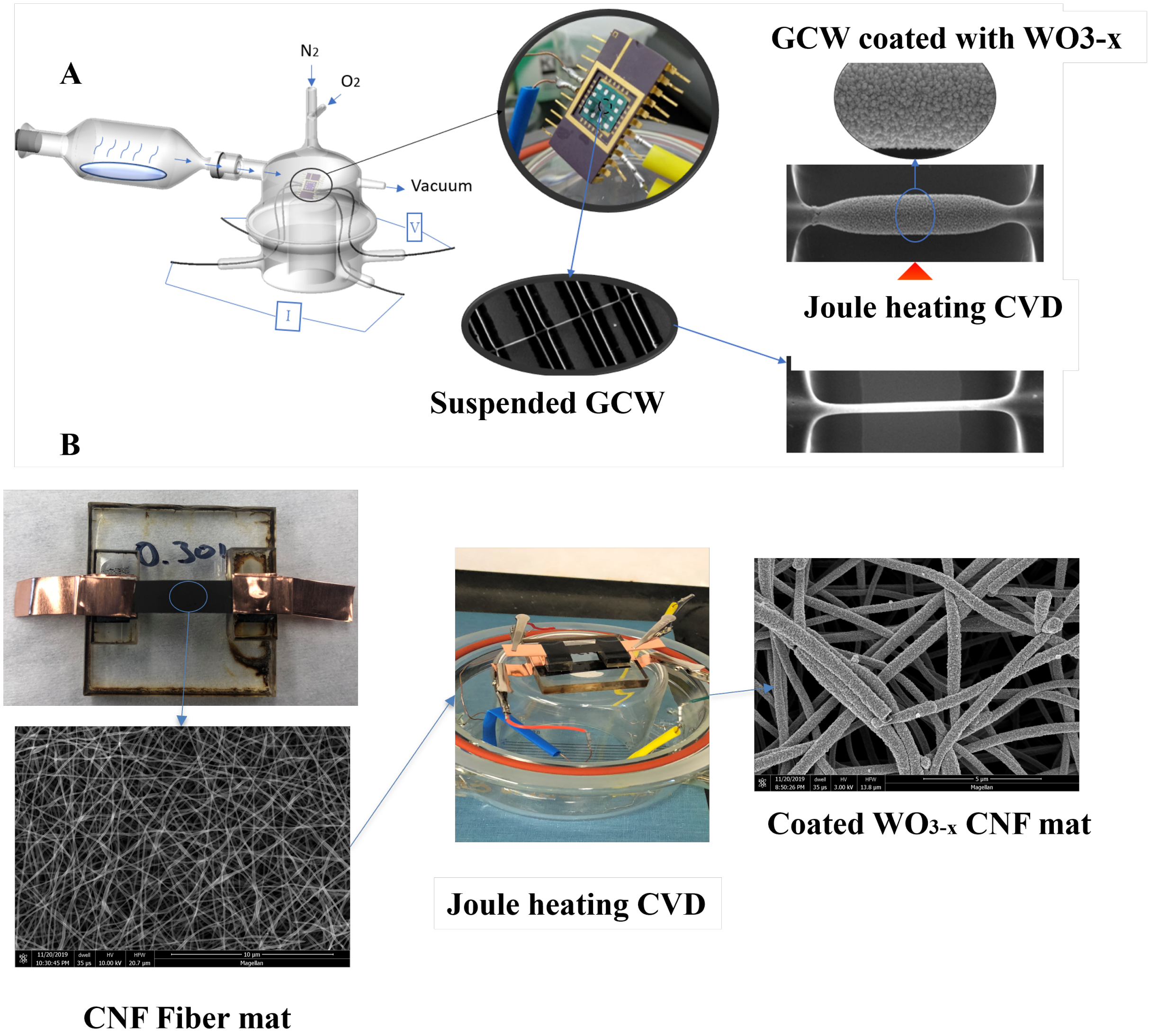

Figure 7.2: A) Joule Heating CVD of a single suspended fiber. B) Joule Heating CVD of a CNF mat.

Bibliography

[1] A. Ali, D. Slawig, A. Schlosser, J. Koch, N. Bigall, F. Renz, C. Tegenkamp, and R. Sindelar. Polyacrylonitrile (pan) based electrospun carbon nanofibers (ecnfs): Probing the synergistic effects of creep assisted stabilization and cnts addition on graphitization and low dimensional electrical transport. *Carbon*, 172:283–295, 2021.

[2] S. Ashraf, C. S. Blackman, R. G. Palgrave, S. C. Naisbitt, and I. P. Parkin. Aerosol assisted chemical vapour deposition of wo 3 thin films from tungsten hexacarbonyl and their gas sensing properties. *J. Mater. Chem.*, 17(35):3708–3713, 2007.

[3] A. A. Bakr. *The Boundary Integral Equatio Method in Axisymmetric Stress Analysis Problems*, volume 14. Springer Science & Business Media, 2013.

[4] C. Balázsi, K. Sedlácková, E. Llobet, and R. Ionescu. Novel hexagonal wo3 nanopowder with metal decorated carbon nanotubes as no2 gas sensor. *Sensors and Actuators B: Chemical*, 133(1):151–155, 2008.

[5] G. S. Bisht, G. Canton, A. Mirsepassi, L. Kulinsky, S. Oh, D. Dunn-Rankin, and M. J. Madou. Controlled continuous patterning of polymeric nanofibers on three-dimensional substrates using low-voltage near-field electrospinning. *Nano letters*, 11(4):1831–1837, 2011.

[6] R. Borrajo-Pelaez and M. Gamero-Castaño. The effect of the molecular mass on the sputtering by electrosprayed nanodroplets. *Applied Surface Science*, 344:163–170, 2015.

[7] R. A. Buerschaper. Thermal and electrical conductivity of graphite and carbon at low temperatures. *J. Appl. Phys.*, 15(5):452–454, 1944.

[8] S. Chandrasekhar. *Hydrodynamic and Hydromagnetic Stability.* Dover Books on Physics Series. Dover Publications, 1981.

[9] C. Chang, K. Limkrailassiri, and L. Lin. Continuous near-field electrospinning for large area deposition of orderly nanofiber patterns. *Applied Physics Letters*, 93(12):123111, 2008.

[10] C. Chang, K. Limkrailassiri, and L. Lin. Continuous near-field electrospinning for large area deposition of orderly nanofiber patterns. *Applied Physics Letters*, 93(12):123111, 2008.

[11] J. Chen, D. Yu, W. Liao, M. Zheng, L. Xiao, H. Zhu, M. Zhang, M. Du, and J. Yao. Wo3–x nanoplates grown on carbon nanofibers for an efficient electrocatalytic hydrogen evolution reaction. *ACS applied materials & interfaces*, 8(28):18132–18139, 2016.

[12] E. Ciftyürek, B. Šmíd, Z. Li, V. Matolín, and K. Schierbaum. Spectroscopic understanding of sno2 and wo3 metal oxide surfaces with advanced synchrotron based; xps-ups and near ambient pressure (nap) xps surface sensitive techniques for gas sensor applications under operational conditions. *Sensors*, 19(21):4737, 2019.

[13] A. Cisquella-Serra, M. Gamero-Castaño, L. Ferrer-Argemi, J. L. Wardini, and M. J. Madou. Controlled joule-heating of suspended glassy carbon wires for localized chemical vapor deposition. *Carbon*, 156:329–338, 2020.

[14] A. Cisquella-Serra, M. Magnani, Á. Gual-Mosegui, S. Holmberg, M. Madou, and M. Gamero-Castaño. Study of the electrostatic jet initiation in near-field electrospinning. *Journal of colloid and interface science*, 543:106–113, 2019.

[15] D. G. Courtney, S. Dandavino, and H. Shea. Comparing direct and indirect thrust measurements from passively fed ionic electrospray thrusters. *Journal of Propulsion and Power*, 32(2):392–407, 2016.

[16] C. Daguenet, P. J. Dyson, I. Krossing, A. Oleinikova, J. Slattery, C. Wakai, and H. Weingaertner. Dielectric response of imidazolium-based room-temperature ionic liquids. *Journal of Physical Chemistry B*, 110(25):12682–12688, 2006.

[17] M. Daniel, B. Desbat, J. Lassegues, B. Gerand, and M. Figlarz. Infrared and raman study of wo3 tungsten trioxides and wo3, xh2o tungsten trioxide tydrates. *Journal of Solid State Chemistry*, 67(2):235–247, 1987.

[18] D. Davazoglou, A. Moutsakis, V. Valamontes, V. Psycharis, and D. Tsamakis. Tungsten oxide thin films chemically vapor deposited at low pressure by w (CO) 6 pyrolysis. *Journal of The Electrochemical Society*, 144(2):595–599, feb 1997.

[19] J. F. De La Mora. The effect of charge emission from electrified liquid cones. *Journal of Fluid Mechanics*, 243:561–574, 1992.

[20] J. F. De La Mora and I. G. Loscertales. The current emitted by highly conducting taylor cones. *Journal of Fluid Mechanics*, 260:155–184, 1994.

[21] B. E. Deal and A. Grove. General relationship for the thermal oxidation of silicon. *Journal of applied physics*, 36(12):3770–3778, 1965.

[22] S. K. Deb. Opportunities and challenges in science and technology of wo3 for electrochromic and related applications. *Solar Energy Materials and Solar Cells*, 92(2):245–258, 2008.

[23] B. Ding, J. Kim, Y. Miyazaki, and S. Shiratori. Electrospun nanofibrous membranes coated quartz crystal microbalance as gas sensor for nh3 detection. *Sensors and Actuators B: Chemical*, 101(3):373–380, 2004.

[24] B. Ding, M. Wang, X. Wang, J. Yu, and G. Sun. Electrospun nanomaterials for ultrasensitive sensors. *Materials today*, 13(11):16–27, 2010.

[25] B. Ding, M. Wang, J. Yu, and G. Sun. Gas sensors based on electrospun nanofibers. *Sensors*, 9(3):1609–1624, 2009.

[26] J. Doshi and D. H. Reneker. Electrospinning process and applications of electrospun fibers. *Journal of electrostatics*, 35(2-3):151–160, 1995.

[27] J. B. Fenn, M. Mann, C. K. Meng, S. F. Wong, and C. M. Whitehouse. Electrospray ionization for mass spectrometry of large biomolecules. *Science*, 246(4926):64–71, 1989.

[28] J. B. Fenn, M. Mann, C. K. Meng, S. F. Wong, and C. M. Whitehouse. Electrospray ionization–principles and practice. *Mass Spectrometry Reviews*, 9(1):37–70, 1990.

[29] J. Fernandez de la Mora. On the outcome of the coulombic fission of a charged isolated drop. *Journal of Colloid and Interface Science*, 178(1):209–218, 1996.

[30] J. Fernández de La Mora. The fluid dynamics of taylor cones. *Annu. Rev. Fluid Mech.*, 39:217–243, 2007.

[31] J. Fernandez de la Mora and I. Loscertales. The current emitted by highly conducting Taylor cones. *Journal of Fluid Mechanics*, 260(special is):155–184, 1994.

[32] L. Ferrer-Argemi, E. S. Aliabadi, A. Cisquella-Serra, A. Salazar, M. Madou, and J. Lee. Size-dependent electrical and thermal conductivities of electro-mechanically-spun glassy carbon wires. *Carbon*, 130:87–93, 2018.

[33] L. Ferrer-Argemi, A. Cisquella-Serra, M. Madou, and J. Lee. Temperature-dependent electrical and thermal conductivity of glassy carbon wires. In *2018 17th IEEE Intersociety Conference on Thermal and Thermomechanical Phenomena in Electronic Systems (ITherm)*, pages 1280–1288. IEEE, 2018.

[34] H. Fong, I. Chun, and D. H. Reneker. Beaded nanofibers formed during electrospinning. *Polymer*, 40(16):4585–4592, 1999.

[35] E. Formo, E. Lee, D. Campbell, and Y. Xia. Functionalization of electrospun tio2 nanofibers with pt nanoparticles and nanowires for catalytic applications. *Nano letters*, 8(2):668–672, 2008.

[36] M. Gamero-Castaño. Characterization of the electrosprays of 1-ethyl-3-methylimidazolium bis(trifluoromethylsulfonyl) imide in vacuum. *Physics of Fluids*, 20(3):032103, MAR 2008.

[37] M. Gamero-Castaño. The structure of electrospray beams in vacuum. *Journal of Fluid Mechanics*, 604:339–368, 2008.

[38] M. Gamero-Castano. Retarding potential and induction charge detectors in tandem for measuring the charge and mass of nanodroplets. *Review of Scientific Instruments*, 80(5), 2009.

[39] M. Gamero-Castaño. Energy dissipation in electrosprays and the geometric scaling of the transition region of cone-jets. *Journal of Fluid Mechanics*, 662:493–513, 2010.

[40] M. Gamero-Castano. Dissipation in cone-jet electrosprays and departure from isothermal operation. *Physical Review E*, 99(6), JUN 26 2019.

[41] M. Gamero-Castaño and A. Cisquella-Serra. Electrosprays of highly conducting liquids: A study of droplet and ion emission based on retarding potential and time-of-flight spectrometry. *Physical Review Fluids*, 6(1):013701, 2021.

[42] M. Gamero-Castano and J. de la Mora. Direct measurement of ion evaporation kinetics from electrified liquid surfaces. *Journal of Chemical Physics*, 113(2):815–832, 2000.

[43] M. Gamero-Castaño and M. Galobardes-Esteban. Electrospray propulsion: Modeling of the beams of droplets and ions of highly conducting propellants. *Journal of Applied Physics*, 131(1):013307, 2022.

[44] M. Gamero-Castaño and V. Hruby. Electrospray as a source of nanoparticles for efficient colloid thrusters. *Journal of Propulsion and Power*, 17:977–987, 2001.

[45] M. Gamero-Castaño and M. Magnani. The minimum flow rate of electrosprays in the cone-jet mode. *Journal of Fluid Mechanics*, 876:553–572, 2019.

[46] M. Gamero-Castano and M. Magnani. Numerical simulation of electrospraying in the cone-jet mode. *Journal of Fluid Mechanics*, 859:247–267, 2019.

[47] M. Gamero-Castaño and M. Mahadevan. Sputtering yields of si, sic, and b 4 c under nanodroplet bombardment at normal incidence. *Journal of Applied Physics*, 106(5):054305, 2009.

[48] M. Gamero-Castaño and V. Hruby. Electric measurements of charged sprays emitted by cone-jets. *Journal of Fluid Mechanics*, 459:245–276, 2002.

[49] A. Gañán-Calvo. On the general scaling theory for electrospraying. *Journal of Fluid Mechanics*, 507:203–212, 2004.

[50] A. Ganan-Calvo, J. Davila, and A. Barrero. Current and droplet size in the electrospraying of liquids. scaling laws. *Journal of aerosol science*, 28(2):249–275, 1997.

[51] A. Gañán-Calvo, J. López-Herrera, M. Herrada, A. Ramos, and J. Montanero. Review on the physics of electrospray: From electrokinetics to the operating conditions of single and coaxial Taylor cone-jets, and AC electrospray. *Journal of Aerosol Science*, 125:32–56, 2018.

[52] A. M. Gañán-Calvo. Cone-jet analytical extension of taylor's electrostatic solution and the asymptotic universal scaling laws in electrospraying. *Physical review letters*, 79(2):217, 1997.

[53] A. M. Ganán-Calvo, J. M. López-Herrera, M. A. Herrada, A. Ramos, and J. M. Montanero. Review on the physics of electrospray: from electrokinetics to the operating conditions of single and coaxial taylor cone-jets, and ac electrospray. *Journal of Aerosol Science*, 125:32–56, 2018.

[54] A. M. Gañán-Calvo, N. Rebollo-Muñoz, and J. M. Montanero. The minimum or natural rate of flow and droplet size ejected by taylor cone–jets: physical symmetries and scaling laws. *New Journal of Physics*, 15(3):033035, mar 2013.

[55] S. P. Garland, T. M. Murphy, and T. Pan. Print-to-pattern dry film photoresist lithography. *Journal of Micromechanics and Microengineering*, 24(5):057002, apr 2014.

[56] R. Gopal, S. Kaur, Z. Ma, C. Chan, S. Ramakrishna, and T. Matsuura. Electrospun nanofibrous filtration membrane. *Journal of Membrane Science*, 281(1-2):581–586, 2006.

[57] E. Grustan-Gutierrez and M. Gamero-Castaño. Microfabricated electrospray thruster array with high hydraulic resistance channels. *Journal of Propulsion and Power*, 33(4):984–991, 2017.

[58] C. Guo, Y. Liu, X. Ma, Y. Qian, and L. Xu. Synthesis of tungsten carbide nanocrystal via a simple reductive reaction. *Chemistry Letters*, 35(11):1210–1211, 2006.

[59] P. Harris. Fullerene-related structure of commercial glassy carbons. *Philosophical Magazine*, 84(29):3159–3167, 2004.

[60] P. Harris, R. Vis, and D. Heymann. Fullerene-like carbon nanostructures in the allende meteorite. *Earth and Planetary Science Letters*, 183(3-4):355–359, 2000.

[61] P. J. Harris, Z. Liu, and K. Suenaga. Imaging the atomic structure of activated carbon. *Journal of physics: Condensed matter*, 20(36):362201, 2008.

[62] B. He, T. J. Morrow, and C. D. Keating. Nanowire sensors for multiplexed detection of biomolecules. *Current opinion in chemical biology*, 12(5):522–528, 2008.

[63] X.-X. He, J. Zheng, G.-F. Yu, M.-H. You, M. Yu, X. Ning, and Y.-Z. Long. Near-field electrospinning: progress and applications. *The Journal of Physical Chemistry C*, 121(16):8663–8678, 2017.

[64] C. Hellmann, J. Belardi, R. Dersch, A. Greiner, J. Wendorff, and S. Bahnmueller. High precision deposition electrospinning of nanofibers and nanofiber nonwovens. *Polymer*, 50(5):1197–1205, 2009.

[65] T. Henning, K. Huhn, S. Feng, Z. Xie, S. Hengsbach, K. Bade, and P. Klar. Three-dimensional lithography for the microfabrication of colloid emitters. In *5th Space Propulsion Conference, Rome*, pages 2–6, 2016.

[66] M. Herrada, J. López-Herrera, A. M. Gañán-Calvo, E. Vega, J. Montanero, and S. Popinet. Numerical simulation of electrospray in the cone-jet mode. *Physical Review E*, 86(2):026305, 2012.

[67] F. Higuera. Flow rate and electric current emitted by a Taylor cone. *Journal of Fluid Mechanics*, 484:303–327, 2003.

[68] A. Hiraki, E. Lugujjo, and J. W. Mayer. Formation of silicon oxide over gold layers on silicon substrates. *Journal of Applied Physics*, 43(9):3643–3649, 1972.

[69] V. Hruby, D. Spence, N. Demmons, T. Roy, E. Ehrbar, J. Zwahlen, R. Martin, J. Ziemer, W. Connolly, S. Rhodes, et al. St7-drs colloid thruster system development and performance summary. In *44th AIAA/ASME/SAE/ASEE Joint Propulsion Conference & Exhibit*, page 4824, 2008.

[70] C. Huang, G. Jian, J. B. DeLisio, H. Wang, and M. R. Zachariah. Electrospray deposition of energetic polymer nanocomposites with high mass particle loadings: a prelude to 3d printing of rocket motors. *Advanced Engineering Materials*, 17(1):95–101, 2015.

[71] J. Huang, S. Chen, Z. Ren, G. Chen, and M. Dresselhaus. Real-time observation of tubule formation from amorphous carbon nanowires under high-bias joule heating. *Nano letters*, 6(8):1699–1705, 2006.

[72] K. Huhn, T. Henning, and P. J. Klar. Colloid emitters in photostructurable polymer technology : Fabrication and characterization progress report iepc-2015. 2015.

[73] K. Huhn, M. Piechotka, T. Henning, and P. Klar. Investigation of the emission behavior of miniaturized su-8 based colloid emitters. In *Proceedings of the 33rd International Electric Propulsion Conference*, 2013.

[74] N. Inoue, M. Nagao, K. Murakami, S. Khumpuang, S. Hara, and Y. Takao. Fabrication of a high-density emitter array for electrospray thrusters using field emitter array process. *Japanese Journal of Applied Physics*, 58(SE):SEEG04, may 2019.

[75] J. V. Iribarne and B. A. Thomson. On the evaporation of small ions from charged droplets. *Journal of Chemical Physics*, 64:2287, 1976.

[76] F. Jeffali, B. Kihel, A. Nougaoui, F. Delaunois, et al. Monitoring and diagnostic misalignment of asynchronous machines by infrared thermography. *J. Mater. Environ. Sci*, 6(4):1192–1199, 2015.

[77] K. Jurkiewicz, S. Duber, H. Fischer, and A. Burian. Modelling of glass-like carbon structure and its experimental verification by neutron and x-ray diffraction. *Journal of Applied Crystallography*, 50(1):36–48, 2017.

[78] R. U. Kirss and L. Meda. Chemical vapor deposition of tungsten oxide. *Applied Organometallic Chemistry*, 12(3):155–160, 1998.

[79] J. Kong, Z. Liu, Z. Yang, H. R. Tan, S. Xiong, S. Y. Wong, X. Li, and X. Lu. Carbon/sno 2/carbon core/shell/shell hybrid nanofibers: tailored nanostructure for the anode of lithium ion batteries with high reversibility and rate capacity. *Nanoscale*, 4(2):525–530, 2012.

[80] L. Kong and G. R. Ziegler. Role of molecular entanglements in starch fiber formation by electrospinning. *Biomacromolecules*, 13(8):2247–2253, 2012.

[81] G. Korotcenkov. Metal oxides for solid-state gas sensors: What determines our choice? *Materials Science and Engineering: B*, 139(1):1–23, 2007.

[82] D. Krejci, F. Mier-Hicks, R. Thomas, T. Haag, and P. Lozano. Emission characteristics of passively fed electrospray microthrusters with propellant reservoirs. *Journal of Spacecraft and Rockets*, 54(2):447–458, 2017.

[83] V. Krohn. Liquid metal droplets for heavy particle propulsion progr. *Astronautics and Rocketry, ACNY*, 5, 1961.

[84] V. E. Krohn Jr. Glycerol droplets for electrostatic propulsion. *Progress in Astronautics and Aeronautics*, 9, 1963.

[85] R. Krpoun and H. R. Shea. Integrated out-of-plane nanoelectrospray thruster arrays for spacecraft propulsion. *Journal of Micromechanics and Microengineering*, 19(4):045019, mar 2009.

[86] F. L. Kunze, T. Henning, and P. J. Klar. Taking internally wetted capillary electrospray emitters to the sub-ten-micrometer scale with 3d microlithography. *AIP Advances*, 11(10):105315, 2021.

[87] J. LaDou. Printed circuit board industry. *International Journal of Hygiene and Environmental Health*, 209(3):211–219, 2006.

[88] J. Lee, Z. Li, J. P. Reifenberg, S. Lee, R. Sinclair, M. Asheghi, and K. E. Goodson. Thermal conductivity anisotropy and grain structure in ge2sb2te5 films. *Journal of Applied Physics*, 109(8):084902, 2011.

[89] T. M. Lee, D. H. Lee, C. Y. Liaw, A. I. Lao, and I.-M. Hsing. Detailed characterization of anodic bonding process between glass and thin-film coated silicon substrates. *Sensors and Actuators A: Physical*, 86(1-2):103–107, 2000.

[90] T. P. Lei, X. Z. Lu, and F. Yang. Fabrication of various micro/nano structures by modified near-field electrospinning. *AIP Advances*, 5(4):041301, 2015.

[91] G. Lenguito, J. Fernandez de la Mora, and A. Gomez. Variable thrust/specific-impulse of multiplexed electrospray microthrusters. In *2013 IEEE Aerospace Conference*, pages 1–8, 2013.

[92] I. Levchenko, K. Bazaka, Y. Ding, Y. Raitses, S. Mazouffre, T. Henning, P. J. Klar, S. Shinohara, J. Schein, L. Garrigues, et al. Space micropropulsion systems for cubesats and small satellites: From proximate targets to furthermost frontiers. *Applied Physics Reviews*, 5(1):011104, 2018.

[93] D. Li and Y. Xia. Direct fabrication of composite and ceramic hollow nanofibers by electrospinning. *Nano letters*, 4(5):933–938, 2004.

[94] Y. Lim, S. Kim, Y. M. Kwon, J. M. Baik, and H. Shin. A highly sensitive gas-sensing platform based on a metal-oxide nanowire forest grown on a suspended carbon nanowire fabricated at a wafer level. *Sensors and Actuators B: Chemical*, 260:55–62, 2018.

[95] X. Liu, W. Liu, M. Ko, M. Park, M. G. Kim, P. Oh, S. Chae, S. Park, A. Casimir, G. Wu, et al. Metal (ni, co)-metal oxides/graphene nanocomposites as multifunctional electrocatalysts. *Advanced Functional Materials*, 25(36):5799–5808, 2015.

[96] P. Lozano and M. Martínez-Sánchez. Ionic liquid ion sources: suppression of electrochemical reactions using voltage alternation. *Journal of colloid and interface science*, 280(1):149–154, 2004.

[97] S. Mantovani, F. Nava, C. Nobili, and G. Ottaviani. In-diffusion of pt in si from the ptsi/si interface. *Physical Review B*, 33(8):5536, 1986.

[98] A. McEwen, H. Ngo, K. LeCompte, and J. Goldman. Electrochemical properties of imidazolium salt electrolytes for electrochemical capacitor applications. *Journal of the Electrochemical Society*, 146(5):1687–1695, 1999.

[99] C. E. Miller and P. C. Lozano. Measurement of the dissociation rates of ion clusters in ionic liquid ion sources. *Applied Physics Letters*, 116(25):254101, 2020.

[100] M. M. Mohamed, T. M. Salama, M. Hegazy, R. M. Abou Shahba, and S. Mohamed. Synthesis of hexagonal wo3 nanocrystals with various morphologies and their enhanced electrocatalytic activities toward hydrogen evolution. *international journal of hydrogen energy*, 44(10):4724–4736, 2019.

[101] R. Natu, M. Islam, J. Gilmore, and R. Martinez-Duarte. Shrinkage of su-8 microstructures during carbonization. *Journal of analytical and applied pyrolysis*, 131:17–27, 2018.

[102] F. Nava Alonso, M. Zambrano Morales, A. Uribe Salas, and J. Bedolla Becerril. Tungsten trioxide reduction-carburization with carbon monoxide-carbon dioxide mixtures: Kinetics and thermodynamics. *International Journal of Mineral Processing*, 20(1):137–151, 1987.

[103] C. Pantano, A. Ganan-Calvo, and A. Barrero. Zeroth-order, electrohydrostatic solution for electrospraying in cone-jet mode. *Journal of Aerosol Science*, 25(6):1065–1077, 1994.

[104] X. Peng and A. Chen. Aligned tio2 nanorod arrays synthesized by oxidizing titanium with acetone. *J. Mater. Chem.*, 14:2542–2548, 2004.

[105] Q. P. Pham, U. Sharma, and A. G. Mikos. Electrospinning of polymeric nanofibers for tissue engineering applications: a review. *Tissue engineering*, 12(5):1197–1211, 2006.

[106] O. Pilloni, M. Madou, D. Mendoza, S. Muhl, and L. Oropeza-Ramos. Methodology and fabrication of adherent and crack-free su-8 photoresist-derived carbon mems on fused silica transparent substrates. *Journal of Micromechanics and Microengineering*, 29(2):027002, 2019.

[107] A. Poghosyan and A. Golkar. Cubesat evolution: Analyzing cubesat capabilities for conducting science missions. *Progress in Aerospace Sciences*, 88:59–83, 2017.

[108] X.-H. Qin and S.-Y. Wang. Filtration properties of electrospinning nanofibers. *Journal of applied polymer science*, 102(2):1285–1290, 2006.

[109] L. Rayleigh. Xx. on the equilibrium of liquid conducting masses charged with electricity. *The London, Edinburgh, and Dublin Philosophical Magazine and Journal of Science*, 14(87):184–186, 1882.

[110] K. M. Reddy, T. Rao, and J. Joardar. Stability of nanostructured w-c phases during carburization of wo3. *Materials Chemistry and Physics*, 128(1):121–126, 2011.

[111] D. H. Reneker and I. Chun. Nanometre diameter fibres of polymer, produced by electrospinning. *Nanotechnology*, 7(3):216–223, sep 1996.

[112] I. Romero-Sanz, R. Bocanegra, J. Fernandez De La Mora, and M. Gamero-Castano. Source of heavy molecular ions based on taylor cones of ionic liquids operating in the pure ion evaporation regime. *Journal of Applied Physics*, 94(5):3599–3605, 2003.

[113] J. Rosell-Llompart and J. Fernandez de la Mora. Generation of monodisperse droplets 0.3 to 4 μm in diameter from electrified cone-jets of highly conducting and viscous liquids. *Journal of Aerosol Science*, 25(6):1093–1119, 1994.

[114] F. Saiz and M. Gamero-Castaño. Atomistic modeling of the sputtering of silicon by electrosprayed nanodroplets. *Journal of Applied Physics*, 116(5):054303, 2014.

[115] A. Salazar, B. Cardenas-Benitez, B. Pramanick, M. J. Madou, and S. O. Martinez-Chapa. Nanogap fabrication by joule heating of electromechanically spun suspended carbon nanofibers. *Carbon*, 115:811–818, 2017.

[116] S. L. Shenoy, W. D. Bates, H. L. Frisch, and G. E. Wnek. Role of chain entanglements on fiber formation during electrospinning of polymer solutions: good solvent, non-specific polymer–polymer interaction limit. *Polymer*, 46(10):3372–3384, 2005.

[117] T. J. Sill and H. A. Von Recum. Electrospinning: applications in drug delivery and tissue engineering. *Biomaterials*, 29(13):1989–2006, 2008.

[118] L. Soukup, I. Gregora, L. Jastrabik, and A. Koňáková. Raman spectra and electrical conductivity of glassy carbon. *Materials Science and Engineering: B*, 11(1):355–357, 1992.

[119] A. Staerz, U. Weimar, and N. Barsan. Understanding the potential of wo3 based sensors for breath analysis. *Sensors*, 16(11):1815, 2016.

[120] D. Sun, C. Chang, S. Li, and L. Lin. Near-field electrospinning. *Nano Letters*, 6(4):839–842, 2006.

[121] K. Suzuki, M. Nagao, Y. Liu, K. Murakami, S. Khumpuang, S. Hara, and Y. Takao. Fabrication of nano-capillary emitter arrays for ionic liquid electrospray thrusters. *Japanese Journal of Applied Physics*, 60(SC):SCCF07, 2021.

[122] G. I. Taylor. Disintegration of water drops in an electric field. *Proceedings of the Royal Society of London. Series A. Mathematical and Physical Sciences*, 280(1382):383–397, 1964.

[123] G. I. Taylor. Electrically driven jets. *Proceedings of the Royal Society of London. A. Mathematical and Physical Sciences*, 313(1515):453–475, 1969.

[124] K. Thummavichai, L. Trimby, N. Wang, C. D. Wright, Y. Xia, and Y. Zhu. Low temperature annealing improves the electrochromic and degradation behavior of tungsten oxide (wox) thin films. *The Journal of Physical Chemistry C*, 121(37):20498–20506, 2017.

[125] N. Uchizono, A. Collins, C. Marrese-Reading, S. Arestie, J. Ziemer, and R. Wirz. The role of secondary species emission in vacuum facility effects for electrospray thrusters. *Journal of Applied Physics*, 130(14):143301, 2021.

[126] I. Usoltsev, R. Eichler, Y. Wang, J. Even, A. Yakushev, H. Haba, M. Asai, H. Brand, A. Di Nitto, C. E. Düllmann, et al. Decomposition studies of group 6 hexacarbonyl complexes. part 1: Production and decomposition of mo (co) 6 and w (co) 6. *Radiochim. Acta*, 104(3):141–151, 2016.

[127] S. Vallejos, P. Umek, and C. Blackman. Aerosol assisted chemical vapour deposition control parameters for selective deposition of tungsten oxide nanostructures. *J. Nanosci. Nanotechnol.*, 11(9):8214–8220, 2011.

[128] C. I. Vargas-Consuelos, K. Seo, M. Camacho-López, and O. A. Graeve. Correlation between particle size and raman vibrations in wo3 powders. *The Journal of Physical Chemistry C*, 118(18):9531–9537, 2014.

[129] L. F. Velásquez-García. Sla 3-d printed arrays of miniaturized, internally fed, polymer electrospray emitters. *Journal of Microelectromechanical Systems*, 24(6):2117–2127, 2015.

[130] G. Vitali, M. Rossi, M. L. Terranova, and V. Sessa. Laser-induced structural modifications of glassy carbon surfaces. *Journal of Applied Physics*, 77(9):4307–4311, 1995.

[131] S. Vyas, C. Dreyer, J. Slingsby, D. Bicknase, J. M. Porter, and C. M. Maupin. Electronic structure and spectroscopic analysis of 1-ethyl-3-methylimidazolium bis (trifluoromethylsulfonyl) imide ion pair. *The Journal of Physical Chemistry A*, 118(34):6873–6882, 2014.

[132] F. Völklein, H. Reith, T. W. Cornelius, M. Rauber, and R. Neumann. The experimental investigation of thermal conductivity and the wiedemann–franz law for single metallic nanowires. *Nanotechnology*, 20(32):325706, jul 2009.

[133] C. Wang, L. Yin, L. Zhang, D. Xiang, and R. Gao. Metal oxide gas sensors: sensitivity and influencing factors. *sensors*, 10(3):2088–2106, 2010.

[134] L. Wang, X. Xu, Z. Feng, L. Bian, and Y. Wang. Wo3-x based composite material with chitosan derived nitrogen doped mesoporous carbon as matrix for oxygen vacancy induced organic pollutants catalytic reduction and ir driven h2 production. *Journal of Solid State Chemistry*, 266:23–30, 2018.

[135] Y. Wang, J. Santiago-Aviles, R. Furlan, and I. Ramos. Pyrolysis temperature and time dependence of electrical conductivity evolution for electrostatically generated carbon nanofibers. *IEEE Trans. Nanotechnol.*, 2(1):39–43, 2003.

[136] K. Woan, G. Pyrgiotakis, and W. Sigmund. Photocatalytic carbon-nanotube–tio2 composites. *Advanced Materials*, 21(21):2233–2239, 2009.

[137] P. Wu, N. Du, H. Zhang, J. Yu, Y. Qi, and D. Yang. Carbon-coated sno 2 nanotubes: template-engaged synthesis and their application in lithium-ion batteries. *Nanoscale*, 3(2):746–750, 2011.

[138] R. Wu, J. Zhang, Y. Shi, D. Liu, and B. Zhang. Metallic wo2–carbon mesoporous nanowires as highly efficient electrocatalysts for hydrogen evolution reaction. *J. Am. Chem. Soc.*, 137(22):6983–6986, 2015. PMID: 25992910.

[139] Y. Xin and D. H. Reneker. Hierarchical polystyrene patterns produced by electrospinning. *Polymer*, 53(19):4254–4261, 2012.

[140] Y. Yao, K. K. Fu, S. Zhu, J. Dai, Y. Wang, G. Pastel, Y. Chen, T. Li, C. Wang, T. Li, et al. Carbon welding by ultrafast joule heating. *Nano letters*, 16(11):7282–7289, 2016.

[141] A. L. Yarin, S. Koombhongse, and D. H. Reneker. Bending instability in electrospinning of nanofibers. *Journal of applied physics*, 89(5):3018–3026, 2001.

[142] S. H. Yeo, H. Ogawa, D. Kahnfeld, and R. Schneider. Miniaturization perspectives of electrostatic propulsion for small spacecraft platforms. *Progress in Aerospace Sciences*, 126:100742, 2021.

[143] M. Yu, C. Wang, Y. Bai, Y. Wang, Q. Wang, and H. Liu. Combined effect of processing parameters on thermal stabilization of pan fibers. *Polym. Bull.*, 57:525–533, 01 2006.

[144] J. Yun, J.-H. Ahn, D.-I. Moon, Y.-K. Choi, and I. Park. Joule-heated and suspended silicon nanowire based sensor for low-power and stable hydrogen detection. *ACS applied materials & interfaces*, 11(45):42349–42357, 2019.

[145] J. Zeleny. The electrical discharge from liquid points, and a hydrostatic method of measuring the electric intensity at their surfaces. *Physical Review*, 3(2):69, 1914.

[146] J. Zeleny. Instability of electrified liquid surfaces. *Physical review*, 10(1):1, 1917.

[147] L. Zeng, T. Zhao, L. An, G. Zhao, X. Yan, and C. Jung. Graphene-supported platinum catalyst prepared with ionomer as surfactant for anion exchange membrane fuel cells. *Journal of Power Sources*, 275:506–515, 2015.

[148] B. Zhang, Y. Yu, Z. Huang, Y.-B. He, D. Jang, W.-S. Yoon, Y.-W. Mai, F. Kang, and J.-K. Kim. Exceptional electrochemical performance of freestanding electrospun carbon nanofiber anodes containing ultrafine sno x particles. *Energy & Environmental Science*, 5(12):9895–9902, 2012.

[149] L.-W. Zhang, H.-B. Fu, and Y.-F. Zhu. Efficient tio2 photocatalysts from surface hybridization of tio2 particles with graphite-like carbon. *Advanced Functional Materials*, 18(15):2180–2189, 2008.

[150] S. Zhang and K. Kawakami. One-step preparation of chitosan solid nanoparticles by electrospray deposition. *International journal of pharmaceutics*, 397(1-2):211–217, 2010.

[151] G. Zheng, W. Li, X. Wang, D. Wu, D. Sun, and L. Lin. Precision deposition of a nanofibre by near-field electrospinning. *Journal of Physics D: Applied Physics*, 43(41):415501, sep 2010.

[152] J. K. Ziemer, C. M. Marrese-Reading, S. M. Arestie, D. G. Conroy, S. D. Leifer, N. R. Demmons, M. Gamero-Castano, and R. E. Wirz. Lisa colloid microthruster technology development plan and progress. 2019.

Appendix A

Chapter 3

Table A.1: SiO_2 deposition recipe using PECVD

Recipe name	**SiO_2_Cisquella**
Calc Dep rate	65,18 nm/min
HF forward	20W
N_2O[sccm]	719
SiH_4 [sccm]	118,6
Temperature ºC	350
Pressure [mTorr]	1000

Table A.2: SiO_2 etch recipe using DRIE

Name	**SiO_2Etch_Cisquella**
Calculated Etch Rate	$\sim$ 30 nm/min
CHF_3[sccm]	75
Ar [sccm]	75
HF forward	200
LF frequency	350
APC/LPC (mTorr)	30

Table A.3: Si etch recipe using DRIE

Name	**Si_Bosch_Cisquella**	
Process	**Etch**	**Passivation**
Time(s)	7	5
C_4F_8[sccm]	1.4	100
SF_6 [sccm]	100	1.3
O_2 [sccm]	0	0
HF forward [W]	25	10
ICP forward [W]	500	500
DC Vias (V)	79.9	54
APC angle	76.2	73.6

Appendix B

Chapter 4

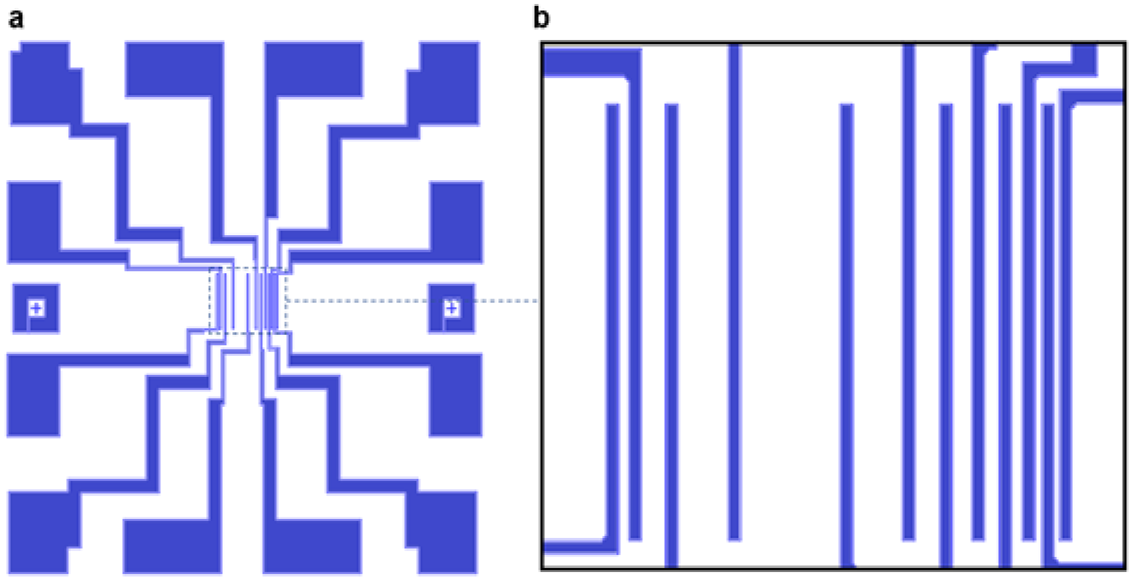

Figure B.1: (a) Overall design of the lithographically patterned structure for suspending the fibers deposited by near-field electrospinning. The scaffold walls in the center of the structure are continued into outer pads used for electrical connections. The cross marks are used as a reference for alignment with the near-field electrospinning source, so that the fibers can be suspended perpendicular to the walls. (b) Detail of the scaffold walls. The widths of the 11 gaps are, from left to right, 20, 50, 100, 200, 100, 50, 40, 30, 20 and 10 µm..

The concentrations of tungsten, oxygen, carbon and other elements present in the sample are computed by EDX standard quantification procedure using the Aztec software suite

(Oxford Instruments, Abingdon, United Kingdom). Copper, gallium and platinum are used as deconvolution elements to improve quantification accuracy. Gallium and platinum are present in the sample as a result of the FIB cutting procedure. The copper signal comes from the copper grid were the sample is mounted on.

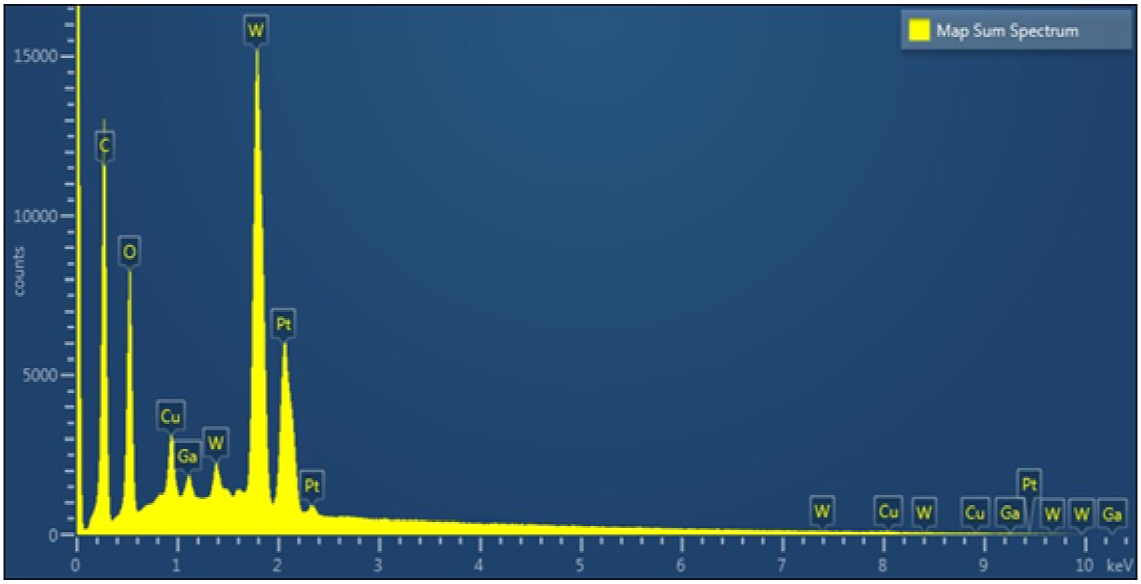

Figure B.2: Complete EDX spectrum from the cross section shown in Figure 6.c.

Element	Line Type	Apparent Concentration	Intensity Correction	Weight %	σ **(Weight** %)	Atomic %
Carbon	K series	0.61	0.52	27.89	0.18	66.82
Oxygen	K series	0.81	1.45	13.33	0.12	23.98
Tungsten	M series	1.95	0.8	58.79	0.21	9.2
Copper	L series	0.14	0.74	3.43	0.09	1.86
Gallium	L series	0.05	0.82	1.03	0.06	0.51
Platinum	M series	0.88	0.71	22.46	0.23	3.98
			Total	100		100

Table B.1: EDX quantitative analysis associated with the spectrum in Figure S6, including concentrations of the main elements present in the sample and the statistical error $\sigma oftheestimation$

d-spacings (Å)	Miller indexes **h k l**
5.38	0 1 1
3.84	0 0 2
3.42	0 1 2
2.69	0 2 2
2.23	-3 1 1
2.07	2 3 0
1.86	0 1 4
1.75	3 0 3
1.71	0 2 4
1.56	-2 2 4
1.54	-2 4 2

Table B.2: Plane d-spacings and corresponding Miller indixes hkl for the SAED pattern in Figures S7 and 7.d.